UNIVERSITY OF CALIFORNIA SAN DIEGO

From light to matter
- linear Breit-Wheeler pair creation and positron acceleration inside laser irradiated plasmas

A dissertation submitted in partial satisfaction of the
requirements for the degree
Doctor of Philosophy

in

Engineering Sciences (Engineering Physics)

by

Yutong He

Committee in charge:

Professor Alexey Arefiev, Chair
Professor Farhat Beg
Professor Sergei Krasheninnikov
Professor Kevin Quest
Professor Clifford Surko

2023

The Dissertation of Yutong He is approved, and it is acceptable in quality and form for publication on microfilm and electronically.

University of California San Diego

2023

DEDICATION

To my parents.

EPIGRAPH

誰念漂零久，漫贏得、幽懷難寫。

TABLE OF CONTENTS

LIST OF FIGURES

LIST OF TABLES

ACKNOWLEDGEMENTS

I would like to first express my earnest gratitude to my advisor, Professor Alexey Arefiev, for all of his support during, and even before my Ph.D. study and research. My Ph.D. career started from the generous offering of Professor Arefiev of the opportunity to work on the intriguing topics discussed in this dissertation. In the past five years, his support and inspiration, especially his enormous patience when I first started my Ph.D. research, have always been invaluable during my growing up towards a more matured researcher.

Next, I want to thank Dr. Zheng Gong for his mentoring in the beginning months of my Ph.D. which guided me through the initial difficulties of transforming from a student to a researcher. Looking back at myself in these old days, I couldn't imagine myself to have the same level of patience and good temper as Dr. Gong.

I am also grateful for other group members and colleagues at UCSD, other close collaborators, and funding manegares. Especially I would like to thank Professor Thomas Blackburn for his crucial inspirations on the choice of research topic, Professor Yasuhiko Sentoku and Mr. Kaoru Sugitomo for their irreplaceable work during our collaboration, and Professor Louise Willingale and Miss Tang for their generous invitation of the visiting of experimental facilities.

Simulations presented in this dissertation except those presented in Chapter 6 are performed on supercomputers at Texas Advanced Computing Center using particle-in-cell code Epoch. Special thanks to the research team at the University of Warwick who wrote Epoch, especially to the following main authors of Epoch: Dr. Chris Brady, Dr. Keith Bennett, Dr. Holger Schmitz, and Professor Christopher Ridgers. Research presented in this dissertation are primarily supported by Air Force Office of Scientific Research (AFOSR). Special thanks to Dr. Riq Parra and Dr. Andrew Stickrath from AFOSR for their consistent support of this research.

I also would like to thank all the committee members of this dissertation. It's a great honor of mine to have each one of them in my committee. Special thanks to Professor Sergei Krasheninnikov for his humor (proudly in Russian style) despite the fact that most of the times I could only pretend to understand the differential equations he wrote.

Writing here, a moist breeze of San Diego spring's night sneaks into this room I temporarily sublease, while a lone lamp is casting still shadows. Looking out of the window, I see traffic lights queuing along the road, and birds with colors I can not distinguish flying afar. Under the lamp, tea leaves of previous years gently unfold in a glass, releasing familiar freshness belonging to the past. Though, I may never know if what I am writing now would ever be read by them sometime in the future, I still want to thank my friends who accompanied me through this lonely journey. I want to thank Yingying Wang, who always lets me know she is there walking with me whenever I feel too tired to continue.

The last words of this acknowledgement I have saved for my parents. Without their unconditional love and support, I would never have been who I am today.

Chapter 2, in part, is a reprint of the material as it appears in *Dominance of γ-γ electron-positron pair creation in a plasma driven by high-intensity lasers* in Communications Physics, 4, 139, by Y. He, T. Blackburn, T. Toncian, and A. Arefiev, 2021. The dissertation author was the primary investigator and author of this paper.

Chapter 3, in part, is a reprint of the material as it appears in *A single-laser scheme for observation of linear Breit-Wheeler electron-positron pair creation* in New Journal of Physics, 23, 115005, by Y. He, I-L. Yeh, T. Blackburn, and A. Arefiev, 2021. The dissertation author was the primary investigator and author of this paper.

Chapter 4, in part, is a reprint of the material as it appears in *Achieving pair creation via linear and nonlinear Breit-Wheeler process in dense plasmas* in Physics of Plasmas, 29, 053105, by Y. He, T. Blackburn, T. Toncian, and A. Arefiev, 2022. The dissertation author was the primary investigator and author of this paper.

Chapter 5, in part, is a reprint of the material as it appears in *Algorithm for computing the electron-positron yield from the linear Breit-Wheeler process in high-intensity laser-plasma interactions* in Computer Physics Communications, 286, 108657, by Y. He, and A. Arefiev, 2023. The dissertation author was the primary investigator and author of this paper.

Chapter 6, in part, is a reprint of the material as it appears in *Positron generation*

and acceleration in a self-organized photon collider enabled by an ultraintense laser pulse, in Physical Review Letters, 131, 065102, by K. Sugimoto, Y. He, N. Iwata, I-L. Yeh, K. Tangtartharakul, A. Arefiev, and Y. Sentoku, 2023. The dissertation author helped conceptualizing the physical argument, and contributed test particle simulation results to help develop analytical model, and kinematic simulation results for the benchmark of the main results.

Chapter 7, in full, is currently being prepared for submission for publication of the material. The dissertation author was the primary investigator and author of this material.

VITA

2014–2018	Bachelor of Science in Physics, Bachelor of Science in Mathematics, University of California San Diego
2018–2023	Graduate Student Researcher, University of California San Diego
2023	Teaching Assistant, University of California San Diego
2018–2023	Doctor of Philosophy in Engineering Sciences (Engineering Physics), University of California San Diego

PUBLICATIONS

K. Sugimoto, **Y. He**, N. Iwata, I-L. Yeh, K. Tangtartharakul, A. Arefiev, Y. Sentoku "Positron generation and acceleration in a self-organized photon collider enabled by an ultra-intense laser pulse," *Physical Review Letters* 131, 065102 (2023)

Y. He, A. Arefiev, "Algorithm for computing the electron-positron yield from the linear Breit-Wheeler process in high-intensity laser-plasma interactions," *Computer Physics Communications* 286, 108657 (2023)

Y. He, T. Blackburn, T. Toncian, A. Arefiev, "Achieving pair creation via linear and nonlinear Breit-Wheeler process in dense plasmas," *Physics of Plasmas* 29, 053105 (2022)

Y. He, I-L. Yeh, T. Blackburn, A. Arefiev, "A single-laser scheme for observation of linear Breit-Wheeler electron-positron pair creation," *New Journal of Physics* 23, 115005 (2021)

Y. He, T. Blackburn, T. Toncian, A. Arefiev, "Dominance of γ-γ electron-positron pair creation in a plasma driven by high-intensity lasers," *Communications Physics* 4, 139 (2021)

ABSTRACT OF THE DISSERTATION

From light to matter
- linear Breit-Wheeler pair creation and positron acceleration inside laser irradiated plasmas

by

Yutong He

Doctor of Philosophy in Engineering Sciences (Engineering Physics)

University of California San Diego, 2023

Professor Alexey Arefiev, Chair

The linear Breit-Wheeler process ($\gamma\gamma \longrightarrow e^- e^+$) is one of the fundamental processes of quantum electrodynamics with many important astrophysical applications. However, almost a century has passed since it was theoretically proposed in 1934, and there is still no experimental observation of the linear Breit-Wheeler process using real photons. To produce linear Breit-Wheeler pairs, the collision of dense and energetic photons is required due to the small cross section and high photon energy threshold of this process, which is challenging to be achieved in laboratory conditions. On the other hand, the rapid development of laser technology has allowed the state-of-the-art laser facilities to produce laser pulses with intensities above $10^{22}\mathrm{Wcm}^{-2}$.

Such high-intensity, multi-PW, and multi-beam laser facilities open up brand new opportunities for the experimental realization of the linear Breit-Wheeler pair creation.

This dissertation presents two schemes for producing the linear Breit-Wheeler pairs using currently available laser pulses, with the assistance of numerical tools we developed. We show that utilizing collective plasma effects beneficial for the linear Breit-Wheeler pair creation, one can achieve pair yields that was previously thought to be unattainable at current laser intensities. Compared to the pair yields reported in previous studies, the pair yields in the systems we propose are approximately two to three orders of magnitudes larger. We further show that by interacting with the strong fields in the laser-plasma system, a large proportion of the produced positrons can be accelerated to form collimated energetic positron beams in hundreds-of-MeV to GeV level. Our studies not only propose possible schemes for the first experimental observation of the linear Breit-Wheeler process in laboratory, but have also emphasized the existence of the previously overlooked linear Breit-Wheeler process in high-intensity laser-plasma interaction systems. The self-organized formation of collimated positron beams may also serve as a potential mechanism for energetic positron source.

Introduction

1.1 Linear Breit-Wheeler process and previous studies

Linear Breit-Wheeler (linear BW) process, or the creation of an electron-positron pair by the collision and annihilation of two photons, is a fundamental prediction of the theory of quantum electrodynamics (QED) [1]. Besides being fundamental in theory, it also has many interesting and important applications in astrophysics, such as in understanding the opacity of the Universe [2] and the pair cascades in pulsar magnetospheres [3, 4, 5]. However, despite this process has been proposed for almost a century since 1934, the linear BW process has never been observed in a laboratory using real photons. The experimental difficulty comes from the smallness of its cross section (of the order of 10^{-30} m^2), and the high energy threshold of the two colliding photons (where the product of the two photon energy needs to be larger than $(0.511\ \text{MeV})^2$). To overcome these experimental difficulties, dense population of colliding photons in at least MeV range will be required, which, unfortunately, is challenging for traditional photon sources to produce.

On the other hand, with the fast development of laser technology and construction of facilities, the state-of-the-art laser facilities are able to deliver multi-beam, high-power, and ultra-intense laser pulses with intensities above 10^{22} Wcm^{-2} [6, 7, 8]. Under the strong fields of the laser pulses of such intensity, matter will be ionized into plasma state almost instantaneously, and electrons can be easily accelerated to ultra-relativistic regime. The interaction of these ultra-relativistic electrons with the strong fields in such systems then allows various strong-field QED processes to emerge, such as electron-positron pair creation and the emission of photons via

various processes. Such unprecedented regime, enabled by the interaction of state-of-the-art laser pulses with matter, leads to brand new opportunities of studying strong-field QED processes [9]. It is then natural to ask whether an opportunity for the first experimental observation of the linear BW process by real photons in history has been opened up by such ultra-intense laser plasma interactions.

Multiple works have been previously done on utilizing high intensity laser pulses to produce linear BW pairs. The experimental setups proposed in these works can be classified into two main types, according to the methods to surpass the four-momentum threshold ($\varepsilon_1\varepsilon_2 > (m_e c^2)^2 \approx (0.511\ \text{MeV})^2$ with $\varepsilon_{1,2}$ being the two photon energies and $m_e c^2$ being electron rest energy) of the linear BW process. In the first type which is shown in Figure 1.1(a), a GeV-level photon beam is produced and collide with photons in the keV energy range. The GeV-level photon beam is typically produced from the Bremsstrahlung process by a laser accelerated electron beam, and the keV photons are, for example, laser photons in an X-ray laser pulse [10] or photons produced from the blackbody radiation inside a laser heated hohlraum [11]. In the second type shown in Figure 1.1(b), two MeV-level photon beams, each of which is produced from a laser-plasma interaction system, collide in vacuum to produce linear BW pairs [12, 13]. In particular, multiple works have been done on using two MeV photon beams produced from two separate direct laser acceleration (DLA) systems [13, 14].

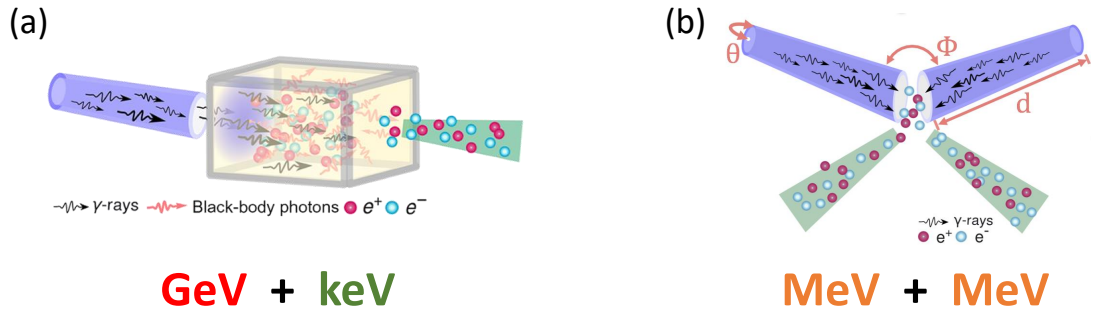

Figure 1.1. Schematic setups of systems proposed in previous researches.

1.2 Linear Breit-Wheeler pair creation inside plasmas: two setups

Examining these setups previously proposed as discussed in Sec. 1.1, we notice a few limitations which hinder the linear BW pair yields.

The first limitation is that in these setups, photons need to travel a long distance before they can collide with other photons. During their travelling, divergence of these photon beams significantly reduces the photon density when these photons collide. For example, in the second type of setups where two MeV-level photon beams collide, photon density n_γ in each beam scales like $n_\gamma \propto L^{-2}$, where L is the distance each photon beam has to travel before colliding with the other photon beam. So the total linear BW pair yield $N_{\text{lin}}^{\text{BW}} \propto n_\gamma^2 \propto L^{-4}$, and the -$4^{th}$ power dependence heavily suppresses the pair yields.

To improve the situation, the most direct idea would be to reduce L as much as possible, where ideally $L = 0$. The case $L = 0$ would corresponds to the physical picture that when a photon is emitted, this photon is already inside the region where photons are colliding with each other. This brings up one of the important underlying ideas of the research discussed in this dissertation, that in order to achieve pronounced linear BW pair creation, ideally, photon collisions should happen inside the plasma where the photons are produced.

The second limitation of these systems is that the potential of the energetic electrons to emit energetic photons may not haven been fully utilized. Radiation reaction (or nonlinear inverse Compton scattering, synchrotron emission) is one of the two main (alone with bremsstrahlung emission) mechanisms for the generation of high energy photons in these systems. As detailed in Sec. 9.3, one important method to leverage energetic photon emission via radiation reaction of electrons in laser-plasma systems is to collide energetic electrons with intense laser pulse. However, although more than one laser pulse is used in these previously proposed setups, each laser pulse is only responsible for generating one of the photon beams. As the scenario of electron-laser collision is not realized in these setups, the potential of energetic electrons on

emitting energetic photons is not fully exploited.

Following these two ideas, which are to collide photons inside plasmas and to leverage energetic photon emission by electron-laser collision, we considered the setup shown in Figure 1.2. In this setup, two intense laser pulses are injected into a solid channel target from two sides. Due to relativistic transparency described in Sec. 9.2, they can propagate in the classically over-dense plasma channel, and each of them drives a strong co-propagating energetic electron beam through the process of DLA (Sec. 9.1 provides a brief summary of DLA). As these two pulses collide in the center of the plasma channel, each of the two electron beams would collide with the other laser pulse, which significantly enhances the quantum nonlinearity parameter of these electrons, leading to the brilliant generation of energetic photons. Since photons from two electron beams are both emitted in the center of the plasma channel, the produced photons start to collide with each other immediately after they are produced. In this dissertation, we show that the linear BW pair yields in this setup can be orders of magnitude larger than what was previously proposed [11, 12], using currently available laser pulses.

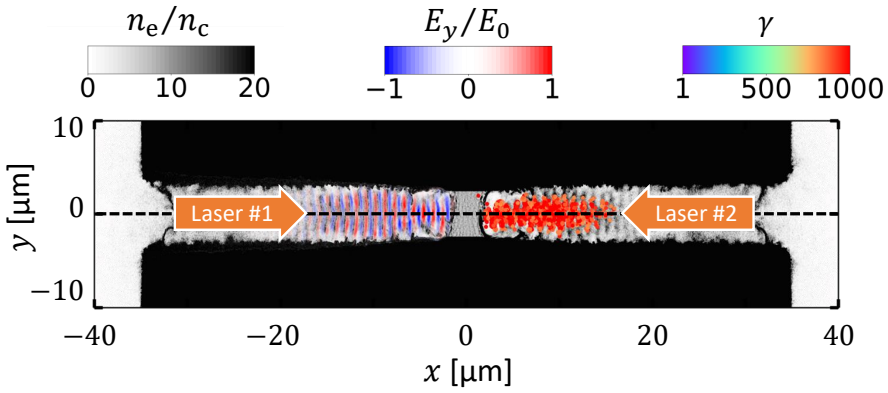

Figure 1.2. scheme of the dual laser setup. Electron density n_e (gray scale), transverse electric field of laser #1 E_y (color scale) and energetic electrons with $\gamma \geq 800$ accelerated by laser #2 (dots, colored by γ). Laser #1 generates a similar population of electrons moving to the right.

Nevertheless, in either the setup shown in Figure 1.2 or the setups previously proposed in other research, we still face the limitation that more than one laser pulse is required. In

another words, the collisional feature of the photon populations would need to come from the synchronization and aiming of different (laser or particle) sources. Experimentally, especially in the cases using high-power and high-intensity laser systems, the synchronization and aiming of pulses can be very challenging. Inspired by some of the findings during working on the dual laser setup we just presented, we also studied and proposed a single laser setup. In this setup, a self-organized photon collider can be achieved by using only one laser pulse with currently available parameters. Utilizing collective plasma effects in the laser-plasma system, the collisional geometry of energetic photons is realized. In this setup, the linear BW pair yields are approximately one orders of magnitude less than the one in the dual laser setup, but are still orders of magnitude larger than numbers reported in any of the previously proposed setups [11, 12], despite of the fact that only one laser pulse is used. The key for the large pair yields is the same with the one in the dual laser setup: colliding photons inside plasmas and leveraging energetic photon emission by electron-laser collision.

Our researches have proposed possible experimental schemes for the realization and observation of the linear BW pair creation using real photons. Moreover, they have also emphasized the previously overlooked existence of the linear BW process inside high-intensity laser-plasma systems. In fact, our numerical reesults show that in both setups, the linear Breit-Wheeler process can be the dominant electron-positron pair creation process over other pair creation processes (namely, the nonlinear Breit-Wheeler (nonlinear BW) process and the Bethe-Heitler (BH) process. Even without our results, one can still see that the linear BW process should not always be ignored when considering the electron-positron pair creation in laser-plasma systems from the following simply back-of-envelope calculation. Take, as comparison, the BH process which is the process of producing an electron-positron pair by the interaction of an energetic photon with the Coulomb field of a nucleus. Multiple experiments have shown the existence of the BH process in laser-matter experiments long before our research [15], and the numerical implementation of the BH process into kinetic simulation codes are also done [16]. The cross section of the BH process can be estimated as $\sigma_{\mathrm{BH}} \approx \alpha Z^2 r_e^2$, where $\alpha \approx 1/137$ is the

fine structure constant, Z is the atomic number, and $r_e \approx 2.8 \times 10^{-15}$ m is the clasical electron radius. On the other hand, the cross section of the linear BW process is approximately $\sigma_{\gamma\gamma} \approx r_e^2$. One can then estimate the linear BW pair yields (per unit volume per unit time) by $N_{\rm lin}^{\rm BW} \sim \sigma_{\gamma\gamma} n_\gamma^2 c$, and the BH pair yields (per unit volume per unit time) by $N_{\rm BH} \sim \sigma_{\rm BH} n_i n_\gamma c$, where n_γ is the density of photons in the MeV energy range and n_i is the ion density. For $n_i \approx n_e/Z$, one has the ratio between pair yields being $N_{\rm lin}^{\rm BW}/N_{\rm BH} \approx n_\gamma/\alpha Z n_e$. For an electron colliding with a laser pulse, the number of photons emitted is approximately $18\alpha a_0$, where $a_0 = e|E|/m_e c\omega$ is the normalized laser amplitude for the peak laser electric fields E and frequency ω, with e, m_e, c being electron charge, electron rest mass, and vacuum speed of light. Estimating $n_\gamma \approx 18\alpha a_0 n_e$, we find:

$$N_{\rm lin}^{\rm BW}/N_{\rm BH} \approx \frac{18 a_0}{Z}. \tag{1.1}$$

For typical values of $Z = 6$ for plastic targets, and $a_0 = 100$, the linear BW pair yields is about 300 times of the BH pair yields. Our estimation is, of course, rough. However, it shows the linear BW process may not be always neglected in high intensity laser-plasma systems, and possibly could even dominate other pair creation processes which agrees with our results shown in this dissertation.

1.3 Numerical tools and dynamics of positrons

In the beginning of our studying of the two setups, one of the major difficulties was the non-existence of numerical tools. Unlike other pair creation processes such as the nonlinear BW process or the BH process, it was commonly assumed that the existence of the linear BW process in laser-plasma systems is negligible, due to its seemingly small cross section. As a result, prior to our research, there were no numerical tools which could compute the linear BW pair yields inside a photon-emitting plasma. To conduct our study, we first developed a post-processing algorithm that could calculate the linear BW pair yields inside such a system. It was with the help of this post-processing algorithm were we able to calculate the large linear BW pair yields

in the two setups we considered and initiate further studies later.

After we validated the potential of our systems on producing the linear BW pairs by showing the large pair yields, our next question was how to detect these produced linear BW positrons. This question boils down to knowing the dynamics of these positrons in the laser-plasma system after they are produced. In collaboration with Professor Yasuhiko Sentoku's research group from Osaka University, we successfully implemented the linear BW process into particle-in-cell (PIC) codes. Professor Yasuhiko Sentoku's group implemented the linear BW process into the PIC code PICLS, and I implemented it into the PIC code Epoch [17] using similar methods. With the help of our newly developed computation tools, we found that in both the dual laser and the single laser setups, the produced linear BW positrons could form collimated energetic positron beams in up to GeV energy level by interacting with the in-situ strong fields in the system. It is important to point out that the formations of these energetic positron beams are self-organized which do not required additional experimental setups. These energetic positron beams not only facilitates the experimental detection of the linear BW positrons, but also are interesting as potential methods to serve as collimated Mev to GeV energy level positron sources for other researches in the future.

1.4 Organization of chapters

Organization of chapters in this dissertation is summarized in Figure 1.3.

In Chapter II, we present results on the linear BW pair creation in the dual laser setup. We show that around the order of 10^8 linear BW pairs can be produced in this setup by currently available laser pulses. Such high pair yields dominate over the ones by the nonlinear BW and BH processes, and are approximately 3 orders of magnitude larger than the linear BW pair yields reported in previous researches.

Following the discussion presented in Chapter II, in Chapter IV, we then examine the impact of the target parameters on the pair yields by the three pair creation processes. We show

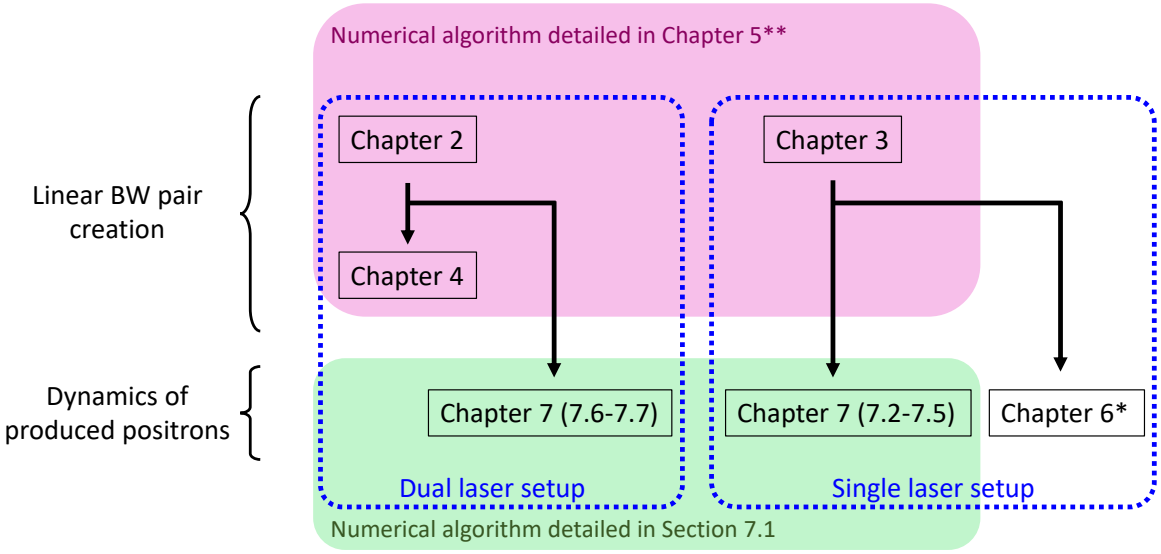

* Chapter 6 contains a description of the numerical algorithm used to obtain the results in the chapter.
** Chapter 5 can be neglected without affecting the understanding of the physics discussed in other chapters.

Figure 1.3. Organization of chapters in this dissertation.

that by changing the length and channel density of the targets which can be controlled during target manufacturing, we can manipulate the energy spectrum of the emitted energetic photons. Since the three pair creation processes favor photons in very different energy range, these target parameters can then be used as control knobs for the ratio of the pair yields by these three processes while keeping the laser parameters unchanged.

In Chapter III, we present the setup where around 10^7 linear BW pairs can be produced by using only a single laser pulse that is currently available. Similar to the dual laser setup, such pair yields dominate over the ones by other pair creation processes, and are around 2 orders of magnitude larger than the linear BW pair yields reported in previous researchers where multiple laser pulses were used.

Chapter V presents the numerical algorithm that was used to obtain the linear BW pair yields presented in Chapter II, III, and IV. Although this is a post-processing method, it was the only numerical tool capable of assessing the linear BW pair yields inside a photon emitting plasma until more advanced numerical tools were later developed by us with our collaborators.

Chapter V can be skipped without affecting the understanding of the physics discussed in other chapters.

In Chapter VI, we implement the linear BW process into PIC code PICLS. The newly implemented codes can simulate the produced linear BW positrons in PIC simulations, which allowed us to study the dynamics of the produced linear BW positrons. With the help of our newly developed codes, we discovered a positron acceleration mechanism in the single pulse setup which leads to the generation of collimated GeV-level positron beams without adding extra experimental stages.

Chapter VII presents results that are currently being prepared for publications. These results are obtained using an implementation of the linear BW process into the PIC code Epoch (Sec.7.1). In Sec.7.2, we present more details on the positron acceleration mechanism discussed in Chapter VI by focusing on the dynamics of individual linear BW positrons. We then benchmark our results discussed in Chapter VI and Sec. 7.2 by 3D PIC simulations in Sec. 7.3. In Sec. 7.4 and 7.5, we investigate the dynamics of the other two groups of energetic positrons we found in the single laser setup. These two groups, together with the one investigated in Chapter VI and Sec. 7.2, constitute the majority of energetic positrons we see so far in our simulations for the single laser setup. Following the discussion on the single laser setup, in Sec. 7.6, we confirm the DLA of the produced linear BW positrons in the dual laser system, which was a major postulation of Chapter II. We further show the positron heating by the overlapping of the two laser pulses, and briefly discuss how such heating impact the dynamics of positrons during their DLA. Finally, in Sec. 7.7, we investigat the impact of oblique laser injection on the linear BW pair creation in the dual laser setup, and benchmark our results in the dual laser setup by 3D PIC simulations.

Dominance of photon-photon electron-positron pair creation in a plasma driven by high-intensity lasers

Creation of electrons and positrons from light alone is a basic prediction of quantum electrodynamics, but yet to be observed. Our simulations show that the required conditions are achievable using a high-intensity two-beam laser facility and an advanced target design. Dual laser irradiation of a structured target produces high-density γ rays that then create $>10^8$ positrons at intensities of 2×10^{22} Wcm^{-2}. The unique feature of this setup is that the pair creation is primarily driven by the linear Breit-Wheeler process ($\gamma\gamma\rightarrow e^+e^-$), which dominates over the nonlinear Breit-Wheeler and Bethe-Heitler processes. The favorable scaling with laser intensity of the linear process prompts reconsideration of its neglect in simulation studies and also permits positron jet formation at experimentally feasible intensities. Simulations show that the positrons, confined by a quasistatic plasma magnetic field, may be accelerated by the lasers to energies >200 MeV.

2.1 Introduction

High-power lasers, focused close to the diffraction limit, create ultrastrong electromagnetic fields that can be harnessed to drive high fluxes of energetic particles and to study fundamental physical phenomena [9]. At intensities exceeding 10^{23} Wcm^{-2}, those energetic particles can drive nonlinear quantum-electrodynamical (QED) processes [18, 19] otherwise only found in extreme astrophysical environments [20, 21]. One such process is the creation of

electron-positron pairs from light alone. Whereas multiphoton (nonlinear) pair creation has been measured once, using an intense laser [22], the two-photon process ($\gamma\gamma \to e^+e^-$, referred to here as the linear Breit-Wheeler process [1]) has yet to be observed in the laboratory with real photons. As the probability of the nonlinear process grows nonperturbatively with increasing field strength [23, 24], it is expected to provide the dominant contribution to pair cascades in high-field environments, including laser-matter interactions beyond the current intensity frontier [25, 26] and pulsar magnetospheres [27].

The small size of the linear Breit-Wheeler cross section means that high photon flux is necessary for its observation. Achieving the necessary flux requires specialized experimental configurations [11, 12] and therefore its possible contribution to *in situ* electron-positron pair creation has hitherto been neglected in studies of high-intensity laser-matter interactions. However, these interactions create not only regions of ultrastrong electromagnetic field, but also high fluxes of accelerated particles, because relativistic effects mean that even a solid-density target can become transparent to intense laser light [28, 29]. In the situation of multiple colliding laser pulses, which is the most advantageous geometry for driving nonlinear QED cascades [25, 30, 31, 32], there are, as a consequence, dense, counterpropagating flashes of γ rays, and so the neglect of linear pair creation may not be appropriate.

Recent construction of multi-beam high-intensity laser facilities, such as Extreme Light Infrastructure Beamlines [33], Extreme Light Infrastructure Nuclear Physics (ELI-NP) [34, 6], and Apollon [35], and a significant progress in fabrication of μm-scale structured targets [36, 37] open up qualitatively novel regimes of pair production for exploration. Specifically, we show that a structured plasma target irradiated by two laser beams creates an environment where the linear process dominates over the nonlinear and over the Bethe-Heitler process. Remarkably, this regime does not require laser intensities beyond than what is currently available. At $I_0 < 5 \times 10^{22}$ Wcm^{-2}, the positron yield from the linear process is $\sim 10^9$, which is four orders of magnitude greater than that envisaged by Pike et al. [11] and Ribeyre et al. [12] These positrons are generated when two high-energy electron beams, accelerated by and copropagating with laser

pulses that are guided along a plasma channel, collide head-on, emitting synchrotron photons that collide with each other and the respective oncoming laser. Not only does this provide an opportunity to study the linear Breit-Wheeler process itself, which is of interest because of its role in astrophysics [2, 38, 39], but also the transition between linear and nonlinear-dominated pair cascades. In an astrophysical context, the balance between these two determines how a pulsar magnetosphere is filled with plasma; as in the laser-plasma scenario, the controlling factors are the field strength and photon flux [3, 4, 5, 40]. We also show that the positrons, created inside the plasma channel coterminously with the laser pulses, may be confined and accelerated to energies of hundreds of MeV, which raises the possibility of generating positron jets. The transverse confinement needed to accelerate positrons is provided by a slowly evolving plasma magnetic field. Crucially, it is the same field that enables acceleration of the ultra-relativistic electrons prior to the collision of the two laser pulses.

An overview of the key results of this chapter is shown in Fig. 2.1: we show that a structured target, when irradiated from both sides by intense laser pulses, enables the creation of a large yield of positrons through γ-γ collisions, i.e. the linear Breit-Wheeler process, at intensities well within the reach of existing high-power laser facilities. Two beams of electrons, accelerated along the plasma channel [Fig. 2.1(a)], collide with the respective counterpropagating laser [Fig. 2.1(b)], and emit γ rays that themselves collide to produce electron-positron pairs [Fig. 2.1(c)]. Furthermore, we show that a quasistatic magnetic field, created by the propagation of the lasers through the plasma channel [Fig. 2.1(c)], is sustained over sufficiently long times, and with the correct topology, to enable confinement and acceleration of the positrons, rather than electrons, so generated [Fig. 2.1(d) and (e)].

2.2 Results

The target configuration considered in this chapter is shown in Fig. 2.1(a). A structured plastic target with a pre-filled channel is irradiated from both sides by two 50-fs, high-intensity

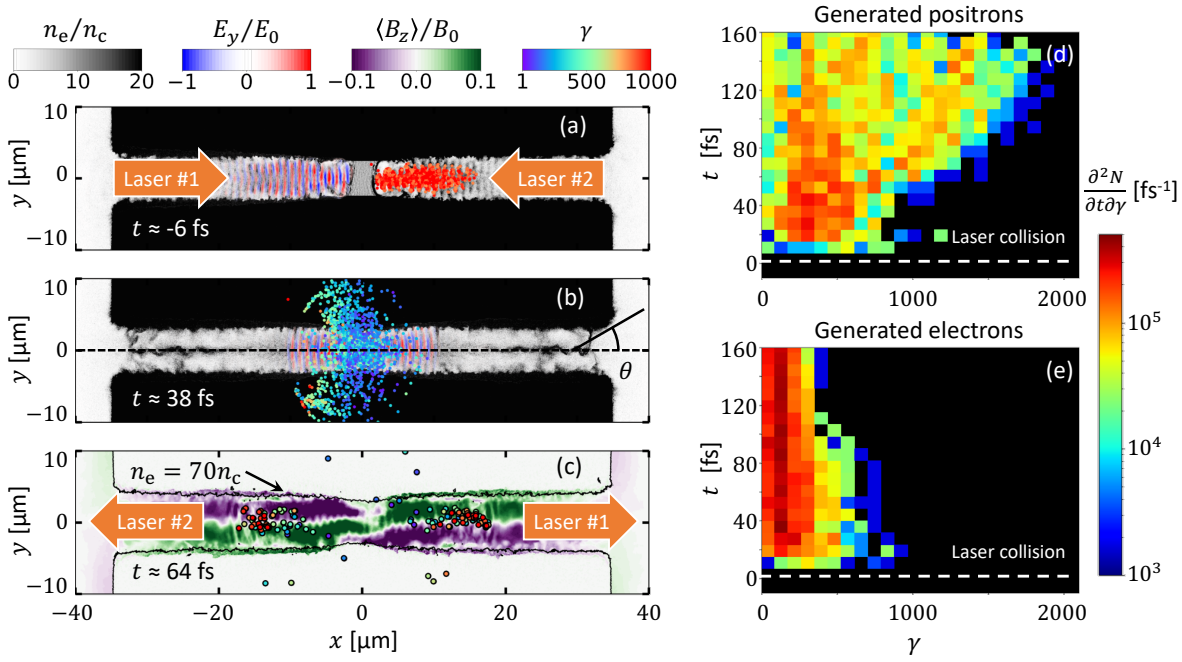

Figure 2.1. Positron production and acceleration in a structured plasma target. Results from a 2D-3V particle-in-cell (PIC) simulation of two laser pulses with $a_0 = 190$ irradiating a structured plasma target. (a) Electron density n_e (gray scale), transverse electric field of laser #1 E_y (color scale) and energetic electrons with $\gamma \geq 800$ accelerated by laser #2 (dots, colored by γ). (b) Total transverse electric field E_y (color scale) and electrons from panel (a). (c) Laser-accelerated positrons (points), confined by the quasistatic plasma magnetic field $\langle B_z \rangle$ (color scale). E_0 and B_0 are the peak laser electric and magnetic fields in vacuum. Time evolution of the energy spectra of (d) positrons and (e) electrons generated by nonlinear Breit-Wheeler pair creation: the horizontal, dashed lines indicates the time at which the lasers collide.

laser pulses that have the same peak normalized laser amplitude a_0, in the range $100 \leq a_0 \leq 190$. Here $a_0 = 0.85 I_0^{1/2} [10^{18} \mathrm{Wcm}^{-2}] \lambda_0 [\mu\mathrm{m}]$, where I_0 is the peak intensity of the laser and $\lambda_0 = 1$ μm its wavelength in vacuum. The target structure, where a channel of width $d_{ch} = 5$ μm and electron density $n_e = (a_0/100)3.8 n_c$ is embedded in a bulk with higher density $n_e = 100 n_c$, enables stable propagation [41] and alignment of the two lasers. Here $n_c = \pi m c^2/(e\lambda_0)^2$ is the so-called critical density, where e is the elementary charge, m is the electron mass, and c is the speed of light. At relativistic laser intensities ($a_0 \gg 1$), the cutoff density for the laser increases roughly linearly with a_0 due to relativistically induced transparency. Scaling the channel density with a_0 ensures that the optical properties of the channel and thus the phase velocity of the laser wave-fronts

are approximately unchanged with increase of a_0. Structured targets with empty channels have successfully been used in experiments [36, 37] and it is now possible to fabricate targets with prefilled channels, similar to those considered in this dissertation [42].

The interaction is simulated in 2D-3V with the fully relativistic particle-in-cell (PIC) code EPOCH [17], which includes Monte Carlo modules for quantum synchrotron radiation and nonlinear pair creation [43]. At each time-step, the quantum synchrotron radiation module computes the quantum nonlinearity parameter,

$$\chi \equiv \frac{\gamma}{E_{\mathrm{S}}}\sqrt{\left(\mathbf{E}+\frac{1}{\mathrm{c}}[\mathbf{v}\times\mathbf{B}]\right)^2-\frac{1}{\mathrm{c}^2}(\mathbf{E}\cdot\mathbf{v})^2}, \tag{2.1}$$

for each charged macro-particle using the electric and magnetic fields ($\mathbf{E}$ and $\mathbf{B}$) at the particle location, as well as the particle relativistic factor γ and velocity $\mathbf{v}$. Here $E_{\mathrm{S}} \approx 1.3 \times 10^{18}$ V/m is the Schwinger field [44, 45, 46]. The parameter χ controls the total radiation power and the energy spectrum of the emitted photons. In the quantum regime $\chi \gtrsim 1$, which is reached in the work presented in this chapter, it is necessary to take into account the recoil experienced by the particle when emitting individual photons. This is done self-consistently by the PIC simulation, which uses the Monte Carlo algorithm described by Ridgers et al. [43] and Gonoskov et al. [47] Note that, since the ion species is fully ionized carbon, Bethe-Heitler pair creation, already demonstrated in laser-driven experiments [15, 48], may be neglected. Detailed simulation and target parameters are provided in the Methods section. All the results presented in this chapter have been appropriately normalized by taking the size of the ignored dimension to be equal to the channel width d_{ch}, i.e. 5 μm.

2.2.1 Electron acceleration

The plasma channel, being relativistically transparent to the intense laser light [28, 29], acts as an optical waveguide. The laser pulses propagate with nearly constant transverse size through the channel, pushing plasma electrons forward. This longitudinal current generates

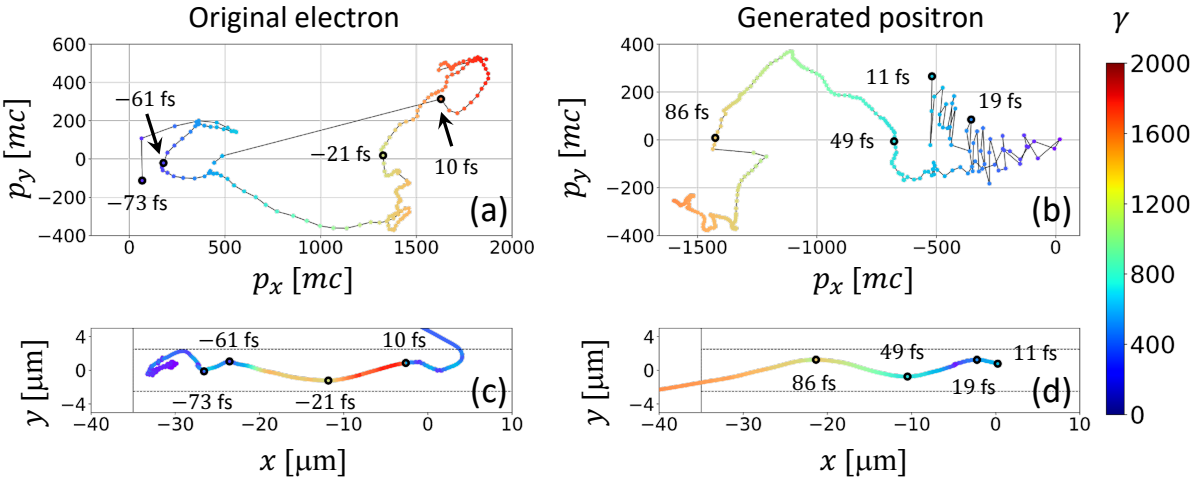

Figure 2.2. Trajectories of an accelerated plasma electron and a generated positron in spatial and phase space. Trajectories of an accelerated plasma electron and a generated positron from the 2D PIC simulation shown in Fig. 2.1: (a, b) tranverse momenta p_x, p_y and (c, d) position in the x-y plane. Color coding denotes the magnitude of the relativistic factor γ. The vertical solid line is the initial position of the left edge of the target. The horizontal dashed lines show the initial location of the channel walls. The timestep between the colored markers is 0.5 fs. Timestamps are provided for selected markers (shown as dark circles) to facilitate comparison between trajectories in (p_x, p_y)-space and (x, y)-space. To improve visibility, the electron trajectory in (a) is shown for -73 fs $\leq t \leq 11$ fs.

a slowly evolving, azimuthal magnetic field with peak magnitude 0.6 MT (30% of the laser magnetic field strength) at $a_0 = 190$, as shown in Fig. 2.1(c). The magnetic field enables confinement and direct laser acceleration of the electrons [41, 49]. After propagating for $\sim$30 μm along the channel, laser #2 in Fig. 2.1(a) has accelerated a left-moving, high-energy, high-charge electron beam that performs transverse oscillations of amplitude $\sim$2 μm: the number of electrons with relativistic factor $\gamma > 800$ is 4×10^{11}, which is equivalent to a charge of 64 nC. Laser #1 generates a similar population of electrons moving to the right, with a representative electron trajectory shown in Fig. 2.2(a) and (c).

The plasma magnetic field has an essential role in enabling generation of ultrarelativistic electrons. Transverse deflections by the magnetic field keep p_y antiparallel to the transverse electric field E_y of the laser, despite the oscillation of the latter. As a result, the electron continues to gain energy while moving along the channel and performing transverse oscillations, as may

be seen in Fig. 2.2(a) and Fig. 2.2(c). In the absence of the magnetic field, the oscillations of E_y would terminate the energy gain prematurely. The magnetic field of the plasma has to be sufficiently strong to ensure that the electron deflections occur on the same time scale as the oscillations of E_y. This criterion can be formulated in terms of the longitudinal plasma current [49]. Note that the same confinement and acceleration would occur for a positron, if the positron were moving in the opposite direction along the x-axis, as its charge has opposite sign. This is shown in Fig. 2.2(b) and (d) and discussed in more detail in Positron acceleration. The evolution of the energy of the electron population as a whole is shown in Fig. 2.3, where we see the bulk of the electrons reach energies of several hundreds of MeV.

2.2.2 Radiation emission

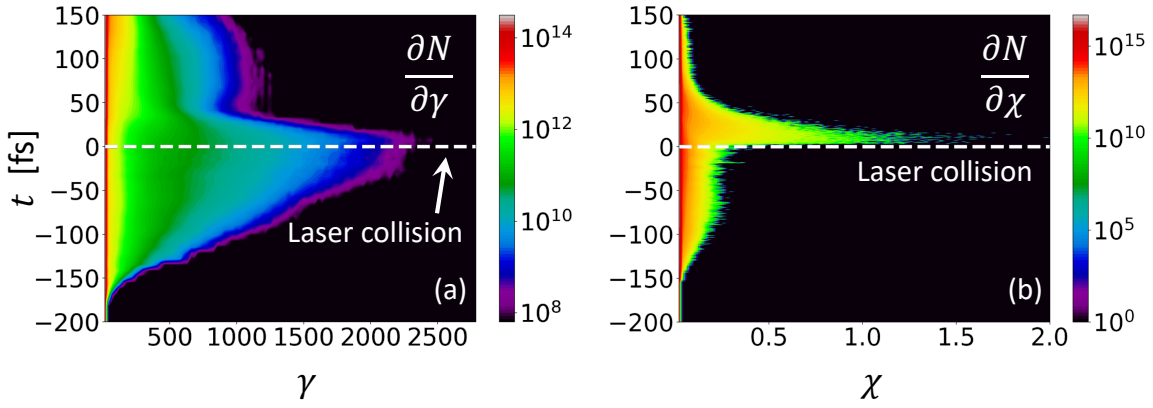

Figure 2.3. Growth and collapse of the electron γ and χ as the laser collision occurs. Time evolution of the distributions of the (a) electron relativistic factor γ and (b) quantum nonlinearity parameter χ, defined by Eq. (2.1), for the 2D PIC simulation shown in Fig. 2.1. The two laser pulses have $a_0 = 190$ and collide at $t = 0$, which is shown by the horizontal dashed lines.

The target length is such that no appreciable depletion of the laser pulses occurs by the time they reach the midplane ($x = 0$), $t = 0$. Here, the high-energy electron beams collide head-on with the respective oncoming laser pulse, each of which has an intensity at least as large as its initial value (the magnitude can increase slightly due to pulse shaping during propagation along the channel). This configuration maximizes the quantum nonlinearity parameter χ for the electrons, as the two terms under the square root in Eq. (2.1) are additive for counterpropagation.

(In copropagation, by contrast, they almost cancel each other, which is why radiation prior to the collision, when electrons propagate in the same direction as the accelerating laser pulse, is driven primarily by the plasma magnetic field.) Figure 2.3(a), as well as Figure 2.1(b), shows the impact of the collision on the energetic electrons from Fig. 2.1(a): they radiate away a substantial fraction of the energy they gained during the acceleration phase and are scattered out of the channel. Similar behavior is shown in Fig. 2.2(c): the electron encounters the counterpropagating laser beam at about $t = 10$ fs and then its energy decreases rapidly. As is shown in Fig. 2.3(b), $\chi \lesssim 0.25$ before the collision occurs; immediately thereafter, the cancellation is eliminated, χ increases rapidly to approximately 1.25, and then it collapses due to the radiative energy loss.

The configuration under consideration here therefore represents a micron-scale, plasma-based realization of an all-optical laser–electron-beam collision [30]. This geometry is the subject of theoretical [50, 51, 52] and experimental [53, 54] investigation into radiative energy loss in the quantum regime, as well as nonlinear pair creation [55]. It is worth emphasizing that the use of the structured target has two key benefits compared to the commonly used gas targets: automatic alignment of the colliding electrons with an oncoming laser beam and a considerably higher density of colliding electrons.

The observed increase in χ during the electron-laser collision increases the radiation power of the individual electrons. The conversion efficiency of the laser energy into photons with energies 100 keV $\leq \varepsilon_\gamma \leq$ 10 MeV is shown in Fig. 2.4(a) over a wide range of a_0. We are interested in the photons in this energy range because these are the photons that participate in the linear Breit-Wheeler process in our setup (see Section 2.5.6). As expected, there is a significant increase in the conversion rate caused by the electron-laser collision. The angularly resolved spectrum of the emitted photons is shown in Fig. 2.4(b). There are approximately 2×10^{14} photons with energies between 100 keV and 10 MeV and with $90^\circ \leq \theta \leq 180^\circ$. This is essentially half of the energetic photons emitted by the left-moving electrons (the other half is emitted with $-180^\circ \leq \theta \leq -90^\circ$ and has a similar spectrum). Furthermore, this emission occurs in a highly localized region, which leads to the marked increase in photon density shown

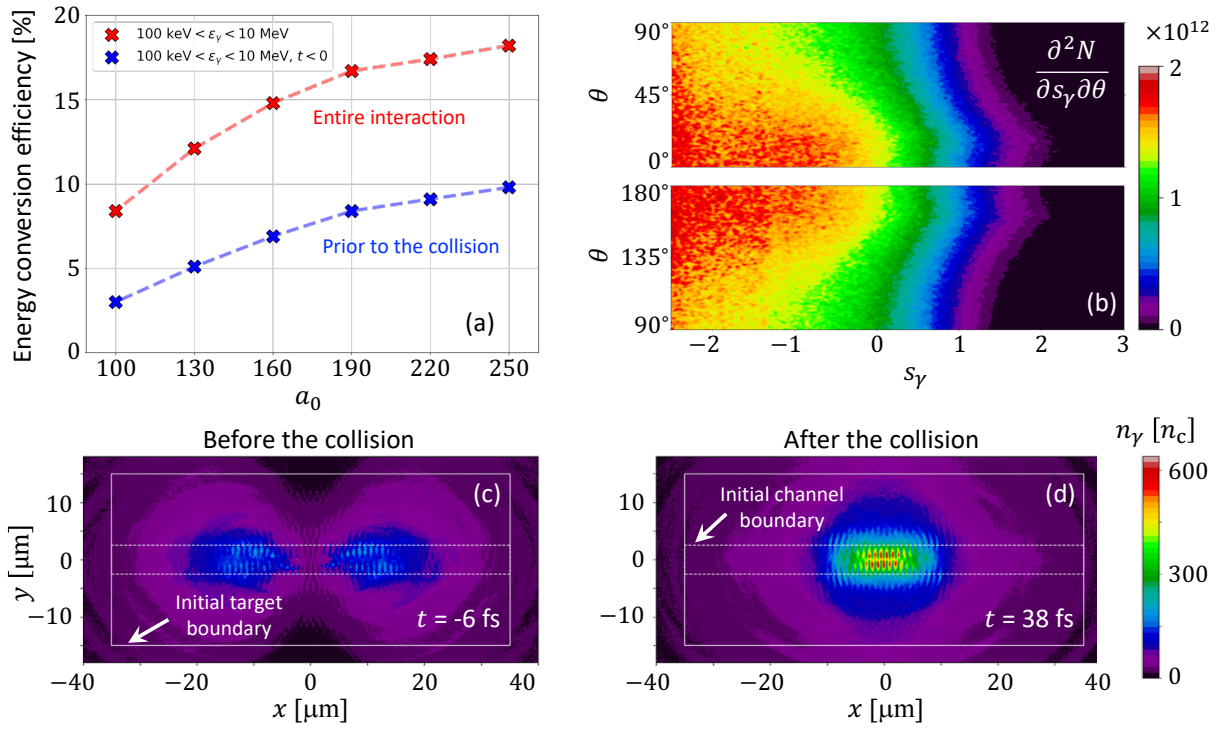

Figure 2.4. MeV photon emission inside the structured target. Results from the 2D PIC simulation shown in Fig. 2.1, where the two counterpropagating lasers have $a_0 = 190$. (a) Conversion efficiency of the laser energy into γ rays with energies 100 keV $\leq \varepsilon_\gamma \leq$ 10 MeV: (blue markers) before the two lasers collide at $x = 0$ and (red markers) over the whole laser-target interaction. (b) Energy-angle spectrum, $\partial^2 N/(\partial s_\gamma \partial\theta)$ [$^{\circ -1}$], of the photons emitted inside the channel. Here θ is the angle defined in Fig. 2.1(b) and $s_\gamma \equiv \log_{10}(\varepsilon_\gamma[\text{MeV}])$. (The spectrum for $-180^\circ \leq \theta \leq 0^\circ$ is similar.) (c) and (d) The density of photons with energy $\varepsilon_\gamma \geq 1$ keV, in units of the critical density n_c, before and after the laser-laser collision.

in Fig. 2.4(c) and (d) for the case where $a_0 = 190$.

2.2.3 Positron acceleration

The photons emitted by one electron beam collide with both the oncoming laser and the photons emitted by the other electron beam. The former drives electron-positron pair creation by the nonlinear Breit-Wheeler process, $\gamma \xrightarrow{\text{EM field}} e^+e^-$ [18, 24]: at $a_0 = 190$, our simulations predict a yield of 5×10^8 pairs.

The positrons subsequently undergo direct laser acceleration in much the way as the electrons: PIC simulations show that the typical relativistic factor of a right-moving positron

increases to $\gamma \approx 1000$ as it propagates from $x \approx 0$ to $x \approx 20$ μm. This is illustrated in Fig. 2.1(c) and corroborated by the time evolution of the positron energy spectrum shown in Fig. 2.1(d). A representative trajectory for a positron moving from the central region towards the left target boundary is shown in Fig. 2.2(d). Acceleration is made possible by the plasma magnetic field, which is confining (on the left-hand side of the target) for electrons moving to the right, or equivalently, positrons moving to the left [compare Fig. 2.2(c) and Fig. 2.2(d)]. Crucially, Fig. 2.1(c) shows that this magnetic field polarity is preserved well after the lasers and electron beams collide. This is why, after the two laser pulses collide and pass through each other, they can accelerate the positrons, but not the electrons, created in by photon-photon collisions, as seen in Fig. 2.1(e). The generated electrons are not transversely confined in our magnetic field configuration when moving from the center towards either of the channel openings. However, the continued propagation of the lasers along the channel raises the possibility of accelerating positron jets, if there is sufficient pair creation in the channel center.

2.2.4 Competing positron generation mechanisms

We now show that there is prolific pair creation in the channel center, and furthermore that it is dominated by the *linear* Breit-Wheeler process. The cross section is [1]:

$$\sigma_{\gamma\gamma} = \frac{\pi r_e^2}{2\varsigma}\left[(3-\beta^4)\ln\left(\frac{1+\beta}{1-\beta}\right) - 2\beta(2-\beta^2)\right], \tag{2.2}$$

where $r_e = e^2/(mc^2)$ is the classical electron radius, $\beta = \sqrt{1-1/\varsigma}$, and $\sqrt{\varsigma}$ is the normalized center-of-mass energy, $\varsigma = \varepsilon_1\varepsilon_2(1-\cos\psi)/(2m^2c^4)$, for two photons with energy $\varepsilon_{1,2}$ colliding at angle ψ. Equation (2.2) is the cross section for two-photon pair creation in vacuum: while it is modified by a strong electromagnetic field [56, 57, 58, 59], these corrections, which scale as $(\chi_\gamma/\varsigma)^2$ for photon quantum nonlinearity parameter χ_γ [60], are negligible for the scenario under consideration here (see Sec. 2.5.5 in the Appendices of this chapter for details).

We take as a representative value $\sigma_{\gamma\gamma} \approx 2r_e^2$ (approximately its maximum, at $\varsigma \approx 2$)

and assume that we have two photon populations of number density n_γ, colliding head-on in a volume of length $c\tau$ (the laser pulse length) and width $d_{\rm ch}$ (the width of the channel). The number of photons (in each beam) is $N_\gamma \approx 10^9 \lambda_0[\mu\text{m}] P_\gamma (n_{\rm e}/n_{\rm c})(c\tau/\lambda_0)(d_{\rm ch}/\lambda_0)^2$, where P_γ is the number of photons emitted per electron, $n_{\rm e}$ is the electron number density and λ_0 is the laser wavelength. The number of positrons produced, $N_{\rm lin}^{\rm BW} = 2N_\gamma^2 \sigma_{\gamma\gamma}/d_{\rm ch}^2$, follows as $N_{\rm lin}^{\rm BW} \approx 40 P_\gamma^2 (n_{\rm e}/n_{\rm c})^2 (c\tau/\lambda_0)^2 (d_{\rm ch}/\lambda_0)^2$. The physical parameters are $n_{\rm e} = 7n_{\rm c}$, $\tau = 50$ fs, $d_{\rm ch} = 5$ μm, and $\lambda_0 = 1$ μm. The number of photons emitted per laser period by a counterpropagating electron is $P_\gamma \approx 18\alpha a_0$, where $\alpha \simeq 1/137$ is the fine-structure constant. By setting $P_\gamma = 20$, we obtain a total number of photons, $2N_\gamma \approx 1.3 \times 10^{14}$, which is approximately consistent with the simulation result. As a consequence, we predict that $N_{\rm lin}^{\rm BW} \approx 7 \times 10^9$. Given that $P_\gamma \propto a_0$ and $n_{\rm e} \propto a_0$, we predict a scaling of $N_{\rm lin}^{\rm BW} \propto a_0^4$.

This is considerably larger than the number of pairs expected from the nonlinear Breit-Wheeler process; moreover, as the probability rate for the latter is exponentially suppressed with decreasing a_0, we expect the yield to be much more sensitive to reductions in laser intensity. The potential dominance of the linear process motivates a precise computation, which takes into the account the energy, angle and temporal dependence of the photon emission.

However, direct implementation of the linear Breit-Wheeler process in a PIC code is a significant computational challenge, as it involves binary collisions of macroparticles and the interaction must be simulated in at least 2D. The simulation at $a_0 = 190$ generates $\sim 10^8$ macrophotons in the energy range relevant for linear Breit-Wheeler pair creation and therefore $\sim 10^{16}$ possible pairings. This can be reduced by using bounding volume hierarchies [61], which is effective if the photon emission and the pair creation are well-separated in time and space. In our case, there is no such separation. As such, we postprocess the simulation output to obtain the yield of linear Breit-Wheeler pairs, using the algorithm described in Sec. 2.5.6, Sec. 2.5.7, and more completely in Chapter V. Note that the photons used to compute this yield are the same photons used by the simulation to compute the yield of *nonlinear* Breit-Wheeler pairs. As such, while the photon number would change if the simulation were performed in 3D rather than 2D,

the yield of both processes would be affected in a similar way.

2.2.5 Positron yield

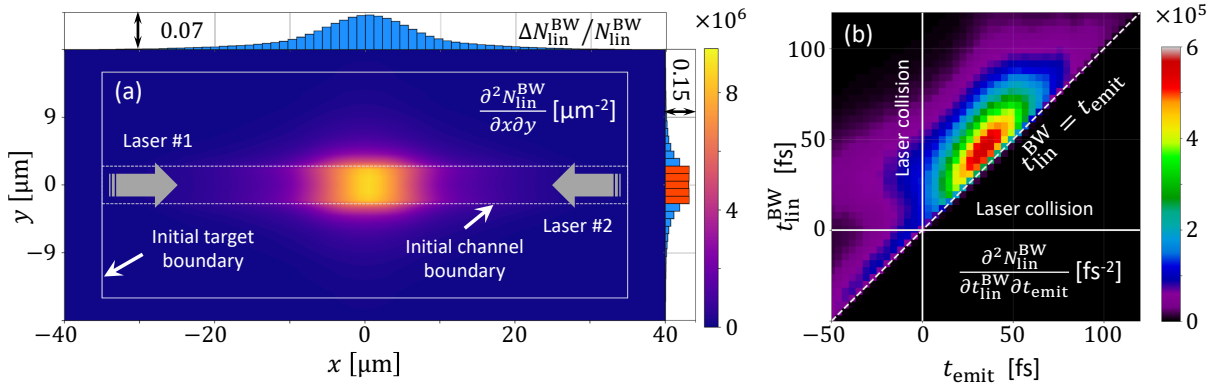

Figure 2.5. Distribution of linear Breit-Wheeler pairs upon their creation. (a) Probability density that an electron-positron pair is created by the linear Breit-Wheeler process at longitudinal and transverse coordinate x and y. The density integrated over x (y), and normalized to the total number of pairs, is shown to the right (above). (b) Probability density that an electron-positron pair is created by the linear Breit-Wheeler process at time $t_{\rm lin}^{\rm BW}$, by photons that were emitted at times $t_{\rm emit}$. The density includes a normalizing factor of $1/2$ because each pair has two parent photons. Both plots are obtained by post-processing the 2D PIC simulation from Fig. 2.1, where the lasers have $a_0 = 190$, using the algorithm described in Chapter V. An equivalent for the nonlinear process is given in Sec. 2.5.3.

The location and time that pairs are created by the linear process, as determined by this algorithm for the case that $a_0 = 190$, are shown in Fig. 2.5(a) and Fig. 2.5(b) respectively. Approximately 59% of the pairs are created inside the original channel boundary. The majority (74%) of pairs are created by photons emitted after $t = 0$, when the high-energy electrons collide with the respective counterpropagating laser. There is a smaller contribution from photons that are emitted during the acceleration phase, $t_{\rm emit} < 0$; radiation in this case is driven by the plasma magnetic field, because the energetic electrons are moving in the same direction as the laser [41, 13]. The dominance of the post-collision contribution is caused by the increase in the quantum parameter χ for counterpropagation. The fact the pair creation overlaps with the laser pulses (in both time and space) indicates that the positrons could be accelerated out of the channel, as the magnetic field, shown in Fig. 2.1(c), has the correct orientation to confine them.

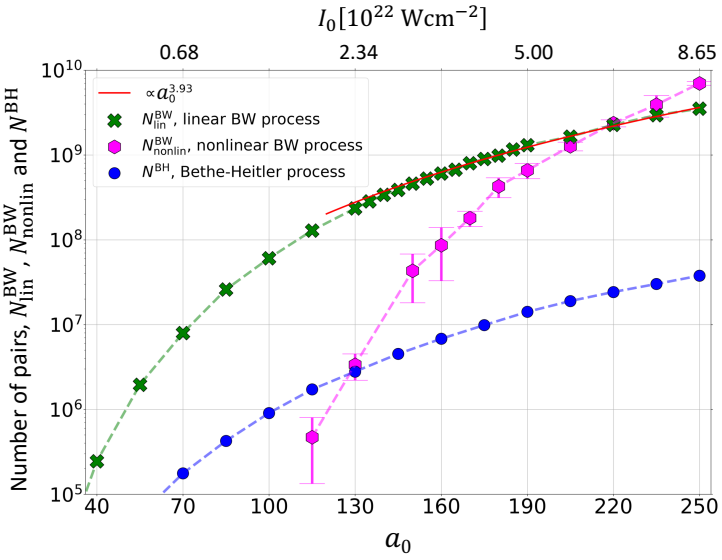

Figure 2.6. Number of electron-positron pairs created by the three most important mechanisms. The number of electron-positron pairs created by the linear, $N_{\mathrm{lin}}^{\mathrm{BW}}$, and nonlinear, $N_{\mathrm{nonlin}}^{\mathrm{BW}}$, Breit-Wheeler processes (green crosses and magenta markers, respectively), for the setup shown in Fig. 2.1, at given normalized laser amplitude a_0 (and equivalent peak intensity I_0). Error bars on the nonlinear results indicate statistical uncertainties (at one standard deviation): see text for details. The estimated background, electron-positron pairs produced by the Bethe-Heitler process, N^{BH}, is shown by blue circles. The nonlinear Breit-Wheeler pair yield is calculated directly by the PIC code, whereas the linear Breit-Wheeler and Bethe-Heitler pair yields are obtained by post-processing, as described in Sec. 2.5.4.

The pair yields for the linear and nonlinear processes are compared in Fig. 2.6. The results for the latter are obtained by performing four simulation runs for each value of a_0 with different random seeds: points and error bars give the mean and standard deviation obtained, respectively. At $a_0 < 145$, fewer than ten macropositrons are generated per run, so the corresponding data points are not shown. Our analytical estimates for linear Breit-Wheeler pair creation lead us to expect a yield that scales as a_0^4: this is consistent with a power-law fit to the data in Fig. 2.6, which gives a scaling $\propto a_0^m$, where $m \approx 3.93$. We find that the linear pair yield is significantly larger for $a_0 < 190$.

The number of positrons produced by the linear Breit-Wheeler process exceeds 10^6 even for $a_0 = 50$, equivalent to $I_0 = 3.4 \times 10^{21}$ Wcm^{-2}, which is well in reach of today's high-power laser facilities. In order to determine whether this is sufficient to be observed, we estimate

the number of pairs produced by the Bethe-Heitler process, which is the principal source of background. In this process, a γ ray with energy $\hbar\omega > 2mc^2$ creates an electron-positron pair by interacting with the Coulomb field of an atomic nucleus. The calculation is described in detail in Sec. 2.5.4. We sum the pair creation probabilities for each simulated photon, taking into account the distance each photon travels in the plasma channel, to obtain the blue circles in Fig. 2.6. The Bethe-Heitler background is smaller than the linear Breit-Wheeler signal by approximately two orders of magnitude, which supports the feasibility of using a plasma channel as a platform for investigating fundamental QED effects.

2.3 Discussion

We have shown that laser-plasma interactions provide a platform to generate and accelerate positrons, created entirely by light and light, at intensities that are within the reach of current high-power laser facilities. While previous research into pair creation at high intensity has focused largely on the nonlinear Breit-Wheeler process, we show that the high density of photons afforded by a laser-plasma interaction can make the linear process dominant instead. As such, the geometry we consider has the potential to enable the first experimental measurement of two-photon pair creation, driven entirely by real photons. More broadly, it motivates reconsideration of the neglect of two-particle interactions in simulations of dense, laser-irradiated plasmas. Such interactions will form a major component of the physics investigated in upcoming high-power laser facilities. From the theory perspective, our results also motivate investigation of field-driven corrections to the two-photon cross section. The theory for the inverse process, pair annihiliation to two photons, has recently been revisited [62].

One of our surprising findings, besides the dominance of the linear Breit-Wheeler process, is that the plasma magnetic field preserves its polarity after the two laser pulses collide and pass through each other. The polarity of the magnetic field enables transverse confinement of the positrons within the channel and their acceleration by one of the laser pulses to energies

approaching 1 GeV. We have confirmed this directly for the positrons generated via the nonlinear Breit-Wheeler process. This should also be the case for the positrons generated via the dominant linear Breit-Wheeler process, because the particles are created inside the channel magnetic field in the presence of a laser pulse, which are the prerequisites for the direct laser acceleration. We therefore expect the positrons to be ejected from the target in the form of collimated jets. (In Chapter VII, we will confirm this expectation.) The collimation should aid positron detection outside of the target. Moreover, their detection at lower values of a_0 should be a clear indicator of the linear Breit-Wheeler process being the source, as the nonlinear process is heavily suppressed for $a_0 \lesssim 150$.

Finally, we point out that our observations regarding the dominance of the linear Breit-Wheeler process apply to a range of channel densities. In our simulations, the electron density in the channel is set at $n_{\mathrm{ch}} = (a_0/100)3.8n_{\mathrm{c}}$, such that it increases linearly with a_0 during the intensity scan. Two channel density scans provided in Sec. 2.5.2 show that our observations hold for channel densities that are within a $\pm 20\%$ window of n_{ch}. A more detailed scan on channel density and target length is also presented in Chapter IV.

2.4 Acknowledgement

Chapter 2, in part, is a reprint of the material as it appears in *Dominance of γ-γ electron-positron pair creation in a plasma driven by high-intensity lasers* in Communications Physics, 4, 139, by Y. He, T. Blackburn, T. Toncian, and A. Arefiev, 2021. The dissertation author was the primary investigator and author of this paper.

This research was supported by AFOSR (Grant No. FA9550-17-1-0382). Simulations were performed with EPOCH (developed under UK EPSRC Grants EP/G054950/1, EP/G056803/1, EP/G055165/1 and EP/ M022463/1) using high performance computing resources provided by TACC.

PIC simulations were performed with the open-source, open-access PIC code EPOCH

[17]. The photon-photon collision code is based on the algorithm detailed in Sec. 2.5.6, Sec. 2.5.7, and Chapter V.

2.5 Appendices

2.5.1 Particle-in-cell simulations

Table 2.1 provides detailed parameters for the simulations presented in this chapter. Simulations in this chapter were carried out using the fully relativistic particle-in-cell code EPOCH [17]. All our simulations in this chapter are 2D-3V.

The axis of the structured target is aligned with the axis of the counterpropagating lasers (laser #1 and laser #2) at $y = 0$. The target is initialized as a fully-ionized plasma with carbon ions. The bulk electron density is constant during the intensity scan while the electron density in the channel is set at $n_{\mathrm{e}} = (a_0/100)3.8n_{\mathrm{c}}$. Each laser is focused at the corresponding channel opening. The lasers are linearly polarized with the electric field being in the plane of the simulation. In the absence of the target, the lasers have the same Gaussian profile in the focal spot with the same Gaussian temporal profile.

We performed additional runs at $a_0 = 190$ with higher spatial resolutions (40 by 40 cells per μm and 80 by 80 cells per μm). There are no significant variations in the photon spectra for multi-MeV photons and for photons with energies above 50 keV. The electrons that emit energetic photons, as the one whose trajectories in physical and momentum space are shown in Fig. 2.2(a) and Fig. 2.2(c), undergo their energy gain without alternating deceleration to non-relativistic energies and re-acceleration. This is likely the reason why they are not subject to a more severe constraint [63, 64, 65] that requires for the cell-size/time-step to be reduced according to the $1/a_0$ scaling in order to achieve convergence.

Table 2.1. 2D PIC simulation parameters.

Laser parameters	
Normalized field amplitude	$a_0 = 100 - 190$
Peak intensity range	$I_0 = 1.4 - 4.9 \times 10^{22}$ W/cm^2
Wavelength	$\lambda_0 = 1$ μm
Focal plane of laser #1	$x = -35$ μm
Focal plane of laser #2	$x = +35$ μm
Laser profile (longitudinal and transverse)	Gaussian
Pulse duration (full width at half maximum for intensity)	50 fs
Focal spot size (full width at half maximum for intensity)	3.6 μm

Target parameters	
Target thickness (along y)	30 μm
Target length (along x)	70 μm
Channel width	$d_{\mathrm{ch}} = 5$ μm
Composition	C^{+6} and electrons
Channel density	$n_{\mathrm{e}} = 3.8 - 7.1 n_{\mathrm{c}}$
Bulk density	$n_{\mathrm{e}} = 100 n_{\mathrm{c}}$

Other parameters	
Simulation box	80 μm in x; 36 μm in y
Spatial resolution	40 cells per μm in x 20 cells per μm in y
Macro-particles per cell	40 for electrons 20 for carbon ions

2.5.2 Channel density scan

In our simulations, the electron density in the channel is set at $n_{\mathrm{ch}} = (a_0/100)3.8 n_{\mathrm{c}}$. This value was chosen to achieve prolonged laser propagation inside the channel, such that each laser pulse can generate ultrarelativistic electrons without becoming significantly depleted prior to the collision. In order to show that the observed trend is valid for a range of channel densities, we have performed channel density scans for $a_0 = 160$ and $a_0 = 190$. The pair yield for the linear and nonlinear Breit-Wheeler processes is given in Table 2.2 for $a_0 = 160$ and in Table 2.3 for

$a_0 = 190$. The ratio of the linear to nonlinear pair yield increases for $0.8 \leq n_e/n_{ch} \leq 1.2$ as we reduce a_0 from 190 to 160. This is the trend that is reported in the main text, which indicates that our observations apply to a range of channel densities and no fine-tuning is necessary.

Table 2.2. Number of pairs at $a_0 = 160$ for different electron densities, n_e, in the channel. The density n_e is given in terms of $n_{ch} = (a_0/100)3.8n_c$, where n_c is the critical density

n_e/n_{ch}	0.8	1.0	1.2
Linear BW pairs ($\times 10^8$)	5.89	6.05	6.21
Nonlinear BW pairs ($\times 10^8$)	1.06	0.86	0.38

Table 2.3. Number of pairs at $a_0 = 190$ for different electron densities, n_e, in the channel. The density n_e is given in terms of $n_{ch} = (a_0/100)3.8n_c$, where n_c is the critical density

n_e/n_{ch}	0.8	1.0	1.2
Linear BW pairs ($\times 10^8$)	17.0	13.1	11.8
Nonlinear BW pairs ($\times 10^8$)	9.2	6.6	4.4

2.5.3 Distribution of nonlinear Breit-Wheeler pairs

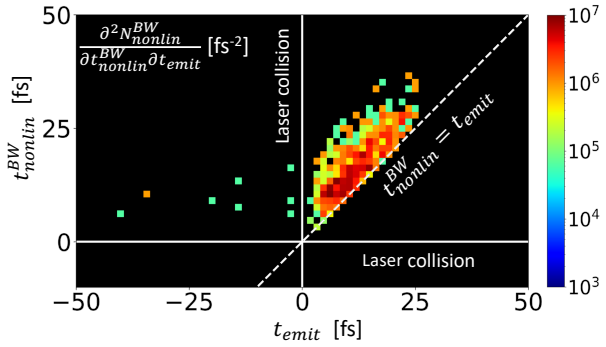

Figure 2.7. Distribution function $\partial^2 N^{\mathrm{BW}}_{\mathrm{nonlin}}/(\partial t^{\mathrm{BW}}_{\mathrm{nonlin}} \partial t_{\mathrm{emit}})$ [fs^{-2}] of the number of electron-positron pairs over the time $t^{\mathrm{BW}}_{\mathrm{nonlin}}$ of pair creation and the t_{emit} of the parent photons. The peak amplitude of each laser peak is $a_0 = 190$.

Figure 2.7 provides additional information on the production of nonlinear Breit-Wheeler pairs. The horizontal scale shows the emission time, t_{emit}, of energetic photons that go on to produce pairs by interacting with the laser photons. The energetic photons are generated and subsequently propagated as particles by the PIC code. The time of the pair production, $t^{\mathrm{BW}}_{\mathrm{nonlin}}$,

is shown along the vertical scale. The number of pairs for each pairing of $t_{\rm emit}$ and $t^{\rm BW}_{\rm nonlin}$ is color-coded. The pair production is directly computed by the PIC code. The numbers shown in the figure are obtained by assuming that the spatial scale along the z axis is equal to the initial width of the channel.

The vast majority of the nonlinear pairs are produced by photons emitted after the two lasers collide. Indeed, $t_{\rm emit} = 0$ is the time when the two laser beams begin to collide. Most of the pairs are located at $t_{\rm emit} > 0$, which indicates that the parent photons were generated after the collision.

2.5.4 Estimated background from Bethe-Heitler pair creation

The principal source of background in a prospective measurement of linear (or nonlinear) Breit-Wheeler pair creation is the Bethe-Heitler process, wherein a photon with energy $\hbar\omega > 2mc^2$ produces an electron-positron pair on collision with an atomic nucleus [66]. In order to estimate the contribution from this process, we sum the pair creation probability for each macrophoton in the simulation: $N_{\rm BH} = \sum_k w_k P_{k,{\rm BH}}$, where w_k is the weight of the kth photon, scaled assuming that the third dimension has size 5 μm. The probability $P_{k,{\rm BH}} = n_{\rm i}\ell_k\sigma_{\rm BH}$, where $n_{\rm i}$ is the density of carbon ions in the channel and ℓ_k is the distance the photon travels before it leaves the channel. We estimate n_i and ℓ_k using the unperturbed properties of the channel, i.e. those at the start of the simulation, and taking into account the photon's point of emission and direction of propagation. Thus $n_{\rm i} = 3.8a_0 n_{\rm c}/(100Z)$. We approximate the cross section $\sigma_{\rm BH}$ by that for an unscreened, fully ionized, point carbon nucleus (formula 3D-0000 given by Motz et al. [67] with $Z = 6$). The functional dependence of the cross section on the normalized photon energy $\gamma = \hbar\omega/(mc^2)$ is given by $\sigma_{\rm BH}(\gamma) \simeq \alpha r_{\rm e}^2 Z^2 (2\pi/3)[(\gamma-2)/\gamma]^3$ for $\gamma - 2 \ll 1$ and $\sigma_{\rm BH}(\gamma) \simeq \alpha r_{\rm e}^2 Z^2 [28\ln(2\gamma)/9 - 218/27]$ for $\gamma \gg 1$, where $r_{\rm e}$ is the classical electron radius [67]. Our results are shown as blue circles in Fig. 2.6. This estimate neglects contributions from pair creation in the plasma bulk, which can be controlled by reducing the thickness of the channel walls. Furthermore, the difference in magnitude between background and signal is sufficiently

large that it provides a margin of safety.

2.5.5 Strong-field modifications to the linear Breit-Wheeler cross section

The cross section we use to determine the number of electron-positron pairs created by the linear Breit-Wheeler process, Eq. (2.2), is calculated assuming that the photons are in vacuum. However, our calculations show that the pairs are created within the plasma channel as the laser pulses overlap, where the background electromagnetic field is strong. The presence of a strong magnetic field [56, 57] or plane EM wave is known to modify the cross section for this process. Calculations of the cross section in the latter case have focused on changes at moderate a_0 [68] or on resonance features [58, 59]. Resonances occur where the intermediate fermion is on mass shell, which corresponds to the incoherent combination of nonlinear pair creation, followed by photon absorption by one of the daughter fermions, in the high-intensity regime. This contribution, which is effectively driven by a single photon, is already counted as our simulations include nonlinear pair creation; photon absorption by an electron in a strong field [24, 69] is suppressed unless the photon and electron are aligned within electron's emission cone. (See supporting simulations by Blackburn et al. [70])

As such, in order to estimate the effect of the strong field at $a_0 \gg 1$, we use the cross section for two-photon pair creation in a constant, crossed field given by Baier et al. [60] (see Sec. 5.7). If two-photon pair creation is kinematically allowed, i.e. $\varsigma > 1$, corrections to the cross section scale as $(\chi_\gamma/\varsigma)^2$, where χ_γ is the quantum nonlinearity parameter [60]: in the scenario under consideration here, the photons which undergo linear pair creation have MeV energies and $\chi_\gamma \ll 1$, and therefore these corrections can be neglected. On the other hand, the fact the laser-plasma interactions provide a platform for prolific two-photon pair creation in a region of strong EM field, as our results show, motivates a more general treatment that can investigate where these field-driven corrections become substantial. We note that a related process, pair annihiliation to two photons in a pulsed, plane EM wave, has recently been revisited [62].

2.5.6 Postprocessing algorithm for determination of the linear Breit-Wheeler pair yield

In this section and Sec. 2.5.7, we present a brief summary of the postprocessing algorithm we use to calculate the linear BW pair yields in this chapter. A more detailed description is presented in Chapter V.

In order to compute the yield and spatial distribution of the linear Breit-Wheeler pairs, we approximate the photon population as a collection of collimated, monoenergetic beamlets. Discretization into beamlets is achieved by recording the location (x_0, y_0), energy ε_γ, and angle θ of each photon macroparticle at the time of the emission t_{emit}. The photon emission pattern suggests that the emission profile across the channel can be approximated as uniform. We thus represent the emitted photons by a time-dependent distribution function $f = f(x_0, s_\gamma, \theta; t_{\text{emit}})$, where $s_\gamma \equiv \log_{10}(\varepsilon_\gamma/\text{MeV})$. It is sufficient to limit our analysis to $-40\ \mu\text{m} \leq x_0 \leq 40\ \mu\text{m}$, $-3 \leq s_\gamma < 3$, and $0^\circ \leq \theta \leq 180^\circ$. We split each interval into 70 equal segments to obtain 2.6×10^5 beamlets. We only check for collisions of beamlets propagating to the right with beamlets propagating to the left. The yield is multiplied by a factor of two to account for beamlets with $-180^\circ \leq \theta \leq 0^\circ$.

The temporal dependence of a beamlet is represented by slices of given density and fixed thickness. For each beamlet pairing, our algorithm finds the interaction volume V, the intersections of the beamlet axes and the crossing angle ψ. The pair yield is given by $\Delta N_{\text{lin}}^{\text{BW}} = \sigma_{\gamma\gamma} c(1-\cos\psi) V \int n_1 n_2 dt$, where n_1 and n_2 are the photon densities in two overlapping slices at the intersection point. In general, the shape of the overlapping region is not rectangular, so the pair creation is visualized by depositing $\Delta N_{\text{lin}}^{\text{BW}}$ onto a rectangular grid, into cells with centers inside volume V. The procedure is repeated for each beamlet pairing to obtain the density of generated pairs.

To show that the limitation $-3 \leq s_\gamma < 3$ is justified, we plot the distribution of linear Breit-Wheeler pairs as a function of photon energies. We use s_γ rather than ε_γ to capture a wide

range of energies. Figure 2.8 confirms that the pair yield drops off for $|s_\gamma| > 2$, which justifies the energy range selected in the chapter.

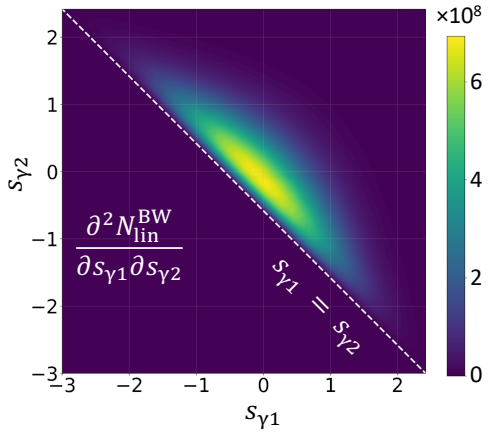

Figure 2.8. Yield of the linear Breit-Wheeler process as a function of photon energies. Distribution of linear Breit-Wheeler pairs as a function of photon energies for colliding laser pulses with $a_0 = 190$.

The algorithm is a simplification that replaces a direct approach of evaluating all possible collisions of beamlet slices. In a head-on collision, each slice collides with many counter-propagating slices within the interaction volume, which makes the calculation computationally intensive. Our algorithm takes advantage of the fact that the typical duration of beamlet emission, τ, is much longer than the time it takes for photons to travel between the sources emitting the two beamlets, ℓ/c, where ℓ is the distance between the sources in the case of near head-on collision. As shown in Sec. 2.5.7, our approach is a good approximation as long as $\ell/c\tau < 1$, with the error scaling as $(\ell/c\tau)^2$.

The postprocessing algorithm neglects the depletion of the photon population due to the linear Breit-Wheeler process. This is justifiable, because only a small fraction of the considered photons actually pair-create (and would therefore be lost). Using the maximum photon density of $n_\gamma \approx 600 n_c$ from Fig. 2.4, we obtain a mean free path with respect to the linear Breit-Wheeler process,

$$1/\sigma_{\gamma\gamma} n_\gamma \approx 6 \times 10^4 \ \mu\mathrm{m}, \tag{2.3}$$

that is much larger than the characteristic size of the photon cloud of 10 μm. We estimate depletion of the photon population due to the linear Breit-Wheeler process (as a fraction of the initial size) to be smaller than 2×10^{-4}.

2.5.7 Pair production algorithm for head-on collisions of beamlets

Our algorithm for computing the pair production yield due to the linear Breit-Wheeler process leverages the fact that the colliding photons are emitted over an extended period of time compared to the characteristic travel time between the emission locations. In what follows, we illustrate its implementation for head-on collisions of two beamlets. Near head-on collisions are the biggest contributor to the pair yield and this is also the regime that greatly benefits from our simplified approach in terms of computational efficiency.

We are considering a head-on collision of two counterpropagating beamlets that have the same transverse area S. The first beamlet is being emitted at $x = x_1$ and it propagates in the positive direction. It is convenient to use the emission time τ as a marker for the photons in each beamlet. The corresponding photon density in the first beamlet is then $n_1(\tau_1)$. The counterpropagating beamlet is emitted at $x = x_2 > x_1$ and its photon density is $n_2(\tau_2)$. The total pair yield by these two beamlets interacting with each other is

$$\Delta N_{\text{pairs}} = \sigma_{\gamma\gamma} S c^2 \int_{-\infty}^{+\infty} d\tau_1 n_1(\tau_1) \left[\int_{\tau_1 - l/c}^{\tau_1 + l/c} d\tau_2 n_2(\tau_2) \right], \tag{2.4}$$

where

$$l \equiv x_2 - x_1. \tag{2.5}$$

Equation (2.4) presents a direct approach to calculating the pair yield and it involves a double integral.

In our case, the typical beamlet emission lasts longer than l/c, which suggests a possible simplification of replacing $n_2(\tau_2)$ with $n_2(\tau_1)$. The inner integral in Equation (2.4) can then be

directly evaluated and we find that

$$\Delta N_{\text{pairs}} \approx 2c\sigma_{\gamma\gamma}V\int_{-\infty}^{+\infty} n_1(\tau)n_2(\tau)d\tau, \tag{2.6}$$

where $V \equiv lS$ is the interaction volume. Note that the two beamlets are interchangeable in this expression. In order to estimate the error, we expand $n_2(\tau_2)$ around $\tau_2 = \tau_1$ and retain linear and quadratic terms in the expansion. The time integral of the linear term in Equation (2.4) is equal to zero, which means that the error in our approach is determined by the quadratic term. We thus estimate that the relative error in the number of produced pairs scales as $(l/c\Delta\tau)^2$, where $\Delta\tau$ is the characteristic duration of beamlet emission.

We compute the spatial distribution of pairs by simply assigning the pair density

$$\Delta n_{\text{pairs}} = \Delta N_{\text{pairs}}/V \tag{2.7}$$

to each position within the interaction volume. We call this the *average density method*. A direct approach would however require us to compute the following integral at each position along the x axis:

$$\Delta n_{\text{pairs}}^{\text{direct}}(x) = 2c\sigma_{\gamma\gamma}\int_{-\infty}^{+\infty} n_1(t_1)\, n_2(t_2)\, dt, \tag{2.8}$$

where

$$t_1 = t - (x - x_1)/c, \tag{2.9}$$

$$t_2 = t - (x_2 - x)/c. \tag{2.10}$$

The direct approach is much more demanding computationally.

Even though our approach for calculating the spatial distribution of pairs is deliberately crude for a single pair of beamlets, it is effective when applied to a large ensemble of spatially distributed beamlets. As an example, we have carried out calculations for approximately 3000

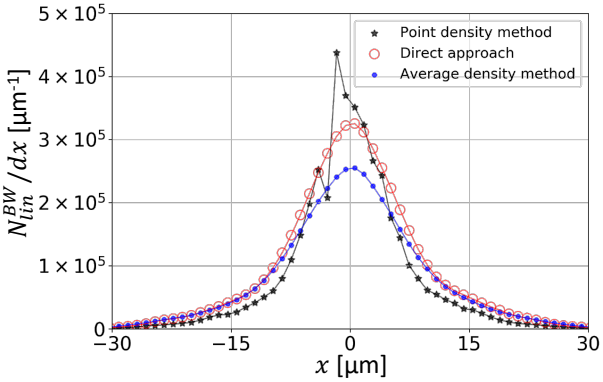

Figure 2.9. Spatial distribution of linear Breit-Wheeler pairs produced in a head-on collision of spatially distributed beamlets. The three curves represent three different approaches: direct approach (open circles), average density method (solid circles), and point density method (star markers).

spatially distributed beamlets, where 1573 beamlets are directed to the right and 1590 beamlets are directed to the left. The photon energy range is 0.19 MeV $< \varepsilon_\gamma <$ 2.05 MeV. We used our PIC simulation to generate these beamlets by selecting photons emitted with $|\theta| < 5.15^\circ$ or $|\theta - \pi| < 5.15^\circ$. The average density method that uses Δn_{pairs} from Equation (2.7) for each beamlet-beamlet collision gives the curve shown with small solid circles. The direct approach detailed by Equation (2.8) gives the curve shown with open circles. The two curves have a similar shape, but the direct approach took almost two orders of magnitude longer in terms of computational time. The relative difference in the total number of pairs between the two methods is less than 17%.

Our method evenly distributes the generated pairs over the interaction volume, which is the key to achieving a good agreement with the direct but more computationally expensive approach. In order to illustrate this aspect, we performed another calculation. In this case, all of the pairs produced by two beamlets are placed into the center of the interaction volume without being evenly distributed. We call this the *point density method*. The density is calculated as $\Delta N_{\text{pairs}}/S\Delta x$, where ΔN_{pairs} is given by Equation (2.6) and Δx is the thickness of slices that we use for spatial discretization into beamlets. The result of this procedure is shown with star markers in Figure 2.9. There are no significant savings in terms of computational costs compared to the

average density method. The characteristic width of the spatial distribution shows considerable deviation from that for the direct approach.

A single-laser scheme for observation of linear Breit-Wheeler electron-positron pair creation

We show that a single laser pulse, travelling through a dense plasma, produces a population of MeV photons of sufficient density to generate a large number of electron-positron pairs via the linear Breit-Wheeler process. While it may be expected that the photons are emitted predominantly in the forward direction, parallel to the laser propagation, we find that a longitudinal plasma electric field drives the emission of photons in the backwards direction. This enables the collision of oppositely directed, MeV-level photons necessary to overcome the mass threshold for the linear Breit-Wheeler process. Our calculations predict the production of 10^7 electron-positron pairs, per shot, by a laser with peak intensity of just 3×10^{22} Wcm^{-2}. By using only a single laser pulse, the scheme sidesteps the practical difficulties associated with the multiple-laser schemes previously investigated.

3.1 Introduction

With the development of modern laser technology, the intensity of state-of-the-art lasers has surpassed the level of 10^{22} Wcm^{-2} [6, 7, 8]. Under electromagnetic fields of such magnitude, which are able to accelerate particles to ultrarelativistic energies, effects of quantum electrodynamics (QED) are expected to become important [19]. This capability has led to wide interest in using ultra-intense lasers to study strong-field QED phenomena, the theory of which has been developed for at least sixty years [71, 72, 9]. Experimental investigation of the strong-field

regime is at an early stage [53, 54], but is expected to develop significantly as the next generation of high-intensity laser facilities are commissioned.

It is of particular interest to investigate the annihilation of two photons into an electron-positron pair, or the linear Breit-Wheeler process ($\gamma+\gamma\rightarrow e^{-}+e^{+}$) [1], using the most advanced laser facilities. The linear Breit-Wheeler process, besides being a fundamental prediction of the theory of QED, also has important applications in astrophysics: for example, in understanding the opacity of the universe [2] and in studying the pair cascade in pulsar magnetospheres [3, 4, 5, 40]. Despite its importance, however, it has never been observed in a laboratory with real photons. The experimental difficulty comes from its small cross section and its MeV center-of-mass energy threshold. To overcome these difficulties, a system with colliding dense multi-MeV photons is required. Various geometries have been proposed, including the combination of GeV bremsstrahlung photons with keV blackbody photons produced in a hohlraum [11] or with an intense x-ray laser pulse [10]; the combination of multi-MeV photon beams each produced by a separate laser-irradiated foil or low-density plasma targets [12, 13, 73, 74, 14]; and the combination of multi-MeV photon beams produced by two colliding laser pulses within a structured target [75].

However, in these works, multiple laser pulses are required in one experiment, which limits the choice of facility where the proposed experiments can be conducted. Moreover, if the photon beams are generated in separate sources, then they must travel over a certain distance to reach the collision point. This leads to two limiting factors for the possible pair yield. First, alignment and overlap of the photon beams is not automatically achieved. Second, during the propagation of beams, the divergence reduces the photon density, which scales as $1/R^2$, where R is the distance between the photon source and the collision region. The number of binary photon collisions scales as the product of photon densities, i.e. as $1/R^4$, and therefore the yield of electron-positron pairs is suppressed.

In this chapter, we show that, during the propagation of a *single* laser pulse along a plasma channel, more than 10^7 pairs can be produced by the linear Breit-Wheeler process inside

the plasma target, where currently available 10^{22} Wcm^{-2} class laser pulses and targets [76] are used. The key feature which explains this high yield is an unexpected emission of MeV photons in the opposite (backward) direction to the laser propagation: indeed, our simulations show that the numbers of photons emitted backwards and forwards, in the keV to MeV energy range, are of the same order of magnitude. This is unexpected because electrons, under the action of the laser fields and the azimuthal magnetic field generated by their collective motion, are expected to be accelerated parallel to the direction of laser propagation [77, 78, 79], and therefore to emit photons overwhelmingly forward. The backward moving photons collide with these forward moving photons, usually focused on in studies of direct laser acceleration (DLA) [41], and produce linear Breit-Wheeler pairs. Since both the backward and forward moving photons are created inside the same plasma channel, photon density remains high at the time of collision.

This chapter examines and explains the origin of the backward-moving MeV photons. We find that, as the laser propagates along the plasma channel, a longitudinal electric field is induced at the leading edge of the laser pulse due to charge separation. The longitudinal field co-propagates with the laser pulse, accelerating some of the channel electrons backwards after they encounter the laser pulse. The interaction of the backward-moving electrons with the propagating laser pulse causes them to emit energetic MeV-level photons. The emission process is enhanced due to the counter-propagating geometry of the interaction. These are the photons that cause the observed two-photon pair production inside the channel when they collide with the forward-emitted gamma-rays.

The rest of this chapter is organized as follows. In Section 3.2, we review the key elements of a laser-plasma interaction where a high-intensity laser pulse propagates through a relativistically-transparent target and the generation of a collimated beam of energetic gamma-rays associated with it . In Section 3.3, we examine the source of backward-directed gamma-rays that are also present, but frequently overlooked, in the considered interaction. In Section 3.4, we show that binary collisions between the forward and backward-directed photons of the right energy range occur frequently enough to generate an appreciable yield of electron-positron

pairs. In Section 3.5, we develop a reduced test-particle model and then apply it to examine the backward electron acceleration that leads to the emission of the backward-directed gamma-rays and assess the impact of the plasma electric and magnetic fields on the electron dynamics. In Section 3.6, we summarize our findings.

3.2 Emission of forward-directed collimated gamma-rays

It is now well-recognized that a high-intensity laser pulse propagating through a relativistically transparent plasma can efficiently generate a collimated beam of energetic gamma-rays [41, 13, 76, 80, 81, 82]. In this section, we review the main physics elements of this process. A comprehensive analysis is available in [13] and [49].

The emission of collimated energetic gamma-rays is closely associated with the presence of a strong quasi-static azimuthal magnetic field inside the laser-irradiated plasma. The field is generated and maintained by a volumetrically distributed longitudinal electron current driven by the propagating laser pulse. Figure 3.1 illustrates this phenomenon for a 25 fs, 800 nm laser beam with a peak intensity of $I_0 \sim 3 \times 10^{22}$ Wcm^{-2} propagating through a structured plastic target with a pre-filled channel. The beam has the parameters similar to those expected at the ELI-NP laser facility [6]. Detailed laser and target parameters and the information regarding the simulation setup are given in Sec. 3.8 of the Appendix. Figure 3.1(a) shows stable propagation of the laser beam through the channel and Fig. 3.1(c) shows a time-averaged magnetic field (the averaging is performed over one laser period) generated as a result of this propagation.

The magnitude of the quasi-static magnetic field in the considered example is very high – it is 3 GG or 20% of the strength of the oscillating laser magnetic field (in the absence of the target). Such a strength is achieved by using a channel with an electron density that is higher than the classical cutoff density $n_c = \pi mc^2/(e\lambda_0)^2$ for a laser with a vacuum wavelength of $\lambda_0 = 800$ nm, where c is the speed of light and e and m are the electron charge and mass. In our example, the normalized laser amplitude, defined as $a_0 = 0.85 I_0^{1/2}[10^{18}\ \text{Wcm}^{-2}]\lambda_0[\mu\text{m}]$,

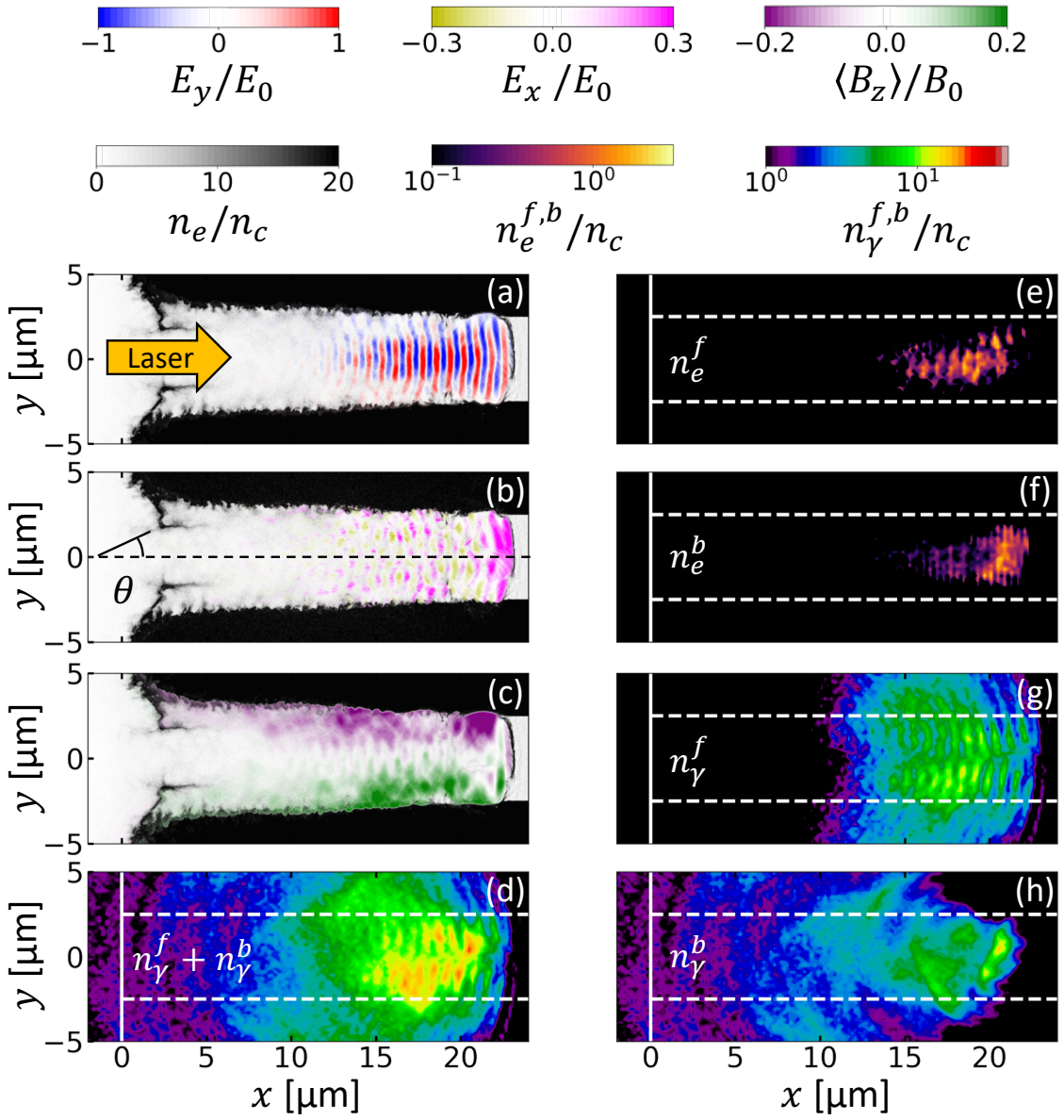

Figure 3.1. Propagation of a laser pulse with $a_0 = 120$ inside a structured target and the resulting generation of gamma-rays. (a) and (b) Transverse, E_y, and longitudinal, E_x, electric fields normalized to $E_0 = 1.61 \times 10^{10}$ statV/cm. (c) Time-averaged (over one laser period) magnetic field, $\langle B_z \rangle$, normalized to $B_0 = 16.1$ GG. (d) The density of emitted photons with energy greater than 100 keV. (e) Density of forward moving electrons with $\chi_e > 0.03$ and $\gamma_e > 15$. (f) Density of backward moving electrons also with $\chi_e > 0.03$ and $\gamma_e > 15$. The characteristic photon energy, $\overline{\varepsilon}_\gamma$, of the photons emitted by the electrons selected in (e) and (f) is greater than 100 keV. (g) Density of forward moving photons with energy greater than 100 keV. (h) Density of backward moving photons with energy greater than 100 keV. Electron and photon densities are normalized to the critical density n_c. All of the snapshots are taken at $t = 67$ fs.

is $a_0 = 120$. The fact that $a_0 \gg 1$ means that the electrons in the irradiated plasma become relativistic. This, in turn, raises the cutoff density to approximately $a_0 n_c = 120 n_c$, making the plasma in the channel, whose density is $n_e \approx 2.8 n_c$, transparent. The increased plasma transparency is a manifestation of a more general phenomenon referred to as *relativistically induced transparency* [28, 29, 83, 84]. The channel is used in our simulation to stabilize the laser propagation [41, 85], with the dense walls ($n_e \approx 28 n_c$) providing optical guiding. The mechanism described here and the resulting electron acceleration and photon emission discussed in this Section have been shown not to be sensitive to the bulk density. For example, similar simulations have been performed in [13] with a bulk electron density of $100 n_c$. Structured targets with foam-filled channels have been successfully fabricated by General Atomics and used for an experimental campaign at the Texas Petawatt laser facility [76].

The plasma magnetic field has two important functions: to enhance laser-driven electron acceleration and to induce emission of energetic photons by the accelerated electrons. At $a_0 \gg 1$, direct laser acceleration produces forward moving electrons due to a forward push by the Lorentz force of the laser magnetic field. Transverse deflections by the plasma magnetic field can keep the transverse electron velocity anti-parallel to the transverse laser electric field and thus enable the accelerated electrons to continue gaining energy despite the oscillations of the laser electric field [49]. The deflections are particularly effective when the frequency of transverse electron oscillations caused by the magnetic field is comparable to the Doppler shifted frequency of the laser [86, 87]. Such a condition can be realized only in a plasma with a sufficiently high current density [49]. In our simulation, the electrons reach a maximum energy of 700 MeV through the described mechanism. The deflections by the magnetic field not only enable the electrons to gain more energy from the laser field, but they also lead to energy losses via synchrotron emission of electromagnetic radiation. The rate of the energy gain typically greatly exceeds the rate of energy losses associated with the emission, so the laser accelerated electrons can efficiently convert the laser energy carried by optical photons into gamma-rays.

The photon emission process by an electron with a velocity $\boldsymbol{v}$ is characterized by a

dimensionless parameter

$$\chi_e = \gamma_e \mathscr{E} / B_{crit}, \tag{3.1}$$

with $\mathscr{E}$ being an effective transverse field strength:

$$\mathscr{E} = \sqrt{\left(\boldsymbol{E} + \frac{1}{c}[\boldsymbol{v} \times \boldsymbol{B}]\right)^2 - \frac{1}{c^2}(\boldsymbol{E} \cdot \boldsymbol{v})^2}. \tag{3.2}$$

Here $\boldsymbol{E}$ and $\boldsymbol{B}$ are the electric and magnetic fields acting on the electron, $\gamma_e = 1/\sqrt{1 - v^2/c^2}$ is the relativistic factor, and $B_{crit} \approx 4.4 \times 10^{13}$ G is the magnetic equivalent of the well-known Schwinger (or critical) electric field [46]. The characteristic energy of emitted photons, $\overline{\varepsilon}_\gamma$, is given by [88]

$$\overline{\varepsilon}_\gamma = 0.44 \gamma_e \chi_e m c^2, \tag{3.3}$$

These photons are emitted in the direction of the electron momentum into a narrow cone whose opening angle is roughly $1/\gamma_e$. As a result, forward moving electrons generate a forward-directed beam of photons.

In the case of ultra-relativistic forward-moving electrons, like those generated by the laser in the presence of the plasma magnetic field, the contributions from the laser electric and magnetic fields to the effective field $\mathscr{E}$ nearly cancel each other out. Therefore, one can estimate $\mathscr{E}$ by simply using the plasma magnetic field B^{pl}, with $\mathscr{E} \approx B^{pl}$, which yields the following approximate expression for χ_e:

$$\chi_e \approx \gamma_e B^{pl} / B_{crit}. \tag{3.4}$$

It follows from this estimate that we have $\chi_e \approx 0.020$ for an electron with $\gamma_e \approx 300$ that is deflected by $B^{pl} \approx 3$ GG $\approx 0.19 B_0$, which is close to the maximum amplitude of the quasi-static field shown in Fig. 3.1(c). The characteristic photon energy is $\overline{\varepsilon}_\gamma \approx 1.4$ MeV. This example illustrates the important role played by the plasma magnetic field in generating energetic gamma-rays.

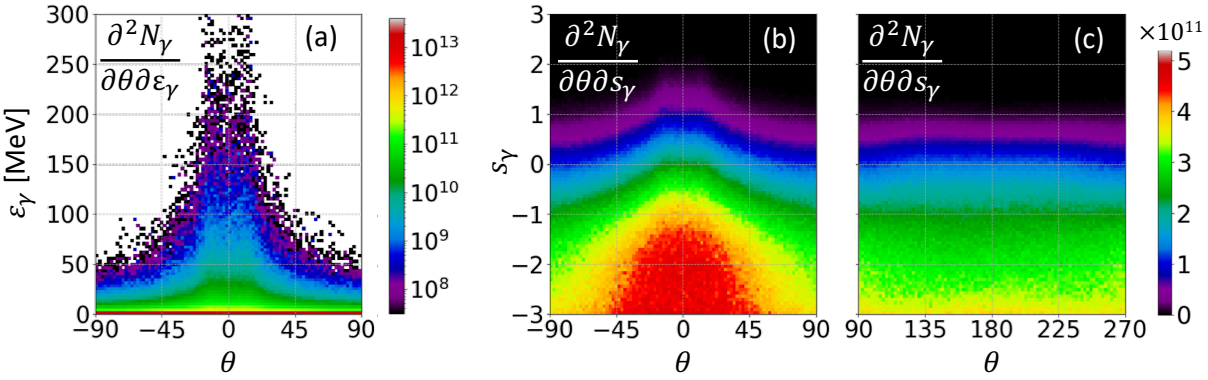

Figure 3.2. Energy-angle spectra of the photons emitted inside the structured target from Fig. 3.1. (a) and (b) The distribution of the forward-directed photons on linear and logarithmic energy scales, where $s_\gamma \equiv \log_{10}(\varepsilon_\gamma[\mathrm{MeV}])$. (c) The distribution of the backward-directed photons on a logarithmic energy scale. Here θ is the angle defined in Fig. 3.1(b).

The spectrum of forward-emitted photons in our simulation is shown in Fig. 3.2(a). It is indeed well-collimated in the forward direction, in agreement with our expectations. The photon spectrum is broad because the synchrotron spectrum is itself broadband and because electrons with a wide range of energies contribute to the emission. In our simulation, the photon emission is modelled using a Monte Carlo module for quantum synchrotron radiation [43]. The module computes χ_e at each time-step for each charged macro-particle. This value is then used to determine the energy and number of emitted photons. The finite width of the emission cone is neglected, so the photons are emitted along the momentum of the emitting particle. The module also self-consistently accounts for the recoil experienced by the particle when emitting individual photons, as described in [43] and [47].

3.3 Emission of backward-directed gamma-rays

In Section 3.2, we reviewed how a high-intensity laser pulse propagating through a relativistically-transparent plasma can efficiently generate a collimated beam of energetic gamma-rays. In what follows, we discuss the source of backward-directed gamma-rays that are also present, but frequently overlooked, in the considered setup.

Figure 3.2(c) shows that indeed, in addition to forward-directed gamma-rays, the plasma

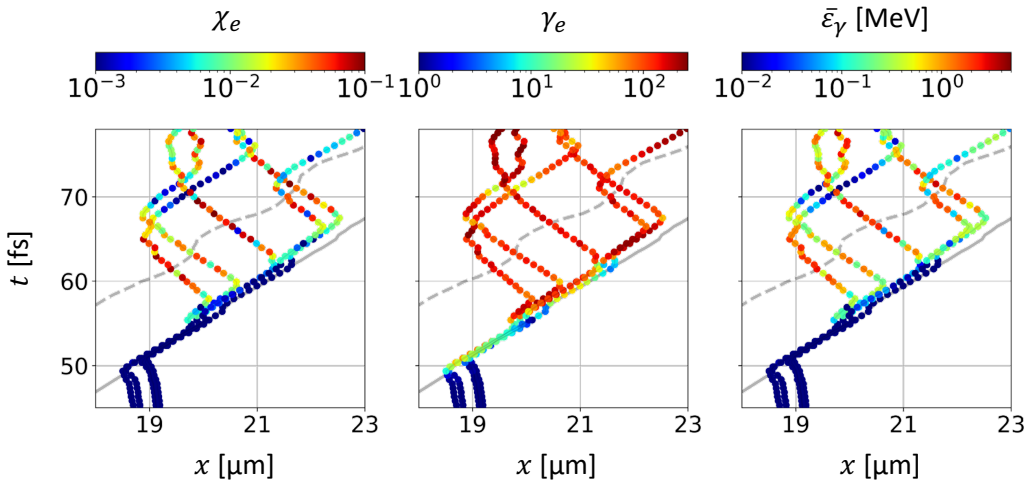

Figure 3.3. Time evolution of χ_e, γ_e, and $\bar{\varepsilon}_\gamma$ along trajectories of five randomly selected electrons from inside the channel. The solid and dashed gray curves indicate the extent of the localized E_x structure shown in Fig. 3.4(a) and located at the front of the propagating laser pulse. The curves show the locations where E_x is 10% of $\max(E_x)$ at each time instant.

electrons in our simulation emit energetic backward-directed photons. These photons, which have an almost uniform angular distribution, originate from electrons that are moving backwards over at least some segments of their trajectories. The backward-emitting electrons are concentrated primarily at the leading part of the laser pulse: this may be seen in Fig. 3.1(f), which shows the density of electrons that have $p_x < 0$, $\gamma_e > 15$ and $\chi_e > 0.03$. In order to identify their origin, we track five randomly selected electrons that are initially located inside the channel prior to the arrival of the laser pulse. The electrons were selected, at $t = 17$ fs, from the region defined by $|y| < 0.5$ μm and 18.75 μm $< x <$ 19.25 μm. As seen in Fig. 3.3, these electrons reverse the direction of their longitudinal motion after being swept up by the leading edge of the laser pulse.

The backward acceleration of the electrons inside the channel is caused by a longitudinal electric field, E_x, which is shown in Fig. 3.1(b) at $t = 67$ fs. This field is concentrated at the leading edge of the laser pulse. It is formed by charge separation as the laser enters the plasma channel, displacing electrons ahead of the much heavier and therefore slower moving ions, and moves forward with the leading edge of the laser pulse. This aspect is shown in Fig. 3.4, where Fig. 3.4(a) shows the time evolution of E_x in the region close to the axis and Fig. 3.4(b) shows

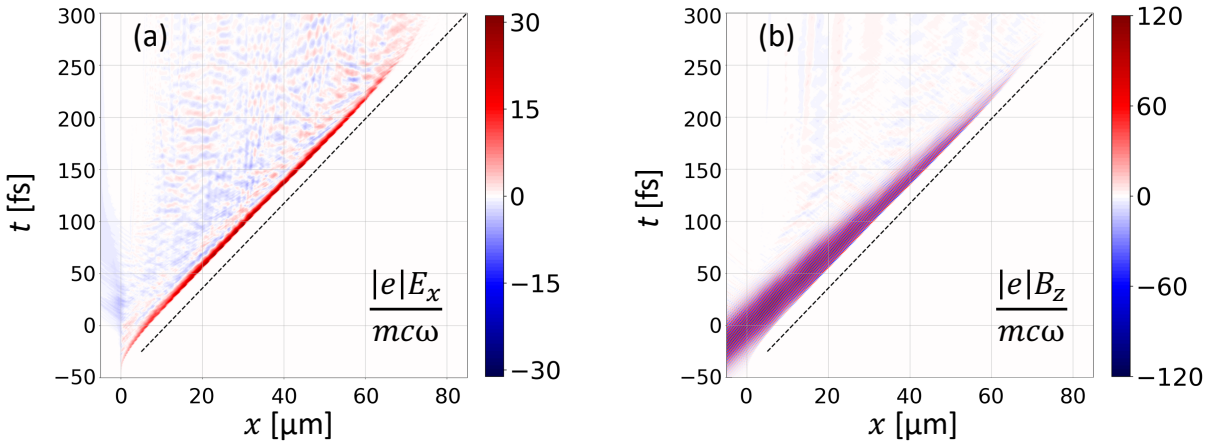

Figure 3.4. Temporal evolution of E_x and B_z in the near-axis region in the PIC simulation shown in Fig. 3.1. The fields are spatially averaged in the transverse direction over a region with $|y| < 1.5$ μm. The dashed black lines is the same in both panels, represent motion along x with velocity $v_x = 0.82c$.

the time evolution of the time-dependent magnetic field B_z, associated primarily with the laser, in the same region. At each location along x, both fields are a spatial average over the region $|y| < 1.5$ μm. We find that the E_x structure moves with a constant speed of $0.82c$ and that its amplitude is slowly varying after the initial ramp-up. The field structure disappears by about $x \approx 70$ μm following the laser depletion, which again confirms that it is driven by the laser pulse itself.

In contrast to the case of the forward-moving electrons, the effective field $\mathscr{E}$ for the backward-propagating electrons is primarily determined by the fields of the laser. The reason for this difference is the lack of compensation between $\boldsymbol{E}$ and $\boldsymbol{B}$ of the laser. These fields are much stronger than the fields created by the plasma, so, in the absence of their compensation, they dominate the expression for $\mathscr{E}$ given by Eq. (3.2). Therefore we neglect the plasma fields, set $\boldsymbol{E}^{laser} = \boldsymbol{B}^{laser}$, and assume that the electron is moving purely backwards to find that the effective field acting on the backward-moving electrons is $\mathscr{E} \approx 2B^{laser}$. This effective field is stronger than the effective field for the forward moving electrons by a factor of $2B^{laser}/B^{pl} \approx 13$ [in our case $\max(B^{laser}) \approx 20$ GG]. Thus, while a relativistic factor of $\gamma_e \approx 300$ would be necessary for a foward-moving electron to have a typical photon energy of 1.4 MeV, only $\gamma_e \approx 80$ is necessary

for a backward-moving electron to emit photons with the same energy.

3.4 Yield of electron-positron pairs via the linear Breit-Wheeler process

As discussed in Section 3.2 and Section 3.3, the laser-plasma interaction under consideration generates a gamma-ray population with both backward and forward moving photons. Figure 3.2(b) and Fig. 3.2(c) show that the energies of these photons exceed 100 keV and reach 10 MeV, even for the backward emission. This energy range is favorable for the electron-positron pair creation via binary photon collisions, i.e. the linear Breit-Wheeler process, because it can overcome the center-of-mass energy threshold:

$$\varepsilon_\gamma^f \varepsilon_\gamma^b > \left(mc^2\right)^2, \tag{3.5}$$

where ε_γ^f and ε_γ^b are the energies of the forward and backward-directed colliding photons. In this section, we show that, in the interaction, binary collisions between photons of the right energy range occur frequently enough to generate an appreciable yield of electron-positron pairs.

Photon collisions are possible only if the backward-moving photons are emitted ahead of forward-moving photons. As these photons are emitted by backward and forward-moving electrons, respectively, we examine the spatial distribution of these two components of the electron population, selecting only those electrons which have $\gamma_e > 15$ and $\chi_e > 0.03$. We apply this selection criterion because, according to Eq. (3.3), the characteristic energy of the photons emitted by such electrons is $\overline{\varepsilon}_\gamma > 100$ keV, which is within the favorable energy range for the linear Breit-Wheeler process. Snapshots of the density for backward and forward-moving electrons, selected according to the described criterion, are shown in Fig. 3.1(e) and Fig. 3.1(f), respectively. The forward-moving and thus forward-emitting electrons are spread throughout entire region occupied by the laser pulse [see Fig. 3.1(a)]. The backward emitting electrons, by contrast, are primarily concentrated at the front of the laser pulse. This is in good agreement with

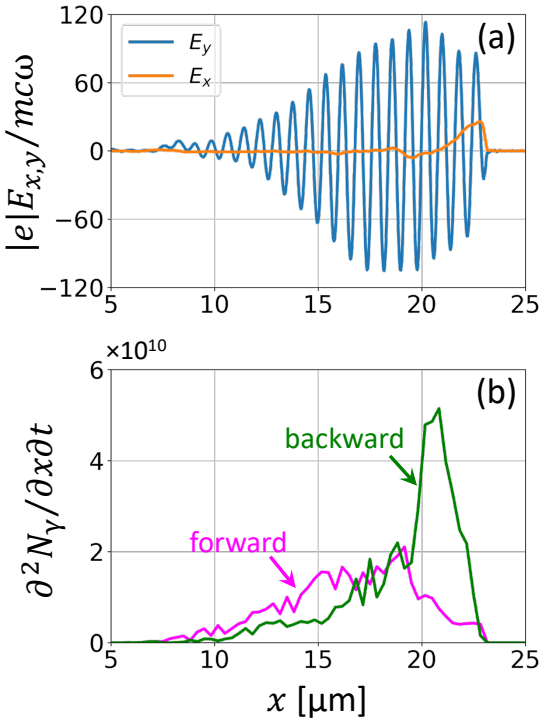

Figure 3.5. Longitudinal profiles of electric fields and photon emission at $t = 67$ fs. (a) Transverse, E_y, and longitudinal, E_x, electric fields spatially averaged in the transverse direction over a region with $|y| < 1.5$ μm. (b) Instantaneous emission rate, $\partial^2 N_\gamma/\partial x\partial t$ [fs^{-1}μm^{-1}], for backward and forward-directed photons, where N_γ is the number of photons with energy between 100 keV and 10 MeV emitted in a thin vertical slice.

the mechanism of their generation by E_x at the leading edge of the laser pulse [see Fig. 3.1(b)].

The difference in the spatial localization of the emitting electrons translates into photon emission profiles that are favorable for the photon-photon collisions. Figure 3.5(b) shows snapshots of $\partial^2 N_\gamma/\partial x\partial t$ for forward and backward-directed photons, where N_γ is the number of photons with energy between 100 keV and 10 MeV emitted in a thin vertical slice. We can see from the two curves that the backward-moving photons are emitted ahead of the forward-moving photons. For completeness, Fig. 3.6 shows the energy distribution of the forward and backward directed electrons in our simulation. The snapshots in Fig. 3.6 and Fig. 3.5 are taken at $t = 67$ fs.

Figure 3.1(d) shows that our setup produces an extremely dense population of gamma-rays with energies greater than 100 keV. What is also remarkable is that this population consists of overlapping forward and backward-moving photons whose densities are shown in Fig. 3.1(g)

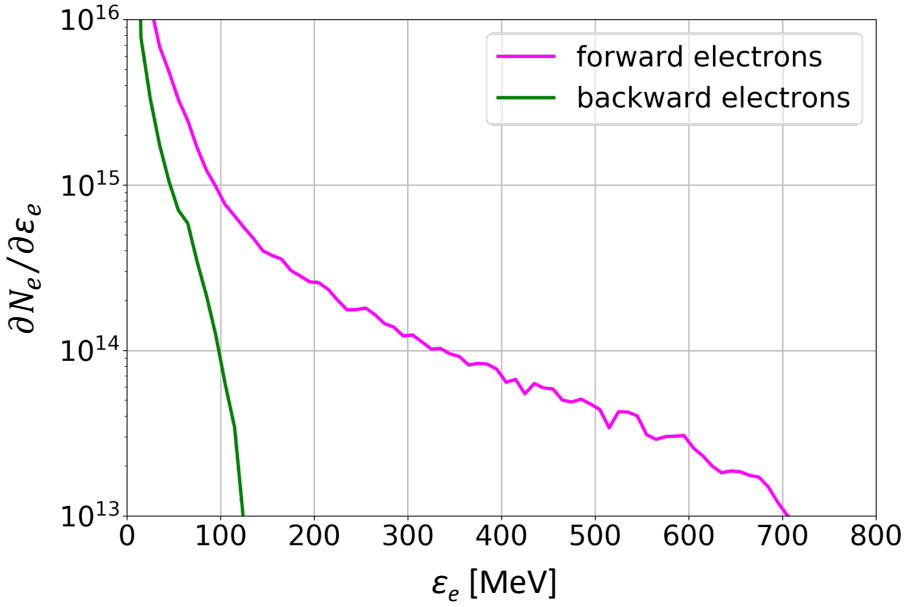

Figure 3.6. Energy distribution, $\partial N_e/\partial \varepsilon_e$, of forward and backward-moving electrons at $t = 67$ fs. The number of electrons N_e is computed by assuming that the width along the third dimension is equal to the channel width $d_{ch} = 5$ μm (our simulation is two-dimensional).

and Fig. 3.1(h), which is a result of the longitudinal offset in the photon emission. As the two populations collide, they produce electron-positron pairs, with the yield being enhanced due to the high photon density.

We first estimate the yield using the density of photons from our simulation. In our system, this density of photons with energy $\varepsilon_\gamma > 100$ keV is $n_\gamma \approx 10 n_c$, as shown in Fig. 3.1(d), where $n_c \approx 1.7 \times 10^{27}$ m^{-3} is the critical density for $\lambda_0 = 0.8$ μm. A useful figure of merit is an approximate macroscopic cross-section for the photons in the MeV energy range: $\Sigma_{\gamma\gamma} = \sigma_{\gamma\gamma} n_\gamma$, where n_γ is their density and $\sigma_{\gamma\gamma}$ is the microscopic cross-section for the linear Breit-Wheeler process. We set $\sigma_{\gamma\gamma} \approx 1.7 \times 10^{-29}$ m^{-2} which is close to its maximum value (a head-on collision of two 700 keV photons). The number of photons with $\varepsilon_\gamma > 700$ keV is about 40% of the number of photons with $\varepsilon_\gamma > 100$ keV. We therefore re-scale the density by setting $n_\gamma \approx 4 n_c$ and use this value to find that $\Sigma_{\gamma\gamma} \approx 1.2 \times 10^{-1}$ m^{-1}. The total number of photons with $\varepsilon_\gamma > 700$ keV is $N_\gamma \approx 4 \times 10^{13}$, where we have assumed that the size of the photon cloud in the third dimension is equal to the channel width $d_{ch} = 5$ μm (our simulation is two-dimensional). It is worth

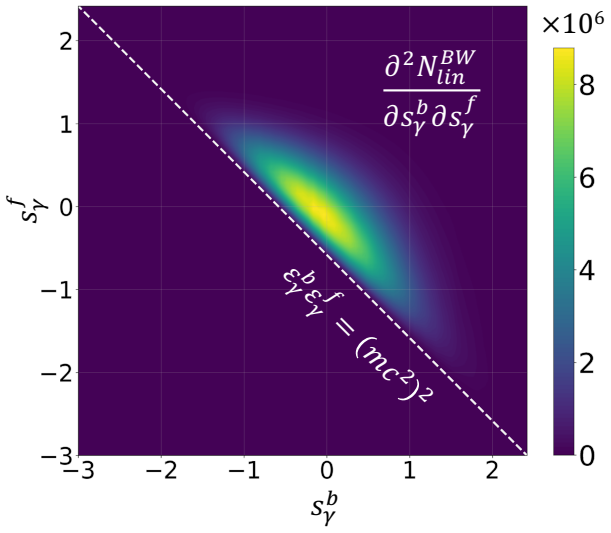

Figure 3.7. Yield of the linear Breit-Wheeler process, N_{lin}^{BW}, in a collision of forward-directed and backward-directed photons as a function of the photon energies. These energies are denoted as ε_γ^f and ε_γ^b, respectively. The yield is shown on a log-log scale, where $s_\gamma^f \equiv \log_{10}(\varepsilon_\gamma^f[\text{MeV}])$ and $s_\gamma^b \equiv \log_{10}(\varepsilon_\gamma^b[\text{MeV}])$.

pointing out that in the energy range between 0.1 and 10 MeV the number of backward-moving photons (4.4×10^{13}) is comparable to the number of forward-moving photons (5.9×10^{13}). The backward-emitted photons are not collimated, so we assume that they leave the cloud after travelling a distance roughly equal to the channel radius, $d_{ch}/2$. This gives the following estimate for the pair yield via the linear Breit-Wheeler process: $N_{lin}^{BW} \approx \Sigma_{\gamma\gamma} d_{ch} N_\gamma \approx 1.2 \times 10^7$.

In order to perform a quantitative assessment of the pair yield, we use the post-processing algorithm developed in [75] (i.e., Chapter II of this dissertation) detailed in Chapter V. The algorithm uses the photon data provided by the PIC simulation, which includes, in addition to the photon energy, the emission time, location, and the macro-particle weight. The photons are grouped into collimated mono-energetic beamlets. Each longitudinal position along the x-axis emits multiple such beamlets. They are assumed to be uniform along the y-axis (the assumption is motivated by the PIC data) with a width equal to the width of the channel.

By applying the described algorithm, we found that the total number of pairs is $N_{lin}^{BW} \approx 1.1 \times 10^7$, which is close to our earlier estimate. The number of generated pairs is three orders of

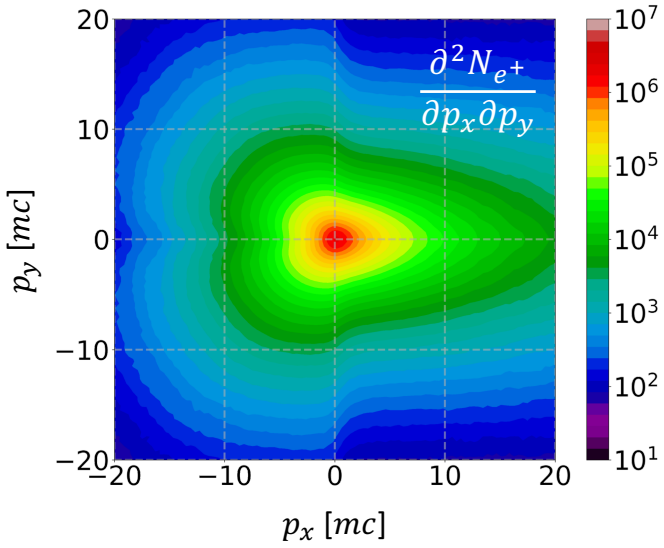

Figure 3.8. Momentum distribution of the positrons generated via the linear Breit-Wheeler process.

magnitude larger than the number of pairs produced by colliding two beams consisting of the collimated forward-emitted photons 250 μm away from each laser-irradiated structured target [13], where each beam is generated by a separate target as described earlier in Section 3.2. The significant increase is due to the increased density of the colliding photons in our configuration. It must be noted that adding a counter-propagating laser to this configuration can boost the yield by an order of magnitude [75] (see Chapter II), but this makes the corresponding experimental setup much more challenging.

Figure 3.7 shows the yield of the linear Breit-Wheeler process in a collision of forward and backward-directed photons as a function of their energies, where the superscripts f and b indicate the direction of the photon motion. As anticipated, the majority of the pairs are produced by photons within the energy range 100 keV$< \varepsilon_\gamma^{f,b} <$ 10 MeV, where ε_γ is the photon energy. This is a consequence of the broad photon spectrum. Figure 3.8 shows the momentum distribution of the generated positrons. We distribute the pairs generated in each photon-photon collision isotropically in the corresponding center of mass frame. The result can be refined by taking into account the differential cross-section [74]. The 'initial' distribution shown in Fig. 3.8

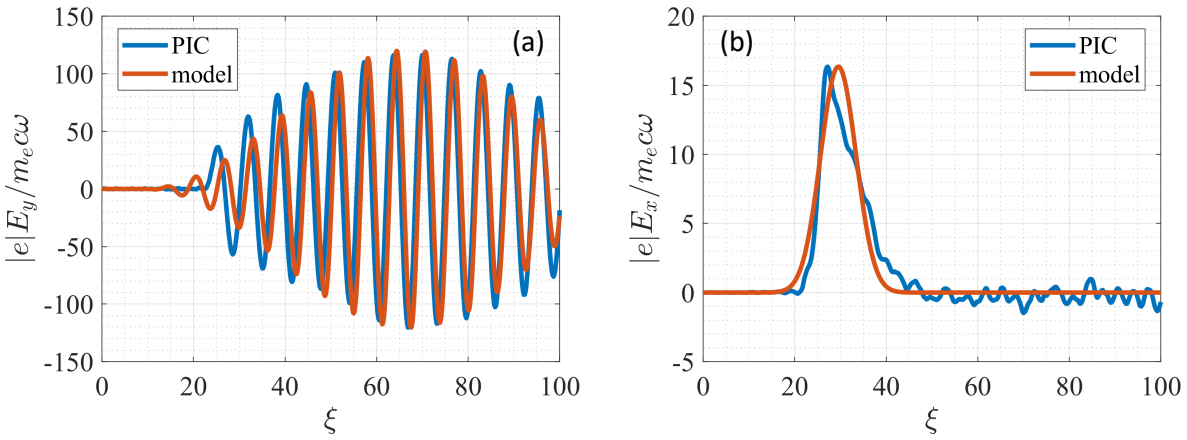

Figure 3.9. Laser and plasma electric fields in the PIC simulation (blue) and in the test-particle model (red). The PIC simulation electric fields are the snapshots taken at $t = 150$ fs and averaged over a region with $|y| < 1.5$ μm. The analytical form of the test-particle fields is given by Eq. (3.15) and Eq. (3.17). The phase variable is given by Eq. (3.14), with $x_{init} = 20$ μm and $t_{init} = 150$ fs.

is likely to evolve because the positrons inside the channel experience a superposition of strong laser and plasma fields.

3.5 Test-particle model for backward electron acceleration and photon emission

In this section, we use a reduced model motivated by the PIC simulation results to examine the backward electron acceleration that leads to the emission of the backward-directed gamma-rays. The purpose is to assess the impact of the plasma electric and magnetic fields on the electron dynamics.

The model is similar to that developed in [49] for analyzing direct laser acceleration of electrons in the presence of a static azimuthal plasma magnetic field. The electron is treated as a test particle, which means that the laser and plasma fields are externally prescribed. There are two modifications that we have made to adapt the model to our problem: we have added a longitudinal plasma field E_x, which moves with the laser pulse, and the force of radiation friction $\boldsymbol{f}_{RF}$ caused by the emission of photons. The force of radiation friction, in the Landau-Lifshitz

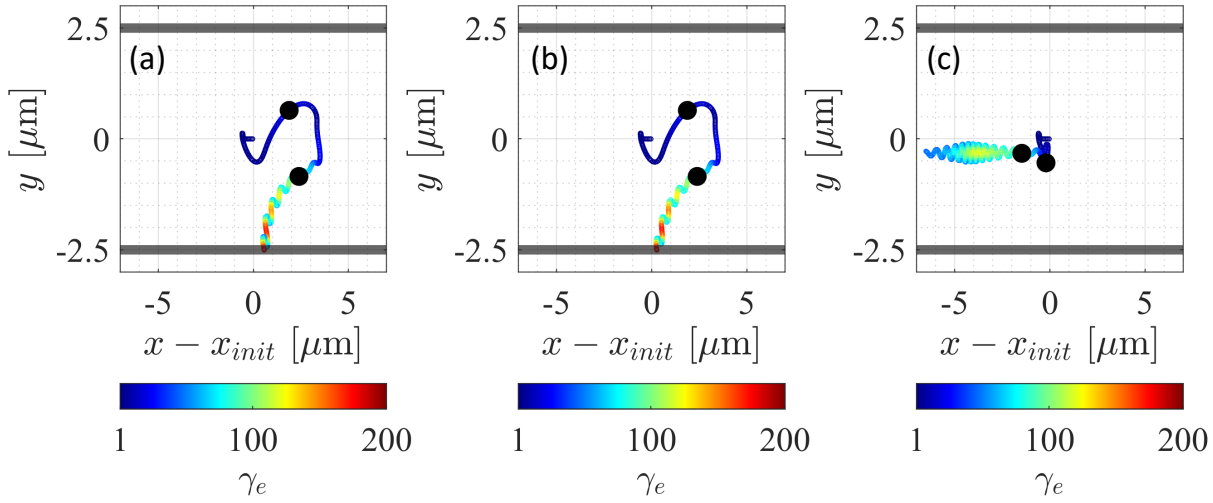

Figure 3.10. Electron trajectories from the test-particle model, with the color indicating the relativistic factor γ_e. (a) Complete electron dynamics. (b) Electron dynamics in the absence of the radiation friction force. (c) Electron dynamics in the absence of the static plasma magnetic field. The thick lines indicate the initial location of the channel wall in the PIC simulation. The electron experiences $E_x \geq 0.1E_x^{\max}$ while moving between the black round markers.

prescription [89], is directed anti-parallel to the electron momentum $\boldsymbol{p}$:

$$\boldsymbol{f}_{RF} = -\gamma_e^2 \frac{8\pi^2}{3} \frac{r_e}{\lambda_0} \frac{m_e c^2}{\lambda_0} \left(\frac{e\mathscr{E}}{m_e c \omega} \right)^2 \frac{\boldsymbol{p}}{p}, \tag{3.6}$$

where $\mathscr{E}$ is the effective field strength given by Eq. (3.2), $r_e \equiv e^2/m_e c^2 \approx 2.8 \times 10^{-13}$ cm is the classical electron radius, ω is the laser frequency, and $\lambda_0 = 2\pi c/\omega$ is the vacuum wavelength.

The equations that describe the electron dynamics are

$$\frac{dp_x}{dt} = -|e|E_x - \frac{|e|}{\gamma_e m_e c} p_y B_z - |\boldsymbol{f}_{RF}| \frac{p_x}{p}, \tag{3.7}$$

$$\frac{dp_y}{dt} = -|e|E_y + \frac{|e|}{\gamma_e m_e c} p_x B_z - |\boldsymbol{f}_{RF}| \frac{p_y}{p}, \tag{3.8}$$

$$\frac{dx}{dt} = \frac{c}{\gamma_e} \frac{p_x}{m_e c}, \tag{3.9}$$

$$\frac{dy}{dt} = \frac{c}{\gamma_e} \frac{p_y}{m_e c}, \tag{3.10}$$

where p_x and p_y are the components of the electron momentum, parallel and perpendicular to

the laser propagation respectively, and x and y are the electron coordinates. The fields are a superposition of the laser and plasma fields:

$$E_x = E_x^{pl}(\xi), \tag{3.11}$$

$$E_y = E_y^{laser}(\xi), \tag{3.12}$$

$$B_z = B_z^{pl}(y) + B_z^{laser}(\xi), \tag{3.13}$$

where

$$\xi = \frac{2\pi}{\lambda_0}\left[c(t - t_{init}) - (x - x_{init})\right] \tag{3.14}$$

is the phase variable, with $\xi = 0$ at the initial location of the electron in our calculations ($x = x_{init}$ at $t = t_{init}$). We neglect the slight superluminosity of the wave fronts (caused by the plasma and the finite transverse size of the channel) by assuming that the phase velocity is equal to c. More importantly, the longitudinal field in this model is also moving with the speed of light for the sake of simplicity. The assumption here is that the difference between the actual speed, $0.82c$, and the speed of light is inconsequential, because the electrons are moving in the opposite to the direction of the laser propagation. It is more important that the envelopes of the laser pulse and the longitudinal electric field should move forward at the same velocity.

We perform our calculations for

$$E_y^{laser} = B_z^{laser} = E_{\rm env}(\xi)\sin(\xi + \pi - \Delta_y), \tag{3.15}$$

where

$$E_{\rm env}(\xi) = \frac{E_0}{2}[1 - \cos(\pi(\xi - \Delta_y)/\sigma_y)] \tag{3.16}$$

for $\xi \geq \Delta_y$ and $E_{\rm env}(\xi) = 0$ otherwise. Here $\Delta_y = 3\pi$ and $\sigma_y = 57.53$, and $a_0 = |e|E_0/m_e c\omega = 120.4$. The values of these parameters are chosen such that the field given by Eq. (3.15)

reproduces the snapshot of the laser electric field shown in Fig. 3.9(a). The longitudinal plasma field in our calculations is

$$E_x(\xi) = E_x^{\max} \exp\left[-\frac{(\xi-\mu-\Delta_x)^2}{\sigma_x^2}\right] \tag{3.17}$$

for $\xi \geq \Delta_x$ and $E_x(\xi) = 0$ otherwise. Here $\Delta_x = 2\pi$, $\sigma_x = 5.5$, $\mu = 20.12$, and $|e|E_x^{\max}/m_e c\omega = 16.34$. The values of these parameters are chosen such that the field given by Eq. (3.17) reproduces the snapshot of the laser electric field shown in Fig. 3.9(b). The plasma magnetic field is

$$B_z^{pl}(y) = 2\pi j_0 y/c. \tag{3.18}$$

The uniform current density is set at $j_0 = 10J_A/\pi\lambda_0^2$ to reproduce the transverse linear profile of the magnetic field in our PIC simulation, where $J_A = m_e c^3/|e|$ is the non-relativistic Alfvén current.

Figure 3.10(a) shows a trajectory of an electron computed using the test-particle model. The electron is located at $x_{init} = 20$ μm at $t_{init} = 150$ fs. In our fully self-consistent PIC simulation, the electrons in the channel typically acquire some negative longitudinal momentum before they encounter the laser beam and the longitudinal electric field structure driven by its front. In order to capture this feature in our test-particle calculations, we set $p_x = -0.3 m_e c$ at $t = t_{init}$. After encountering the laser pulse, the electrons gets pushed in the forward direction. As it slips further into the laser pulse, the longitudinal plasma field, associated with the leading edge of the laser pulse, ramps up at the electron location. The increase in E_x causes the electron to reverse the direction of its longitudinal motion while gaining energy. In order to make the correlation evident, we use black round markers to show the beginning and the end of that segment of the trajectory where $E_x \geq 0.1E_x^{\max}$. The calculation confirms the role of the plasma E_x in generating relativistic ($\gamma_e \approx 100$) backward-moving electrons.

The plasma magnetic field also has a profound impact on the electron trajectory. As seen

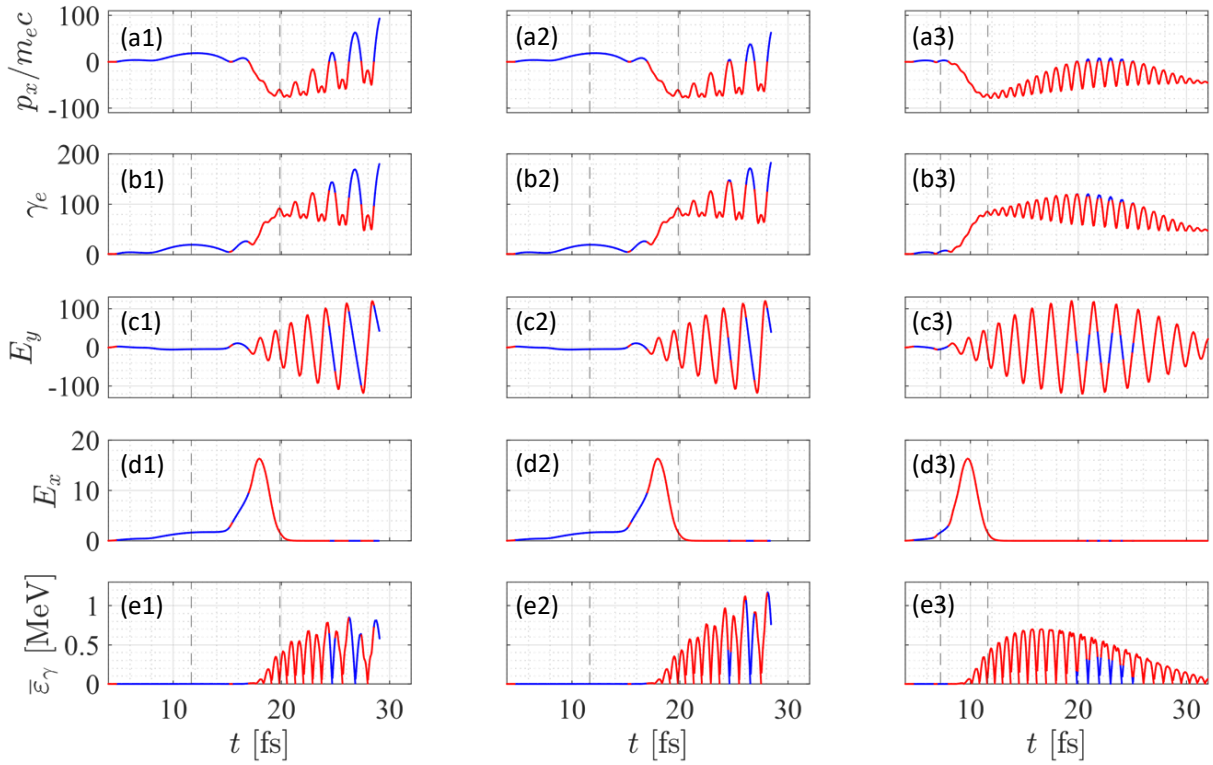

Figure 3.11. Details of electron dynamics along the trajectories shown in Fig. 3.10, with the red color corresponding to $p_x < 0$. Left column: complete electron dynamics. Middle column: electron dynamics in the absence of the radiation friction force. Right column: electron dynamics in the absence of the static plasma magnetic field. (a1) - (a3) Longitudinal electron momentum. (b1) - (b3) Relativistic factor γ_e. (c1) - (c3) Transverse laser electric field acting on the electron. (d1) - (d3) Longitudinal plasma electric field acting on the electron. (e1) - (e3) Characteristic energy of emitted photons calculated according to Eq. (3.3). The region between the vertical dashed lines corresponds to that part of the electron trajectory where $E_x \geq 0.1E_x^{\max}$.

in Fig. 3.10(c), the electron moves backwards while performing transverse oscillations after its interaction with E_x. This trajectory is obtained by setting $j_0 = 0$ in the electron equations of motion, so that there is no plasma magnetic field. The energy gain is comparable to that seen in Fig. 3.10(a). However, the magnetic field in Fig. 3.10(a) causes appreciable transverse electron deflection that leads to electron loss once the electron reaches the wall of the channel. The deflection is in qualitative agreement with the magnetic field orientation. We terminate the calculation once the electron cross the initial channel boundary shown with the thick lines.

Figure 3.11 provides additional information regarding the electron dynamics, including the characteristic energy of emitted photons $\overline{\varepsilon}_\gamma$. In order to clearly distinguish the backward electron motion, we use the red color to indicate $p_x < 0$. The region between the vertical dashed lines corresponds to that part of the electron trajectory where $E_x \geq 0.1E_x^{\max}$. Figure 3.11(e1) shows that $\overline{\varepsilon}_\gamma$ reaches the 0.5 MeV level towards the end of the electron interaction with E_x. More importantly, the emission occurs in the backward direction. The electron continues to emit in the backward direction even after the interaction with E_x, which indicates the long-lasting effect of the plasma electric field. Our result confirms that E_x at the leading edge of laser pulse can indeed lead to emission of energetic backward-directed photons suitable for the pair production.

Figure 3.11 also provides details of the electron dynamics without radiation friction and without the plasma magnetic field. By comparing Fig. 3.11(e1) and Fig. 3.11(e3), we find that $\overline{\varepsilon}_\gamma$ is essentially the same in the absence of the plasma magnetic field. The backward emission is prolonged because the electron remains within the channel. The middle column in Fig. 3.11 shows the electron dynamics in the absence of the radiation friction. Even though the electron trajectory in the absence of the radiation friction remains relatively unaffected [compare Figs. 3.10(a) and 3.10(b)], the energy of the emitted photons changes appreciably. As seen from comparing Figs. 3.11(e1) and 3.11(e2), the difference occurs after the interaction with E_x. The conclusion then is that the photon emission should be calculated self-consistently, with radiation friction taken into account in real-time.

3.6 Summary and discussion

We have shown that electron-positron pair creation by the linear Breit-Wheeler process is possible when a single laser travels through a dense plasma target. In particular, using a laser pulse with parameters similar to those at the ELI-NP laser facility, it is possible to produce 10^7 linear Breit-Wheeler pairs in a single shot with a peak laser intensity of just 3×10^{22} Wcm^{-2}.

The mechanism involves a strong longitudinal electric field driven by the laser pulse. As the laser pulse travels through the plasma channel, it induces a longitudinal electric field at the front of the laser pulse due to charge separation. The electric field pulls the channel electrons back when they encounter the laser pulse, causing them to travel opposite to the direction of laser propagation. The backward-moving electrons experience strong acceleration from the laser pulse, causing them to emit energetic backward-directed photons. These photons are in the energy range suitable for the linear Breit-Wheeler process, and therefore when they collide with forward moving photons that are typically associated with the considered setup, electron-positron pairs are created. The high pair yield is due to the fact that the photon collisions occur locally, i.e. close to the point of emission, and thus at high density. The practical advantage of the scheme presented is that only a single laser pulse is required and therefore the difficulty of spatially and temporally overlapping multiple laser pulses is avoided.

The number of positrons produced by the linear Breit-Wheeler process in our setup is 10^7 even for $a_0 = 120$, equivalent to $I_0 \approx 3 \times 10^{21}$ Wcm^{-2}, which is within reach of today's high-intensity laser facilities. The uniqueness of our setup compared to the setup that involves two lasers [75] (presented in Chapter II) is that it produces virtually no pairs via the nonlinear Breit-Wheeler process, i.e. no pairs were produced in our simulation by the module that computes the corresponding yield. For this process to become significant for a single laser pulse propagating in a plasma channel, we would need intensities $\geq 10^{24}$ Wcm^{-2} [90], or if the laser pulse is subsequently reflected from a high-density mirror, $\geq 10^{23}$ Wcm^{-2} [91]. The linear Breit-Wheeler process then only needs to compete with the Bethe-Heitler process. In this process, a γ-ray with

energy greater than $2m_ec^2$ creates an electron-positron pair by interacting with the Coulomb field of an atomic nucleus. Using a simple post-processing algorithm detailed in [75] (Chapter II of this dissertation), we determine that the Bethe-Heitler process generates 5.7×10^5 pairs inside the channel. This number is roughly 20 times lower than the yield from the linear Breit-Wheeler process, so we conclude that the linear Breit-Wheeler process is the primary source of positrons in our setup.

Figure 3.8 shows the momentum distribution of the positrons right after they were created, but this 'initial' distribution is likely to change before the positrons leave the plasma. The positrons created inside the channel are subject to the influence of the laser and plasma fields. One would need to develop a PIC code that can produce the linear Breit-Wheeler pairs in order to reliably assess the impact of these fields on the positron momentum. The plasma magnetic field is likely to have a confining effect. The transverse confinement however causes charged particles to slide along the magnetic filament [49], with the direction dependent on the polarity of the field and the particle charge. In the magnetic field configuration shown in Fig. 3.1(c), the electrons slide forward, which enables the increased energy gain from the laser [49], so we anticipate that the positrons are likely to slide back towards the channel opening. (Subsequent dynamics of these produced positrons are discussed in detail in Chapter VI and Sec. 7.2, 7.3, 7.4, 7.5.)

The backward emission of energetic photons by a similar mechanism related to the charge separation at the leading edge of the laser pulse was previously discussed in [92], albeit in the case of a much higher laser intensity. This regime was then further investigated in [93]. The strength of the longitudinal electric field goes up with the laser intensity or, equivalently, with a_0, which means that the energies of backward accelerated electrons and the energies of the photons they emit also increase with a_0. Even though the nonlinear Breit-Wheeler process is inefficient for the value of a_0 considered in our work in this chapter, it can become an import source of electron-positron pairs at much higher a_0 due to the discussed increase of the photon energies [92, 93]. It must be pointed out that Refs. [92, 93] only considered the nonlinear Breit-Wheeler process, so further research is needed to determine at what value of a_0 the nonlinear

Breit-Wheeler process becomes the dominant mechanism.

3.7 Acknowledgement

Chapter 3, in part, is a reprint of the material as it appears in *A single-laser scheme for observation of linear Breit-Wheeler electron-positron pair creation* in New Journal of Physics, 23, 115005, by Y. He, I-L. Yeh, T. Blackburn, and A. Arefiev, 2021. The dissertation author was the primary investigator and author of this paper.

This research was supported by AFOSR (Grant No. FA9550-17-1-0382). Simulations were performed with EPOCH (developed under UK EPSRC Grants EP/G054950/1, EP/G056803/1, EP/G055165/1, and EP/ M022463/1) using high performance computing resources provided by TACC.

3.8 Appendix

2D-3V kinetic simulations presented in this chapter were performed using the fully relativistic particle-in-cell code EPOCH [17]. Detailed simulation parameters are given in Table 3.1. The laser beam is injected into the rectangular simulation domain at the left boundary located at $x = -5$ μm and it propagates in the positive direction along the x-axis. The laser is linearly polarized, so that its electric field has only x and y components and its magnetic field has only a z component. The laser is focused at the surface of the target located at $x = 0$ μm. The time t is defined such that the laser reaches its peak intensity in the focal plane (in the absence of the target) at $t = 0$ fs.

The plastic structured target contains a pre-filled channel whose axis is aligned with the axis of the laser beam. The target is initialized as a fully ionized plasma. The density of the carbon ions is set to be equal to the density of the protons in the bulk and inside the channel. The values of the electron density in the bulk and inside the channel are listed in Table 3.1.

Table 3.1. 2D PIC simulation parameters.

Laser parameters	
Normalized field amplitude	$a_0 = 120$
Peak intensity	$I_0 = 3.11 \times 10^{22}$ W/cm^2
Wavelength	$\lambda_0 = 800$ nm
Focal plane of laser	$x = 5$ μm
Laser profile (longitudinal and transverse)	Gaussian
Pulse duration (FWHM for intensity)	25 fs
Focal spot size (FWHM for intensity)	4.0 μm

Target parameters	
Target thickness (along y)	30 μm
Target length (along x)	120 μm
Channel width	$d_{ch} = 5$ μm
Composition	C^{6+} ions, H^+ ions, and electrons
Ion density ratio	$n_{C^{6+}} : n_{H^+} = 1 : 1$
Electron density in the channel	$n_e = 2.8\ n_c$
Electron density in the bulk	$n_e = 28\ n_c$
Channel density	15 mg cm^{-3}
Bulk density	150 mg cm^{-3}

Other simulation parameters	
Simulation box size	130 μm along x 36 μm along y
Spatial resolution	40 cells per μm along x 40 cells per μm along y
Number of macro-particles per cell	40 for electrons 20 for carbon ions 20 for hydrogen ions

Achieving pair creation via linear and non-linear Breit-Wheeler processes in dense plasmas irradiated by high-intensity laser pulses

It has been recently shown that over 10^9 electron-positron pairs can be produced from light alone at experimentally accessible laser intensity of $5 \times 10^{22}\mathrm{Wcm}^{-2}$ by irradiating a target with a pre-formed channel by two counter-propagating laser pulses (see Chapter II). Although targets of variable length and channel density have been successfully fabricated and used in recent experiments involving high-intensity lasers, the impact of these parameters on the pair yield by different pair creation processes is yet to be understood. In this chapter, we explore, using two-dimensional particle-in-cell simulations, the impact of the channel density and length on pair production by linear Breit-Wheeler process, nonlinear Breit-Wheeler process, and Bethe-Heitler process at fixed laser intensity. We find that these parameters can be successfully used to increase the linear Breit-Wheeler pair yield. More importantly, the relative contribution of each process can be adjusted by varying the same parameters. We show that this approach allows us to completely eliminate the yield from the nonlinear Breit-Wheeler process while maintaining a significant yield from the linear Breit-Wheeler process. The Bethe-Heitler process plays a secondary role in the considered system, so the majority of the positrons inside the channel are produced from light alone. Our results indicate that a structured target irradiated by two laser beams has the potential to be a versatile platform for future experimental studies of the Breit-Wheeler pair production processes, with the target parameters serving as control knobs.

4.1 Introduction

Creation of electron-positron pairs in photon collisions is probably one of the most striking predictions of quantum electrodynamics. The process is often referred to as the Breit-Wheeler process [1]. The linear Breit-Wheeler process involves two photons, with these photons typically being energetic gamma-rays. The nonlinear Breit-Wheeler process involves multiple (more than two) photons. One example is a collision of an energetic gamma-ray with multiple optical photons. Both linear and nonlinear Breit-Wheeler (BW) processes play an important role in astrophysics [2, 3, 4, 5]. However, they are notoriously hard to observe in laboratory conditions. The nonlinear BW process has been observed once before [22] by colliding a 46.6 GeV electron beam with a terawatt laser pulse. The yield was less than one pair per shot. The linear BW process has only been observed via the use of virtual photons [94].

There are two aspects that make BW processes challenging to recreate: the smallness of the cross section and the high photon energy threshold. For example, in the case of the linear BW process, the conservation of momentum and energy requires $\varepsilon_1\varepsilon_2 > (mc^2)^2$, where $\varepsilon_{1,2}$ are the energies of the colliding photons, m is the electron mass, and c is the speed of light. This condition translates into a requirement to have an MeV-level photon population. The cross section of the linear BW process is only about r_e^2 [95], where $r_e \approx 2.82 \times 10^{-15}$ m is the classical electron radius. It is about ten orders of magnitude smaller than the cross section for electron impact ionization.

High-power, high-intensity lasers have the potential to overcome the described difficulties. The existing state-of-art laser facilities are able to achieve laser intensities that exceed 10^{22} W/cm^2 [6, 7, 8], whereas the systems that are currently under construction are expected to approach intensities of 10^{23} W/cm^2 [7]. Most of the BW-related research has been focused on leveraging the anticipated ultra-high intensities (beyond 10^{23} W/cm^2) to achieve a significant yield from the nonlinear-BW process (e.g. see Refs. [96, 97]). It has also been claimed that, by leveraging multi-GeV electron acceleration in hollow cones, the intensity required to produce

dense pairs via the nonlinear BW process can be as low as 10^{22} Wcm^{-2} [30, 98]. The linear-BW process has received less attention due to a perceived difficulty to create adequate conditions [99].

In the context of laser driven experiments, the key difference between the nonlinear and the linear processes is that the nonlinear process is a collision of gamma-rays with the laser photons, whereas the linear process is a collision of gamma-rays with other gamma-rays. This means that the linear process does not directly utilize the high density of optical photons provided by an ultra-high intensity laser beam. One way to utilize high-intensity lasers for the linear-BW process is by converting the optical photons into gamma-rays. It has been shown that dense laser-irradiated plasmas can efficiently convert laser energy into gamma-rays. The laser first transfers its energy to plasma electrons, accelerating them to ultra-relativistic energies. Energetic gamma-rays are then efficiently emitted by these relativistic electrons via synchrotron emission during electron deflections by laser and plasma fields [80, 100, 41, 101, 102, 82, 103]. Even though this is not a threshold process, laser intensities above 10^{22} W/cm^2 are required to achieve a conversion efficiency that is in the range of a percent.

There has been an increased interest in utilizing gamma-rays emitted during ultra-intense laser plasma interactions to develop setups that can be used to experimentally observe the linear BW process [11, 12, 74, 73, 13, 10, 75]. One general approach is to use two lasers, each irradiating its own target and generating a beam of gamma-rays [73]. The gamma-rays are then collided in vacuum some distance away from the targets. The appeal of this approach is that the pairs are created in vacuum. The drawback however is that, due to the divergence of the gamma-ray beams, the yield strongly depends on the distance from the targets to the collision location. In practical terms, this means that the distance should not exceed several hundred microns in order to achieve a yield that is more than just a few pairs [13], which makes experimental implementation challenging.

One can dramatically increase the pair yield by easing the requirement that the pairs must be produced in vacuum. In two recent publications (whose reprints are Chapter II and Chapter III of this dissertation), we considered the pair production via the linear BW process

inside a laser-irradiated plasma [104, 75]. We found that over 10^7 pairs can be produced using laser intensity of $\sim 3 \times 10^{22}$ Wcm^{-2}, which is a significant increase in the pair yield compared to the approach where the pair production takes place in vacuum [13]. Our simulations have revealed that this yield can be achieved either by using a single laser beam [104] (Chapter III) or by using two laser beams in a colliding geometry [75] (Chapter II). A distinctive feature of the setup with two beams is that it generates an accelerating configuration for the positrons after they have been created. A synergistic combination of the laser fields and a quasi-static plasma magnetic field driven by the laser beams enables the positrons to gain hundreds of MeV of energy. The energetic positrons leave the target in the form of collimated jets, which can facilitate the detection of the produced positrons in experiments.

In Ref. [75] (Chapter II), the colliding laser setup [also shown in Fig. 4.1(a)] was used for a proof-of-principle calculation demonstrating that the linear BW process can be the dominant source of positrons at experimentally accessible intensities. Specifically, the yield was compared to that of two competing processes, the nonlinear BW process and Bethe-Heitler process (a collision of a gamma-ray with an atomic nucleus that results in an electron–positron pair), for different laser intensities. The laser collision in Ref. [75] was achieved using a structured target with a pre-filled channel whose plasma density is lower than the density in the bulk. The channel provides optical guiding to the laser pulses, preventing possible misalignment that can be caused by laser-plasma instabilities in a uniform plasma. Similar structured targets with a foam-filled channel have been fabricated and used for a recent experiment [76]. It remains to be understood how the target parameters impact the pair yield from all three processes.

Recent progress in target fabrication techniques makes it possible to create a wide range of target configurations and parameters [105, 106]. Relevant capabilities include production of targets with a cylindrical channel of variable length [37, 36] and production of low-mass foam targets ($\sim$10–80 mg/cm^3) [107]. Both channel density and target length are known to have a considerable impact on electron acceleration and, as a result, on the photon emission. It is therefore worth asking whether target parameters, such as channel length and density, can serve

as effective control-knobs in the context of pair production for the purpose of enhancing the pair yields and experimentally distinguishing different pair creation processes.

In this chapter, we examine the impact of target parameters on pair production by linear BW process, nonlinear BW process, and Bethe-Heitler (BH) process at fixed laser intensity. In order to make our predictions relevant to such multi-beam laser facilities as Extreme Light Infrastructure Nuclear Physics (ELI-NP) [34, 6], we use a peak intensity of 5×10^{22} Wcm^{-2} for our study. We show that, by varying the channel density and length of the structured target, one can increase the linear BW pair yield compared to the yield achieved in Ref. [75] (Chapter II). More importantly, the relative contribution of each process can be adjusted by varying the same parameters. For example, we show that this approach allows us to completely eliminate the yield from the nonlinear BW process while maintaining a significant yield from the linear BW process. Our results indicate that a structured target irradiated by two laser beams has the potential to be a versatile platform for future experimental studies of BW pair production processes, with the target parameters serving as control knobs.

The rest of this chapter is organized as follows. In Section 4.2, we review the results of Ref. [75] (Chapter II) and the original setup used to obtain them. In Section 4.3, we investigate the impact of channel density $n_{\rm ch}$ and length L on the pair yields of linear BW, nonlinear BW, and BH processes at fixed peak laser intensity of 5×10^{22}Wcm^{-2}. In Section 4.4, we summarize the key findings from the parameter scan presented in Section 4.3.

4.2 Review of previous results

In order to set the stage for the parameter scan discussed in Section 4.3, we start by reviewing the results of Ref. [75] (of which Chapter II is a reprint) and the original setup used to obtain them.

In Ref. [75], the pair production was studied with the help of 2D particle-in-cell (PIC) simulations using the setup schematically shown in Fig. 4.1(a). In the setup, two identical

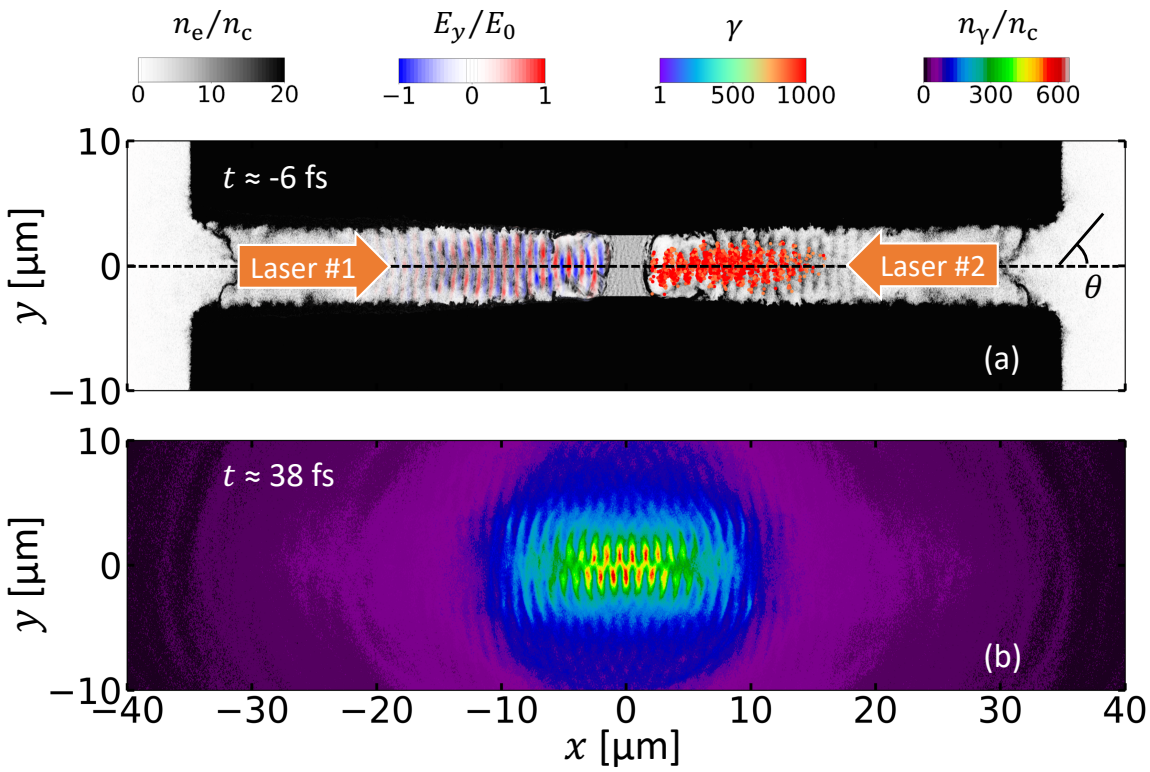

Figure 4.1. Generation of energetic photons in a structured target irradiated by two counter-propagating laser beams with $a_0 = 190$. (a) Electron density n_e (gray scale), transverse electric field of laser #1 E_y (color scale) and energetic electrons with $\gamma \geq 800$ accelerated by laser #2 (dots, colored by γ). The snapshot is taken at $t \approx -6$ fs and prior to the laser-laser collision. The laser pulses arrive to the mid-plane ($x = 0$) and collide at $t = 0$. (b) The density of photons with energy $\varepsilon \geq 1$ keV, in units of the classical critical density n_c at $t \approx 38$ fs and after the laser-laser collision. Reproduced with permission from He *et al.*, Communications Physics, **4**, 139 (2021). Copyright 2021 Authors, licensed under a Creative Commons Attribution (CC BY 4.0) license. Adapted from original.

counter-propagating ultra-intense laser pulses are injected into a solid micro-tube. The two laser pulses are linearly polarized with 50 fs duration, 1 μm wavelength λ_0, and normalized peak amplitude a_0 in the range $40 \leq a_0 \leq 250$, where $a_0 := 0.85 I_0^{1/2} [10^{18}\ \mathrm{Wcm}^{-2}] \lambda_0 [\mu\mathrm{m}]$, and I_0 is the dimensional peak intensity. The target is a micro-tube with channel diameter $d_{ch} = 5$ μm and bulk electron density $n_{\mathrm{bulk}} = 100 n_c$, where $n_c := \pi mc^2/|e|\lambda_0$ is the classical critical or cutoff density with e being the electron charge. The target channel is filled with a lower density plasma. The electron density in this plasma is set according to the laser intensity, $n_{\mathrm{ch}} := (a_0/100) 3.8 n_c$, to ensure that the optical properties of the channel stay approximately unchanged. One way

to achieve such a target configuration is by filling a pre-formed channel with a low-mass foam whose pore size is smaller than the laser wavelength [76]. Additional details regarding the simulation setup can be found in Table 4.1 of Section 4.6.1.

Even though the channel electron density exceeds the classical cutoff density n_c, the channel becomes transparent to the laser electromagnetic fields due to the relativistically induced transparency. The transparency is caused by electron heating to relativistic energies by the intense laser fields (the typical requirement is $a_0 \gg 1$). As the two laser beams propagate along the channel, each of them drives a strong longitudinal electron current that induces a strong slowly evolving azimuthal magnetic field. The magnetic field provides transverse electron confinement [108], while, at the same time, it also enhances electron energy gain from the laser fields [49]. Each laser beam generates its own co-propagating beam of ultra-relativistic electrons. The electrons continue gaining kinetic energy, $(\gamma-1)mc^2$, prior to encountering a counter-propagating laser pulse, which occurs at $t \geq 0$. Here γ stands for the electron relativistic Lorentz factor. Figure 4.2(a) shows the time evolution of the electron distribution as a function of γ. It is worth noting that our previous studies have shown that the discussed magnetic field generation and electron acceleration in 2D PIC simulations are qualitatively similar to the magnetic field generation and electron acceleration in 3D PIC simulations [41, 13, 49].

A qualitative change in the dynamics of the accelerated electrons occurs when they encounter a counter-propagating laser beam. The change can be quantified using the quantum nonlinearity parameter χ defined as

$$\chi = \frac{\gamma}{E_s}\sqrt{\left(\boldsymbol{E}+\frac{1}{c}\left[\boldsymbol{v}\times\boldsymbol{B}\right]\right)^2-\frac{1}{c^2}\left(\boldsymbol{E}\cdot\boldsymbol{v}\right)^2} \tag{4.1}$$

where $\boldsymbol{E}$ and $\boldsymbol{B}$ are the electric and magnetic fields acting on the considered electron with velocity $\boldsymbol{v}$ and $E_s \approx 1.32\times10^{18}$ V/m is the Schwinger field. The quantum nonlinearity parameter χ is proportional to the electron acceleration in an instantaneous rest frame. This is the reason why the value of χ increases when the energetic electrons collide head-on with another laser

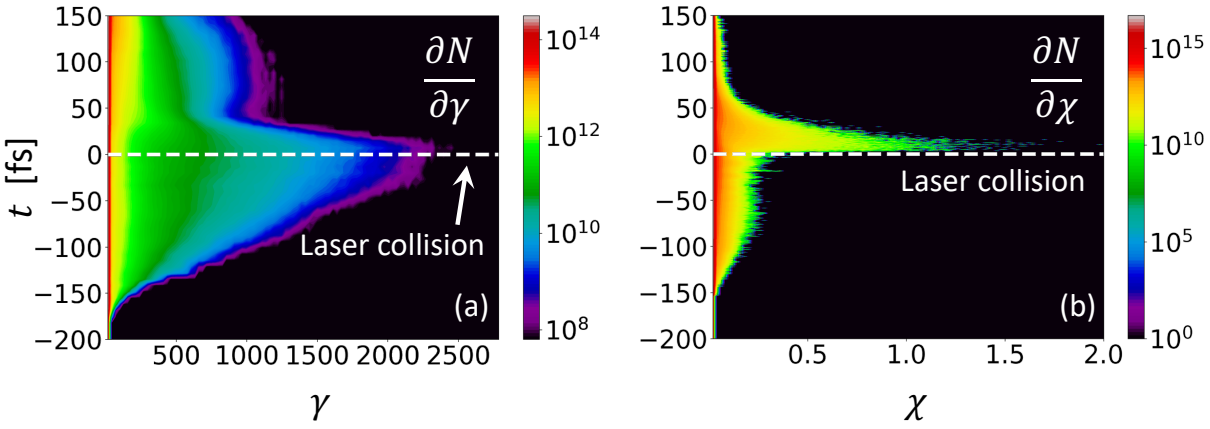

Figure 4.2. Time evolution of the electron distribution in the simulation shown in Fig. 4.1. (a) Electron distribution as a function of the relativistic factor γ. (b) Electron distribution as a function of the quantum nonlinearity parameter χ defined by Eq. (4.1). The two laser pulses collide at $t = 0$, marked with a horizontal dashed line in each plot. Reproduced with permission from He *et al.*, Communications Physics, **4**, 139 (2021). Copyright 2021 Authors, licensed under a Creative Commons Attribution (CC BY 4.0) license.

beam. The collision occurs at $t \geq 0$, with the exact time determined by the electron position within its parent laser beam (the co-propagating beam responsible for the electron energy gain). Figure 4.2(b) confirms that a dramatic change in the electron distribution as a function of χ indeed occurs at $t \approx 0$ when the two laser beams collide in the mid-plane.

The power of synchrotron emission by the electrons scales as

$$P_{synch} \propto \chi^2. \tag{4.2}$$

The spectrum emitted by the electrons peaks at photon energy

$$\varepsilon_* \approx 0.44\chi\gamma mc^2. \tag{4.3}$$

The increase in χ causes the energetic electrons to emit a large proportion of their energy. This process is evident in Fig. 4.2(a) and Fig. 4.2(b) at $t > 0$. Figure 4.3 shows the angular-energy spectrum of the emitted photons. In our simulation carried out using the PIC code EPOCH [17], the photon emission is modelled with the help of a Monte Carlo module for quantum synchrotron

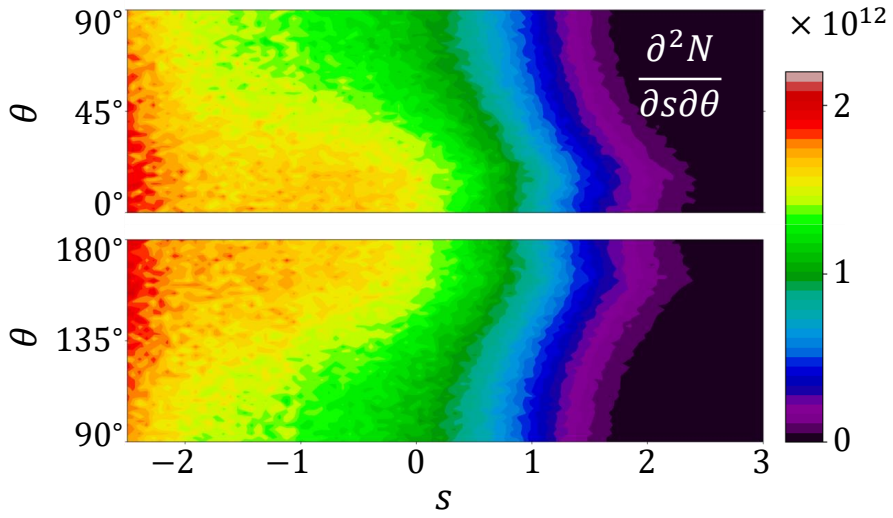

Figure 4.3. Energy-angle spectrum $\partial^2 N/\partial s \partial \theta$ [$^{\circ -1}$] of emitted photons in the simulation shown in Fig. 4.1. Here, θ is the angle between the photon momentum $\boldsymbol{p}$ and the x-axis and s is a dimensionless energy variable defined to be $s := \log_{10}(\varepsilon/mc^2)$ with ε being the photon energy. The photon number N is calculated by taking the size of the third dimension to be equal to the channel width $d_{\mathrm{ch}} = 5$ μm. Reproduced with permission from He *et al.*, Communications Physics, **4**, 139 (2021). Copyright 2021 Authors, licensed under a Creative Commons Attribution (CC BY 4.0) license. Adapted from original.

radiation that emits photons as individual particles. Due to the high power of emission at $t > 0$, the energetic electrons rapidly emit their energy and the density of high energy photons becomes very high at the place where the two laser beams overlap. For example, for $a_0 = 190$, the density of photons with energy above 1 keV reaches several hundreds of n_c, as shown in Fig. 4.1(b).

In the considered setup, the dense population of generated counter-propagating energetic gamma-rays overlaps with the two laser pulses, which creates favorable conditions for linear and nonlinear BW processes. The gamma-rays can also collide with the plasma ions, which can lead to pair production via the BH process. Currently (by the time of the publication of materials in this chapter), none of the PIC codes used for simulating high-intensity laser-plasma interactions are capable of calculating the yield from the linear BW process because this requires simulating binary collisions (PIC codes with such implementation are already done

which are shown in Chapter VI and Chapter VII). We compute the yield using a post-processing algorithm detailed in Ref. [75] (More details about the post-processing algorithm can be found in Chapter V). The algorithm uses 2D PIC simulation data, leveraging the fact that the photons only move in the plane of the simulation. No algorithm currently exists that can treat 3D photon motion (PIC codes with such implementation are already done which are shown in Chapter VII). Previous studies [41, 13] show that the divergence of the emitted photons in 3D simulations is not symmetrical, with most of the divergence taking place in the laser polarization plane. Our 2D PIC simulations already capture this divergence while neglecting the much weaker photon divergence out of the polarization plane. The yield from the nonlinear BW process is computed using a standard module that is a part of the PIC code EPOCH [17]. In Ref. [75], the same simulation (same parameters) was repeated four times with different random seeds to get a more accurate assessment at lower a_0 when the code generates only a few macro-particles as a result of the nonlinear BW process. We calculate the yield from the BH process using a post-processing algorithm as well. This basic algorithm is described in Ref. [75]. Only the positrons created inside the channel have the opportunity of being accelerated by one of the laser beams and becoming a part of a collimated positron jet. This is the reason why we compute the BH yield just inside the channel.

The yields for all three processes as a function of laser amplitude a_0 are shown in Fig. 4.4. The BW processes dominate over the BH process over the entire range of a_0, which confirms that the considered setup can be used to study the pair production via BW processes inside a plasma. The plot also indicates that the linear BW process dominates over the nonlinear BW process at lower intensity, with the two yields becoming comparable only when a_0 reaches the value of 220. However, it is important to point out that this trend is obtained for a specific target length and a specific channel density that is set according to a_0. Indeed, our setup uses $n_{\text{ch}} = (a_0/100)3.8n_c$ with a fixed channel length $L = 70$ μm, which means that, for each a_0, the trend corresponds to only a single combination of n_{ch} and L. This raises a question of whether the trend will persist for other combinations of n_{ch} and L or whether it can be altered.

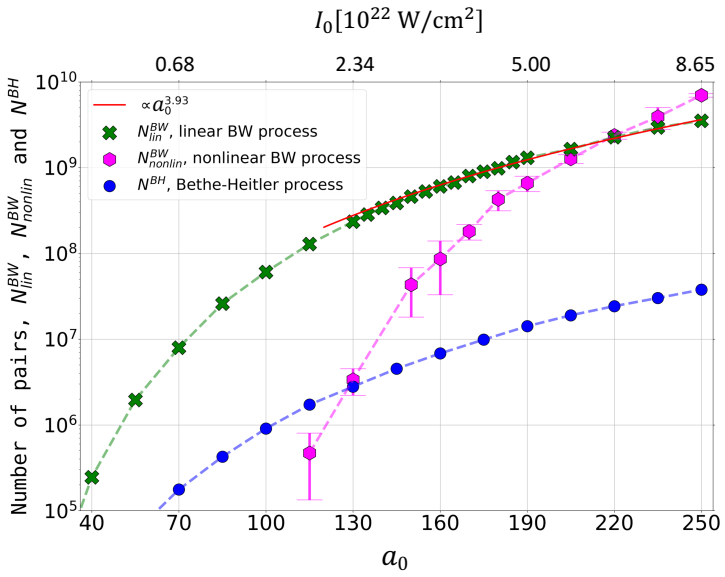

Figure 4.4. Number of electron-positron pairs created by the linear, $N_{\mathrm{lin}}^{\mathrm{BW}}$, and nonlinear, $N_{\mathrm{nonlin}}^{\mathrm{BW}}$, BW processes (green crosses and magenta markers, respectively), for the setup discussed in Ref. [75], at given normalized laser amplitude a_0 (and equivalent peak intensity I_0). Error bars for the nonlinear BW process indicate statistical uncertainties. The number of electron-positron pairs produced by the BH process, N^{BH}, is shown by blue circles. Reproduced with permission from He *et al.*, Communications Physics, **4**, 139 (2021). Copyright 2021 Authors, licensed under a Creative Commons Attribution (CC BY 4.0) license.

4.3 Impact of channel density and length on electron-positron pair yields

All three pair production processes (linear BW, nonlinear BW, and BH) rely on energetic gamma-rays, but the sensitivity to different parts of the spectrum varies greatly from process to process. The nonlinear BW process is also sensitive to the field strength in a counter-propagating laser at the time of collision between gamma-rays and the laser beam. The intensity in each laser beam changes during laser propagation along the channel, so the intensity during the collision with gamma-rays is dependent on the channel length and channel density. The yield from the BH process depends on the ion density in the channel, whereas it is independent of the intensity in the colliding lasers. These very different dependencies on channel parameters suggest that, by adjusting the channel density and length, one can control the pair yield by each of the three

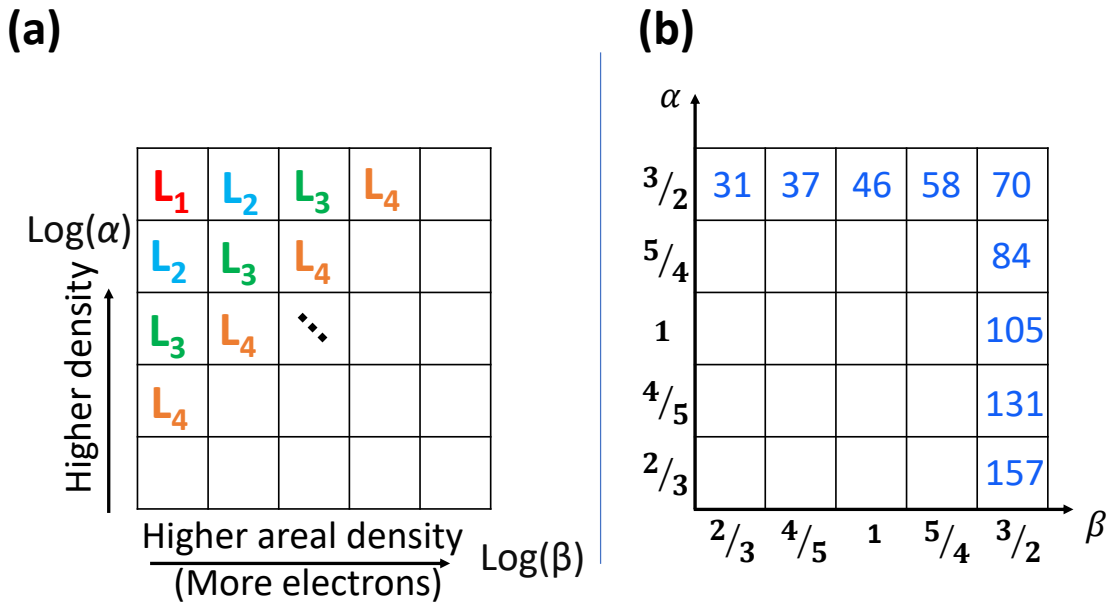

Figure 4.5. Parameter scan over channel density and and length. (a) Schematic plot that illustrates the relation between the parameters α and β and the physical quantities, such as the number density, the areal density, and the channel length. (b) The discretization for α and β used in our scan. The values of L covered by this scan are shown in blue (the length is given in μm).

processes.

In order to gain more insight, in this section we investigate the impact of channel density $n_{\rm ch}$ and length L on the pair yields of linear BW, nonlinear BW, and BH processes at fixed peak laser intensity of $5 \times 10^{22}\mathrm{Wcm}^{-2}$. The basic setup is similar to that described in Section 4.2. Table 4.2 provides the key parameters, including the range for $n_{\rm ch}$ and L. The parameters not listed in Table 4.2 should be assumed to be the same as those used in Section 4.2 and listed in Table 4.1. The pair yields for the three processes under consideration are calculated as described in Section 4.2. We only count and compare the positrons generated inside the channel, because these are the positrons that can potentially form jets after being accelerated by one of the laser beams.

As shown in Fig. 4.5(a), we parameterize our scan using

$$\alpha := n_{\mathrm{ch}}/n_*, \tag{4.4}$$

$$\beta := Ln_{\mathrm{ch}}/\sigma_*, \tag{4.5}$$

where $n_* = 7.1n_c$ is the electron density in the channel considered in Section 4.2 and $\sigma_* = n_* L^*$ is the areal density of electrons in this channel, whose length is $L_* = 70$ μm. Parameter α quantifies the relative change in electron number density, whereas parameter β quantifies the relative change in electron areal density. A family of channels that have the same length but different density have $\beta/\alpha = Ln_*/\sigma_*$. This dependence is schematically shown in Fig. 4.5(a) that uses a log-log scale. The exact values of α and β used in our parameter scan are given in Fig. 4.5(b). Note that the discretization is close to uniform on a log scale for both α and β. In total, we examine 25 different pairings of α and β. We perform a 2D PIC simulation for each set of parameters. The scan corresponds to a range of values for L that spans from 31 μm to 157 μm. The exact values of L are listed in Fig. 4.5(b) inside the domain. To find the value of L for a given set of parameters, use the values listed in Fig. 4.5(b) and the rule shown in Fig. 4.5(a) that indicates that the length is the same along diagonal lines.

Figure 4.6 shows the result of our parameter scan and contains eight panels in order to provide detailed information regarding the yield from each of the processes. Figure 4.6(e) gives the total pair yield that consists of the yield from the linear BW process, $N_{\mathrm{lin}}^{\mathrm{BW}}$, the nonliner BW process, $N_{\mathrm{nonlin}}^{\mathrm{BW}}$, and the BH process, N^{BH}. The three yields are shown individually in Figs. 4.6(a), 4.6(f), and 4.6(g). The same information is provided in Table 4.3, Table 4.4, and Table 4.5. Figures 4.6(b), 4.6(c), and 4.6(d) quantify the relative contribution of the linear BW process. Finally, Fig. 4.6(h) shows the combined yield of the nonlinear BW and BH processes.

In our scan, the nonlinear BW process shows the strongest sensitivity. This is why the general trend for the total yield in Fig. 4.6(e) matches the trend for $N_{\mathrm{nonlin}}^{\mathrm{BW}}$ in Fig. 4.6(f). At $\alpha = 2/3$ and $\beta = 3/2$, the nonlinear BW process produces no pairs in our simulation, whereas,

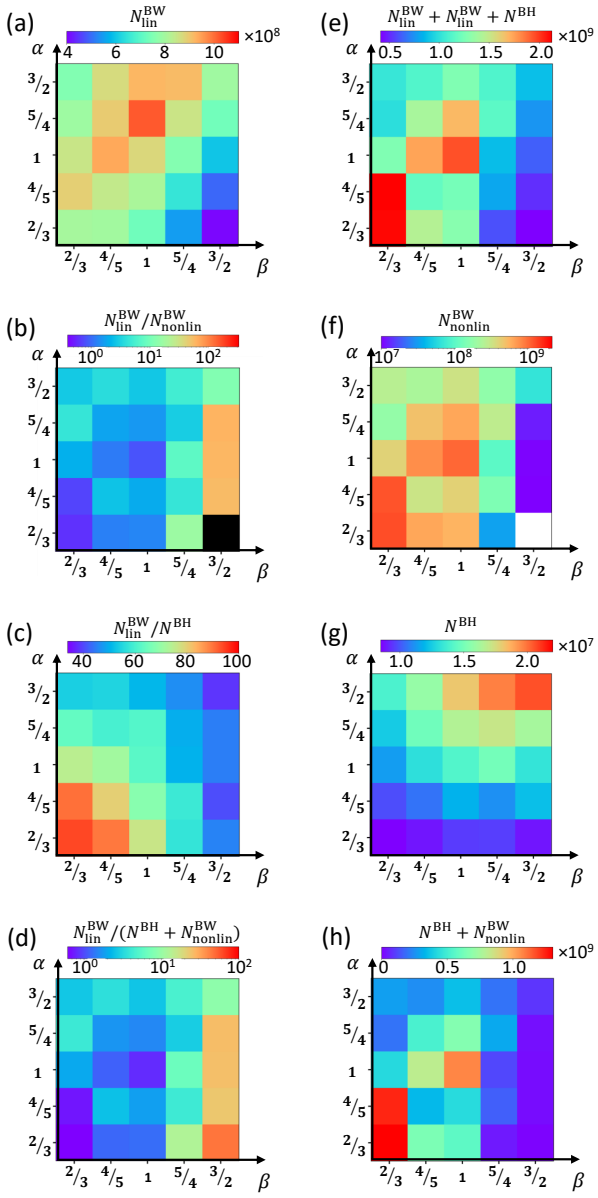

Figure 4.6. (a), (f) and (g) Pair yield inside the initial channel boundary for the parameter space shown in Fig. 4.5 and $a_0 = 190$, where (a) $N_{\rm lin}^{\rm BW}$ is the yield from the linear BW process, (f) $N_{\rm nonlin}^{\rm BW}$ is the yield from the nonlinear BW process, and (g) $N^{\rm BH}$ is the yield from the BH process. $N_{\rm nonlin}^{\rm BW}$ is shown in log scale, whereas $N_{\rm lin}^{\rm BW}$ and $N^{\rm BH}$ are shown in linear scale. (b), (c) and (d) The ratio of the yields from the linear BW to the yields by the other two processes. At $\alpha = 2/3$ and $\beta = 3/2$, $N_{\rm nonlin}^{\rm BW} = 0$ in (f) and $N_{\rm lin}^{\rm BW}/N_{\rm nonlin}^{\rm BW} \to \infty$ in (b). (e) The total yields from the three processes, and (h) the sum of the yields from nonlinear BW and BH processes. All the yields assume that the size along the third dimension is equal to the channel width $d_{\rm ch} = 5$ μm. Note that in (b), (d), and (f) the color-coding uses a log-scale.

at $\alpha = 2/3$ and $\beta = 2/3$, it produces 13×10^8 pairs. In contrast to that, the yield from the linear BW process increases by a factor of 2.5 (from 4×10^8 to 10×10^8) and they yield from the BH process increases only by a similar factor of 2.4 (from 8.5×10^6 to 20.6×10^6). Moreover, the highest yield from the nonlinear BW process exceeds the highest yield from the other two processes.

In agreement with our expectations, we find from Figs. 4.6(a), 4.6(f), and 4.6(g) that each process indeed has its own unique dependence on α and β over the considered parameter range. The result of the presented scan confirms that it is possible to control the pair yield of different processes by only changing the target parameters. One key feature is that the BH process plays a secondary role in the considered system, so the majority of the positrons inside the channel are produced via the BW processes. Another important feature is that the setup makes it possible to switch from a regime where the linear and the nonlinear BW processes have a comparable yield ($N_{\text{lin}}^{\text{BW}}/N_{\text{nonlin}}^{\text{BW}} \sim 1$) to a regime where the linear BW process completely dominates the yield ($N_{\text{lin}}^{\text{BW}}/N_{\text{nonlin}}^{\text{BW}} \gg 1$). Specifically, by choosing $\alpha = 2/3$ and $\beta = 3/2$, we can eliminate the yield from the nonlinear BW process, as seen in Fig. 4.6(f), while maintaining a high absolute yield from the linear BW process.

The rest of this section is dedicated to explaining the trends for each of the three processes.

4.3.1 Yield from the linear Breit-Wheeler process

The linear BW process has a threshold that sets a lower limit for the product of energies ε_1 and ε_2 of the colliding photons. This product has the lowest value for a head-on collision of the two photons, so the corresponding condition reads $\varepsilon_1\varepsilon_2 > (mc^2)^2$. It follows from this relation that the range of photon energies relevant to the linear BW process is set by the energetic tail of the photon spectrum with $\varepsilon \gg mc^2$. In other words, if the system has photons with $\varepsilon \gg mc^2$, then these photons make the photons with $\varepsilon \ll mc^2$ useful. It is convenient to introduce a dimensionless energy variable $s = \log_{10}\left(\varepsilon/mc^2\right)$. Then the discussed relation takes the form $s_1 + s_2 > 0$. We conclude that the lowest photon energy that can lead to pair production via the

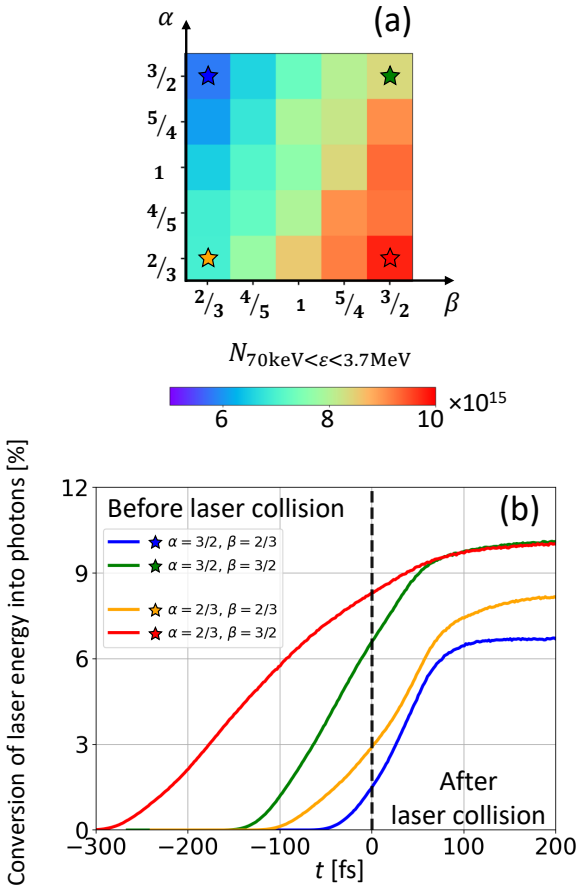

Figure 4.7. Generation of photons with energies between 70 keV and 3.7 MeV. (a) The total number of generated photons $N_{70\text{keV}<\varepsilon<3.7\text{MeV}}$ for each pairing of α and β in our parameter scan. (b) Time evolution of the laser energy conversion into photons with energies between 70 keV and 3.7 MeV. The corresponding parameters are shown in (b) using star markers. The photon yield assumes that the size along the third dimension is equal to $d_{\text{ch}} = 5$ μm.

linear BW process corresponds to $s_{\text{min}} = -s_{\text{max}}$. For the set of parameters considered in Sec. 4.2, $s_{\text{max}} \approx 3.25$, so we have $s_{\text{min}} \approx -3.25$. This means that the relevant range of photon energies is roughly 0.3 keV $< \varepsilon <$ 900 MeV. The most productive energy range is however much more narrow than the range set by s_{min} and s_{max} because of the slope of the photon energy distribution function [109]. For the set of parameters considered in Section 4.2, the most productive range is roughly between 70 keV and 3.7 MeV, accounting for 47% of the total yield.

The pair yield by the linear BW process increases as the square of the number of colliding photons, so the number of photons in the range between 70 keV and 3.7 MeV can serve as a

useful figure of merit. Figure 4.7(a) shows the total number of photons with energies in this range emitted for each pairing of α and β in our parameter scan. The photon number increases with the channel length L at fixed density n_{ch} (increasing β for fixed α). The channel length influences the photon yield by limiting the time given to plasma electrons to gain energy before their collision with a counter-propagating laser beam. Figure 4.6(a) shows that the increase in the total number of photons translates into an increase in $N_{\mathrm{lin}}^{\mathrm{BW}}$, albeit only up to a certain L. In our scan, this length is independent of the channel density and it is about 58 μm.

In order to better understand the impact of the channel length L, we have computed the laser energy conversion into photons in the range between 70 keV and 3.7 MeV. The time evolution of the conversion for three different channel lengths (31 μm, 70 μm, and 157 μm) is shown in Fig. 4.7(b). By comparing the curves that corresponds to the markers in the same horizontal row, we compare channels that have the same density but different length. We find that, even though the conversion rate for the 157 μm long channel (red curve) is higher than that for the 70 μm long channel (orange curve), most of the photons in the 157 μm setup are produced well before the two lasers collide in the mid-plane. In contrast to that, the 70 μm channel setup generates the majority of the photons after the two laser collide. The trends are the same for the blue and green curves that represent 31 μm and 70 μm long channels with the same channel density.

There are two aspects of the photon emission that set the observed trend. In a longer channel, laser-accelerated electrons travel a longer distance before colliding with another laser. Therefore, they spend more time emitting photons prior to the collision, with the emission is primarily caused by the plasma magnetic field [41]. This is the reason why the conversion rate for $L = 157$ μm (red curve) is about three times higher than for $L = 70$ μm (orange curve) at $t = 0$. The emission after the two lasers collide depends on laser amplitude via the quantum nonlinearity parameter χ defined by Eq. (4.1). In the case of a longer channel, both laser pulses experience significant depletion, which reduces the strength of the laser fields at the time of the collision. This is the reason why the photon emission is less effective for $L = 157$ μm (red curve)

than for $L = 70$ μm (orange curve) at $t > 0$.

A photon cloud emitted at $t < 0$ must travel towards the mid-plane before it encounters counter-propagating photons and can produce pairs. During its travel time, the cloud expands because its photons have an angular distribution (e.g. see Fig. 4.3). The expansion increases with L. Once this cloud collides with a counter-propagating cloud that was also emitted at $t < 0$, the density of both clouds is lower than the original density right after the emission and, as a result, the yield from the linear BW process is reduced. The expansion also causes some of the photons in the cloud to miss the photons emitted at $t \geq 0$, because these photons are emitted inside the channel. The conclusion then is that the photons emitted at $t < 0$ are either not fully utilized or not utilized efficiently. This is the reason why, at $\alpha = 2/3$, $N_{\text{lin}}^{\text{BW}}$ for $L = 157$ μm is lower than $N_{\text{lin}}^{\text{BW}}$ for $L = 70$ μm.

The main takeaway point from our scan is that there is an optimal length for a given channel density. Remarkably, this optimal length appears to be not very sensitive to the channel density for the considered range of parameters.

4.3.2 Yield from the nonlinear Breit-Wheeler process

The nonlinear BW process is the process where a high energy photon and multiple lower energy photons are annihilated creating an electron-positron pair. In our case, the energetic photon is a gamma-ray produced by one of the laser-accelerated electrons, whereas the lower energy photons are the optical photons in a counter-propagating laser beam. The probability to produce pairs is negligible if the gamma-ray is moving in the same direction as the laser beam that provides optical photons, so the focus is on collisions of gamma-rays with a counter-propagating laser beam.

The sensitivity of the pair yield to laser amplitude and gamma-ray energy can be assessed using a previously derived result for a head-on collision of a gamma-ray with a Gaussian pulse [110]. The probability for a gamma-ray with energy ε to produce an electron positron-pair

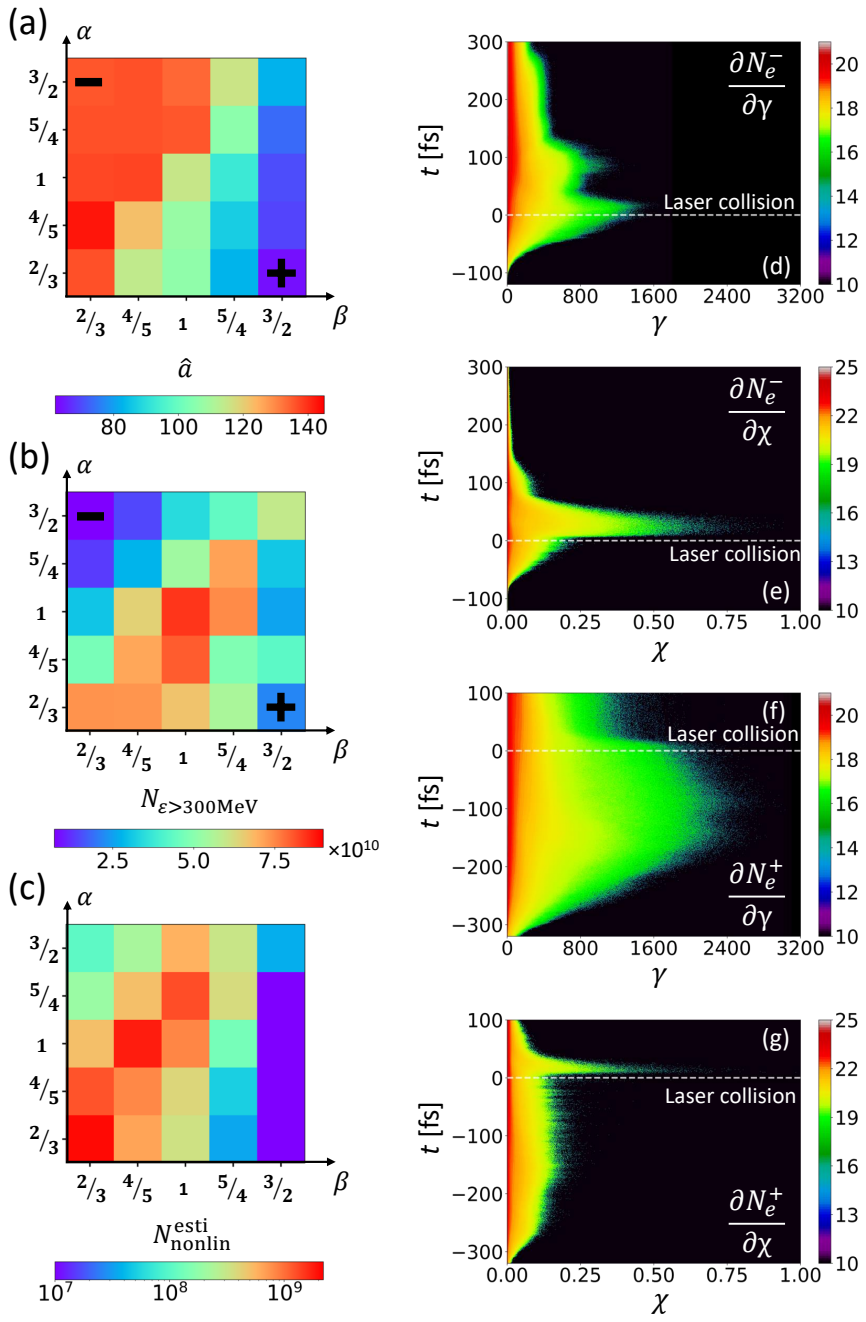

Figure 4.8. (a) Maximum normalized laser amplitude right before the collision, $\hat{a}$. (b) Total number of emitted photons with energy above 300 MeV, $N_{\varepsilon>300\mathrm{MeV}}$. (c) Estimated total yield from the nonlinear BW process, $N^{\mathrm{esti}}_{\mathrm{nonlin}}$. (d) - (g) Time evolution of the electron distribution as a function of γ and χ for two sets of parameters. The "+" and "–" superscripts are used to distinguish the two systems whose parameters are marked by "+" and "–" in (a). The photon, electron, and positron numbers assume that the size along the third dimension is equal to $d_{\mathrm{ch}} = 5$ μm.

while passing through a Gaussian beam with a peak normalized amplitude $a_{\max}$ is

$$P_{\pm} \approx \alpha_{\rm fsc} a_{\max} n \mathscr{R}\left(2a_{\max}\varepsilon_L \varepsilon / m^2 c^4\right), \tag{4.6}$$

where $\alpha_{\rm fsc} \approx 1/137$ is the fine structure constant, n is the number of cycles at the full width at half maximum, and $\varepsilon_L = hc/\lambda_0$ is the energy of the optical photons (h is the Planck constant). In Eq. (4.6), $\mathscr{R}$ is a super-exponential function defined as

$$\mathscr{R}(x) = \frac{0.453K_{1/3}^2(4/3x)}{1+0.145x^{1/4}\ln(1+2.26x)+0.330x}, \tag{4.7}$$

where K_ν is a modified Bessel function of the second kind. Therefore, the probability to produce pairs strongly increases with the increase of the product $a_{\max}\varepsilon$.

The described sensitivity indicates that the most energetic photons are the biggest contributor to the pair yield. These photons are produced at $t > 0$, i.e. when energetic electrons collide with a counter-propagating laser. The collision greatly increases the value of the quantum nonlinearity parameter χ given by Eq. (4.1). The increase of χ shifts the peak of the emitted photon spectrum to a higher energy given by Eq. (4.3). Since the relevant photons are produced at $t > 0$, then the pair creation also takes place at $t > 0$. We therefore conclude that the laser amplitude that determines the yield is the laser amplitude at $t > 0$, which can be drastically different from the laser amplitude at the entrance into the channel.

Figure 4.8(a) shows the maximum value of the normalized laser amplitude a right before the two lasers collide. We denote this quantity as $\hat{a}$ (see Section 4.6.3 for a detailed explanation of how we determine this quantity). Figure 4.8(a) shows $\hat{a}$ for the entire parameters scan. As expected, $\hat{a}$ decreases with the increase of the channel length at fixed channel density (horizontal rows) due to the depletion. For the same channel length L, $\hat{a}$ decreases with the increase of the channel density (diagonally upward direction). This is also a result of the depletion caused by an increased number of electrons accelerated by the laser in the channel. Figure 4.8(b) shows the

total number of energetic photons, $N_{\varepsilon>300\text{MeV}}$, with energy above 300 MeV produced for each set of parameters. The exact value of the cutoff energy has no significance and it is used only to select energetic photons. We find that the trend differs from that for $\hat{a}$, as there is an optimal length for a given density (horizontal rows).

The trend for $N_{\varepsilon>300\text{MeV}}$ can be understood from scalings for the emitted power $P_{synch} \propto \chi^2$ and the characteristic emitted photon energy $\varepsilon_* \propto \gamma\chi$. For an electron with a given relativistic factor γ, the value of ε_* needs to satisfy $\varepsilon_* \gtrsim 300$ MeV in order for the electron to contribute to $N_{\varepsilon>300\text{MeV}}$. The value of P_{synch} determines how many photons the electron can contribute. In our case, the electrons collide head-on with a laser pulse, so we have $\chi \propto \gamma\hat{a}$. The electron spectrum becomes more energetic with the increase of L since the electrons have more time to gain energy before their collision with the laser pulse. This means that more electrons can emit the photons in the considered energy range and we can expect for $N_{\varepsilon>300\text{MeV}}$ to go up with L. This trend is observed in Fig. 4.8(b) for all α at $L \leq 70$ μm. However, as we increase L, we must pay a penalty associated with the laser depletion that reduces our χ through $\hat{a}$. The reduction of χ not only prevents some energetic electrons from emitting sufficiently energetic photons, but it also reduces the emitted power for those electrons that emit in the desired energy range. The depletion causes the rollover in $N_{\varepsilon>300\text{MeV}}$ at $L > 70$ μm for all values of α.

Figures 4.8(d) - (g) provide additional information regarding the time evolution of the electron γ and χ. In order to see the impact of L, we consider the shortest ($L = 31$ μm) and the longest ($L = 157$ μm) channels in our scan. The α and β parameters for these channels are marked with "+" and "–" in Fig. 4.8(a) and Fig. 4.8(b). A comparison of Figs. 4.8(d) and 4.8(f) confirms that the electrons in a longer channel are able to gain much higher energies. The energy gain in Fig. 4.8(f) saturates well before the collision, which happens because the energy gain during direct laser acceleration has an upper limit [49]. A comparison of Figs. 4.8(e) and 4.8(g) provides an example of the detrimental effect of depletion on χ. Even though the electrons are more energetic in the longer channel, the maximum value of χ following the collision is lower than that for the shorter channel. The significant depletion that takes place in the longer channel

reduces $\hat{a}$ and, as a result, it reduces χ whose scaling is $\chi \propto \gamma\hat{a}$.

The discussed trend for the number of energetic photons translates into a trend for $N_{\text{nonlin}}^{\text{BW}}$ shown in Fig. 4.6(f). For a given channel density (fixed α), $N_{\text{nonlin}}^{\text{BW}}$ experiences a roll over with the increase of L (increase of β). It is instructive to show that this trend can also be captured by the approximate expression for the probability of the pair-production given by Eq. (4.6). We calculate the corresponding yield, N_{nonlin}^{esti}, by binning the photon spectrum and then applying Eq. (4.6) for each energy bin. We use $\hat{a}$ from Fig. 4.8(a) instead of $a_{\max}$. The exact value of n in Eq. (4.6) is not very important, since the trends are set by the strong dependence of $\mathscr{R}$. We take $n = 15$, which is the value of n for our laser pulses before they enter the channel. Figure 4.8(c) shows N_{nonlin}^{esti} as a function of α and β. The general trend matches that in Fig. 4.6(f).

One important consequence of the observed trend is that, by increasing the length of the channel, the yield from the nonlinear BW process can be almost completely eliminated while retaining a significant yield from the linear BW process. Figures 4.6(a), 4.6(b), and 4.6(f) provide a specific parameter range needed to realize this regime within our scan.

4.3.3 Bethe-Heitler Pair Yields

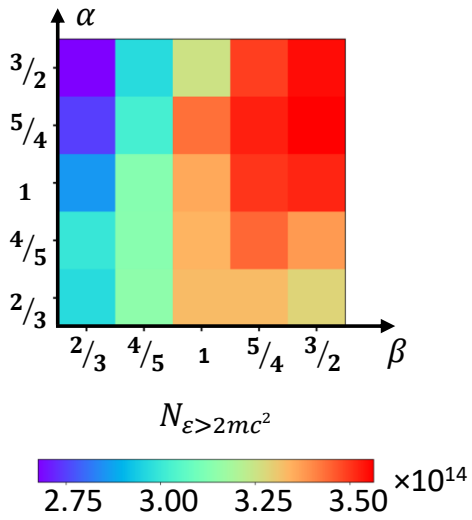

Figure 4.9. Total number of emitted photons with energy above $2mc^2$ as a function of α and β (assuming that the size along the third dimension is equal to $d_{\text{ch}} = 5$ μm).

The BH process takes place when gamma-rays pass through the Coulomb field of ions. In order to estimate the yield from this process while keeping the calculations as simple as possible, we treat our ions as immobile and use their initial or unperturbed density to calculate the yield. We use a cross-section for a fully ionized unscreened nuclei given by formula 3D-0000 in Ref. [67]. This cross-section is monotonically increasing with the energy of the gamma-ray ε, and for $\varepsilon > 4mc^2$, the leading term is proportional to $\ln(2\varepsilon/mc^2)$. The most energetic photons emitted in our system have about 900 MeV of energy. Between $4mc^2$ and 900 MeV, the value of $\ln(2\varepsilon/mc^2)$ changes by only about a factor of four. This means that the BH process has a relatively low sensitivity to gamma-ray energies in our range.

Figure 4.9 shows the number of photons with $\varepsilon > 2mc^2$ in our parameter scan. The photon number tends to increase with length (with β), but the change is moderate. In order to obtain an approximate trend for the yield, we need to multiply the photon number by the ion density or, equivalently, by α. This would compress the red region in Fig. 4.9 upwards, which qualitatively agree with the trend shown in Fig. 4.6(g).

A comparison between Fig. 4.6(b) and Fig. 4.6(c) reveals that by reducing the relative contribution of the nonlinear BW process by going to lower α and higher β we can automatically reduce the contribution of the BH process. In general, the BH process inside the channel produces a number of pairs that is at least an order of magnitude smaller than the number of pairs produced by the linear BW process. This suggests that our setup can serve as useful platform for studies of the BW processes.

4.4 Summary and discussion

Using two-dimensional PIC simulations, we have investigated the impact of the channel density and length on pair production by linear Breit-Wheeler process, nonlinear Breit-Wheeler process, and Bethe-Heitler process at fixed laser intensity of 5×10^{22} Wcm^{-2}. We found that these parameters can be successfully used to increase the linear Breit-Wheeler pair yield. More

importantly, the relative contribution of each process can be adjusted by changing the same parameters. We show that this approach allows us to completely eliminate the yield from the nonlinear Breit-Wheeler process while maintaining a significant yield from the linear Breit-Wheeler process. The Bethe-Heitler process plays a secondary role in the considered system, so the majority of the positrons inside the channel are produced from light alone.

Our results indicate that a structured target irradiated by two laser beams can serve as a versatile platform for future experimental studies of the Breit-Wheeler pair production processes. The scalings shown in Fig. 4.6 can be used to distinguish between different pair production processes by performing experiments with targets of various density and length. These target parameters are adjustable via target fabrication [105, 106, 37, 36, 107].

Another advantage of using structured targets with a prefilled channel is that these targets mitigate effects of laser prepulse. In our setup, the channel density exceeds n_c, which means that the channel remains opaque as long as the laser amplitude remains non-relativistic (normalized laser amplitude being less than unity). This means that non-relativistic laser prepulse is unable to enter the target. In contrast to the prefilled channels, hollow channels can be sensitive to laser prepulse. For example, it has been shown that the pre-expansion of the channel walls caused by prepulse can change electron acceleration [111] and photon emission [112] in hollow channels.

Our parameter scan is performed using 2D PIC simulations. One of the main reasons for using 2D PIC simulations is the computational difficulty of calculating the linear BW yield for 3D photon motion (This was so by the time of the publication of materials in this chapter. PIC codes with such implementation are done which are shown in Chapter VI and Chapter VII). The post-processing algorithm that we use has been developed specifically for 2D photon motion (no algorithm currently exists that can treat 3D photon motion). Previous studies [41, 13] show that the divergence of the emitted photons in 3D simulations is not symmetrical, with most of the divergence taking place in the laser polarization plane. Our 2D PIC simulations already capture this divergence while neglecting the much weaker photon divergence out of the polarization plane. Therefore, it is reasonable to expect that our approach that uses 2D simulations captures

the key trends of the pair production. Moreover, in our calculations, the same photons are used to compute the yield for all three processes. An important implication of this is that possible differences in photon numbers between 2D and 3D simulations would impact all three processes in a similar way.

4.5 Acknowledgement

Chapter 4, in part, is a reprint of the material as it appears in *Achieving pair creation via linear and nonlinear Breit-Wheeler process in dense plasmas* in Physics of Plasmas, 29, 053105, by Y. He, T. Blackburn, T. Toncian, and A. Arefiev, 2022. The dissertation author was the primary investigator and author of this paper.

This research was supported by AFOSR (Grant No. FA9550-17-1-0382). Simulations were performed with EPOCH (developed under UK EPSRC Grants EP/G054950/1, EP/G056803/1, EP/G055165/1, and EP/ M022463/1) using high performance computing resources provided by TACC. This work also used the Extreme Science and Engineering Discovery Environment (XSEDE), which is supported by National Science Foundation grant number ACI-1548562. The XSEDE resource Stampede2, under allocation TG-PHY190034, was used for performing the 2D PIC simulations shown in this chapter.

4.6 Appendices

4.6.1 Particle-in-cell simulation setups

All simulations presented in this chapter were carried out using the fully relativistic particle-in-cell code EPOCH [17]. All our simulations are 2D-3V. The axis of the target is always aligned with the axis of the counter-propagating lasers at $y = 0$. Each laser beam is focused at the corresponding channel opening. The lasers are linearly polarized (the electric field is in the plane of the simulation). In the absence of the target, the lasers have the same Gaussian profile in the focal spot and the same Gaussian temporal profile. The target is initialized as a fully-ionized

plasma with carbon ions.

Table 4.1 provides detailed parameters for the simulations presented in Section 4.2. The bulk electron density is constant during the intensity scan while the electron density in the channel is set at $n_{\mathrm{ch}} = (a_0/100)3.8n_{\mathrm{c}}$. Table 4.2 provides simulation parameters of the scan discussed in Section 4.3. In order to avoid repetition, Table 4.2 only lists those parameters that differ from the parameters listed in Table 4.1.

Table 4.1. Parameters of the 2D PIC simulations of Sec. 4.2.

Laser parameters	
Normalized peak amplitude	$a_0 = 40 - 250$
Peak intensity range	$I_0 = 0.2 - 8.5 \times 10^{22}$ Wcm^{-2}
Wavelength	$\lambda_0 = 1$ μm
Focal plane of laser #1	$x = -L/2$ μm
Focal plane of laser #2	$x = L/2$ μm
Laser profile (longitudinal and transverse)	Gaussian
Pulse duration (full width at half maximum for intensity)	50 fs
Focal spot size (full width at half maximum for intensity)	3.6 μm

Target parameters	
Target thickness (along y)	30 μm
Target length (along x)	$L = 70$ μm
Channel width	$d_{\mathrm{ch}} = 5$ μm
Composition	C^{+6} and electrons
Channel density	$n_{\mathrm{ch}} = 1.5 - 9.5n_{\mathrm{c}}$
Bulk density	$n_{\mathrm{bulk}} = 100n_{\mathrm{c}}$

Simulation parameters	
Simulation box in x	$-(L/2+5\ \mu\mathrm{m}) < x < (L/2+5\ \mu\mathrm{m})$
Simulation box in y	$-18\ \mu\mathrm{m} < y < 18\ \mu\mathrm{m}$
Spatial resolution	40 cells per μm in x 20 cells per μm in y
Macro-particles per cell	40 for electrons 20 for carbon ions

Table 4.2. Simulation parameters used for the scan presented in Sec. 4.3.

Parameters of the scan	
Normalized field amplitude	$a_0 = 190$
Peak intensity range	$I_0 = 4.9 \times 10^{22}$ Wcm^{-2}
Target length (along x)	$L = 31$ μm, 37 μm, 46 μm, 58 μm, 70 μm, 84 μm, 105 μm, 131 μm, 157 μm
Channel density	$n_{\rm ch}/n_c = 4.7$, 5.7, 7.1, 8.9, 10.6
Spatial resolution	80 cells per μm in x 80 cells per μm in y
Macro-particles per cell	10 for electrons 5 for carbon ions

Table 4.3. Pair yield from the linear BW process in the parameter scan of Section 4.3.

Linear Breit-Wheeler pair yield $N_{\rm lin}^{\rm BW}$ [10^8]					
α \ β	2/3	4/5	1	5/4	3/2
3/2	7.53	8.69	9.22	9.16	7.94
5/4	7.94	8.93	10.21	8.52	7.34
1	8.50	9.38	8.75	7.56	5.98
4/5	8.88	8.43	8.09	6.50	4.95
2/3	8.02	7.98	7.29	5.49	4.06

4.6.2 Positron yield from linear BW, nonlinear BW, and BH processes

Tables 4.3, 4.4, and 4.5 show the pair yields by different processes for the parameter scan of Section 4.3. The yields $N_{\rm lin}^{\rm BW}$ and $N^{\rm BH}$ are computed only in the region set by the initial location of the channel walls, $|y| \leq d_{\rm ch}/2$. The calculation method is described at the end of Section 4.2.

4.6.3 Definition of $\hat{a}$

In Section 4.3.2, we use the value of $\hat{a}$ that essentially stands for the maximum value of the normalized electric field in the laser pulses prior to their collision. However, the field experiences fluctuations in addition to the oscillations associated with the laser wavelength. By

Table 4.4. Pair yield from the nonlinear BW process in the parameter scan of Section 4.3.

Nonlinear Breit-Wheeler pair yield $N^{\mathrm{BW}}_{\mathrm{nonlin}}$ [10^8]					
α \ β	2/3	4/5	1	5/4	3/2
3/2	2.68	2.32	3.35	1.79	0.67
5/4	1.84	5.02	6.47	2.87	0.12
1	4.13	7.93	10.61	1.02	0.10
4/5	12.29	3.26	4.21	1.48	0.09
2/3	12.96	6.38	5.61	0.33	0

Table 4.5. Pair yield from the BH process in the parameter scan of Section 4.3.

Bethe-Heitler pair yield N^{BH} [10^6]					
α \ β	2/3	4/5	1	5/4	3/2
3/2	13.92	15.88	18.15	19.73	20.61
5/4	12.49	14.88	16.59	17.11	16.27
1	11.37	13.12	14.04	14.97	13.29
4/5	9.83	10.53	11.86	11.12	12.19
2/3	8.54	8.91	9.54	9.59	8.91

taking the maximum of E_y for a given snapshot can introduce uncertainties in $\hat{a}$ that depend on the timing of the snapshot. In order to reduce the impact of these uncertainties, we introduce an averaging procedure. For a given snapshot, we first average $a_y = E_y|e|/mc\omega_0$ in the transverse direction within a window with $|y| < 2$ μm. This window and the profile of a_y (for a channel with $\alpha = \beta = 1$) are shown in Fig. 4.10(a). The result of this averaging is $\overline{a_y}$. Figure 4.10(b) shows $\overline{a_y}$ for a_y from Fig. 4.10(b). We next divide the domain in Fig. 4.10(b) into four quadrants and pick three tallest spikes of $|\overline{a_y}|$ in each quadrant, as shown in Fig. 4.10(b). Finally, we define $\hat{a}$ as an average of these twelve values.

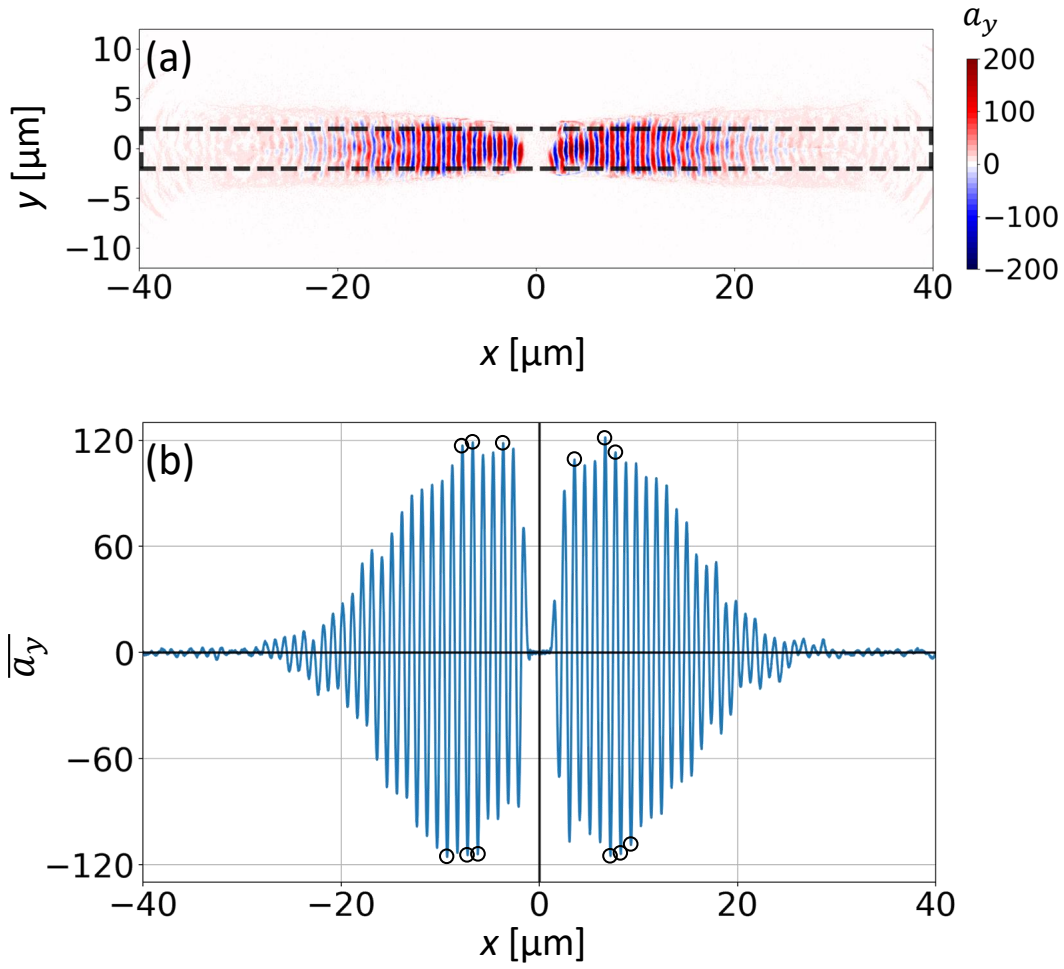

Figure 4.10. (a) Normalized transverse electric field $a_y = |e|E_y/mc\omega_0$ before the collision of two laser beams in a channel with $\alpha = \beta = 1$. The region of averaging is marked by dashed black lines. (b) $\overline{a_y}$, which is a_y from the upper panel averaged over y, as a function of x. Solid black lines show how we split the domain in four quadrants. The black circles mark three tallest spikes of $|\overline{a_y}|$ in each quadrant.

Algorithm for computing the electron-positron yield from the linear Breit-Wheeler process in high-intensity laser-plasma interactions

High-intensity laser-plasma interactions have been shown to generate dense populations of gamma-rays, so these interactions are expected to generate electron-positron pairs via binary photon collisions (linear Breit-Wheeler process). However, particle-in-cell (PIC) codes that are used for studies of laser plasma interactions are not yet equipped to compute the yield from the linear Breit-Wheeler process. We present a post-processing algorithm that allows one to quickly calculate the yield of the linear Breit-Wheeler process inside a photon-emitting plasma using PIC simulation data. The algorithm splits the PIC computational domain into smaller sub-domains whose shape and size are determined based on a specific problem. The photons emitted within each sub-domain are grouped into collimated mono-energetic beams called beamlets. The algorithm computes the yield by evaluating beamlet-beamlet collisions without the spatial integration over the interaction region. Presented benchmarking shows that the computational time is reduced by two orders of magnitude compared to the direct approach that involves the spatial integration, while the resulting error in the total yield remains around 10%. We also show how the algorithm can be leveraged to compute the density of the pair-producing events and the positron momentum distribution at the time of their creation. The ability of our algorithm to quickly compute the pair yield makes it a useful tool for studies of high-intensity laser-plasma interactions. It can also be useful for testing future implementations of the linear Breit-Wheeler

process into plasma simulation codes.

5.1 Introduction

One of the fundamental predictions of quantum electrodynamics (QED) is the annihilation of two photons into an electron-positron pair, or the linear Breit-Wheeler (linear BW) process [1]. Besides playing a fundamental role in QED, the linear BW process also plays an important role in astrophysics. For example, it determines the opacity of our Universe to high energy photons [2] and the pair cascades in pulsar magnetospheres [3, 4, 5, 40]. However, the linear BW process is yet to be observed in a laboratory using real photons (the nonlinear Breit-Wheeler process has been observed [22], whereas the linear BW process has been observed only via the use of virtual photons [94]). The obstacles are its small cross section and a high photon energy threshold. In order to achieve a detectable yield, a dense photon population with energies at least in the multi-MeV range is required, which none of the traditional photon sources are capable of achieving.

The invention of the chirped pulse amplification technique has stimulated a rapid ongoing development of ultra-intense laser systems. The existing state-of-art laser facilities are able to achieve laser intensities that exceed 10^{22} W/cm^2 [6, 7, 8], whereas the systems that are currently under construction are expected to approach intensities of 10^{23} W/cm^2. A material irradiated by such intense electromagnetic fields is quickly ionized, turning into a plasma with relativistic electrons. Energetic gamma-rays are efficiently emitted by these relativistic electrons via synchrotron emission during electron deflections by laser and plasma fields [80, 41, 101, 102, 82, 103]. There has been increased interest in utilizing energetic photons emitted during the ultra-intense laser plasma interactions to experimentally observe the linear BW process [11, 12, 74, 73, 13, 10, 75].

Computational studies can facilitate the search for optimal setups, but, being a binary process, the linear BW process is challenging to implement into kinetic simulations. In fact,

none of the modern particle-in-cell (PIC) simulation codes are able to compute the yield for the linear BW process even though other pair production processes like the nonlinear BW and Bethe-Heitler (BH) processes are routinely used in PIC simulations (This was so by the time of the publication of materials in this chapter. Implementation of the linear BW process into PIC codes are done which are shown in Chapter VI and Chapter VII). The linear BW process requires simulating binary photon collisions under conditions where the photon mean free path greatly exceeds the size of the physical system under consideration, i.e. the photon population is very much collisionless. Directly simulating these collisions requires performing N^2 queries, where N is the number of photons in the system. If the photons are represented by N_{macro} macro-particles, then the number of queries is significantly smaller, provided that $N_{macro} \ll N$. However, this number is still too large for this approach to be feasible for ultra-intense laser-plasma interactions. For example, in the setup investigated in Ref. [75], $N_{macro} \approx 10^9$ for photons with energies above 50 keV, which means that the number of required queries is 10^{18}.

In some cases, the difficulty associated with the large number of queries can be circumvented using a random pairing approach. The domain is typically separated into sub-domains where the particles are randomly paired up every time-step, and only these random pairs are checked for collisions. This procedure is repeated each time-step. The random pairing approach has been shown to work well for Coulomb collisions [113, 114, 115, 116, 117]. Repeated over many time-steps, it correctly recovers plasma relaxation processes. It must be stressed that the random pairing algorithm for Coulomb collisions is usually used for those systems where the electrons experience multiple collisions during the simulation time, i.e. the electrons are collisional. The effectiveness of the random pairing method in the case of a photon population with a very low collision rate is not clear and it remains to be investigated.

Other algorithms exist that can directly compute binary collisions without performing all the possible queries. One such algorithm has been recently developed for the linear BW process [61]. A significant reduction in the number of queries is achieved by grouping the photons and only checking the photons for collisions if the corresponding groups collide. This

method works well if the emission and collision regions are spatially separated. This is the case for those setups where two photons beams produced inside two separate targets have to travel in vacuum before colliding with each other [12, 61, 13]. In contrast to that, if two lasers pulses collide inside a target [75], then new photons are emitted within the region where the photon collisions take place, with the emissions and collisions happening concurrently. These features make it impossible to pre-sort the photons in order to reduce the number of queries and this then reduces the efficiency of the method relying on grouping the photons [61]. The same difficulty arises in a recently discussed setup that uses a single laser pulse [104] where the emissions and collisions also happen concurrently.

In this chapter, we present a post-processing algorithm that allows one to quickly calculate the yield of the linear BW process inside a photon-emitting plasma using PIC simulation data. The algorithm splits the PIC computational domain into smaller sub-domains whose shape and size are determined based on a specific problem, with each sub-domain typically containing multiple cells used by the PIC simulation. The photons emitted within each sub-domain are grouped into "beamlets" – collimated mono-energetic beams whose density varies along the beam. The cross-section of the linear BW process depends on the energy and relative orientation of the colliding photons, so that it is the same for all photon collisions for a given pair of beamlets. The algorithm computes the yield of electron-positron pairs for every possible combination of two beamlets and then these contributions are added up.

The algorithm is made fast by replacing integration over space and time with a single integral over time when computing a collision of two beamlets. This is an important and justifiable simplification for beamlets with a temporal duration longer than the typical photon travel time through the region where most of the photon-photon collisions take place. The simplification dramatically reduces the required computational time. The algorithm is designed to perform better for systems with a large number of photons concentrated in a small region, which are the conditions relevant to high-intensity laser-plasma interactions. It is straightforward to parallelize the algorithm because it treats beamlet-beamlet collisions as independent by ignoring the very

weak reduction in the number of photons due to the linear BW process. The weak attenuation of the photon population due to pair production suggests that the developed algorithm can be used in conjunction with algorithms for simulating other pair production processes (the nonlinear BW and BH processes) in the laser-irradiated plasmas.

The rest of this chapter is organized as follows. Section 5.2 presents an example of a high-intensity laser-plasma interaction that motivated the development of our post-processing algorithm. Section 5.3 provides a detailed description of our algorithm. Section 5.4 then presents an accuracy analysis. In Section 5.5, we benchmark the algorithm using a reduced photon data set from the simulation presented in Section 5.2. In Section 5.6, we apply our algorithm to the entire data set to find the total pair yield and their spatial and momentum distribution. Finally, Section 5.7 summarizes our results and provides an additional discussion of the algorithm.

5.2 Motivating example

The development of the post-processing algorithm presented in this chapter is motivated by the need to evaluate the yield of the linear BW process inside a photon-emitting laser-irradiated plasma. We have previously investigated two setups that can produce a plasma with dense colliding populations of energetic photons [75, 104] (shown in Chapter II and III) and thus enable an appreciable yield from the linear BW process. It is instructive to review one of the setups here before describing the algorithm. We specifically focus on the key features of the photon emission in order to make the assumptions made by the algorithm easier to rationalize and understand.

We review the setup used in Ref. [75] (which is the one presented in Chapter II) and shown in Fig. 5.1. It involves a structured target with a pre-filled channel that is irradiated from both sides by two ultra-high-intensity laser pulses. The channel, whose electron density is lower than the electron density in the bulk, enables stable propagation [41] and alignment of the two lasers. The laser peak intensity is the same for both lasers and it is $I_0 = 4.9 \times 10^{22}$ Wcm^{-2}. The

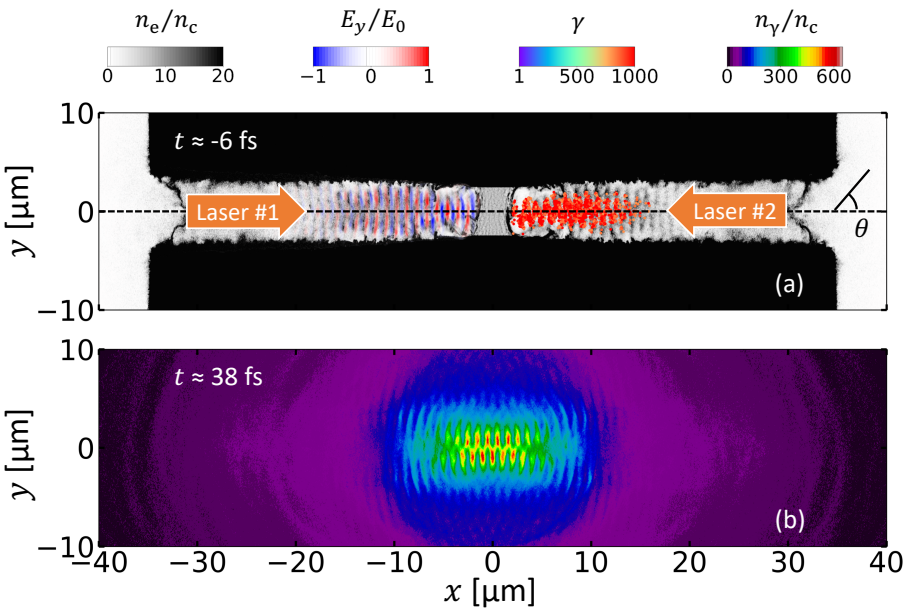

Figure 5.1. Photon generation in a structured target irradiated by two counter propagating laser beams. (a) Electron density n_e (gray scale), transverse electric field of laser #1 E_y (color scale) and energetic electrons with $\gamma \geq 800$ accelerated by laser #2 (dots, colored by γ). The snapshot is taken prior to the laser-laser collision at $t \approx -6$ fs. The laser pulses arrive to the mid-plane ($x = 0$) and collide at $t = 0$. (b) The density of photons with energy $\varepsilon \geq 1$ keV, in units of the critical density n_c after the laser-laser collision at $t \approx 38$ fs. Reproduced with permission from He *et al.*, Communications Physics, **4**, 139 (2021). Copyright 2021 Authors, licensed under a Creative Commons Attribution (CC BY 4.0) license. Adapted from original.

corresponding peak normalized laser amplitude, defined as $a_0 = 0.85 I_0^{1/2} [10^{18} \mathrm{Wcm}^{-2}] \lambda_0 [\mu\mathrm{m}]$, is $a_0 = 190$, where $\lambda_0 = 1$ μm is the laser wavelength in vacuum. Detailed laser and plasma target parameters are listed in Table 5.1.

The channel becomes transparent when irradiated by the laser beams due to relativistically induced transparency [28, 29]. The cutoff electron density for a laser with $a_0 \gg 1$ is roughly $a_0 n_c$ rather than n_c, where $n_c = \pi m c^2/(e\lambda_0)^2$ is the conventional cutoff density at $a_0 \ll 1$. Here m is the electron mass, e is the electron charge, and c is the speed of light. In our case, the channel electron density, $n_e \approx 7 n_c$, is much higher than n_c, but it is much lower than $a_0 n_c$, which enables unimpeded laser propagation. By using such a high channel density we increase the number of laser-accelerated electrons and, as a consequence, the number of generated energetic photons. The density in the bulk is set at $n_e = 100 n_c \sim a_0 n_c$, which enables the channel walls to

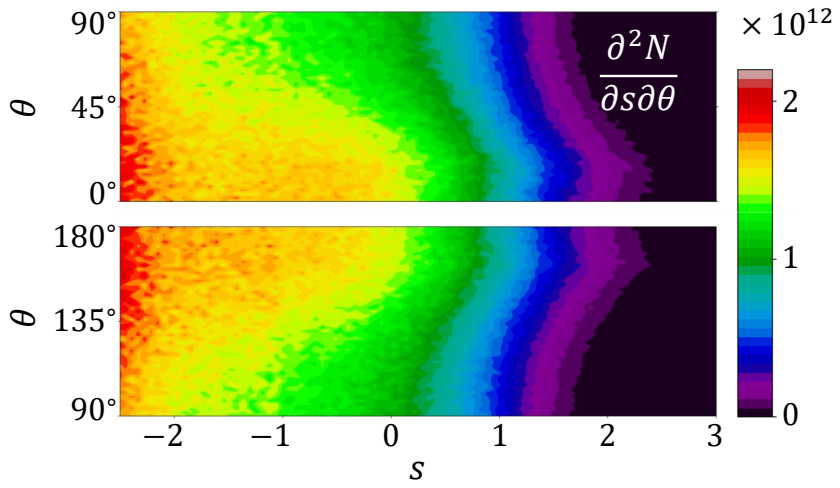

Figure 5.2. Energy-angle spectrum $\partial^2 N/\partial s \partial \theta$ [$^{\circ -1}$] of emitted photons in the 2D-3V PIC simulation shown in Fig. 5.1. Here, θ is the angle between the photon momentum $\boldsymbol{p}$ and the x-axis and s is a dimensionless energy variable defined by Eq. (5.2). The photon number N is calculated by taking the size of the ignored dimension to be equal to the channel width $d_{\text{ch}} = 5$ μm. Reproduced with permission from He *et al.*, Communications Physics, **4**, 139 (2021). Copyright 2021 Authors, licensed under a Creative Commons Attribution (CC BY 4.0) license. Adapted from original.

guide both beams. Structured targets, similar to the one considered here, have been fabricated and used for a recent experiment at the Texas Petawatt Laser Facility [76].

In the considered setup and for the chosen parameters, most of the energetic photons are produced when the electrons accelerated by one of the laser beams collide with the other beam. Electron energy gain prior to the collision is aided by a strong slowly evolving, azimuthal magnetic field driven by each laser beam [49, 118]. Transverse deflections by the magnetic field lead to enhanced direct laser acceleration of electrons where the electrons gain energy with each transverse oscillation while moving forward with the laser beam [49, 118]. For example, after propagating for ~ 30 μm along the channel, laser #2 in Fig. 5.1(a) has generated a left-moving beam of ultra-relativistic electrons with a peak energy reaching 800 MeV. Laser #1 generates a similar electron beam moving to the right.

The electron beams scatter after colliding with a corresponding counter-propagating laser

and this rapid change in the direction of electron motion leads to emission of electromagnetic radiation in the form of energetic gamma-rays. The gamma-rays are essentially emitted along the electron momentum (at the time of the emission) because the emitting electrons are ultra-relativistic. In our 2D simulation that was performed using PIC code EPOCH [17], the photon emission is modelled using a Monte Carlo module for quantum synchrotron radiation [43] that neglects the finite width of the emission cone. The photons are emitted as macro-particles that have energy (ε), momentum ($\boldsymbol{p}$), and weight (w). In total, there are 6×10^8 macro-particles representing photons with energies above 1 keV in the simulation. To reduce the use of storage space, we randomly select 5% of the macro-particles with photon energies between 1 keV and 50 keV and 10% of the macro-particles with energies above 50 keV. In order to preserve the photon distribution, we multiply the weight w of the first group by 20 and the weight of the second group by 10. The resulting angularly resolved spectrum of the photons is given in Fig. 5.2.

The photon spectrum in Fig. 5.2 shows that 1) the emitted photons move in both directions along the x-axis and 2) our setup produces energetic gamma-rays whose energy can reach tens of MeV. The combination of these two features creates favorable conditions for photon-photon collisions that can produce electron-positron pairs via the linear BW process. The process has a threshold [95]

$$\frac{\varepsilon_1 \varepsilon_2}{(mc^2)^2} \frac{1-\cos\varphi}{2} > 1 \tag{5.1}$$

set by energy and momentum conservation requirements, where ε_1 and ε_2 are the energies of the colliding photons and φ is the collision angle. The threshold has the lowest value for a head-on collision ($\varphi = \pi$), with $\varepsilon_1 \varepsilon_2 > (mc^2)^2 \approx (0.511 \text{ MeV})^2$. Therefore, the pair production requires, at the very least, photons with energies in the MeV range. Our photon population easily satisfies this requirement. The colliding geometry is created by the two counter-propagating electron beams generated by the counter-propagating laser beams.

The range of photon energies relevant to the linear BW process is set by the most energetic part of the photon spectrum. It is convenient to introduce a dimensionless energy variable defined

as

$$s = \log_{10}\left(\varepsilon/mc^2\right). \tag{5.2}$$

Equation (5.1) can then be rewritten in the following form

$$s_1 > -s_2 + \log_{10}\left(\frac{2}{1-\cos\varphi}\right) \tag{5.3}$$

where s_1 corresponds to ε_1 and s_2 corresponds to ε_2. The lowest photon energy that can lead to pair production is determined by setting $\varphi = \pi$ and $s_2 = s_{\max}$. It follows from Eq. (5.3) that

$$s_{\min} = -s_{\max}. \tag{5.4}$$

According to Fig. 5.2, $s_{\max} \approx 2$ in our simulation, so we have $s_{\min} \approx -2$. This means that the relevant range of photon energies spans roughly four orders of magnitude.

The last aspect that needs to be discussed is the concurrency of the photon emission and photon collisions in the considered setup. The enhanced photon emission starts as soon as the leading part of an ultra-relativistic electron beam produced by one of the lasers meets a counter-propagating laser beam. This happens roughly at the time ($t = 0$) when the lasers reach the mid-plane ($x = 0$). We define a region of active emission as the region where one of the electron beams overlaps with a counter-propagating laser. This region increases in time at $t > 0$. As seen in Fig. 5.1, the electron beam in our case is roughly 15 μm long, which means that the rear side of each electron beam starts to emit with at least a 25 fs delay. On the other hand, the photons that have been emitted by this point keep moving forward and can potentially collide with each other. The collisions can happen in the region of active emission, which distinguishes this setup from the one used in Refs. [12] and [13] where the collisions occur away from the emission region. Figure 5.1(b) shows the density of photons with $\varepsilon > 1$ keV at $t = 38$ fs. At this stage, the density of the photon population is extremely high. The population contains photons moving in the opposite directions, so this is the stage when the pair production is likely to occur

in our setup. This example emphasizes that a suitable algorithm must be able to evaluate the pair yield in the region of the photon emission.

5.3 Algorithm description

We are interested in a system, similar to that discussed in Section 5.2, where the photons emitted by plasma electrons experience collisions with each other within the same plasma. We assume that the photon emission process is modelled using a PIC code such that the emitted photons are represented by macro-particles that have energy (ε), momentum ($\boldsymbol{p}$), and weight (w). For example, this is the case for simulations performed with the PIC code EPOCH [17].

Our algorithm is a post-processing algorithm for computing the yield from the linear BW process using the PIC simulation data. In addition to ε, $\boldsymbol{p}$, and w, the algorithm uses the time t_0 and location $\boldsymbol{r}_0$ of emission for each photon macro-particle. In the case of EPOCH, the emission time t_0 is not one of the output quantities, so we had to modify the source code in order to output t_0 for each photon macro-particle. We limit our analysis to a two-dimensional setup where the photon macro-particles move in the (x,y)-plane and have only p_x and p_y components of the momentum. Our goal is to compute the total number and spatial distribution of the pairs created as a result of the photon-photon collisions.

We make the problem computationally manageable by grouping emitted photons into "beamlets". A beamlet consists of collimated monoenergetic photons emitted within a fixed sub-domain. The photons are assigned to sub-domains based on their emission location $\boldsymbol{r}_0$. It is convenient to number the sub-domains, so they are represented by $\boldsymbol{r}_0^j$, where j is an integer that runs from 1 to N_{sub} – the total number of sub-domains. We use rectangular sub-domains, with $\boldsymbol{r}_0^j$ being the sub-domain center. For a given sub-domain, we define beamlets using two variables: angle θ, which is the angle between $\boldsymbol{p}$ and the x-axis, and a dimensionless energy variable s, defined by Eq. (5.2). We use s rather than ε because the energy range relevant to the linear BW process can span four orders of magnitude, as shown in the example discussed in Section 5.2.

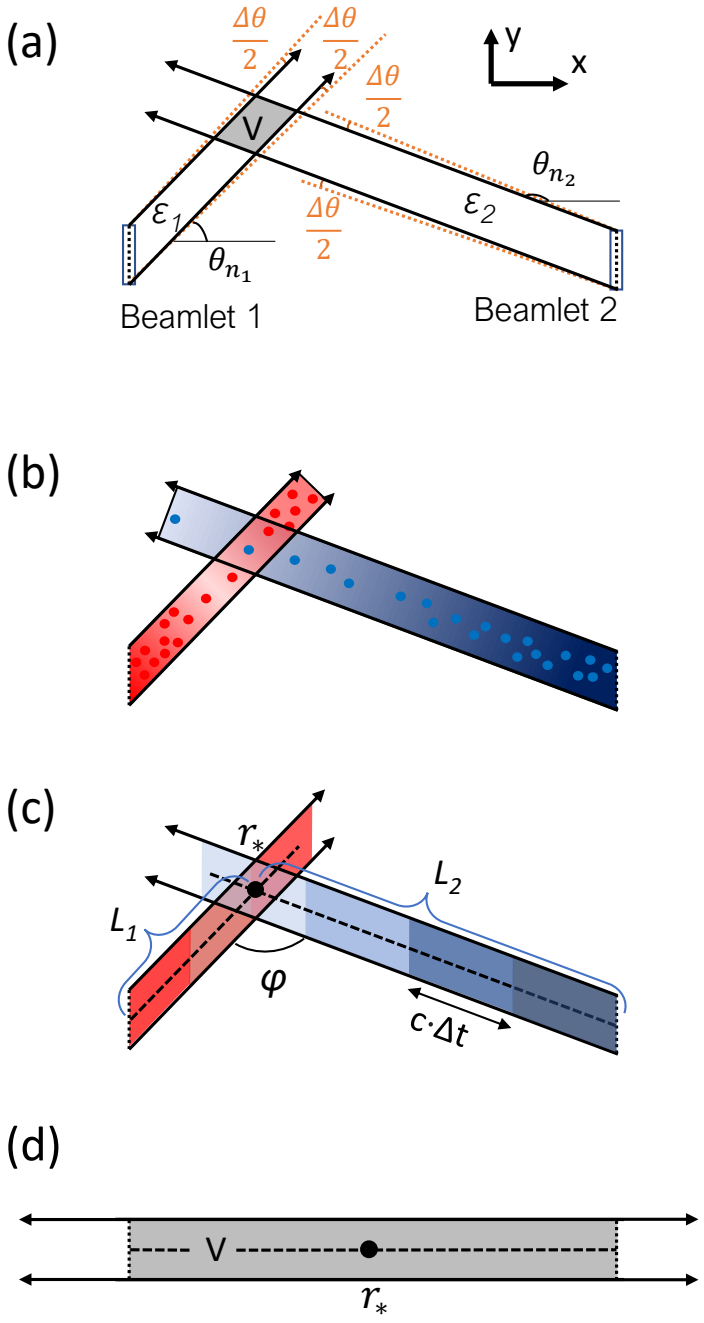

Figure 5.3. (a) Two beamlets, Beamlet 1 and Beamlet 2, that overlap in region V. The small rectangles show the sub-domains that emit each of the beamlets. (b) Beamlet shape, when the beamlet widening is neglected. The color schematically shows the density variation. (c) Density variation along each beamlet can be calculated by emission time t_{emit} of photons. (d) Region V for head-on collision of two beamlets. Our algorithm uses the photon density at the location marked by r_* (black circle) to compute the yield.

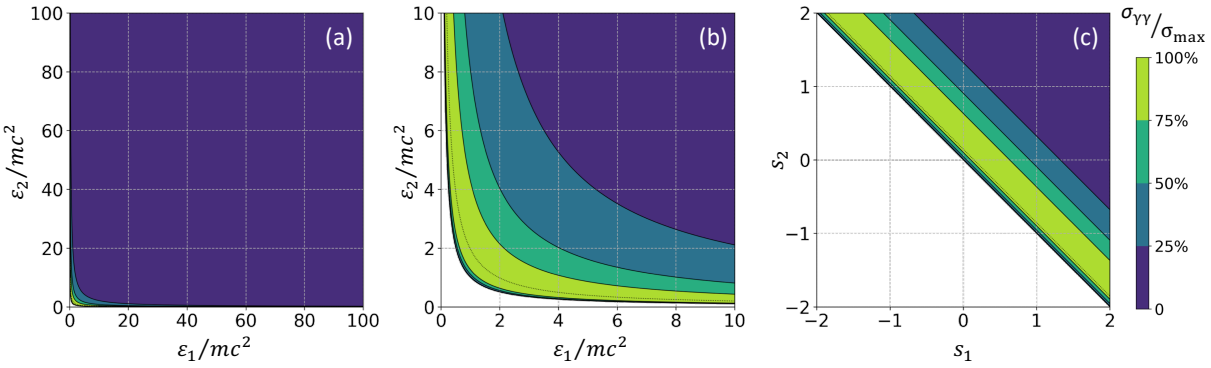

Figure 5.4. Contour plots of the cross section $\sigma_{\gamma\gamma}$ for the linear BW process, given by Eq. (5.9), for $\varphi = \pi$. (a) and (b) $\sigma_{\gamma\gamma}$ as a function of energies ε_1 and ε_2 of the two colliding photons. The difference between (a) and (b) is the energy range. (c) $\sigma_{\gamma\gamma}$ as a function of $s_{1,2} = \log_{10}\left(\varepsilon_{1,2}/mc^2\right)$. The cross section is normalized to its maximum value $\sigma_{\max} \approx 1.70 \times 10^{-29}$ m^2.

The beamlets are defined by

$$\theta_n = (n-1)\Delta\theta \tag{5.5}$$

and

$$s_k = s_{\min} + (k-1)\Delta s, \tag{5.6}$$

where n and k are integers and $\Delta\theta$ and Δs are input parameters that set the discretization in θ and s. The index n runs from 1 to $N_\theta = \lfloor 2\pi/\Delta\theta \rfloor$, whereas the index k runs from 1 to $N_s = \lfloor (s_{\max} - s_{\min})/\Delta s \rfloor$. A beamlet labeled by θ_n and s_k contains the photons whose angle and energy meet the following criteria:

$$\theta_n - \Delta\theta/2 < \quad \theta \quad \leq \theta_n + \Delta\theta/2, \tag{5.7}$$

$$s_k - \Delta s/2 < \quad s \quad \leq s_k + \Delta s/2. \tag{5.8}$$

Figure 5.3(a) provides a graphical representation of two colliding beamlets.

The discretization in s also makes it easier to capture the dependence of the cross section for the linear BW process on energies of the colliding photons. The cross section of the linear

BW process [95] for photons with energies ε_1 and ε_2 colliding at an angle φ is

$$\sigma_{\gamma\gamma} = \frac{\pi r_e^2}{2}(1-\nu^2) \times \left[-2\nu(2-\nu^2) + (3-\nu^4)\log\left(\frac{1+\nu}{1-\nu}\right)\right], \tag{5.9}$$

where

$$\nu = \sqrt{1-1/\xi}, \tag{5.10}$$

$$\xi = \frac{\varepsilon_1\varepsilon_2}{(mc^2)^2}\frac{1-\cos\varphi}{2}, \tag{5.11}$$

and $r_e = e^2/mc^2 \approx 2.82\times10^{-15}$ m is the classical electron radius. The photon collision produces an electron-positron pair only if $\xi > 1$, which is the threshold given by Eq. (5.1). Figure 5.4(a) shows $\sigma_{\gamma\gamma}$ for a head-on collision ($\varphi = \pi$) as a function of ε_1 and ε_2 for $0 \le \varepsilon_{1,2}/mc^2 \le 100$. Figure 5.4(b) is a zoomed-in version for $0 \le \varepsilon_{1,2}/mc^2 \le 10$. What stands out is that $\sigma_{\gamma\gamma}$ has a very narrow peak for $\varepsilon_{1,2} \gg \varepsilon_{2,1}$. This sensitivity requires extremely fine discretization in ε, which can lead to a large number of beamlets. For example, if $\Delta\varepsilon \approx 0.01mc^2$, then we would need to split the energy range $0.01 \le \varepsilon/mc^2 \le 10^2$ into $\sim 10^4$ segments. As shown in Section 5.2, such a wide range is required to compute the pair yield in the considered example. The plot of $\sigma_{\gamma\gamma}$ as a function of s_1 and s_2, shown in Fig. 5.4(c), is qualitatively different, because it no longer has a narrow peak. Note that the energy range covered by this plot is the same as that in Fig. 5.4(a). The dependence on s can then be sufficiently well-resolved with $\Delta s = 0.05$. In this case, we would need only $N_s \approx 80$ segments to represent the range $-2 \le s \le 2$, which is equivalent to the energy range $0.01 \le \varepsilon/mc^2 \le 10^2$.

The advantage of representing photons by beamlets is that instead of considering binary photon-photon collisions we can work with a much smaller number of beamlet-beamlet collisions. The total number of beamlets, $N_{beamlets} = N_{sub}N_\theta N_s$, is set by the described discretization rather than by the number of photon macro-particles created in the PIC simulation. By properly choosing the discretization parameters, $N_{beamlets}$ can be made much smaller than the number

of the photon macro-particles such that the number of beamlet-beamlet collisions becomes computationally manageable.

We now consider two beamlets: the first beamlet has $s = s_{k_1}$, $\theta = \theta_{n_1}$, and a time-dependent photon density $\rho_1(\boldsymbol{r},t)$; the second beamlet has $s = s_{k_2}$, $\theta = \theta_{n_2}$, and a time-dependent photon density $\rho_2(\boldsymbol{r},t)$. We neglect the spread in s and θ within each beamlet set by the discretization. The linear BW reaction rate is given by

$$R(\boldsymbol{r},t) \;=\; \kappa c \sigma_{\gamma\gamma}(s_{k_1}, s_{k_2}, \varphi)\rho_1(\boldsymbol{r},t)\rho_2(\boldsymbol{r},t), \tag{5.12}$$

where

$$\varphi = \theta_{n_2} - \theta_{n_1} \tag{5.13}$$

is the collision angle and

$$\kappa = 1 - \cos(\varphi) = 1 - \cos(\theta_{n_2} - \theta_{n_1}) \tag{5.14}$$

is a kinematic factor. The total yield (per unit length along the z-axis) for the two considered beamlets is

$$\begin{aligned} N_{pairs} \;=\; & \int_{-\infty}^{\infty} dt \iint_V R(\boldsymbol{r},t)dxdy = \kappa c \sigma_{\gamma\gamma}(s_{k_1}, s_{k_2}, \varphi) \\ & \times \int_{-\infty}^{\infty} dt \iint_V \rho_1(\boldsymbol{r},t)\rho_2(\boldsymbol{r},t)dxdy, \end{aligned} \tag{5.15}$$

where the spatial integration is performed over the two-dimensional region V where the two beamlets overlap. The expression given by Eq. (5.15) involves a triple integral, which makes it computationally demanding.

We simplify our calculation by assuming that the photon density changes insignificantly within the integration region V. We replace $\rho_{1,2}(\boldsymbol{r},t)$ with their values at the intersection of the beamlet axes $\boldsymbol{r} = \boldsymbol{r}_*$. Figure 5.3(c) shows how the axis of a given beamlet is defined – it is the

central axis whose angle with the x axis is $\theta = \theta_n$. The simplified expression for the number of pair then only involves the temporal integration:

$$\widetilde{N}_{pairs} \approx \kappa c \sigma_{\gamma\gamma}(s_{k_1}, s_{k_2}, \varphi) V \int_{-\infty}^{\infty} \rho_1(\boldsymbol{r}_*, t) \rho_2(\boldsymbol{r}_*, t) dt. \tag{5.16}$$

We use $\widetilde{N}_{pairs}$ rather N_{pairs} for the number of pairs in order to distinguish this result from that obtained using the direct approach that involves spatial integration. In the case of a head-on collision of two beamlets, the central axes overlap rather than intersect. We therefore assign $\boldsymbol{r}_*$ to be the midpoint between the two sources of beamlets, i.e. their parent sub-domains.

In order to make further progress, we need a procedure for calculating $\rho(\boldsymbol{r},t)$ for a given beamlet labeled by θ_n and s_k. We neglect beamlet widening, so that the beamlet is a stripe originating at the parent sub-domain and directed according to θ_n, as shown in Fig. 5.3(b). The photons emitted by the sub-domain move with the speed of light c along the stripe without overtaking each other. We group them by their emission time t_0 using a finite time interval Δt. We introduce $t_i = t_{start} + i\Delta t$, where t_{start} is the start of the simulation and i is an integer. The index i runs from 1 to $N_t = \lfloor (t_{end} - t_{start})/\Delta t \rfloor$, where t_{end} is the end of the simulation. We define δN_i as the number of photons emitted during a time interval $t_i - \Delta t \leq t_0 < t_i$. The density of this photon cloud is $\rho^i \approx \delta N_i / hc\Delta t |\cos(\theta_n)|$, where h is the height of the sub-domain. This result assumes that the width of the sub-domain is much smaller than $c\Delta t$. The values of δN_i must be obtained from the PIC simulation data by summing up the weights of emitted photon macro-particles that satisfy conditions (5.7) and (5.8).

The photon density ρ^i represents each beamlet as a sequence of uniform slices/clouds shown in Fig. 5.3(c). This representation enables us to easily find the photon density at the intersection of two beamlets. A photon slice with density ρ^i emitted by a sub-domain located at $\boldsymbol{r} = \boldsymbol{r}_0^j$ arrives at $\boldsymbol{r} = \boldsymbol{r}_*$ at $t = (t_i - \Delta t) + |\boldsymbol{r}_* - \boldsymbol{r}_0^j|/c$. The next slice arrives at $\boldsymbol{r} = \boldsymbol{r}_*$ at

$t = t_i + |\boldsymbol{r}_* - \boldsymbol{r}_0^j|/c$. We thus conclude that

$$\rho(\boldsymbol{r}_*, t) = \rho^i, \tag{5.17}$$

where

$$i = 1 + \left\lfloor \frac{t - t_{start} - |\boldsymbol{r}_* - \boldsymbol{r}_0^j|/c}{\Delta t} \right\rfloor. \tag{5.18}$$

We can now use the obtained discretization to simplify the temporal integral in Eq. (5.16) by a sum. A slice with index i_1 from beamlet 1 collides with one or two slices from beamlet 2. For compactness, we introduce

$$L_{1,2} = |\boldsymbol{r}_* - \boldsymbol{r}_0^{j_{1,2}}| \tag{5.19}$$

shown in Fig. 5.3(c). The first scenario occurs if $|L_1 - L_2|/c\Delta t$ is an integer. The corresponding index i_2 of the slice in beamlet 2 is

$$i_2 = i_1 + (L_1 - L_2)/c\Delta t. \tag{5.20}$$

We then find that

$$\int_{-\infty}^{\infty} \rho_1(\boldsymbol{r}_*, t)\rho_2(\boldsymbol{r}_*, t)dt \approx \Delta t \sum_{i_1 = i_{\min}}^{i_{\max}} \rho_1^{i_1}\rho_2^{i_2} \tag{5.21}$$

where i_2 is given by Eq. (5.20). For $L_1 \geq L_2$, $i_{\min} = 1$ and $i_{\max} = N_t - (L_1 - L_2)/c\Delta t$. For $L_1 < L_2$, $i_{\min} = 1 + (L_2 - L_1)c\Delta t$ and $i_{\max} = N_t$.

A slice from beamlet 1 collides with two consecutive slices from beamlet 2 if $|L_1 - L_2|/c\Delta t$ is not an integer. Without any loss of generality, we assume that $L_1 \geq L_2$. The index of the first slice in beamlet 2 that experiences the collision is

$$i_2 = i_1 + \lfloor (L_1 - L_2)/c\Delta t \rfloor. \tag{5.22}$$

This slice is already at $\boldsymbol{r} = \boldsymbol{r}_*$ by the time the considered slice from beamlet 1 with the index i_1

arrives. Therefore, their overlap time δt is shorter than Δt and it is given by

$$\frac{\delta t}{\Delta t} = 1 - \left(\frac{L_1 - L_2}{c\Delta t} - \left\lfloor \frac{L_1 - L_2}{c\Delta t} \right\rfloor \right). \tag{5.23}$$

We then find that

$$\int_{-\infty}^{\infty} \rho_1(\boldsymbol{r}_*, t)\rho_2(\boldsymbol{r}_*, t)dt \approx \sum_{i_1=i_{\min}}^{i_1=i_{\max}-1} \left[\rho_1^{i_1}\rho_2^{i_2}\delta t + \rho_1^{i_1}\rho_2^{i_2+1}(\Delta t - \delta t) \right] + \rho_1^{i_{\max}}\rho_2^{N_t}\delta t, \tag{5.24}$$

where $i_{\min} = 1$ and $i_{\max} = N_t - \lfloor (L_1 - L_2)/c\Delta t \rfloor$. Note that i_1 in the sum runs only to $i_{\max} - 1$ to make sure that $i_2 + 1$ does not exceed N_t in the second term inside the square brackets. The last term on the right-hand side of Eq. (5.24) accounts for the collision with the last slice of beamlet 2. Ideally, the duration of the simulation should be set such that no considerable emission occurs at t_{end} at any of the sub-domains, so that the discussed truncation of the sum has little effect on the result.

The total yield (per unit length along the z-axis) for two beamlets is then given by the following approximate expression

$$\begin{aligned} \widetilde{N}_{pairs} &\approx \kappa c \sigma_{\gamma\gamma}(s_{k_1}, s_{k_2}, \varphi) V \\ &\times \left(\sum_{i_1=i_{\min}}^{i_1=i_{\max}-1} \left[\rho_1^{i_1}\rho_2^{i_2}\delta t + \rho_1^{i_1}\rho_2^{i_2+1}(\Delta t - \delta t) \right] + \rho_1^{i_{\max}}\rho_2^{N_t}\delta t \right). \end{aligned} \tag{5.25}$$

The expressions for i_2 and δt are given by Eq. (5.22) and Eq. (5.23). In the limit of $(L_1 - L_2)/c\Delta t \to \lfloor (L_1 - L_2)/c\Delta t \rfloor$, $\delta t \to \Delta t$ and the expression in the brackets in Eq. (5.25) reduces to the expression given by the right-hand side of Eq. (5.21). An important feature of Eq. (5.25) is that it only involves a single sum, which reduces the time required to compute the pair yield. A detailed error analysis of this simplification is presented in Section 5.4.

Our approach for computing the photon density implies that the photon depletion due to the linear BW process is negligible. In order to estimate the maximum depletion, we use

Algorithm 1: Linear BW process yield for beamlets emitted from two fixed locations

```
/* The two beamlet emission locations are set as r_0^{j_1} and r_0^{j_2}   */
Use PIC data to set s_max and Eq. (5.4) to set s_min
User provides Δt, Δθ and Δs
Set θ_n and s_k using Eqs. (5.7) and (5.8)
/* Loops over θ_{n_1} and s_{k_1} at r_0^{j_1}                             */
for n_1 ← 1 to N_θ do
    for k_1 ← 1 to N_s do
        /* Loops over θ_{n_2} and s_{k_2} at r_0^{j_1}                     */
        for n_2 ← 1 to N_θ do
            for k_2 ← 1 to N_s do
                /* Check if the beamlets overlap                           */
                if V ≠ ∅ then
                    /* Check if s_{k_1} and s_{k_2} satisfy the energy threshold */
                    if Eq. (5.1) is true then
                        Compute Ñ_pairs from Eq. (5.25)
                    end
                end
            end
        end
    end
end
Sum up Ñ_pairs for the total yield: Ñ_pairs^tot = Σ Ñ_pairs
```

the maximum value for the cross section, $\sigma_{\max} \approx 1.70 \times 10^{-29}$ m^2, and the maximum photon density from Fig. 5.1(b), which is $500n_c$, where $n_c \approx 1.1 \times 10^{21}$ cm^{-3}. We then find that the photons in our setup have to travel a distance that exceeds

$$l_{\text{mfp}} \approx (500 n_c \sigma_{\max})^{-1} \approx 0.10 \text{ m} \tag{5.26}$$

before experiencing a collision that results in the linear BW process. The size of our photon cloud is roughly 20 μm, so the probability for the photons to collide and disappear is 20 μm/0.10 m $\approx$ 2×10^{-4}. We then conclude that only a small fraction of the photons disappears due to the linear BW process (2×10^{-4}), so the depletion is indeed negligible. It was shown in Refs. [75]

(Chapter II) and [119] (Chapter IV) that the pair yield by the nonlinear BW and BH processes are at best comparable to the pair yield by the linear BW process in the considered system. Moreover, the cross sections for the nonlinear BW and BH processes have a different photon energy dependence from that for the linear BW process, so that the photons used by these two processes do not necessarily participate in the linear BW process. We then conclude that, for the purpose of calculating the linear BW pair yield, the impact of the nonlinear BW and BH processes on the photon population can be ignored.

Algorithm 1 illustrates our approach for beamlets emitted from sub-domains labeled by $\boldsymbol{r}_0^{j_1}$ and $\boldsymbol{r}_0^{j_2}$. The result is a total pair yield from all possible beamlet pairings for the two considered sub-domains. Each sub-domain emits $N_\theta N_s$ beamlets, so the number of pairings is $(N_\theta N_s)^2$. The total yield from the entire simulation domain is obtained by considering all possible pairings of $\boldsymbol{r}_0^{j_1}$ and $\boldsymbol{r}_0^{j_2}$, with $\boldsymbol{r}_0^{j_1} \neq \boldsymbol{r}_0^{j_2}$. Using Algorithm 1, we can independently compute the yield for different sub-domain pairings. The total number of electron-positron pairs is obtained by summing up these results, $\widetilde{N}_{pairs}^{tot} = \sum \widetilde{N}_{pairs}$.

Algorithm 1 requires only a slight modification in order to find the density of the pair-production events in the interaction of two considered beamlets. We denote this quantity as $\widetilde{\rho}_{pairs}$. The two beamlets overlap inside a two-dimensional region V. For a given region V, the algorithm identifies all cells with a center located inside the region V, as schematically shown in Fig. 5.5. Here we assume that the algorithm uses the cells of the PIC simulation, but any cells can be used to perform this calculation. The algorithm uniformly distributes $\widetilde{N}_{pairs}$ for the considered beamlet-beamlet collision over the selected cells. After dividing the number of generated pairs in each cell by the cell size we obtain $\widetilde{\rho}_{pairs}(x,y)$. This process is repeated for all beamlet-beamlet pairings and the calculated numbers are accumulated for each cell. The result is the spatial density distribution of pair-producing events generated by all beamlets: $\widetilde{\rho}_{pairs}^{tot}(x,y) = \sum \widetilde{\rho}_{pairs}(x,y)$.

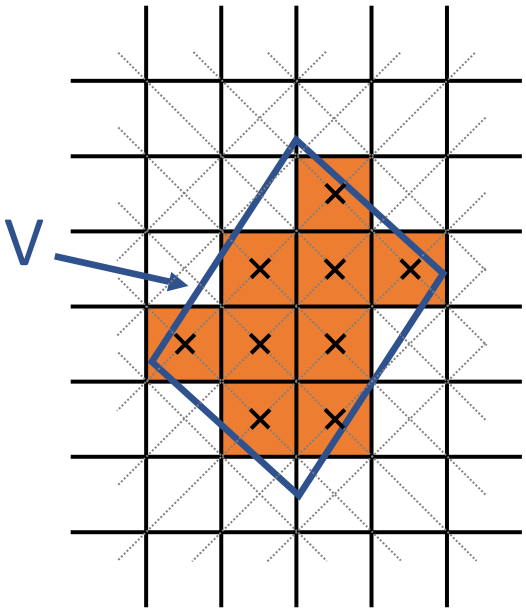

Figure 5.5. The cells (orange) used to compute the spatial distribution of the pair-producing events $\widetilde{\rho}_{pairs}$ in a collision of two beamlets. The two beamlets overlap inside region V.

5.4 Accuracy Analysis

In this section, we examine the accuracy of the algorithm detailed in Section 5.3. Let us again consider two overlapping beamlets, as shown in Fig. 5.3(a). The area of the region V where the two beamlets overlap increases with the angle φ between the two beamlets, defined by Eq. (5.13). Our approximate expression for N_{pairs} given by Section 5.3 was derived by assuming that $\rho_1(\boldsymbol{r},t)$ and $\rho_2(\boldsymbol{r},t)$ do not change significantly within the region V. Therefore, the beamlet pairings that are likely to give the most inaccurate result are those with $\varphi = \pi$, i.e, when the two beamlets collide head-on, as illustrated in Fig. 5.3(d). Therefore, we focus the analysis that follows on the case of a head-on collision.

We start with the general expression (5.15) for the number of pairs produced by two colliding beamlets. Without any loss of generality, we consider two beamlets emitted by sub-domains with $x = x_0^{j_1}$ and $x = x_0^{j_2}$, where $x_0^{j_1} < x_0^{j_2}$. We again neglect the beamlet widening and,

for simplicity, we also assume that the photon density has no dependence on y (the y variable will be omitted for compactness). The kinematic factor, defined by Eq. (5.14), is $\kappa = 2$ for the considered head-on collision. Since we neglect the depletion of the photon population due to the linear BW process as they travel through the system, the two photon densities $\rho_1(x,t)$ and $\rho_2(x,t)$ are only functions of $(x-ct)$ and $(x+ct)$, respectively. We therefore replace $\rho_1(x,t)$ with $\rho_1(x-ct)$ and $\rho_2(x,t)$ with $\rho_2(x+ct)$. Then the total yield from the considered head-on collision of two beamlets is

$$N_{pairs} = 2c\sigma_{\gamma\gamma}(s_{k_1}, s_{k_2}, \varphi)h \times \int_{-\infty}^{\infty} dt \int_{x_0^{j_1}}^{x_0^{j_2}} \rho_1(x-ct)\rho_2(x+ct)dx, \tag{5.27}$$

where h is the sub-domain height. The density of the pair-producing events is given by

$$\rho_{pairs}(x) = 2c\sigma_{\gamma\gamma}(s_{k_1}, s_{k_2}, \varphi) \int_{-\infty}^{\infty} \rho_1(x-ct)\rho_2(x+ct)dt, \tag{5.28}$$

such that

$$N_{pairs} = \int_{x_0^{j_1}}^{x_0^{j_2}} \rho_{pairs} h dx. \tag{5.29}$$

We denote the pair yield given by our algorithm as $\widetilde{N}_{pairs}$ to distinguish it from the exact result given by Eq. (5.27). For the same head-on collision of two beamlets, the yield from our algorithm is given by Eq. (5.16), where $\boldsymbol{r}_*$ is the midpoint between the two sources of beamlets because we are considering a head-on collision. We introduce $l = x_0^{j_2} - x_0^{j_1}$ and $x_* = (x_0^{j_1} + x_0^{j_2})/2$ to find

$$\widetilde{N}_{pairs} = 2c\sigma_{\gamma\gamma}(s_{k_1}, s_{k_2}, \varphi)hl \times \int_{-\infty}^{\infty} \rho_1(x_*-ct)\rho_2(x_*+ct)dt, \tag{5.30}$$

where it has been taken into account that ρ_1 and ρ_2 are functions of $(x-ct)$ and $(x+ct)$. According to Section 5.3, the density of the pair-producing events generated by our algorithm

for the considered head-on collision is simply $\widetilde{\rho}_{pairs} = \widetilde{N}_{pairs}/hl$, because $V = hl$. We then have

$$\widetilde{\rho}_{pairs} = 2c\sigma_{\gamma\gamma}(s_{k_1}, s_{k_2}, \varphi) \times \int_{-\infty}^{\infty} \rho_1(x_* - ct)\rho_2(x_* + ct)dt. \tag{5.31}$$

We next quantify the accuracy of our algorithm by comparing $\widetilde{N}_{pairs}$ with N_{pairs} and $\widetilde{\rho}_{pairs}$ with ρ_{pairs}.

5.4.1 Accuracy of the pair yield

In what follows, we compare $\widetilde{N}_{pairs}$ given by Eq. (5.30) with N_{pairs} given by Eq. (5.27). It is evident that the major difference between the two equations is the integral over x in Eq. (5.27). We thus start by considering this integral.

We use the definition of l to re-write the integral as

$$\int_{x_0^{j_1}}^{x_0^{j_2}} \rho_1(x-ct)\rho_2(x+ct)dx = \int_{-l/2}^{l/2} \rho_1(x-ct)\rho_2(x+ct)d(x-x_*). \tag{5.32}$$

In Eq. (5.30), ρ_1 is a function of $x_* - ct$, which motivates us to expand $\rho_1(x-ct)$ in Eq. (5.32) about $x_* - ct$:

$$\rho_1(x-ct) \approx \rho_1(x_*-ct) + (x-x_*)\left.\frac{\partial\rho_1(\xi_1)}{\partial\xi_1}\right|_{\xi_1=x_*-ct} + \frac{1}{2}(x-x_*)^2\left.\frac{\partial^2\rho_1(\xi_1)}{\partial\xi_1^2}\right|_{\xi_1=x_*-ct}. \tag{5.33}$$

Following similar logic, we expand $\rho_2(x+ct)$ in Eq. (5.32) about $x_* + ct$:

$$\rho_2(x+ct) \approx \rho_2(x_*+ct) + (x-x_*)\left.\frac{\partial\rho_2(\xi_2)}{\partial\xi_2}\right|_{\xi_2=x_*+ct} + \frac{1}{2}(x-x_*)^2\left.\frac{\partial^2\rho_2(\xi_2)}{\partial\xi_2^2}\right|_{\xi_2=x_*+ct}. \tag{5.34}$$

The product $\rho_1(x-ct)\rho_2(x+ct)$ contains linear terms, i.e the terms proportional to $x - x_*$, but their integral over $(x-x_*)$ vanishes. After retaining quadratic terms, i.e the terms proportional

to $(x-x_*)^2$ and performing the integration over $(x-x_*)$ in Eq. (5.32), we find that

$$\begin{aligned}
&\int_{-l/2}^{l/2} \rho_1(x-ct)\rho_2(x+ct)d(x-x_*) \\
\approx\ & l\rho_1(x_*-ct)\rho_2(x_*+ct) + \frac{l^3}{12}\left.\frac{\partial\rho_1(\xi_1)}{\partial\xi_1}\right|_{\xi_1=x_*-ct}\left.\frac{\partial\rho_2(\xi_2)}{\partial\xi_2}\right|_{\xi_2=x_*+ct} \\
&+\frac{l^3}{24}\rho_1(x_*-ct)\left.\frac{\partial^2\rho_2(\xi_2)}{\partial\xi_2^2}\right|_{\xi_2=x_*+ct} + \frac{l^3}{24}\rho_2(x_*+ct)\left.\frac{\partial^2\rho_1(\xi_1)}{\partial\xi_1^2}\right|_{\xi_1=x_*-ct}. \qquad (5.35)
\end{aligned}$$

We now substitute the approximate expression given by Eq. (5.35) into Eq. (5.27). The integral over t of the first term on the right side of Eq. (5.35) yields $\widetilde{N}_{pairs}$, as evident from Eq. (5.30). Therefore, the l^3-terms in Eq. (5.35) represent the difference between N_{pairs} and $\widetilde{N}_{pairs}$, with

$$\begin{aligned}
&N_{pairs}-\widetilde{N}_{pairs} \\
\approx\ & c\sigma_{\gamma\gamma}\frac{hl^3}{6}\int_{-\infty}^{\infty}\left[\left.\frac{\partial\rho_1(\xi_1)}{\partial\xi_1}\right|_{\xi_1=x_*-ct}\left.\frac{\partial\rho_2(\xi_2)}{\partial\xi_2}\right|_{\xi_2=x_*+ct}\right]dt \\
+\ & c\sigma_{\gamma\gamma}\frac{hl^3}{12}\int_{-\infty}^{\infty}\left[\rho_1(x_*-ct)\left.\frac{\partial^2\rho_2(\xi_2)}{\partial\xi_2^2}\right|_{\xi_2=x_*+ct}\right. \\
+\ & \left.\rho_2(x_*+ct)\left.\frac{\partial^2\rho_1(\xi_1)}{\partial\xi_1^2}\right|_{\xi_1=x_*-ct}\right]dt. \qquad (5.36)
\end{aligned}$$

The derived expression indicates that the duration of the shortest beamlet sets an upper limit on the error that we denote as $\Delta N_{\max}$. We estimate $\Delta N_{\max}/\widetilde{N}_{pairs}$ using Eq. (5.35). Without any loss of generality, we assume that the beamlet with density ρ_1 is shorter than the beamlet with density ρ_2. Then the last term on the right-hand side of Eq. (5.35) provides the largest correction to the value given by the first term on the right-hand side. The latter determines $\widetilde{N}_{pairs}$, so that the ratio of the considered two terms is roughly $\Delta N_{\max}/\widetilde{N}_{pairs}$. We estimate the last term in Eq. (5.35) as $(l^3/24)\rho_1(x_*-ct)\rho_2(x_*+ct)/(\Delta\xi_1)^2$, where $\Delta\xi_1/c$ is the characteristic duration of the beamlet

with density ρ_1. We can then formulate the following general condition:

$$\frac{|N_{pairs} - \widetilde{N}_{pairs}|}{\widetilde{N}_{pairs}} \lesssim \frac{\Delta N_{\max}}{\widetilde{N}_{pairs}} \approx \frac{l^2}{24(\Delta\xi_{\min})^2}, \tag{5.37}$$

where $\Delta\xi_{\min} = \Delta\xi_1$ if ρ_1 is shorter than ρ_2 (as in the considered example) and $\Delta\xi_{\min} = \Delta\xi_2$ if ρ_2 is shorter than ρ_1, where $\Delta\xi_2/c$ is the characteristic duration of the beamlet with density ρ_2.

To provide an example of the algorithm's accuracy, we have considered two beamlets with

$$\rho_{1,2}(\xi_{1,2}) = \frac{\rho_{\max}}{2}\left[1 + \cos\left(\pi\frac{\xi_{1,2} - d_{1,2}}{\Delta\xi_{1,2}}\right)\right] \tag{5.38}$$

for $|\xi_{1,2} - d_{1,2}| < \Delta\xi_{1,2}$ and $\rho_{1,2}(\xi_{1,2}) = 0$ for $|\xi_{1,2} - d_{1,2}| \geq \Delta\xi_{1,2}$, where $\xi_1 = x - ct$ and $\xi_2 = x + ct$. We set $d_1 = -d_2 = -36l$ and $x_* = 0$. We found directly from Eqs. (5.27) and (5.30) that $|N_{pairs} - \widetilde{N}_{pairs}|/\widetilde{N}_{pairs} \approx 4.9 \times 10^{-4}$ for $\Delta\xi_1 = 15l$ and $\Delta\xi_2 = 40l$. This value is comparable to $\Delta N_{\max}/\widetilde{N}_{pairs} \approx 1.9 \times 10^{-4}$ given by Eq. (5.37), where we set $\Delta\xi_{\min} = \Delta\xi_1 = 15l$. We have then increased the duration of the longer beamlet to $\Delta\xi_2 = 80l$ and repeated the calculation using Eqs. (5.27) and (5.30) to find that the error has reduced by roughly a factor of seven to $|N_{pairs} - \widetilde{N}_{pairs}|/\widetilde{N}_{pairs} \approx 1.3 \times 10^{-4}$. On the other hand, $\Delta N_{\max}/\widetilde{N}_{pairs}$ given by Eq. (5.37) remains unchanged, because the parameters of the shortest beamlet are unchanged, which suggests that Eq. (5.37) overestimates the error if the two beamlets are very different in duration.

We have performed two additional scans to substantiate our observation. In the first scan, we varied $\Delta\xi_1$ from $10l$ to $40l$ with $\Delta\xi_2 = 60l$. We found that the error reduces with the increase of $\Delta\xi_1$, but the change is relatively small. Specifically, $|N_{pairs} - \widetilde{N}_{pairs}|/\widetilde{N}_{pairs} \approx 2.3 \times 10^{-4}$ for $\Delta\xi_1 = 10l$ and $|N_{pairs} - \widetilde{N}_{pairs}|/\widetilde{N}_{pairs} \approx 1.9 \times 10^{-4}$ for $\Delta\xi_1 = 40l$. In our second scan, we varied $\Delta\xi_2$ from $10l$ to $80l$ with $\Delta\xi_1 = 10l$. The errors has reduced with the increase of $\Delta\xi_2$ by roughly a factor of four hundred from $|N_{pairs} - \widetilde{N}_{pairs}|/\widetilde{N}_{pairs} \approx 5.5 \times 10^{-3}$ to $|N_{pairs} - \widetilde{N}_{pairs}|/\widetilde{N}_{pairs} \approx 1.3 \times 10^{-5}$. In contrast to the scaling of $\Delta N_{\max}$, the observed scaling is closer to $l^2/(\Delta\xi_{\max})^2$. This result can be understood by examining the right-hand side of Eq. (5.36). The last term has

the biggest absolute value for a given t. However, it is an oscillating term for the considered shape of ρ_1. Moreover, the integral over t of the second derivative alone is equal to zero. This means that the contribution from the considered term greatly reduces with the increase of $\Delta\xi_2$, which characterizes the duration of the beamlet whose photon density is ρ_2. A similar argument applies to the first term on the right-hand side, because the first derivative of ρ_1 is also an oscillating function. The second term on the right-hand side is different from the other two terms because the second derivative of ρ_2 does not experience significant oscillations on the time scale comparable to the duration of the shortest beamlet. We can then conclude that the second term that scales as $l^2/(\Delta\xi_2)^2$ should determine the error in the limit of $\Delta\xi_2 \gg \Delta\xi_1$, which matches our numerical results.

We conclude the discussion of our algorithm's accuracy by examining a regime where $\Delta\xi_{1,2}$ are comparable to l. We set $\Delta\xi_1 = \Delta\xi_2 = 5l$. We found directly from Eqs. (5.27) and (5.30) that the error, $|N_{pairs} - \widetilde{N}_{pairs}|/\widetilde{N}_{pairs} \approx 2 \times 10^{-2}$, remains relatively small even in this regime. It is worth pointing out that Eq. (5.37) predicts the error to be even smaller because the corresponding expression is derived by assuming that both beamlets are much longer than l.

5.4.2 Accuracy of the density of the pair-producing events

In this subsection, we examine how our algorithm performs in computing the density of the pair-producing events by comparing $\widetilde{\rho}_{pairs}$ given by Eq. (5.31) with ρ_{pairs} given by Eq. (5.28).

To assess the error, we again use the approximate expressions for $\rho_1(x-ct)$ and $\rho_2(x+ct)$ given by Eqs. (5.33) and (5.34). We retain only linear terms in the expansion and in the product

$\rho_1(x-ct)\rho_2(x+ct)$, which yields

$$\begin{aligned}\rho_{pairs}(x) &\approx 2c\sigma_{\gamma\gamma}\int_{-\infty}^{\infty}\rho_1(x_*-ct)\rho_1(x_*+ct)dt \\ &+ 2c\sigma_{\gamma\gamma}\int_{-\infty}^{\infty}\left[\rho_1(x_*-ct)\left.\frac{\partial\rho_2(\xi_2)}{\partial\xi_2}\right|_{\xi_2=x_*+ct}\right](x-x_*)dt \\ &+ 2c\sigma_{\gamma\gamma}\int_{-\infty}^{\infty}\left[\rho_2(x_*+ct)\left.\frac{\partial\rho_1(\xi_1)}{\partial\xi_1}\right|_{\xi_1=x_*-ct}\right](x-x_*)dt. \qquad (5.39)\end{aligned}$$

We now take into account the definition of $\widetilde{\rho}_{pairs}$ given by Eq. (5.31) to obtain

$$\begin{aligned}\rho_{pairs}(x)-\widetilde{\rho}_{pairs} &\approx 2c\sigma_{\gamma\gamma}\int_{-\infty}^{\infty}\left[\rho_1(x_*-ct)\left.\frac{\partial\rho_2(\xi_2)}{\partial\xi_2}\right|_{\xi_2=x_*+ct}\right](x-x_*)dt \\ &+ 2c\sigma_{\gamma\gamma}\int_{-\infty}^{\infty}\left[\rho_2(x_*+ct)\left.\frac{\partial\rho_1(\xi_1)}{\partial\xi_1}\right|_{\xi_1=x_*-ct}\right](x-x_*)dt. \qquad (5.40)\end{aligned}$$

This expression indicates that the duration of the shortest beamlet sets an upper limit on the error that we denote as $\Delta\rho_{\max}$. We again assume that the beamlet with density ρ_1 is shorter than the beamlet with density ρ_2. Then the last term on the right-hand side of Eq. (5.40) provides the largest correction. To estimate this term, we replace $(x-x_*)$ with $l/2$ and the first derivative of ρ_1 with $\rho_1(x_*-ct)/\Delta\xi_1$. The ratio of this term to $\widetilde{\rho}_{pairs}$ [see the first term on the right-hand side of Eq. (5.39)] gives

$$\frac{\Delta\rho_{\max}}{\widetilde{\rho}_{pairs}} \approx \frac{l}{2\Delta\xi_{\min}}, \qquad (5.41)$$

where $\Delta\xi_{\min}=\Delta\xi_1$ if ρ_1 is shorter than ρ_2 (as in the considered example) and $\Delta\xi_{\min}=\Delta\xi_2$ if ρ_2 is shorter than ρ_1.

As in the case of the total pair yield, the error given by $(\rho_{pairs}(x)-\widetilde{\rho}_{pairs})/\widetilde{\rho}_{pairs}$ dramatically reduces if one of the beamlets is much longer than the other one. This feature can be understood by considering the right-hand side of Eq. (5.40). We assume that the duration of ρ_2 is much longer than the the duration of ρ_1, i.e. $\Delta\xi_2 \gg \Delta\xi_1$. Then the last term has the biggest absolute value for a given t. However, the integral over t of the first derivative of ρ_1 that

enters this term is equal to zero. This means that the contribution from the considered term in the limit of $\Delta\xi_2 \gg \Delta\xi_1$ is reduced due to the time integration. The integral is determined by the change of ρ_2 over the duration of the shorter beamlet rather than by the value of ρ_2 itself. The contribution to the integral from the first term on the right-hand side of Eq. (5.40) is also determined by the change of ρ_2 due to the presence of the first derivative. However, this term contains ρ_1 rather than $\partial\rho_1/\partial\xi_1$, which suggests that the first term becomes the dormant one in the limit of $\Delta\xi_2 \gg \Delta\xi_1$. We can then estimate the error as

$$\frac{|\rho_{pairs} - \widetilde{\rho}_{pairs}|}{\widetilde{\rho}_{pairs}} \approx l/\Delta\xi_{\max}, \tag{5.42}$$

where $\Delta\xi_{\max} = \Delta\xi_2$ if ρ_1 is shorter than ρ_2 (as in the considered example) and $\Delta\xi_{\max} = \Delta\xi_1$ if ρ_2 is shorter than ρ_1.

5.5 Benchmarking

In this section, we benchmark our algorithm by comparing the results given by our algorithm to the results of an exact calculation using the photon data from the PIC simulation detailed in Section 5.2.

The photons emitted in the simulation of Section 5.2 have a wide angular distribution and a significant energy spread that spans several orders of magnitude. As a result, a direct calculation of the linear BW yield is not feasible, which is the original motivation for developing our algorithm. In order to benchmark our algorithm against an exact calculation, we must reduce the size of the data set. We consider only a subset of photons with $0^\circ < \theta < 10^\circ$ and $170 < \theta < 180^\circ$. To simplify the exact calculation, we treat beamlet-beamlet collisions as head-on collisions when assigning the integration region V for two beamlets and set the kinematic factor $\kappa = 2$. The angular dependence is retained only for the calculation of the cross-section $\sigma_{\gamma\gamma}$. These simplifications enable us to calculate N^{tot}_{pairs} and ρ^{tot}_{pairs} needed to perform the comparison. Note that $\widetilde{N}^{tot}_{pairs}$ and $\widetilde{\rho}^{tot}_{pairs}$ calculated without the described simplifications are presented in

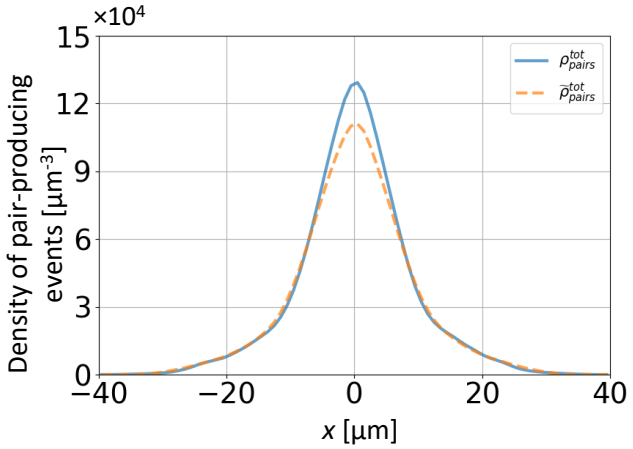

Figure 5.6. The density of the pair-producing events in the benchmark calculation. The solid curve is $\rho^{tot}_{pairs}(x)$ computed using the direct approach and the dashed curve is $\widetilde{\rho}^{tot}_{pairs}(x)$ obtained using our algorithm.

Section 5.6.

We discretize the angle, the energy, and the longitudinal position. The longitudinal discretization is performed by splitting our domain along the x into 80 subdomains with $\Delta x = 1$ μm. In the transverse direction, the majority of photons are emitted inside the channel. We thus forgo the discretization in the transverse direction and instead unifromly distribute the photons emitted within a given range of longitudinal positions set by our discretization between $y = -2.5$ μm and $y = 2.5$ μm. The width of the emission region in the third direction is set to be equal to the channel width, $h = 5$ μm. The angle $0^\circ < \theta < 10^\circ$ is discretized into eight segments. We use the same number of segments for $170 < \theta < 180^\circ$. We limit the considered photon energy range to 100 keV$< \varepsilon <$ 10 MeV. It corresponds to $-0.7 < s < 1.3$ that we split into eight equally-spaced segments. The resulting number of beamlets moving in the positive direction along the x-axis is 4753, whereas the number of beamlets moving in the opposite direction is 4781. The number of beamlets differs and it is less than 5120 because the empty beamlets or the beamlets that containing no photons have been eliminated from the consideration. The time interval that sets the discretization in time for each beamlet is set at $\Delta t = \Delta x/c \approx 3.3$ fs.

Using the direct approach, we found the total pair yield $N^{tot}_{pairs} \approx 5.36 \times 10^7$ and the density

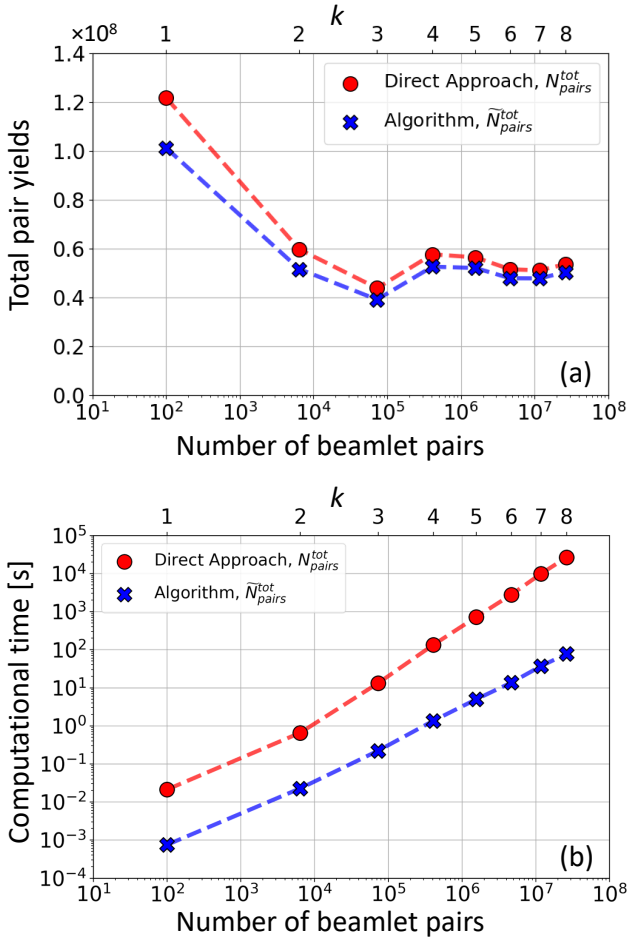

Figure 5.7. Total pair yield (a) and the required computational time (b) as a function of the number of beamlet-beamlet collisions in the benchmark calculation. The o-markers correspond to the exact calculation, whereas the x-markers represent our algorithm. All of the computations are performed on a single core of Intel i7-8700 @3.20GHz cpu.

of the pair-producing events ρ^{tot}_{pairs}, shown in Fig. 5.6. Our algorithm predicts $\widetilde{N}^{tot}_{pairs} \approx 5.04 \times 10^7$ pairs, so the error is $|N^{tot}_{pairs} - \widetilde{N}^{tot}_{pairs}|/\widetilde{N}^{tot}_{pairs} \approx 0.06$. The density $\widetilde{\rho}^{tot}_{pairs}$ calculated using our algorithm is shown in Fig. 5.6 with a dashed curve. The standard deviation calculated for the curve given by $\rho^{tot}_{pairs}(x)$ is 8.64 μm, whereas the standard deviation calculated for the curve given by $\widetilde{\rho}^{tot}_{pairs}(x)$ is 9.03 μm. There is a relatively good agreement between the density generated by our algorithm and the result of the exact calculation.

We have performed a series of calculations to determine how the discretization impacts the pair yield. In our scan, we use a single parameter k to adjust the discretization for θ, s, and x

while keeping the range for all three quantities the same as in the already discussed example. The angle θ ($0^\circ < \theta < 10^\circ$ and $170 < \theta < 180^\circ$) is discretized into $2k$ segments, the energy range set by s is discretized into k segments, and the spatial range set by x is discretized into $10k$ segments. In the scan, the integer k runs from 1 to 8, with $k = 8$ corresponding to the already considered calculation (see Fig. 5.6). The total number of beamlets for a given value of k is $N_{beamlets} = 20k^3$ (some of these might contain no photons). Half of these beamlets are directed to the right and the other half is directed to the left. The maximum number of beamlet pairs that represents beamlet-beamlet collisions in our system is $(N_{beamlets}/2)^2 = 100k^6$. Figure 5.7(a) shows N^{tot}_{pairs} and $\widetilde{N}^{tot}_{pairs}$ versus the number of beamlet pairs set by k. At $k = 4$, the relative error of $\widetilde{N}^{tot}_{pairs}$ compared to N^{tot}_{pairs} is $|(N^{tot}_{pairs} - \widetilde{N}^{tot}_{pairs})/N^{tot}_{pairs}| \approx 8.8\%$. Our results indicate that increasing the discretization above that set by $k = 4$ may be of diminishing return. This conclusion is further reinforced by the plots of the required computational time in Fig. 5.7(b) that increases significantly with k.

We observe that the ratio of the computational time using the exact method to the computational time using our algorithm increases as we increase the discretization. The primary cause is the increased discretization along x that increases the cost of the spatial integration in the direct approach. Our algorithm requires no spatial integration, which leads to significant computational savings as we increase k. The key conclusion is that our algorithm computes the yield with an error around 10% while reducing the computational time by two orders of magnitude compared to the direct approach. (and below 10% for $k \geq 4$).

We now examine the impact of the beamlet duration on the pair yield. The estimate derived in Section 5.4 and given by Eq. (5.37) indicates that the error in the total pair yield calculation should decrease with the increase of the beamlet duration. We perform our analysis using the discretization set by $k = 8$. The time-dependence of each beamlet is set by the physics of the laser-plasma interaction rather than by the discretization. To quantify the beamlet duration, we introduce the standard deviation τ calculated for each beamlet using the time dependence of its photon density ρ. For each pair of beamlets, we quantify the error by

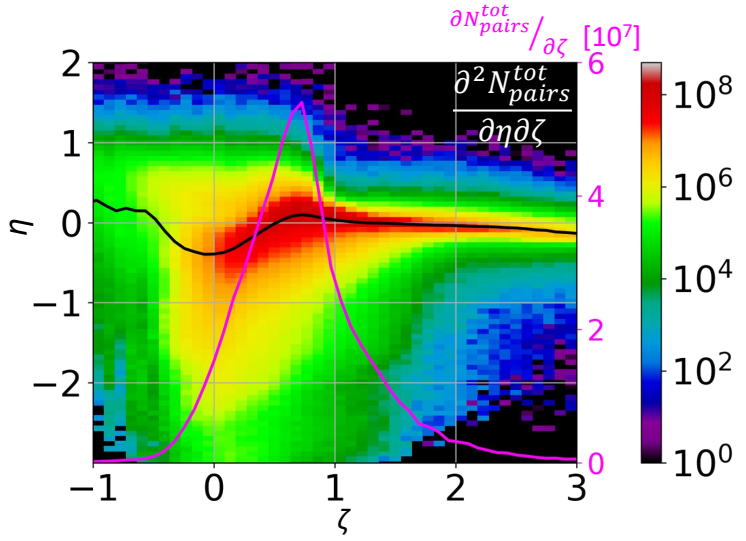

Figure 5.8. Dependence of the pair yield from the direct approach and the corresponding error in $\widetilde{N}_{pairs}$ on the beamlet duration. The magenta curve is the yield from the direct approach, $\partial N^{tot}_{pairs}/\partial\zeta$, as a function of $\zeta = \log_{10}(24c^2\tau^2_{\min}/l^2)$, where $\tau_{\min}$ is the duration of the shorter beamlet in a beamlet-beamlet collision. The color-coding shows $\partial^2 N^{tot}_{pairs}/\partial\eta\partial\zeta$, where $\eta = \log_{10}(\widetilde{N}_{pairs}/N_{pairs})$ characterizes the discrepancy between $\widetilde{N}_{pairs}$ and N_{pairs}. The black curve is the weight-averaged η for a given ζ.

computing $\eta = \log_{10}(\widetilde{N}_{pairs}/N_{pairs})$. The criterion given by Eq. (5.37) involves $l^2/24(\Delta\xi_{\min})^2$, which motivates us to introduce $\zeta = \log_{10}(24c^2\tau^2_{\min}/l^2)$ for each pair of colliding beamlets, where l is the length of the interaction region and $\tau_{\min}$ is τ of the shorter beamlet. Figure 5.8 shows $\partial^2 N^{tot}_{pairs}/\partial\eta\partial\zeta$, which is the total pair yield (on a log-scale) computed using the direct approach as a function of ζ and η. The vertical axis represents the error introduced by our algorithm. The magenta curve, $\partial N^{tot}_{pairs}/\partial\zeta$, shows how the pair yield computed using the direct approach depends on the beamlet duration.

We can make several observations based on the information presented in Fig. 5.8. We find that $\partial^2 N^{tot}_{pairs}/\partial\eta\partial\zeta$ becomes primarily localized near $\eta = 0$ with the increase of ζ. This means that $\widetilde{N}_{pairs}/N_{pairs}$ indeed converges to unity with the increase of ζ, as predicted by Eq. (5.37). The value of $\widetilde{N}_{pairs}/N_{pairs}$ does fluctuate between 0.01 and 10 for ζ in the range (from 0 to 1) responsible for the majority of the pair yield. We find that, despite these fluctuations, the average η for a given ζ, shown in Fig. 5.8 with a back curve, remains close to unity. The weighted

averaging is performed using $\partial N^{tot}_{pairs}/\partial\zeta$ to account for the fact that the yield can vary greatly between different pairs of beamlets with the same ζ. The key conclusion is that the algorithm performs well in computing $\widetilde{N}^{tot}_{pairs}$ even though $\widetilde{N}_{pairs}$ can contain significant errors for some beamlet-beamlet collisions.

We conclude this section by examining the impact of the number of macro-particles contained in each beamlet on our results. In our benchmark system, there are 1.6×10^6 macro-particles representing a subset of photons with $0^\circ<\theta<10^\circ$ and $170<\theta<180^\circ$. As we increase the discretization parameter k, the number of beamlets grows like $N_{beamlets}\propto k^3$, so the number of macro-particles in each beamlet decreases. By going from $k=4$ to $k=8$, we reduce the average number of macro-particles in each beamlet from 1319 to 172, which agrees with the reduction factor predicted by the k^3 dependence. Figure 5.7(a) shows that the pair yield computed using our algorithm ($\widetilde{N}^{tot}_{pairs}$) remains roughly unchanged despite the significant reduction in the number of macro-particles in each beamlet. Therefore, in the considered setup, the accuracy of our algorithm is insensitive to the number of macro-particles contained in each beamlet.

Additional insight regarding the number of macro-particles can be gained using Fig. 5.8. It shows that the majority of the pairs is produced by beamlet pairings concentrated around the line $\eta=0$ with $0\lesssim\zeta\lesssim2$. We then select beamlet pairings with $-0.5<\eta<0.5$ and $0<\zeta<2$. They account for 82% of $\widetilde{N}^{tot}_{pairs}$. The pair yield for these pairings is calculated with good accuracy by our algorithm. The average number of macro-particles in these beamlets is 188, where we took into account the occurrence of each beamlet in the selected subset of beamlet pairings. This number is close to the averaged number of macro-particles in each beamlet (172) calculated using all beamlets. Therefore, we can conclude that the number of macro-particles in a given beamlet has relatively little impact on the accuracy compared to the other factors discussed earlier.

Finally, we would like to stress that the number of photon macro-particles produced in a PIC simulation can be made arbitrarily large, if computational resources permit, by increasing the

number of electron macro-particles representing real electrons. The QED modules used in most PIC codes treat the photon emission by each electron macro-particle independently [43], so an increase in the number of electron macro-particles automatically translates into a similar increase in the number of photon macro-particles. Therefore, the number of photon macro-particles contained in individual beamlets can always be increased if necessary; while such increase in the number of photon macro-particles does not increase the computation time of our algorithm.

5.6 Application

In this section, we employ our algorithm to examine the pair yield in the simulation with two colliding laser pulses detailed in Section 5.2. In contrast to Section 5.5, we no longer limit our analysis to head-on collisions, so a direct calculation of the pair yield is not feasible in this case and the use of our algorithm is essential for obtaining quantitative results.

The discretization is similar to that used in Section 5.5, with the major difference being that we now use wider ranges for the energy and the angle. We again forgo the discretization in y and instead unifromly distribute the photons emitted within a given range of longitudinal positions (set by our discretization) between $y = -2.5$ μm and $y = 2.5$ μm. We consider the photons with 1 keV$< \varepsilon <$ 857 MeV, which means $-3 < s < 2.93$. This range for s is divided into 70 equal segments. The axial coordinate x runs from -40 μm to 40 μm. We split this range into 70 segments. The time interval that sets the discretization in time for each beamlet is set at $\Delta t = \Delta x/c$.

Instead of discretizing θ in the range from -180° to 180°, we limit our consideration to $0^\circ \leq \theta \leq 180^\circ$ only. The photon spectrum for $0^\circ \geq \theta \geq -180^\circ$ is similar to the photon spectrum for $0^\circ \leq \theta \leq 180^\circ$. We additionally split the beamlets into two groups: group 1 contains beamlets with $0^\circ \leq \theta \leq 90^\circ$ and group 2 contains beamlets with $90^\circ \leq \theta \leq 180^\circ$. The range for each group is split into 70 segments. We only pair up beamlets from group 1 with beamlets from group 2. Even though beamlets from group 1 can collide with each other, the angle of the

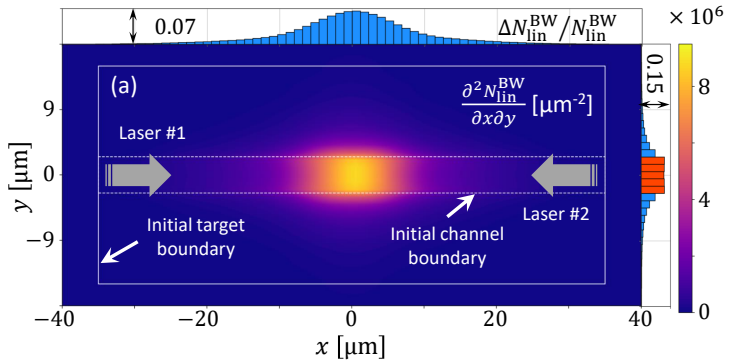

Figure 5.9. Spatial distribution $\partial^2 N_{\mathrm{lin}}^{\mathrm{BW}}/\partial x \partial y$ [μm^{-2}] of created pairs in the simulation detailed in Section 5.2. The horizontal and vertical histograms show how the yield is distributed along the x and y axes. Reproduced with permission from He *et al.*, Communications Physics, **4**, 139 (2021). Copyright 2021 Authors, licensed under a Creative Commons Attribution (CC BY 4.0) license. Adapted from original.

collision is likely to be small. This is the reason for neglecting these collisions and those between the beamlets in group 2 to reduce the computational time. It is important to point out that we underestimate rather than overestimating the pair yield using the described simplifications.

It must be pointed out that beamlets with $-180^\circ \leq \theta \leq 0^\circ$ can in general collide with the considered group of beamlets. We neglect these collision because of their relatively small contribution for the considered system, which allows us to simplify our calculation. Let us introduce two additional groups to facilitate an explanation: group 3 contains beamlets with $-180^\circ \leq \theta \leq -90^\circ$ and group 4 contains beamlets with $-90^\circ \leq \theta \leq 0^\circ$. A collision between groups 1 and 4 and groups 2 and 3 has a small collision angle φ, which increases the threshold for $\varepsilon_1 \varepsilon_2$ given by Eq. (5.1) and thus reduces the pair yield for the considered photon spectrum. A collision between groups 1 and 3 and groups 2 and 4 can happen only if the beamlets are emitted sufficiently close to each other or if the collision is nearly head-on. We expect only a few beamlet pairs from groups 1 and 3 and groups 2 and 4 to overlap with a relatively large V. Therefore, we expect for the pair yield from the collisions between the considered beamlet groups to be relatively small.

Using our algorithm, we found that the total pair yield is almost two orders of magnitude

higher than what we obtained in the benchmarking calculation that used a reduced data set. We have $N_{\text{lin}}^{\text{BW}} = 1.3 \times 10^9$, where we denote the total pair yield as $N_{\text{lin}}^{\text{BW}}$ in order to be consistent with the notations used in Ref. [75] (Chapter II) where the result was first reported. The calculation of the yield assumes that the width of each beamlet in the third direction is equal to 5 μm. Figure 5.9 shows the spatial distribution of the created linear BW pairs calculated using the algorithm discussed in Section 5.3. Figure 5.10(a) shows how the pair yield depends on the energies of the colliding beamlets. The yield is spread over a wide range of s, which justifies the use of s rather than ε as our discretization variable. The shown distribution was computed by binning the yield for beamlet pairs based on their energies.

Our algorithm can also be readily leveraged to compute the initial momentum distribution of the created electron-positron pairs. The mono-energetic nature of the beamlets particularly facilitates the calculation. The photons in each beamlet have the same momentum $\boldsymbol{p}_\gamma$. Let us then consider two beamlets with photon momenta $\boldsymbol{p}_{\gamma 1}$ and $\boldsymbol{p}_{\gamma 2}$. There exists a frame of reference where the total momentum of two colliding photons from the considered beamlets is zero. The velocity of this frame of reference is

$$\boldsymbol{v}_{cm} = \frac{\boldsymbol{p}_{\gamma 1} c + \boldsymbol{p}_{\gamma 2} c}{\varepsilon_1 + \varepsilon_2}, \tag{5.43}$$

where $\varepsilon_1 = p_{\gamma 1} c$ and $\varepsilon_2 = p_{\gamma 2} c$. It is often referred to as the 'center of mass' frame of reference because a created electron-positron pair has no net momentum in this frame of reference. The energy of the generated electrons and positrons in this frame of reference is the same and it is equal to

$$\varepsilon_{cm} = \sqrt{[1 - \cos(\theta_1 - \theta_2)]\varepsilon_1 \varepsilon_2 / 2}, \tag{5.44}$$

where θ_1 and θ_2 are the angles associated with each beamlet. The corresponding amplitude of the momentum (it is again the same for all electron and positrons) is

$$p_{cm} = (1/c)\sqrt{\varepsilon_{cm}^2 - m^2 c^4}. \tag{5.45}$$

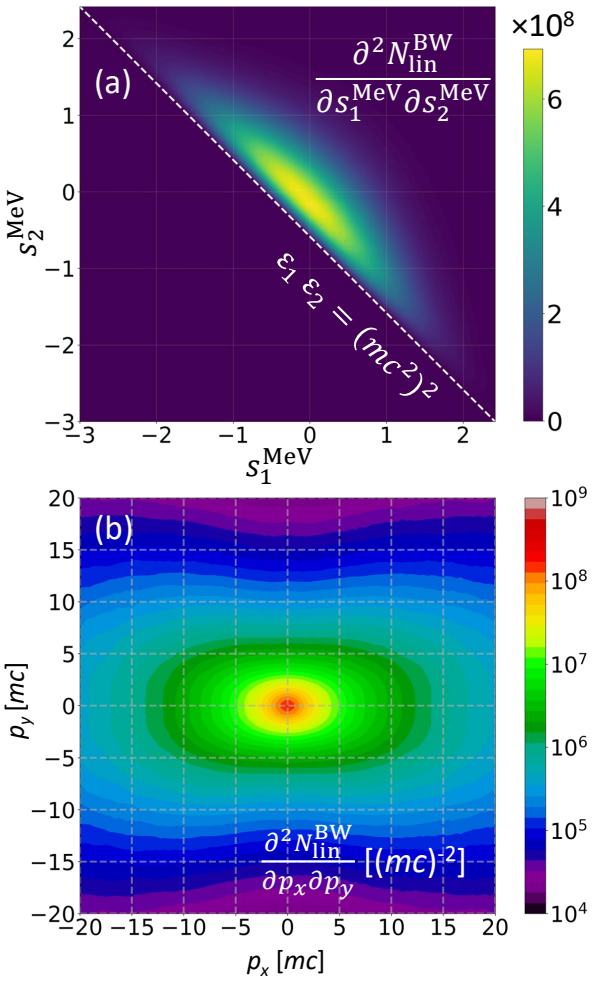

Figure 5.10. The pair yield computed using our algorithm as a function of (a) photon energies and (b) positron momentum. (a) $\partial^2 N_{\rm lin}^{\rm BW}/\partial s_1^{\rm MeV}\partial s_2^{\rm MeV}$ for the pairs created by colliding photons with energies ε_1 and ε_2, where $s_{1,2}^{\rm MeV} = \log_{10}(\varepsilon_{1,2}[\rm MeV])$. (b) $\partial^2 N_{\rm lin}^{\rm BW}/\partial p_x \partial p_y$ of created positrons, where p_x and p_y are the components of the positron momentum right after the positron is created. Panel (a) is reproduced with permission from He *et al.*, Communications Physics, **4**, 139 (2021). Copyright 2021 Authors, licensed under a Creative Commons Attribution (CC BY 4.0) license. Adapted from original.

Therefore, the only extra step that is required once the pairs are generated by our algorithm is the assignment of their angular distribution.

The angular distribution of the created positrons in the center of mass frame of reference is somewhat anisotropic [74]. This can be accounted for using the differential cross section to distribute the generated pairs. Since the anisotropy is not particularly strong, we neglect it here, treating the distribution in the center of mass frame of reference as isotropic instead. Due to the large number of beamlet-beamlet collisions, we choose not to differentiate between the pairs produced in a single beamlet-beamlet collision. All of the positrons produced in a single collision are thus assigned the same $\boldsymbol{p}_{cm}$. The direction is decided by randomly placing a point onto a sphere with radius p_{cm} in momentum space. The resulting $\boldsymbol{p}_{cm}$ is then transformed into the laboratory frame of reference to obtain $\boldsymbol{p}$ for a given beamlet-beamlet collision. It must be stressed that the resulting momentum distribution of positrons is necessarily three-dimensional even though the colliding photons have no momentum along the z-axis. Figure 5.10(b) shows how the positrons generated by our algorithm are distributed in the (p_x, p_y) plane. The plot is obtained by binning the yield from each beamlet-beamlet collisions according to the values of p_x and p_y.

The momentum distribution in Fig. 5.10(b) is clearly anisotropic even though there is no preferred direction in the center of mass reference frame that we use to generate pairs for each beamlet-beamlet collision. The anisotropy results from the fact that, in most cases, colliding photons have very different energies, as seen in Fig. 5.10(a). Due to the difference in energy, v_{cm} is typically relativistic. For example, $v_{cm} \approx 0.82c$ for a head-on collision with $|p_{\gamma 1}| = 0.1|p_{\gamma 2}|$. Such a high velocity causes a significant change of momentum when converting $\boldsymbol{p}_{cm}$ into the momentum in the laboratory frame of reference. Most importantly, the momentum is enhanced in the direction of the beamlet with more energetic photons. As seen from the spectrum in Fig. 5.2, the most energetic photons in the considered simulation are emitted along the axis of the channel. This is why the momentum distribution of positrons in Fig. 5.10(b) is elongated along p_x. It is worth pointing out that the observed anisotropy is much more pronounced than the neglected

anisotropy in the center of mass reference frame [74], which suggests that any corrections due to the differential cross section [74] may be inconsequential for our system.

The example considered in this section illustrates that the developed algorithm can indeed provide useful and otherwise unavailable information about the pair production via the linear BW process in high-intensity laser-plasma interactions.

5.7 Summary and discussion

We have presented a post-processing algorithm that can efficiently compute the linear Breit-Wheeler pair yield inside a laser-irradiated plasma. The efficiency of our algorithm is based upon a simplification in computing the number of collisions by two photon beamlets. Presented benchmarking shows that the computational time is reduced by two orders of magnitude compared to the direct approach, while the resulting error remains around 10%. The algorithm can also be leveraged to compute the density of the pair-creating events and the initial momentum distribution of generated positrons.

Our algorithm offers a novel tool for studies of the linear Breit-Wheeler process in laser-irradiated plasmas. This process has been omitted from previous studies of high-intensity laser-plasma interactions because none of the PIC codes used for these studies are currently capable of computing the pair yield from the linear Breit-Wheeler process. The application of our algorithm in Refs. [75] (Chapter II) and [104] (Chapter III) has revealed that the yield is much higher than previously anticipated, indicating that the linear Breit-Wheeler process must be taken into account. Studies of positron dynamics will require implementation of the linear BW process into a PIC code. However, even in this case, the developed post-processing algorithm can serve an important role in assessing the pair yield and the pair distribution. Moreover, the density of the pair-producing events $\widetilde{\rho}_{pairs}$ can be used to assess the number of positrons that can undergo acceleration by one of the laser pulses in the set up considered in Section 5.6 and discussed in more detail in Ref. [75] (Chapter II). This is because only those positrons that are

produced inside the channel that guides the laser propagation can experience acceleration.

The current version of the algorithm neglects the divergence of colliding beamlets. To include the impact of the beamlet divergence, we would have to modify the shape of the interaction region for each pair of beamlets, which can potentially have a non-negligible detrimental effect on computational time. However, as the resolution for θ goes up, the impact of the divergence decreases, so the divergence of beamlets is likely to be important only for low resolutions. Moreover, as seen in Fig. 5.9, most of the pairs are created relatively near to the region where the photon are emitted, which further reduces the impact of the beamlet divergence. One easy way to take the divergence into consideration without changing the shape of the interaction region is by introducing a multiplier for the densities of the colliding photons.

Our algorithm explicitly assumes that modifications to the emitted photon spectrum during photon propagation through the plasma can be neglected. This is definitely the case for the set up shown in Fig. 5.9 where the characteristic spatial scale is about ten microns. However, the user of the algorithm should check this key assumption, as the assessment might change for a setup with drastically different parameters. If there is a need to include the attenuation of the photon population, then one can add extra multiplicative factors on the right hand side of Eq. (5.16) to account for the change of photon density. Our partitioning of the photon population into beamlets makes it easy to include the energy dependence into consideration.

5.8 Acknowledgments

Chapter 5, in part, is a reprint of the material as it appears in *Algorithm for computing the electron-positron yield from the linear Breit-Wheeler process in high-intensity laser-plasma interactions* in Computer Physics Communications, 286, 108657, by Y. He, and A. Arefiev, 2023. The dissertation author was the primary investigator and author of this paper.

This research was supported by AFOSR (Grant No. FA9550-17-1-0382). The authors are thankful to Prof. T. Blackburn for constructive comments.

Table 5.1. 2D-3V PIC simulation parameters.

Laser parameters	
Normalized field amplitude	$a_0 = 190$
Peak intensity range	$I_0 = 4.9 \times 10^{22}$ W/cm^2
Wavelength	$\lambda_0 = 1$ μm
Focal plane of laser #1	$x = -35$ μm
Focal plane of laser #2	$x = +35$ μm
Laser profile (longitudinal and transverse)	Gaussian
Pulse duration (FWHM for intensity)	50 fs
Focal spot size (FWHM for intensity)	3.6 μm

Target parameters	
Target thickness (along y)	30 μm
Target length (along x)	70 μm
Channel width	$d_{\text{ch}} = 5$ μm
Composition	C^{+6} and electrons
Channel density	$n_e = 7.1 n_c$
Bulk density	$n_e = 100 n_c$

Other parameters	
Simulation box	80 μm in x; 36 μm in y
Spatial resolution	40 cells per μm in x 20 cells per μm in y
Macro-particles per cell	40 for electrons 20 for carbon ions

5.9 Appendix

Table 5.1 provides detailed parameters for the PIC simulation presented in the chapter. The 2D-3V simulation was performed using the fully relativistic PIC code EPOCH [17].

The simulation setup follows the one used in Ref. [75] (Chapter II). The axis of the structured target ($y = 0$) is aligned with the axis of the counter-propagating lasers. We initialize the target as a fully-ionized carbon plasma. Each of the lasers is focused at the corresponding channel opening. The lasers are linearly polarized (their electric field is directed in the simulation

plane). In the absence of the target, the lasers have the same spatial Gaussian profile in the focal spot with the same Gaussian temporal profile.

A resolution scan reported in Ref. [75] (Chapter II) indicates that the resolution used here produces a converged photon spectrum for photons with energies above 50 keV. The electrons that emit energetic photons undergo their energy gain without alternating deceleration to non-relativistic energies and re-acceleration. This is likely the reason why they are not subject to a more severe resolution constraint [63, 64, 65] that requires for the cell-size/time-step to be reduced according to the $1/a_0$ scaling in order to achieve convergence.

Positron generation and acceleration in a self-organized photon collider enabled by an ultraintense laser pulse

We discovered a simple regime where a near-critical plasma irradiated by a laser of experimentally available intensity can self-organize to produce positrons and accelerate them to ultra-relativistic energies. The laser pulse piles up electrons at its leading edge, producing a strong longitudinal plasma electric field. The field creates a moving gamma-ray collider that generates positrons via the linear Breit-Wheeler process – annihilation of two gamma-rays into an electron-positron pair. At the same time, the plasma field, rather than the laser, serves as an accelerator for the positrons. The discovery of positron acceleration was enabled by a first-of-its-kind kinetic simulation that generates pairs via photon-photon collisions. Using available laser intensities of $10^{22}\,\mathrm{W/cm^2}$, the discovered regime can generate a GeV positron beam with divergence angle of $\sim 10^{\circ}$ and total charge of 0.1 pC. The result paves the way to experimental observation of the linear Breit-Wheeler process and to applications requiring positron beams.

In astrophysics, creation of matter from light is ubiquitous, playing an important role for various astrophysical objects (e.g. see [120, 121, 122, 123, 124]). The advent of ultra-high-intensity laser facilities [7, 125, 126] promises to enable, for the first time, creation of electron-positrons pairs from light alone on a macroscopic scale in laboratory. If successfully implemented, this capability will open a new area of QED research [9, 19, 127] and it will enable laboratory studies of astrophysically relevant electron-positron plasmas [128]. The ability to generate positrons by a laser is also likely to impact the research on laser-driven positron

acceleration. Currently, positrons are produced by an external source and the focus is on finding augmented configurations that facilitate positron acceleration [129, 130, 131, 132].

In the context of pair production from light alone, it is important to distinguish between the non-linear [22] and linear [1] Breit-Wheeler (BW) processes. The nonlinear BW or the multiphoton process is the decay of a γ-ray propagating through a laser pulse into a pair. The decay involves multiple coherent optical photons. The linear BW or the two-photon process is the annihilation of two energetic γ-rays that leads to pair production. The setups that many pairs via the nonlinear BW [26, 133, 134, 135, 136, 137, 138] require a laser intensity in excess of $10^{23}\,\mathrm{W/cm^2}$. The two-photon process has no laser intensity requirement, but it does require a dense population of energetic γ-rays to overcome the smallness of the cross-section, $\sigma_{\gamma\gamma} \sim 10^{-25}\,\mathrm{cm^2}$, and the energy threshold. A laser-irradiated plasma can efficiently generate a γ-ray beam [80, 139, 41], so colliding in vacuum two such beams (produced by two different laser) is a possible approach to produce pairs [12, 13]. The inherent γ-ray beam divergence requires the targets generating γ-rays to be close to each other and makes experimental implementation challenging. A conceptually different approach is to generate and collide γ-ray beams inside one target [75] (Chapter II). It not only allows to overcome the divergence and thus boost the pair yield [75], but, more importantly, it offers an unexplored opportunity to accelerate the linear BW positrons. If the positrons can be accelerated and collimated, then this would facilitate their detection, making a first laboratory observation of the linear BW process possible, and enable their use for applications like positron annihilation lifetime spectroscopy [140, 141].

In this chapter, we present a simple but previously unknown regime where a dense plasma irradiated by a laser of experimentally achievable intensity self-organizes to produce positrons from light alone and accelerate them to ultra-relativistic energies. The laser pulse piles up electrons at its leading edge, producing a strong longitudinal plasma electric field that moves with the pulse. The field creates a moving γ-ray collider that generates positrons via the linear BW process and, at the same time, serves as an accelerator for the produced positrons. The discovery of the new positron acceleration mechanism and the synergistic interplay between the

photon collider and the plasma accelerator was enabled by a first-of-its-kind kinetic simulation that generates pairs via photon-photon collisions. This work builds on an important observation based on post-processed photon data that a single laser-pulse can generate a colliding population of γ-rays in a dense structured plasma [104] (Chapter III). We find that the linear BW process produces about 10^7 pairs at $3\times10^{22}\,\mathrm{W/cm^2}$, whereas the nonlinear BW process produces no pairs at all. About 10% of the positrons experience the forward acceleration and form a GeV beam with a divergence angle of 10°. The advantage of our regime is that it uses a simple setup and requires only a single laser with intensity already accessible at ELI [142] and CoReLS [143].

The laser-plasma interaction is self-consistently simulated in 2D-3V with the PIC code PICLS that includes a radiation transport module [144] for energetic photons emitted via synchrotron radiation [145] and Bremsstrahlung [146]. We have developed a module for simulating the linear BW process [see Sec. 6.2.2 in Appendices of this chapter], making PICLS the first PIC code capable of generating linear BW pairs during the laser-plasma interaction and thus suitable for studies of positron dynamics. In our setup, a 25 fs, 3×10^{22} W/cm^2 laser pulse irradiates a dense uniform carbon plasma (see Sec. 6.2.1 for simulation parameters). We normalize all electric fields, $\boldsymbol{E}$, and use a dimensionless quantity $\boldsymbol{a}=|e|\boldsymbol{E}/m_e c\omega_0$ instead, where e and m_e are the electron charge and mass, c is the speed of light, and ω_0 is the laser frequency corresponding to vacuum wavelength $\lambda=0.8$ μm. The laser amplitude is $a_L=120$. This laser makes electrons ultra-relativistic and renders a plasma with electron density n_e less than $\gamma_L n_c\sim a_L n_c$ transparent, where $\gamma_L\equiv\sqrt{1+a_L^2/2}$ is the electron Lorentz factor for ponderomotive energy [147] and $n_c=m_e\omega_0^2/4\pi e^2$ is the classical critical density. In our main simulation, the initial electron density is $n_{e0}=2.8n_c\ll a_L n_c$, so the laser easily propagates into the plasma.

Figure 6.1 illustrates key aspects of the laser-plasma interaction. All snapshots are taken when the laser pulse reaches $x=30$ μm. The corresponding time is $t=117\,\mathrm{fs}$, with $t=0\,\mathrm{fs}$ being the time when the pulse reaches the target. Figure 6.1(a) shows the normalized transverse electric field a_y that is dominated by the field of the laser. Due to the relativistic self-focusing, the beam remains tightly focused after having traveled a distance greater than the Rayleigh

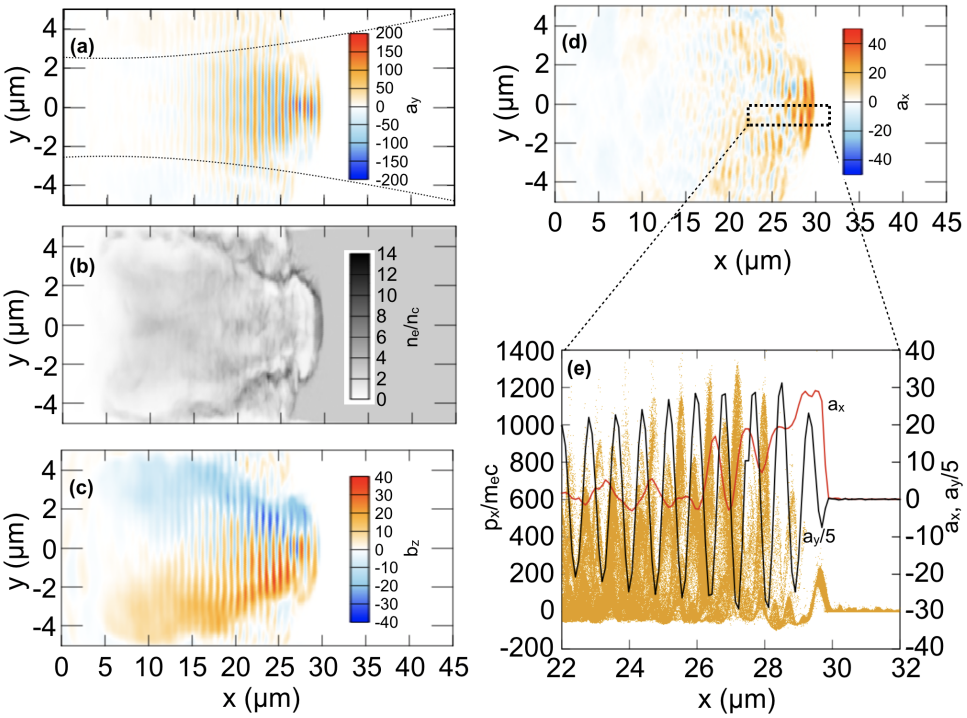

Figure 6.1. Laser interaction with a dense plasma. (a) Normalized transverse electric field a_y. Dashed lines indicate the beam waist in the absence of the plasma. (b) Electron density. (c) Normalized magnetic field b_z averaged over one laser period. (d) Normalized longitudinal electric field a_x. (e) Electron distribution in the x-p_x plane, and a_x and a_y in the vicinity of the pulse front [dashed rectangle in (d)]. The electric fields a_x and a_y in (e) are averaged over $|y| \leq 0.5$ μm. The snapshots in (a) - (e) are taken at $t = 117$ fs.

length ($l_R = \pi w_0^2/\lambda \simeq 25$ μm for a focal spot with radius $w_0 = 2.5$ μm). The dashed curves mark the expected beam waist in the absence of the target. The self-focusing also increases the laser amplitude to $a_y = 150$. The beam becomes fully depleted after propagates 70 μm into the plasma. The profiles of electron density and generated azimuthal magnetic field are shown in Figs. 6.1(b)&(c). Transverse electron expulsion by the ponderomotive force produces a density pileup ($n_e \sim 10n_c$) at the periphery of the beam that helps guide the laser. The electrons remaining in the beam accelerate forward in the laser field and form longitudinal current. The current generates a strong quasi-static magnetic field B_z [41] whose peak strength is 30% of that for the laser magnetic field. Figure 6.1(c) shows the field profile while providing an additional figure of merit $b_z = \omega_c/\omega_0$, where $\omega_c = |e|B_z/m_ec$ is the cyclotron frequency.

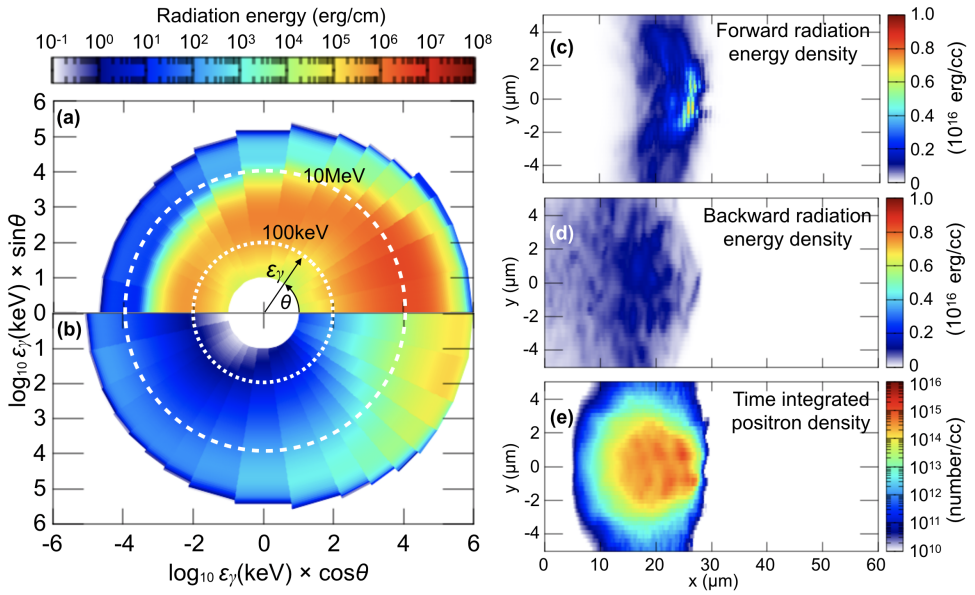

Figure 6.2. Self-organized photon collider. (a)&(b) Angular distribution of synchrotron and Bremsstrahlung photons in the region with 22 μm $\leq x \leq$ 27.5μm and $|y| \leq 1$ μm. The radius is $\log_{10}\varepsilon_\gamma$[keV]. The dashed circles are $\varepsilon_\gamma = 100$ keV and 10 MeV. (c)&(d) Energy density of forward and backward emitted photons via synchrotron emission. (e) Time integrated number density of the linear BW pair production events. The snapshots in (a) - (e) are taken at $t = 117$ fs.

The B-field plays a key role in generating forward-directed γ-rays. It transversely confines the electrons that are accelerated and pushed forwarded by the laser. The B-field defects electrons forward instead of causing the conventional rotation and the deflections change the orientation of the transverse velocity $v_\perp$ with respect to $E_\perp$ of the laser. If their frequency is comparable to the Doppler-shifted frequency of the laser, then $v_\perp$ remains antiparallel to $E_\perp$ as the laser field and the electron oscillate. This mechanism of direct laser acceleration assisted by the plasma B-field [49] produces ~ 500 MeV electrons with a forward momentum of $1000\, m_e c$. They are located in Fig. 6.1(e) at 22 μm $\leq x \leq$ 28 μm. The deflections of the electrons by the magnetic field has another important effect – they cause the electrons to emit MeV γ-rays in the direction of laser propagation [41, 13, 14].

Due to the high plasma density, the laser also generates a strong longitudinal plasma electric field that is essential for the production of backward-directed γ-rays. This is a charge-separation field that arises as the leading edge of the laser pulse sweeps up plasma electrons. Its

peak amplitude is 25% of a_y and it dominates over the oscillating longitudinal field of the laser. The positive plasma field is clearly visible in Fig. 6.1(d) at $x \approx 29.5$ μm. After initial forward acceleration to $p_x \sim 200\, m_e c$, the electrons swept up by the leading edge of laser pulse slow down under the influence of a_x and then re-accelerate in the backward direction to $p_x \sim -100\, m_e c$.These electrons emit backward-directed photons. In contrast to the forward-moving electrons, the emission is induced by the laser field [148] that is much stronger than the plasma magnetic field. This makes the emission more efficient, causing the electrons to quickly lose a large portion of their energy, as seen in Fig. 6.1(e) at $x > 28$ μm. The emission process accompanies laser propagation since the population of backward-moving electrons is constantly replenished by a_x that is moving forward with the laser pulse.

The two photon populations form a moving γ-ray collider. Figures 6.2(a)&(b) show photon spectra versus the polar angle θ in the region where the energy density of forward- and backward-moving photons ($|\theta| \leq \pi/2$ and $|\theta| > \pi/2$) overlap (22 μm $\leq x \leq$ 27.5 μm; $|y| \leq 1$ μm). The corresponding energy density plots are shown in Figs. 6.2(c)&(d). The Bremsstrahlung that plays a secondary role is included for completeness. The synchrotron emission converts 40% of the laser energy into photons over the entire simulation (vs. 2% for Bremsstrahlung). The linear BW process has a threshold of $\varepsilon_{\gamma 1}\varepsilon_{\gamma 2} > m_e^2 c^4 \approx 0.26$ MeV^2, where $\varepsilon_{\gamma 1,2}$ are the energies of colliding photons. Therefore, linear BW pairs are mainly produced by forward-moving photons with 0.5 MeV $\lesssim \varepsilon_\gamma \lesssim$ 100 MeV colliding with backward-moving photons with 10 keV $\lesssim \varepsilon_\gamma \lesssim$ 1 MeV. The photon densities in these two groups are comparable, with $n_\gamma \sim 10^{22}$ cm^{-3}. The probability for a backward-moving photon to produce a pair is $\sigma_{\gamma\gamma} n_\gamma l \sim 10^{-6}$, where $l \sim 10$ μm is the length of the forward-moving photon cloud. The total number of backward-photons is $n_\gamma SL \sim 10^{13}$, where $L \approx 70$ μm is the laser depletion length and $S \approx 25$ μm^2 is the cross-section of the cloud, assuming the length in the third dimension is the laser spot diameter. The predicted pair yield is 10^7, which matches the yield evaluated using the developed module for the linear BW process. A similar module implemented by us into the PIC code EPOCH [17] that has a different approach for treating emitted photons produced a

comparable yield. A time integrated density of the pair-production events is shown in Fig. 6.2(e).

The γ-ray collider is moving with the laser, continuously producing positrons with a mildly relativistic momentum $p \sim m_e c$ within the laser pulse [see Fig. 6.3(a)]. The positron dynamics is strongly influenced by the laser and plasma fields, with two distinct populations emerging over time: forward-moving positrons whose energies reach 1 GeV and backward-moving positrons whose energies reach 100 MeV. Figures 6.3(c)&(d) show terminal positron distributions in the energy-angle space for the forward- and backward positrons. Figure 6.3(e) shows the electron and positron energy spectra, distinguishing the linear BW and Bethe-Heitler [see Sec. 6.2.4 in the Appendices of this chapter] positrons to emphasize the dominant role of the linear BW process. A striking feature of Fig. 6.3(e) is that the peak energy of forward positrons exceeds the peak energy of forward electrons by a factor of two. The electrons gain their energy from the laser via the direct laser acceleration assisted by the plasma magnetic field [49], but the positrons are not able to do that because they are positively charged. The plasma magnetic field deflects positrons backward rather than forward, which causes the formation of the backward positron population.

We tracked the energetic forward-moving positrons and found that they gain most of their energy (80%) from the strong forward-moving longitudinal plasma electric field, thus discovering a new positron acceleration mechanism. Figure 6.3(b) confirms that the energetic positrons are surfing with the spike in a_x. The positrons continue accelerating until they overtake the laser pulse or leave the acceleration region in lateral direction. The acceleration by a_x only works for positrons, whereas the same field pulls plasma electrons backward creating the backward emission that contributes to the photon collider.

The discovered acceleration mechanism produces 10^6 or 0.1 pC of positrons with energies above 100 MeV and average divergence angle $|\theta| \sim 10^\circ$. The high plasma density is not only important for generating strong a_x needed for positron acceleration (no a_x spike is produced at subcritical densities [138]), but it is also crucial for achieving a high number of accelerated positrons. Positrons must catch up with a_x to experience the acceleration, but this is hard to

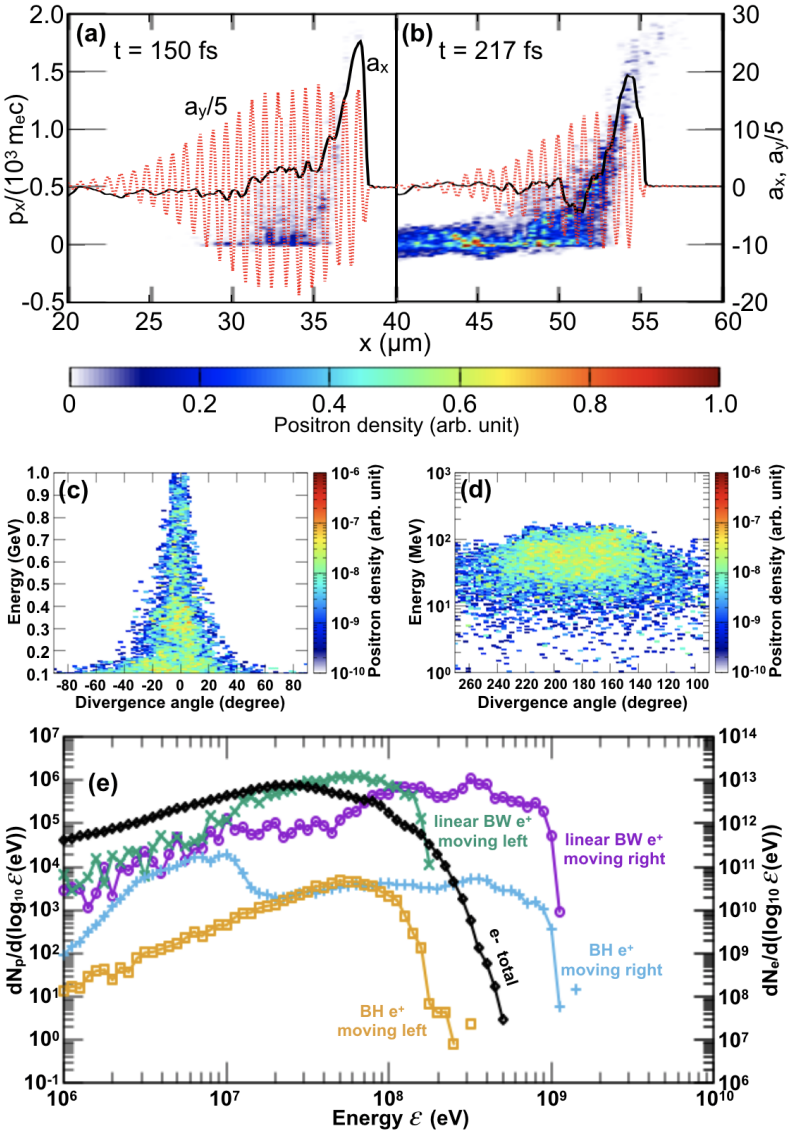

Figure 6.3. Laser-driven positron accelerator. (a)&(b) Positron distribution in (x,p_x) space for $|y| \leq 2$ μm and electric field profiles at $t = 150$ fs and 217 fs. The fields are averaged over $|y| \leq 2$ μm. (c)&(d) Energy vs. divergence angle of forward- and backward-moving positrons at $t = 317$ fs. (e) Energy spectra at $t = 317$ fs of positrons produced via the linear BW process and via the BH process, and electrons. The 3rd dimension is set to 5 μm to evaluate number of particles.

achieve if a_x, whose speed is u, moves too fast. In a low density plasma, u is close to the group velocity $v_g/c \approx \sqrt{1-n_e/\gamma_L n_c}$ [149]. In a dense plasma, u is lower than v_g due to laser depletion, which enables more positrons to experience acceleration. In our case, $u/c \approx 0.8$, but $v_g/c \approx 0.98$. Only relativistic positrons with $v_x \approx c\cos\theta > u$ are able to catch up with a_x. We have $v_x \approx c\cos\theta > u$ for $|\theta| \leq 37^\circ$, whereas $v_x \approx c\cos\theta > v_g$ for $|\theta| \leq 11^\circ$. The 20% reduction in u compared to v_g increases the range of θ by a factor of three and thus significantly increase the number of positrons that can catch up with a_x.

To examine the impact of the plasma density n_{e0} on the strength of a_x and the positron energy gain, we performed extra simulations with $n_{e0}/n_c = 0.5$, 1.0, 1.75, and 5.6. Figures 6.4(a)&(b) show a_x at the leading edge of the pulse and the energy gain by forward-moving positrons versus n_{e0}. We average a_x over y at the time when the laser peak intensity reaches the pulse leading edge to obtain the values in Fig. 6.4(a). The energies in Fig. 6.4(b) were averaged over the top 5, 10, and 20 percent of the positron spectrum to confirm the trend. The discovered regime is robust and can be achieved over a wide range of plasma densities. For $n_c \leq n_{e0} \leq 5.6\,n_c$, the number of positron with energies above 100 MeV and $|\theta| \lesssim 10^\circ$ is consistently about 10^6. At $n_{e0}/n_c = 0.5$, the speed of a_x is very close to c, which makes a_x too fast to effectively accelerate positrons that are originally only mildly relativistic.

We next use estimates for a_x and the positron energy gain to determine their scaling at high n_{e0}. The electron density pileup responsible for a_x is sustained due to force balance, $0 = F_p + F_s$, between the laser ponderomotive force $F_p = -m_e c^2 \nabla_x \gamma_L$ and $F_s = -a_x m_e c \omega_0$. We estimate that $\gamma_L/|\nabla_x \gamma_L| \simeq l_{\rm skin}$, where $l_{\rm skin} = \sqrt{\gamma_L} c/\omega_{pe}$ is the relativistic skin depth. Taking into account that $a_L \gg 1$, we obtain

$$a_x \simeq \sqrt{\gamma_L n_e/n_c}, \tag{6.1}$$

where n_e is the density of the electron pileup. The shaded area in Fig. 6.4(a) shows a_x from Eq. (6.1) for $a_L = 120$ and $2n_{e0} \leq n_e \leq 6n_{e0}$. The latter is the entire range of n_e observed in the simulations, with $n_e \approx 2n_{e0}$ for $n_{e0} = 5.6n_c$ and $n_e \approx 6n_{e0}$ for $n_{e0} = 0.5n_c$. The momentum

gain, Δp_{e^+}, from a_x can be estimated by integrating the positron equation of motion $dp_{e^+}/dt \simeq m_e c\omega_0 \bar{a}_x$ over the acceleration time interval $\Delta t_{\rm acc}$, where $\bar{a}_x = a_x/2$ is the average field amplitude in the acceleration region. The length of the region with positive a_x is the width of the electron pileup, $l_{\rm skin}$, plus the length of the positively-charged electron cavity, $l_{\rm cav}$, formed behind the pulse leading edge. We estimate $l_{\rm cav}$ from the charge conservation: $(n_{e0} - n_c)\, l_{\rm cav} = (n_e - n_{e0})\, l_{\rm skin}$ for $n_{e0} > n_c$. The acceleration region is moving forward with velocity u while the positron velocity is v_x, so that $\Delta t_{\rm acc} \equiv (l_{\rm cav} + l_{\rm skin})/(v_x - u)$. Assuming an ultra-relativistic positron, we set $v_x \sim c$. After taking into account that $\gamma_L n_c \gg n_e$ for $a_L \gg 1$, we find that that the positron momentum gain is

$$\Delta p_{e^+} \simeq \frac{\gamma_L m_e c}{2} \frac{1}{1-u/c}\, \frac{n_e - n_c}{n_{e0} - n_c}. \tag{6.2}$$

Equation (6.2) gives $\Delta p_{e^+}/m_e c \simeq 1200$ for $n_{e0} = 2.8\, n_c$, $a_L = 120$, $u = 0.8c$, and $n_e = 4 n_{e0}$, reproducing the significant positron momentum increase at the pulse leading edge seen in Fig. 6.3(b). The energy gain, $\Delta\varepsilon_{e^+} = c\Delta p_{e^+}$, obtained from Eq. (6.2) is shown in Fig. 6.4(b) with a dashed curve. For high densities, $\Delta\varepsilon_{e^+}$ has a weak dependence on n_{e0}, because the increase in a_x is counteracted by the reduction in the acceleration time caused by lower u.

In summary, we discovered a robust regime where a laser-irradiated plasma self-organizes to produce positrons and accelerate them. The GeV-level positron beam can be generated using just a single laser with an experimentally available intensity. The regime requires the use of a dense plasma that can create a strong longitudinal electric field via electron pileup. The field is crucial for creating the γ-ray collider and for accelerating positrons. The positron acceleration was discovered by a first-of-its-kind simulation code generating pairs via photon-photon collisions. This code has direct relevance to astrophysics research since correct treatment of secondary pairs is one of the main problems facing modern PIC simulations of pulsars [122, 124] The uniform density is a simplification and not a requirement. A simulation with n_e ramping up from 0.5 to $3n_c$ over 60 μm has a similar pair yield of 10^7. 3D simulations with PICLS (see Sec. 6.2.3) and EPOCH [17] have n_γ that is similar to that in our 2D simulations, confirming the robustness of

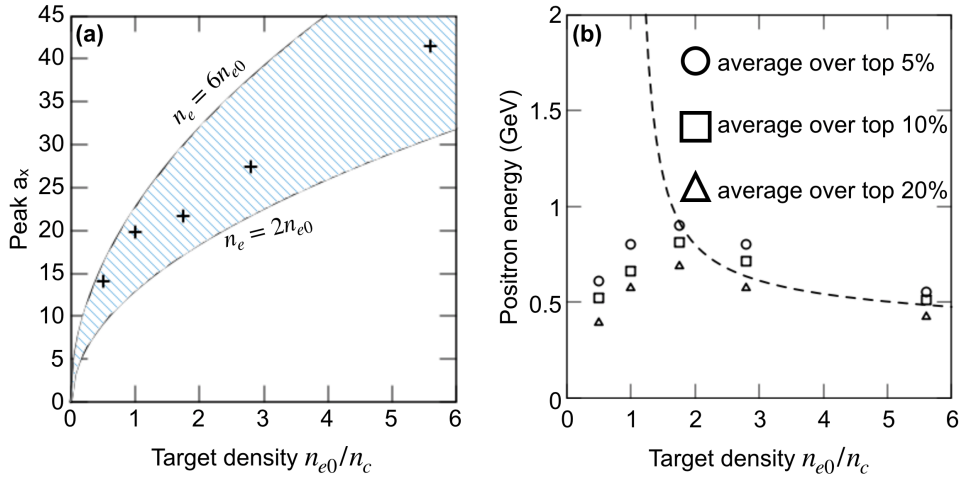

Figure 6.4. (a) Normalized electric field a_x at the leading edge of the laser pulse as a function of target density. The shaded area is given by Eq. (1) for $2n_{e0} \leq n_e \leq 6n_{e0}$, $a_L = 120$, and $u = 0.8c$. (b) Positron energies averaged over the top 5%, 10%, and 20% of the positron spectra for different target densities. The dotted curve is $\Delta\varepsilon_{e^+} = c\Delta p_{e^+}$ obtained from Eq. (2) for $a_L = 120$, $u = 0.8c$, and $n_e = 4n_{e0}$.

the discussed phenomena. Lastly, our regime can be instrumental in gauging the focal intensity of multi-PW lasers. At 10^{21} W/cm^2, the positron yield is five orders of magnitude lower than at 10^{22} W/cm^2. Therefore, the presence of energetic positrons in the laser direction can be a confirmation of laser intensity exceeding 10^{22} W/cm^2.

6.1 Acknowledgement

Chapter 6, in part, is a reprint of the material as it appears in *Positron generation and acceleration in a self-organized photon collider enabled by an ultra-intense laser pulse*, in Physical Review Letters, 131, 065102, by K. Sugimoto, Y. He, N. Iwata, I-L. Yeh, K. Tangtartharakul, A. Arefiev, and Y. Sentoku, 2023.

The dissertation author implemented the linear BW process into EPOCH and performed 2D and 3D EPOCH simulations with particle tracking. This study and the work by K.S., N.I., and Y.S. was supported by JSPS KAKENHI Grants No. JP19KK0072, No. JP20K14439, No. JP20H00140, No. JP22J10867, JP23K03354, and JST PRESTO Grant No. JPMJPR21O1. The work by Y.H., I.-L. Y., K. T., and A. A. was supported by AFOSR (Grant No. FA9550-17-1-

0382) and by National Science Foundation – Czech Science Foundation partnership (NSF award PHY-2206777).

6.2 Appendices

6.2.1 Setup of 2D particle-in-cell simulations

The 2D-3V simulations of laser-plasma interactions were carried out using the PIC code PICLS that includes a radiation transport module with a newly implemented linear BW process for pair creation. The size of the simulation box is 110 μm by 10 μm. The grid size and the time step are set to Δx=Δy=$c\Delta t$=0.025 μm. Initially, the target is a uniform fully ionized carbon plasma with electron density set by n_{e0}. The plasma occupies the region with $5 \leq x \leq 105\,\mu$m. The plasma is represented by macro-participles, with 30 macro-participles per cell for electrons and 5 macro-particles per cell for ions. The laser pulse is injected from the left boundary ($x = 0$) and it is focused on the plasma surface at $x = 5\,\mu$m with a Gaussian focal spot of diameter 5.0 μm (FWHM of intensity). The laser is linearly polarized with the electric field E_L being in the plane of the simulation.The wavelength and pulse duration are set to 0.8 μm and 25 fs, respectively. The peak amplitude in the focal plane in the absence of the target is a_L=120, which corresponds to the intensity of 3×10^{22}W/cm^2. The corresponding laser electric field strength of $E_L = 3.6$ kV/Å is sufficiently strong to strip electrons from the K-shell of carbon within femtoseconds [150].

The simulations include two photon emission processes: synchrotron emission and Bremsstrahlung. Details of their implementation into PICLS are provided in [145, 146]. The code accounts for electron recoil that is modelled in the case of synchrotron emission as a radiation friction force. Rather than treating photons as individual particles, the code uses a photon distribution function. In our simulations, the distribution function covers a photon energy range from 10 keV to 1 GeV. We use a log-scale to uniformly discretize this range into 100 energy segments, producing 100 photon energy groups. The transport of the emitted photons is simulated

self-consistently by solving a radiation transport equation within the PIC simulation. The details of the radiation transport module are provided in Ref. [144, 151]. To reduce the computational cost, the grid size and the time step for the radiation transport calculation are ten times larger than those of the PIC simulation: $\Delta x_{rad} = \Delta y_{rad} = 0.25\,\mu\text{m}$. We use open boundary conditions (in the x- and y-directions) for particles, fields, and radiation fluxes. The electron-positron pair yield is computed in each grid of the radiation transport calculation.

6.2.2 Algorithm for computing the linear Breit-Wheeler pair yield

In the simulations, the high-energy photons from 10 keV to 1 GeV are treated as a ray. Their radiation energies are characterized by using specific intensity. We implemented a physics model of positron production in the pair creation process, e.g. linear BW process, as opacity in the radiation transport. The new algorithm consists of three parts: (1) randomly sampling two photons and move to the center of momentum (CM) frame, (2) evaluate the cross section of the pair creation and produce a positron particle in the CM frame, and (3) transform the positron momentum to the laboratory frame via the Lorentz transformation.

In one radiation grid at (x, y) for radiation transport, the specific intensity is discretized in the solid angle $\Omega(\theta, \phi)$ where θ is the polar angle with respect to the positive x-direction and ϕ is the azimuthal angle using the discrete ordinate method[152]. Using the discretized photon energy ε, a specific intensity in the unit of J/cm^2/s/Hz/str is expressed as a function of the discretized angles and photon energy: $I(x_\mathrm{i}, y_\mathrm{j}, \theta_\mathrm{k}, \phi_\ell, \varepsilon_\mathrm{m})$ where the subscripts are indexes. The amount of energy of radiation traveling in the direction in a solid angle $d\Omega\,(\theta_\mathrm{k}, \phi_\ell)$ and with the energy width $d\varepsilon_\mathrm{m}$ is expressed as $I(x_\mathrm{i}, y_\mathrm{j}, \theta_\mathrm{k}, \phi_\ell, \varepsilon_\mathrm{m}) d\Omega\,(\theta_\mathrm{k}, \phi_\ell)\, d\varepsilon_\mathrm{m}/c$. In the current research, the angles are divided into 16 directions (N=16 in $\mathrm{S_N}$ method), and thus the 2π solid angle for the upper hemisphere is discretized into 146 directions, while the lower hemisphere is assumed symmetric. Using the intensity I and the total cross-section of the linear BW process σ_BW, the number of generated positrons is calculated. The σ_BW for the colliding photons with energy of

ε_1 and ε_2 at colliding angle ψ is :

$$\sigma_{\mathrm{BW}} = \frac{\pi r_e^2}{2}\left(1-\beta^2\right) \times \left[\left(3-\beta^4\right)\ln\left(\frac{1+\beta}{1-\beta}\right) - 2\beta\left(2-\beta^2\right)\right], \tag{6.3}$$

where r_e is the classical electron radius, $\beta = \sqrt{1-1/s}$, and $\sqrt{s}$ is the normalized energy of each colliding photons in the CM frame, $s = \varepsilon_1\varepsilon_2\left(1-\cos\psi\right)/\left(2m_e^2c^4\right)$. Then, the number of generated positrons N_p via collision among two groups of radiation field, $I_1\left(x_{\mathrm{i}}, y_{\mathrm{j}}, \theta_1, \phi_1, \varepsilon_1\right)$ and $I_2(x_{\mathrm{i}}, y_{\mathrm{j}}, \theta_2, \phi_2, \varepsilon_2)$ during Δt, is obtained as :

$$N_{p,\mathrm{BW}} = n_{\gamma,1} n_{\gamma,2} \sigma_{\mathrm{BW}} c \Delta t, \tag{6.4}$$

where n_γ is the photon density defined as $n_\gamma = I(x_{\mathrm{i}}, y_{\mathrm{j}}, \theta_{\mathrm{k}}, \phi_\ell, \varepsilon_{\mathrm{m}}) d\Omega\left(\theta_{\mathrm{k}}, \phi_\ell\right) d\varepsilon_{\mathrm{m}}/\varepsilon_{\mathrm{m}} c$. When we compute 100 groups in photon energies and 146 solid angles, more than 10^4 number of radiations in one radiation grid. Therefore, there are potentially hundred millions of the radiative collisions. However, calculation of such a large mount of combinations every time step in every cell is too expensive to complete the simulation. Instead of doing all the possible collisions, we produce random pairs, $I(x_{\mathrm{i}}, y_{\mathrm{j}}, \theta_{\mathrm{rand1}}, \phi_{\mathrm{rand1}}, \varepsilon_{\mathrm{rand1}})$ and $I(x_{\mathrm{i}}, y_{\mathrm{j}}, \theta_{\mathrm{rand2}}, \phi_{\mathrm{rand2}}, \varepsilon_{\mathrm{rand2}})$, as many times as the number of photon groups and compute photon collisions. This random pairing reduces the total number of calculations of photon collisions to about 10^4, but underestimates the number of events. To compensate the underestimation, we adjust the time step for the positron generation as $\Delta t' = \Delta t \times g_\varepsilon \times g_{\theta,\phi}$ in Eq. (6.4), where g_ε and $g_{\theta,\phi}$ are number of groups for photon energies and solid angles, respectively. This random paring of photons is the similar to the random pairing of charged particles in the Coulomb collision calculation used in PICLS code, see Ref. [116].

In order to obtain the momentum of generated positron, we first calculate the magnitude of momentum $\boldsymbol{p}_{e^+,\mathrm{cm}}$ of the generated positron in the CM frame :

$$p_{e^+,\mathrm{cm}} = \sqrt{\frac{\varepsilon_1\varepsilon_2\left(1-\cos\psi\right)}{2c^2} - m_e^2c^2}. \tag{6.5}$$

We assume that the generated positrons are emitted isotropically in the CM frame. Using random variables $0 \leq \Theta \leq 2\pi$ and $0 \leq \Phi \leq \pi$, we obtain the momentum in the CM frame :

$$\boldsymbol{p}_{e^+,\mathrm{cm}} = p_{e^+,\mathrm{cm}} \times (\cos\Theta \sin\Phi \boldsymbol{e}_x + \sin\Theta \sin\Phi \boldsymbol{e}_y + \cos\Phi \boldsymbol{e}_z), \tag{6.6}$$

where $\boldsymbol{e}_x$, $\boldsymbol{e}_y$, and $\boldsymbol{e}_z$ are the unit vectors in the x-, y-, and z-direction. With the velocity of the CM $\boldsymbol{v}_{\mathrm{cm}} = c^2 \left(\boldsymbol{p}_{\gamma 1} + \boldsymbol{p}_{\gamma 2}\right) / (\varepsilon_1 + \varepsilon_2)$ where $\boldsymbol{p}_{\gamma 1}$ and $\boldsymbol{p}_{\gamma 2}$ are the momentum of colliding photons in the laboratory (LAB) frame, we perform Lorentz transformation of positron momenta from CM to LAB frame [116].

During one time step, the density of newborn positrons are accumulated at a grid while their momenta are averaged :

$$\begin{aligned} n_{\mathrm{tot}} &= \sum_{\theta}\sum_{\phi}\sum_{\varepsilon} N_{p,\mathrm{BW}} \\ \overline{\boldsymbol{p}}_{e^+} &= \frac{\sum_\theta \sum_\phi \sum_\varepsilon N_{p,\mathrm{BW}} \boldsymbol{p}_{e^+}}{n_{\mathrm{tot}}}, \end{aligned} \tag{6.7}$$

where $\boldsymbol{p}_{e^+}$ is the positron momentum in the LAB frame. We then produce positron particles with the particle weight and averaged momentum in the simulation per time step, which were located initially at the center of the grid.

We also have implemented the BH process. Here, the numerical particles of positrons are produced in the same manner with the linear BW process. We compute the cross-section of BH σ_{BH} described in Ref. [153]. Then, the number of generated positrons via collision between a radiation field with intensity $I(x, y, \theta, \phi, \varepsilon)$ and ions with density n_i is calculated as :

$$N_{p,\mathrm{BH}} = n_\gamma n_i \sigma_{\mathrm{BH}} c \Delta t. \tag{6.8}$$

We assumed that the momentum of positrons is the half of the colliding photon momentum, since the other half is taken by the electron born together. The direction of momentum is the same

with the photon :

$$\boldsymbol{p}_{e^+} = \frac{\boldsymbol{p}_\gamma}{2}. \tag{6.9}$$

The density of positrons, which create the pairs, accumulated during one time step and averaged momentum can be obtained by using Eqs. (6.7), (6.8), and (6.9) and a positron particle is produced at the center of the grid.

6.2.3 3D particle-in-cell simulation without pair creation

To confirm the robustness of the self-organized field structure observed in 2D PIC simulations, we performed a 3D PIC simulation with $n_{e0} = 2.8 n_c$. We used the PICLS PIC code without the radiation transport module to make the simulation computationally feasible. The simulation does include the electron recoil during the photon emission.

Figure 6.5 shows instantaneous profiles of the magnetic field B_y, electric field E_x, and electron density n_e. The snapshots are taken at $t = 117$ fs, which is the time of snapshots shown in Fig. 1 for the 2D PIC simulation. We confirm that the 3D simulation has a channel and field structure that is qualitatively similar to that observed in 2D. Most importantly, there is a strong positive longitudinal electric field at the leading edge of the laser pulse. It moves forward with a velocity close to $0.8c$, which is the propagation velocity in 2D. The laser depletion length is similar to that in the 2D simulation as well ($\sim 70\,\mu$m).

6.2.4 Comparison with the Bethe-Heitler process

In addition to the linear BW process, there are two other processes that can generate electron-positron pairs from gamma-rays: the nonlinear BW process and the Bethe-Heitler (BH) process. In the nonlinear BW process, backward moving photons shown in Fig. 6.2 collide with optical photons representing the laser. The yield is extremely low for our laser intensity and gamma-ray energies, which means that the linear BW process dominates over the nonlinear BW process [104]. To assess the role of the BH process, we performed a simulation with an additional module that generates pairs using the BH cross-section [153].

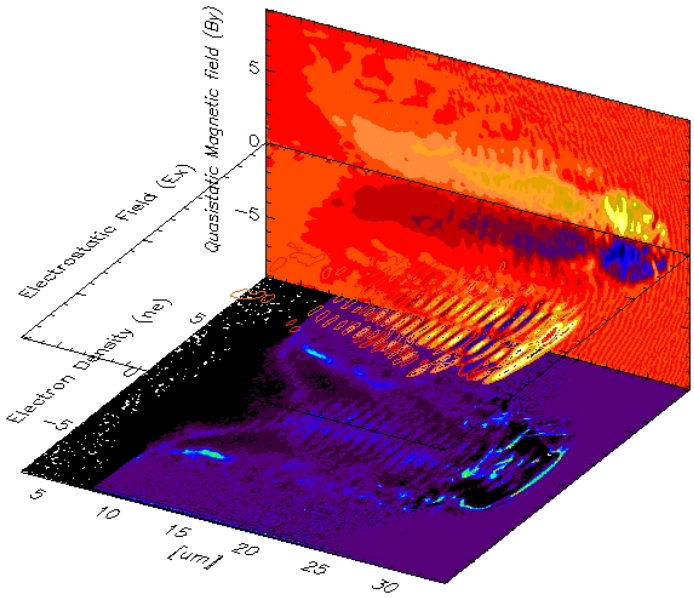

Figure 6.5. 3D PIC simulation of the laser-plasma interaction with parameters the same as those in the 2D PIC simulation of Fig. 6.1. The vertical slice is a snapshot of B_y, whereas the horizontal slices are snapshots of E_x and n_e. All three snapshots are taken at $t = 117$ fs (same snapshot time with Fig. 1(a)-(e)). The contour levels are set for B_y as $-30 \leq B_y(b_y) \leq +30$, E_x as $-30 \leq E_x(a_x) \leq +30$, and n_e as $0 \leq n_e(n_c) \leq 8$, respectively.

Figure 6.3(e) shows positron energy spectra at $t = 317$ fs, where we distinguish four groups of positrons based on the direction of their longitudinal motion and the process that created them. The spectra of the backward-moving linear BW and BH positrons have similar shapes, but the number of BH positrons is three orders of magnitude smaller. The spectra of the forward-moving positrons differ. The linear BW spectrum dominates for energies above 10 MeV. In the 'low-energy' range between 3 and 10 MeV, the spectrum of the BH positrons has an elevated plateau such that the number of BH positrons in this range becomes non-negligible compared to the number of linear BW positrons. The BH positrons were produced mostly outside of the laser beam and thus have not experienced acceleration. Figure 6.3(e) also shows that the positron cutoff energy exceeds the electron cutoff energy by a factor of three, emphasizing the importance of the longitudinal positron acceleration.

Dynamics of linear Breit-Wheeler positrons produced inside laser irradiated plasmas

In this chapter, we investigate dynamics of positrons in the two setups proposed in this dissertation. Enabled by a new implementation of the linear BW proces into the PIC code Epoch, we study the dynamics of positrons in these systems both 2D and 3D PIC simulations.

7.1 Numerical implementation of the linear BW process into Epoch

In Chapter VI, a numerical implementation of the linear BW process was done on the PIC code PICLS. PICLS uses a module where photon emission by electrons are treated as deterministic continuous radiation. Such photon emission module, although being fully effective, is different those usually implemented to PIC codes for ultra-intense laser-plasma interactions. Moreover, the photon emission module in PICLS is computationally expensive in 3D simulation for the regime of our systems. Finally, unlike the nonlinear BW process or the BH process, the linear BW pair creation inside laser irradiated plasmas is relatively unstudied prior to our work. Therefore, there are few results with which we could benchmark our work. For these reasons, we decided to also implemented the linear BW process into the PIC code Epoch. Epoch uses a photon emission module (discrete and stochastic semi-classical module) different from the one in PICLS, which makes 3D simulations of the systems we study feasible. We also benchmarked the linear BW pair yields given by the three implementations we have (post-processing algorithm detailed in Chapter V, implementation into PICLS as described in Chapter VI, and implementation into

Epoch described in this section), and we found they agree with each other.

In Epoch, photons emitted by electrons are treated as individual macro-particles with weight (w), momentum ($\vec{p}$), and positron ($\vec{r}$). The recoil on electrons when they emit photons is calculated for the emission of photons of all energies. The maximum energy of photons produced in our systems is approximately less than 1 GeV and the threshold for linear BW pair creation is $\varepsilon_\gamma \varepsilon_\gamma > (mc^2)^2 \approx (0.5\text{MeV})^2$. Furthermore, our previous studies also show that most of the linear BW positrons are produced by photons approximately within the range of tens of keV to hundreds of MeV. So, in the simulations discussed in this chapter, we only create photon macro-particles whose energy reach the keV range. A typical value we use for such cutoff energy is 1 keV.

From our studies presented in previous chapters, we found that the total linear BW pair yields in our systems are typically no greater than the order of 10^9. This number is very small compared to the number of other charged particles in our systems. Therefore, the influence of the produced electrons and positrons on the collective plasma fields is negligible. Because the purpose of our research is to examine dynamics of the produced positrons in our systems, to reduce memory usage, we only create macro-particles for the produced positrons in our simulation. Moreover, to avoid numerical instabilities caused by changing local charge density in the simulation, we set these positron macro-particles as tracer particles, which means they do not contribute to the collective plasma fields. They will only passively move in simulations according to the background fields, with the synchrotron emission of photons by these positrons taken into account in the simulation.

A schematics of our implementation is shown in Algorithm (2). In our implementation, at each time step of the simulation, we first check photon density in each simulation cell. To save memory usage, we proceed in each cell only if photon density in this cell is greater than the classical critical density n_c. This is justified by the scaling of the pair yields n_{pairs} on the photon density n_γ: $n_{\text{pairs}} \propto n_\gamma^2$. Next, suppose there are N (pair creation is calculated only if $N \geq 2$) photon macro-particles in this cell at this time step, in principle, there will be $N(N-1)/2$ binary

Algorithm 2: Linear BW pair creation in EPOCH

```
/* Main loop of the PIC simulation with N_t total time steps     */
for t ← 1 to N_t do
    /* Loop over simulation cell with N_x, N_y, and N_z cells in each
       dimension                                                  */
    for i_x ← 1 to N_x do
        for i_y ← 1 to N_y do
            for i_z ← 1 to N_z do
                /* Check photon density n_γ and number of photon
                   macro-particles N                              */
                if n_γ > n_c & N ≥ 2 then
                    Randomly pick two out of these N photon macro-particles;
                    /* Check picked photons satisfies momentum threshold
                       (Eq. (5.9))                                */
                    if Momentum threshold then
                        Compute N_yield according to Eq. (7.1);
                        Compute positron momentum p⃗_e;
                        Create a tracer positron macro-particle with weight
                         N_yield * N(N−1)/2 and momentum p⃗_e located at the
                         mid-point of the two photon macro-particles;
                    end
                end
            end
        end
    end
end
```

pairings of these N particles. As each of these $N(N-1)/2$ pairings will create positrons with momentum different from each other, in principle, $N(N-1)/2$ positron macro-particles need to be produced. To save memory usage, we adapt the idea of random pairing method which is widely used in simulating binary collisional process in PIC codes. We randomly select two out of the N photon macro-particles. If their momentum does not satisfy the condition on the momentum threshold for the linear BW pair creation (shown in Eq. (5.1)), we assume there is no pair creation happening in this cell for this time step. If the condition is satisfied, we compute the pair yields N_{yield} by these two photon macro-particles. We then create a positron macro-particle with weight $N_{\text{yield}} * N(N-1)/2$ as an estimation to account for the pair creation from other

binary pairs of photon macro-particles in the cell.

The value of N_{yield} which is the number of linear BW pairs produced by two photon macro-particles is calculated by the formula:

$$N_{\text{yield}} = \kappa \cdot \sigma_{\gamma\gamma} \cdot w_{\gamma 1} \cdot w_{\gamma 2} \cdot \frac{c\Delta t}{V_{\text{cell}}}. \tag{7.1}$$

In this equation, $\kappa := 1 - \cos(\varphi)$ is the kinematic factor for the angle between the two photons being φ (same as defined in Eq. (5.14)), $\sigma_{\gamma\gamma}$ is the cross section for the linear BW process calculated from the momentum of the two photons as defined in Eq. (5.9), $w_{\gamma 1}$ and $w_{\gamma 2}$ are the weights of the two photon macro-particles, Δt is the time step of the PIC simulation, and V_{cell} is the volume of the cell of the PIC simulation.

Momentum of the produced positron $\vec{p}_e$ is determined in the following way. Suppose θ_p is the angle between the colliding photons, $\varepsilon_{\gamma 1}$ and $\varepsilon_{\gamma 2}$ are energy of photon macro-particles in the lab frame, and $\vec{p}_{\gamma 1}$ and $\vec{p}_{\gamma 2}$ are their momenta in the lab frame. We first compute energy $\varepsilon_{e,cm}$ and magnitude of the momentum of the produced positron $|\vec{p}_{e,cm}|$ in the center of mass frame of the colliding photons:

$$\varepsilon_{e,cm} = \sqrt{\frac{\varepsilon_{\gamma 1}\varepsilon_{\gamma 2}(1 - cos(\theta_p))}{2}}, \tag{7.2}$$

$$|\vec{p}_{e,cm}| = \sqrt{\frac{\varepsilon_{\gamma 1}\varepsilon_{\gamma 2}(1 - cos(\theta_p))}{2c^2} - m_e^2 c^2}, \tag{7.3}$$

The angular distribution of $\vec{p}_{e,cm}$ in center of mass frame is assumed to be isotropic by the following procedure. We first generate two random variables (u, v) each with uniform distribution on the interval $(0, 1)$. Then we define spherical coordinates (θ, ϕ) by:

$$\theta = 2\pi u, \tag{7.4}$$

$$\phi = cos^{-1}(2v - 1), \tag{7.5}$$

where $\theta \in (0, 2\pi)$ is the azimuthal angle, and $\phi \in (0, \pi)$ is the polar angle. By defining θ and ϕ) this way, we ensure the random angle we assign to $\vec{p}_{e,cm}$ has a uniform distribution on the surface of a unit sphere. We can then define $\vec{p}_{e,cm}$ by:

$$\vec{p}_{e,cm} = |\vec{p}_{e,cm}| * (sin\phi cos\theta\, \hat{\boldsymbol{x}} + sin\phi sin\theta\, \hat{\boldsymbol{y}} + cos\phi\, \hat{\boldsymbol{z}}). \tag{7.6}$$

Finally, $\vec{p}_e$ is calculated by transforming the four vector $(\varepsilon_{e,cm}, \vec{p}_{e,cm})$ in the center of mass frame to the lab frame with respect to the velocity

$$\vec{v} = -c * \frac{\vec{p}_{\gamma 1} + \vec{p}_{\gamma 2}}{\varepsilon_{\gamma 1} + \varepsilon_{\gamma 2}}. \tag{7.7}$$

After the momentum of the produced positron $\vec{p}_e$ is calculated, we create a positron with momentum $\vec{p}_e$ and weight $N_{\text{yield}} * N(N-1)/2$ at the mid-point of the positrons of the two selected photons. This pair creation process is then repeated inside each cell at every simulation time step.

7.2 Longitudinal acceleration of positrons by a single laser pulse

In Chapter VI, we discussed acceleration of linear BW positrons by the longitudinal electric field co-propagating with the laser pulse created by charge separation in the laser front. In this section, we examine the dynamics of these positrons, with the focus on the dynamics of individual positron particles.

We first confirmed that forward-moving energetic positrons we saw in Chapter VI are indeed accelerated by the longitudinal electric field. We performed PIC simulation with the same parameters used in Chapter VI (with initial target density being $2.8n_c$). We randomly selected 15 positrons in our simulation who are accelerated to near GeV level. Figure 7.1 shows the trajectories of these positrons as well as their position with respect to the longitudinal electric

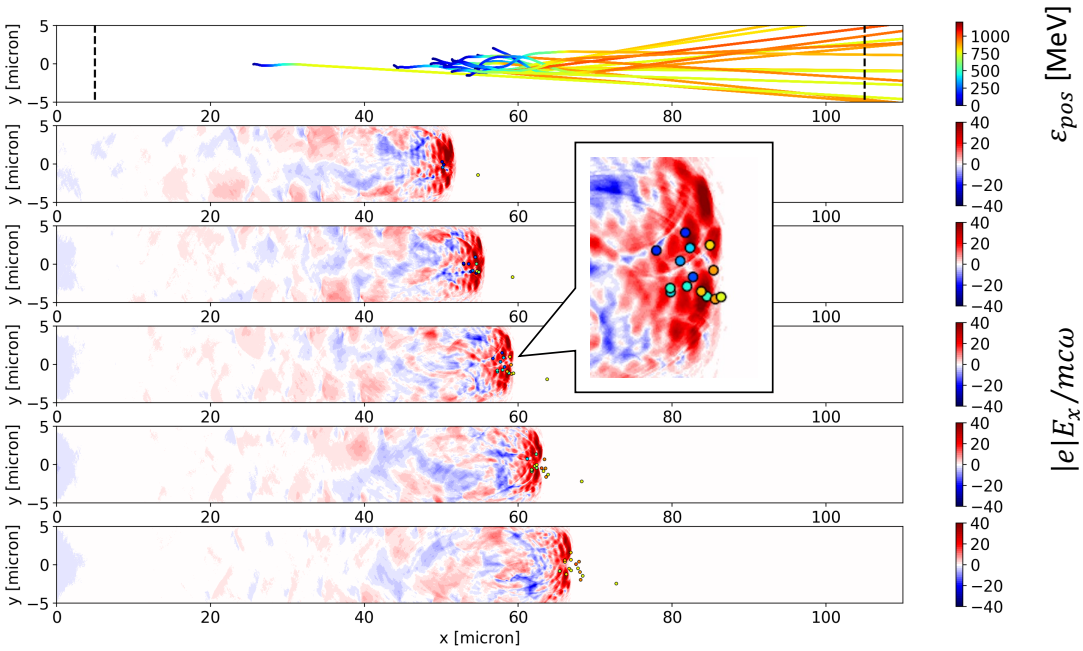

Figure 7.1. Positron generation and acceleration simulated by EPOCH. Upper panel: trajectories of 15 randomly selected positrons produced via the linear BW process who are accelerated to high energies. Bottom four panels: longitudinal electric field and positron positions at four different times. The color of each marker represents the positron energy.

fields E_x in the simulation. From this figure, we confirm that they are in the region of the co-propagating electric field in the laser front during their acceleration to GeV energy level. Figure 7.2 shows the work done on these 15 positrons by the longitudinal (W_x) and transverse (W_y) electric fields in the simulation. Figure 7.2 further confirms that these positrons are mainly accelerated by the longitudinal electric fields (in our case, the co-propagating charge-separation electric fields), rather than the transverse laser fields.

From Figure 7.2, we see that the transverse fields can do work on these positrons shortly after they are produced. However, as these positrons gain longitudinal momentum from the co-propagating longitudinal fields, eventually they enter the regime of $p_x \gg p_y$, where p_x and p_y are their momentum in x and y. In this regime, the velocity vector of these positrons are predominantly along the longitudinal direction x, which causes strong cancellation between the acceleration by the laser electric and magnetic fields. As a result, the acceleration of these positrons are primarily along the longitudinal direction, causing them to continuously gain

longitudinal momentum. The trajectories of these positrons thus stay approximately linear, while the azimuthal plasma magnetic fields slowly deflect these positrons transversely outward as shown in Figure 7.1.

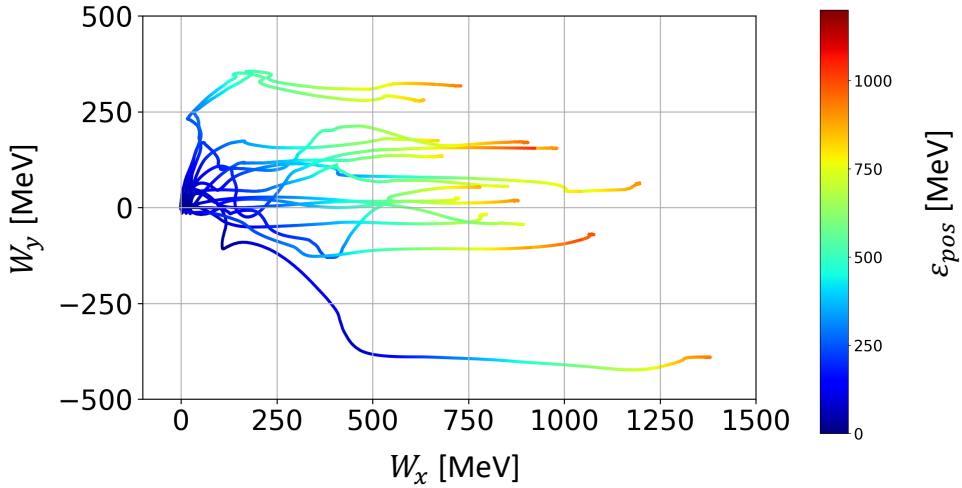

Figure 7.2. Energy gain (color) for the positrons shown in Fig. 7.1, with the horizontal axis showing the contribution from E_x and the vertical axis showing the contribution from E_y.

7.3 3D results of the a single laser setup

Our new implementation discussed in Sec. 7.1 also allows us to simulate our systems in 3D. We checked the linear BW pair yields in same system presented in Chapter VI (with initial target density being $2.8n_c$) in 3D simulation. As a process of binary collision of photons, the linear BW pair yields depend heavily on the density of colliding photons. Therefore, one might expect the pair yields in 3D to be significantly reduced compared to the yields in 2D simulations. However, in our simulations, we observed that the laser self-focusing inside the plasma in 3D simulation is much stronger than the one in 2D simulation. Figure 7.3 (a,d) shows the amplitude of the laser fields after propagating for the same distance into the plasma in 2D and 3D simulations. After propagating in the plasma for approximately 25 microns, the peak amplitude of the laser pulse increases from $a_0 = 120$ (the peak normalized laser amplitude in vacuum) to $a_0 \approx 200$ in 2D simulation, and to $a_0 \approx 300$ in 3D simulation. This is because

while the laser pulse is self-focused along the two transverse dimensions, which is accurately simulated in 3D simulation, 2D simulation can only account for the self-focusing of the laser pulse from the only transverse dimension (in our simulation setup, y). This can be seen from the ratio of the peak laser amplitudes after self-focusing over the peak amplitudes in vacuum. Our simulations show that this ratio in 3D is approximately equal to square of this ratio in 2D: $(200/120)^2 \approx (300/120)$.

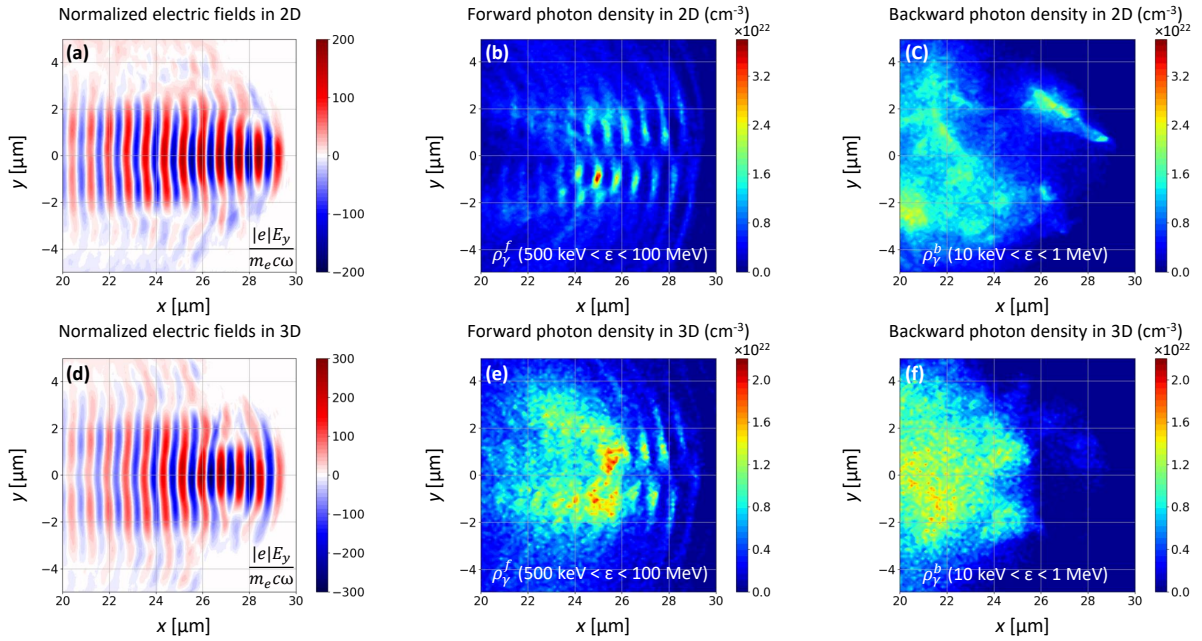

Figure 7.3. Comparison of instantaneous laser amplitude and densities of backward-moving and forward-moving photon populations between 2D and 3D PIC simulations. All snapshots are taken at $t = 117$ fs where laser peak amplitude in vacuum reaches target boundary at $t = 0$. (d) E_y on the plane $z = 0$. Density for backward-moving photons are for those with energy greater than 10 keV and less than 1 MeV. Density for forward-moving photons are for those with energy greater than 0.5 MeV and less than 100 MeV. Photon densities for 3D simulation are averaged over a 2 μm slice ($|z| < 1$ μm).

Figure 7.3 shows that, as expected, densities of both forward-moving and backward-moving photons in 3D simulation are less than these densities in 2D simulation. However, due to the enhanced self-focusing of the laser pulse, both photon densities in 3D simulation are approximately of the same orders of magnitude ($\sim 10^{22}$ cm^{-3}) with the photon densities in 2D

simulation. As a result, the linear BW pair yield calculated from our 3D simulation is 2.6×10^6, which is only about 4 times smaller than the pair yields in 2D simulation (1×10^7).

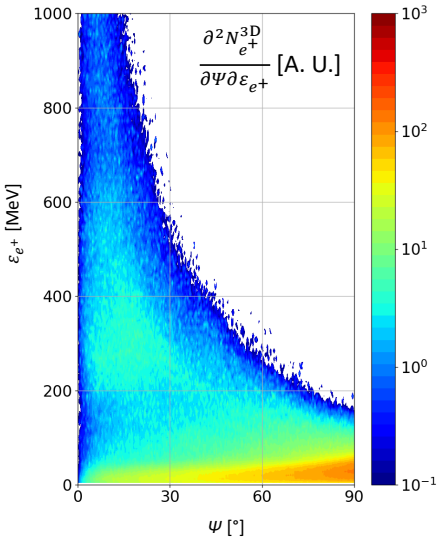

Figure 7.4. Angle-energy spectrum $\partial^2 N_{e^+}^{3D}/\partial\psi\partial\varepsilon_{e^+}$ [A. U.] of the linear BW positrons in 3D PIC simulation. Here, ψ is the polar angle to the axis of laser propagation, x.

Lastly, the angle-energy spectrum of the linear BW positrons in the 3D simulation is shown in Figure 7.4, which confirms the acceleration of the produced positrons in our setup observed from 2D simulations.

7.4 Sideways acceleration of positrons in the single pulse setup

The longitudinally accelerated positrons discussed in Chapter VI and Sec. 7.2 and Sec. 7.3 co-propagate with the longitudinal electric field and the laser pulse. Therefore, they can stay inside the PIC simulation box for a extended amount of time. During our study of this population of energetic positrons, positrons who leave the simulation box are generally neglected. However, as the azimuthal plasma magnetic fields (shown in, e.g., Figure 3.1(c), Figure 6.1(c), and Figure 7.10(a)) generated by the laser-accelerated electron current are with the orientation which

will deflect positrons outward, one may wonder whether there were positrons who do not interact with the co-propagating electric fields leaving the plasma channel and the simulation box from transverse directions.

In this section, we give an affirmative answer to this postulation. The same 2D PIC simulation with those in Chapter VI for $n_e = 2.8n_c$ (which is also the same simulation as in Sec. 7.2 and Sec. 7.3) is run. In this simulation, we record information of positrons who leave the simulation box. We then calculate the angle-energy spectrum of linear BW positrons in the simulation box at the end of the simulation alone with positrons who have left the simulation box. The result in shown in Figure 7.5. By including both of these positrons, Figure 7.5 covers all of the produced positrons in our system.

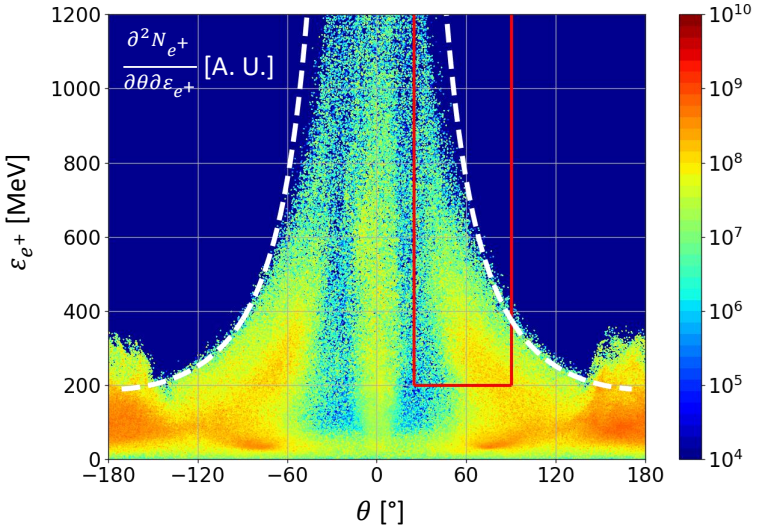

Figure 7.5. Angle-energy distribution $\partial^2 N_{e^+}/\partial\theta\partial\varepsilon_{e^+}$ of positron in the single pulse setup including positrons leaving the simulation box. The white dashed lines are the upper bounds of the angle of sideways-moving positrons defined in Eq. (7.21) with $\langle\widetilde{B}_z\rangle_{max} = 20$ and $R = 6\lambda$. The red rectangular box is defined by $25^\circ < \theta < 90^\circ$ and $\varepsilon_{e^+} > 200$ MeV.

From Figure 7.5, we see the central spike around the angle range $-25^\circ \lesssim \theta \lesssim 25^\circ$ which corresponds to the longitudinally accelerated positrons discussed previously. Besides this central spike, we also observe two extra spikes on the left and right sides of the central spike. These

are the positrons who are not able to enter the region of the co-propagating longitudinal electric field, thus are deflected transversely outward by the azimuthal plasma magnetic fields. Figure 7.6 shows trajectories of 20 randomly selected positrons from these two side spikes. From this figure we see that these positrons started to be deflected transversely outward almost immediately after their production, quickly leaving the plasma channel and the simulation. This is the reason why the existence of these sideways-moving positrons was not noticed in our previously studies, for only positrons inside the simulation box were analyzed.

.

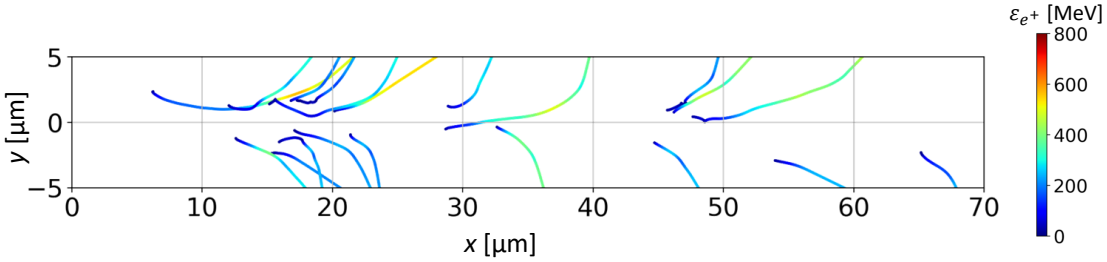

Figure 7.6. Characteristic trajectories of sideways-moving positrons in PIC simulation. 20 positrons are randomly selected from positrons with final energy greater than 200 MeV and final angle θ in the range $25^\circ < |\theta| < 90^\circ$.

7.4.1 Absence of the interaction with co-propagating longitudinal fields

Before examining the dynamics of these positrons, we first need to clarify what background fields they experience. Specifically, we would like to confirm that these positrons do not interact with the co-propagating electric fields. One thing we can quickly check is to make a histogram of these positrons on the instantaneous longitudinal electric field they experience. The result is shown in Figure 7.7. Here, we first take a snapshot of the longitudinal electric field E_x and plot it in Figure 7.7(b) when the laser pulse propagates 30μm into the plasma. From this figure we see that the strength of the co-propagating longitudinal field in the laser front is approximately $|e|E_x/m_e c\omega \approx 40$. We then record the longitudinal electric fields experienced

by positrons at this time snap. Figure 7.7(a) shows the number of positrons as a function of longitudinal electric fields they experience. Here we plot two distributions, with one for all of the positrons in the simulation box and the other one only for positrons who are sideways-moving. The definition of being sideways-moving is to be inside the red rectangle in Figure 7.5 defined by $25^\circ < \theta < 90^\circ$ and $\varepsilon_{e^+} > 200$ MeV. The comparison between the red and black curves in Figure 7.7(a) near the range of $|e|E_x/m_e c\omega \approx 40$ suggests that sideways positrons do not interact with the co-propagating longitudinal fields.

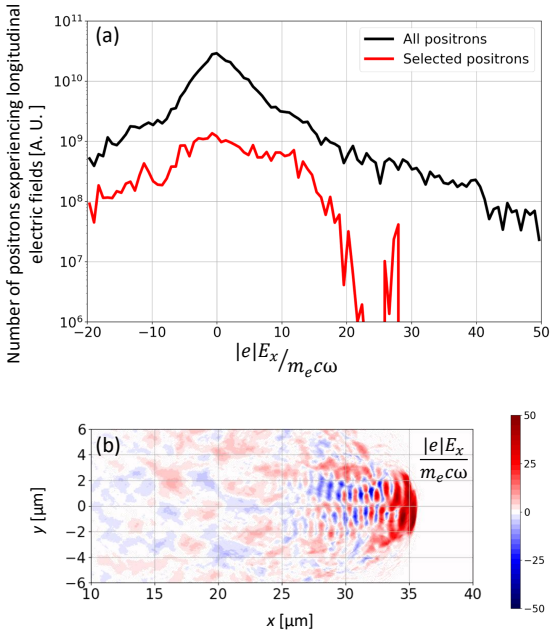

Figure 7.7. (a) Distribution of positrons with respect to the instantaneous normalized longitudinal fields $eE_x/m_e c\omega$ they experience at the same time snap with panel (b). The black curve is for all positrons in the simulation box, and the red curve is for positrons inside the red rectangular box of Figure 7.5. (b) Spatial distribution of the normalized longitudinal electric fields $eE_x/m_e c\omega$ as the laser pulse travels 30μm into the plasma.

We can further confirm this by examining their integral of motion. Assuming the laser pulse is a plane wave with phase ξ, the azimuthal magnetic fields are generated by uniform longitudinal current density, and the strength E_s of the co-propagating longitudinal electric field

is a constant. It is easy to check that a positron in such a system has the integral of motion:

$$\frac{d}{dt}(\gamma - p_x/m_e c - \pi\alpha(\frac{y}{\lambda})^2 - a_s\xi) = 0, \tag{7.8}$$

where γ and p_x are the Lorentz factor and longitudinal momentum of the positron, α is a factor quantifying the strength of the azimuthal magnetic fields, λ is the laser wavelength, and $a_s := eE_s/m_e c\omega$ is the normalized longitudinal field. The cross-section of the linear BW process peaks at around $\varepsilon_{\gamma 1}\varepsilon_{\gamma 2} \approx [0.7\ \text{MeV}]^2$ for head-on collisions. Therefore, we estimate the initial condition of positrons in our system by

$$\gamma - p_x/m_e c \approx 1. \tag{7.9}$$

On the other hand, positrons gain relativistic energies by interacting with the strong fields in the plasma channel. By the time they leave the plasma channel, we have

$$\gamma - p_x/m_e c \approx p_y/m_e c, \tag{7.10}$$

where p_y is the y component of the positron momentum. Plugging Eq. (7.9) and (7.10) into the integral of motion (7.8), we obtain

$$\frac{p_y^{final}}{mc} = \pi\alpha(\frac{y^{final}}{\lambda})^2 + 1 - \pi\alpha(\frac{y^{initial}}{\lambda})^2 - \Delta(a_s\xi), \tag{7.11}$$

where p_y^{final} is the final transverse momentum p_y, $y^{initial}$ and y^{final} are the initial and final transverse position y, and $\Delta(a_s\xi)$ is the change of the term $a_s\xi$. Because the strong fields in our system only exists inside the plasma channel expelled by the propagation of the laser pulse, positron momentum are not expected to change after positrons leave the channel. Therefore,

y_{final} in Eq. (7.11) can be replaced by the radius R of the channel:

$$\frac{p_y^{final}}{mc} = \pi\alpha(\frac{R}{\lambda})^2 + 1 - \pi\alpha(\frac{y^{initial}}{\lambda})^2 - \Delta(a_s\xi). \tag{7.12}$$

The important conclusion we would like to make is that in Eq. (7.12), in the case of $a_s = 0$ which means positrons do not interact with the co-propagating longitudinal field, the final transverse momentum p_y^{final} depends only on the initial transverse coordinate $y^{initial}$:

$$\frac{p_y^{final}}{mc} = \frac{p_y^{final}(y^{initial})}{mc} = \pi\alpha(\frac{R}{\lambda})^2 + 1 - \pi\alpha(\frac{y^{initial}}{\lambda})^2. \tag{7.13}$$

We then check whether this is the case in the simulation by calculating the distribution of the sideways positrons as a function of p_y^{final} and $y^{initial}$. In comparison, we have also calculated the same distribution for positrons who are longitudinally accelerated. The result is shown in Figure 7.8. In this figure, we have estimated the upper and lower bounds of p_y^{final} for each value of $y^{initial}$ using white dashed lines. This is because as the channel continue expanding after the passing of the laser pulse, both the radius R and the radial gradient of the azimuthal magnetic fields (thus α) are not fixed. Figure 7.8(a) shows that p_y^{final} of the sideways-moving positrons are overall within the two bounds, and the distribution captures the trends of the two bounds. This shows that sideways positrons satisfy Eq. (7.13). In contrast, from Figure 7.8(b) we can see that longitudinally accelerated positrons are overall not inside the two dashed lines predicted by Eq. (7.13). This is because the co-propagating longitudinal fields contributes to the integral of motion, therefore the $\Delta(a_s\xi)$ term in Eq. (7.12) is not zero. We thus conclude that these sideways-moving positrons do not interact with the co-propagating longitudinal electric fields in our system.

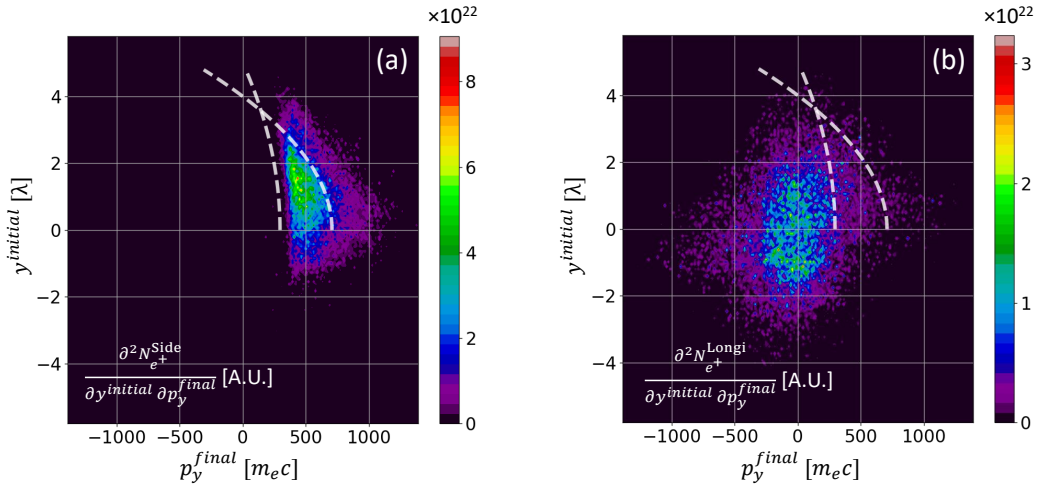

Figure 7.8. Distribution of positrons as a function of their initial transverse coordinate $y^{initial}$ and final transverse momentum p_y^{final}. (a) For sideways-moving positrons $\partial^2 N_{e^+}^{\text{Side}}/\partial y^{initial}\partial p_y^{final}$. (b) For longitudinally accelerated positrons $\partial^2 N_{e^+}^{\text{Longi}}/\partial y^{initial}\partial p_y^{final}$. The sideways positrons are those in the red rectangular box in Figure 7.5. The longitudinally accelerated positrons are those with final angle $|\theta| < 25^\circ$ and final energy $\varepsilon_{e^+} > 250$ MeV. The white dashed line on both panels on the left is for $R = 5\lambda$ and $\alpha = 2.4$. The white dashed line on both panels on the right is for $R = 4\lambda$ and $\alpha = 9$.

7.4.2 Upper bound on energy and angle of positrons

We first give an rough upper bound on the energy gain of the sideways-moving positrons. Taking the derivative of positrons' Lorentz factor:

$$\frac{d\gamma}{dt} = \frac{e}{m_e c^2} * \left[v_x E_x + v_y E_y\right], \tag{7.14}$$

where v_x and v_y are the x and y components of the velocity, and E_x and E_y are the x and y components of the electric fields. In Sec. 7.4.1, we confirmed that sideways positrons do not experience the co-propagating electric fields. Therefore their energy gain is expected to be from E_y by doing transverse displacement:

$$\Delta\gamma \approx 2\pi \int a_y \, d\left(\frac{y}{\lambda}\right), \tag{7.15}$$

where $a_y = e|E_y|/m_e c\omega$ is the normalized electric fields in y, and λ is the laser wavelength. We then approximate the transverse profile of the laser pulse as a cos function: $a_y = a * \cos(\pi y/2R) * \cos(\xi)$ for some peak amplitude a, channel radius R, and laser phase ξ. In our system, as a positron move transversely outward, the term for the transverse profile of the laser profile $\cos(\pi y/2R)$ decreases. So, the ideal case for the energy gain of sideways-moving positrons is that when $|y|$ is small, the phase ξ is around 0 so that $\cos(\xi) \approx 1$. In this case, the positron experience efficient energy gain while the laser profile $\cos(\pi y/2R)$ is at largest. In this case, the impact of the fields when $|y|$ is large will have a relatively minor contribution to $\Delta\gamma$. We thus estimate the upper bound for the energy gain as

$$\Delta\gamma \lesssim 2\pi \int_0^R a * \cos(\pi y/2R)\, d\left(\frac{y}{\lambda}\right) = 4a * \left(\frac{R}{\lambda}\right). \tag{7.16}$$

For values we observe from the simulation where $a \approx 150$ (after self-focusing) and $R \approx 5\lambda$, we obtain the upper bound for sideways-moving positrons being

$$\Delta\gamma \lesssim 3000. \tag{7.17}$$

This upper bound is slightly larger than what we see from our simulation, but this is expected because here $\xi = 0$ is assumed throughout the positron motion.

We can also estimate the upper bound for the angle of these sideways-moving positrons for a given final energy. The angle θ of a positron is affected by the laser fields (E_y^{laser} and B_z^{laser}) and the azimuthal plasma magnetic fields ($\langle B_z \rangle$) of our system:

$$\frac{d\theta}{dt} = \frac{e}{\gamma m_e c} * \left[\cos(\theta) E_y^{laser} - B_z^{laser} - \langle B_z \rangle\right]. \tag{7.18}$$

Positrons are produced with relatively small gamma factor, and are accelerated to high energy (up to hundreds of MeV) as they leave the plasma channel. Overall, these positrons are gaining energy from the laser pulse. Since when a positron is gaining energy from the laser pulse, the

laser fields are in the orientation that will confine the positron. We can therefore approximate

$$\left|\frac{d\theta}{dt}\right| \lesssim \left|\frac{e\langle B_z\rangle}{\gamma m_e c}\right|. \tag{7.19}$$

Figure 7.6 shows that sideways positrons transversely move out of the channel without significant oscillations on their trajectory. Therefore, the azimuthal plasma magnetic fields $\langle B_z\rangle$ they experience are approximately monotonically increasing. On the other hand, their gamma factor overall is also increasing as they transversely move out. We thus assume that the ratio $\langle B_z\rangle/\gamma$ is approximately a constant, and set it to equal to $\langle B_z\rangle_{max}/\gamma^{final}$, where $\langle B_z\rangle_{max}$ is the azimuthal magnetic fields at the boundary of the channel, and γ^{final} is the final Lorentz factor of the positrons. We thus have:

$$\left|\frac{d\theta}{dt}\right| \lesssim \left|\frac{e\langle B_z\rangle_{max}}{\gamma^{final} m_e c}\right|. \tag{7.20}$$

Eq. (7.20) corresponds to the physical picture that the minimum local gyro radius of the sideways positrons is $\gamma^{final} m_e c/e\langle B_z\rangle_{max}$. We therefore assume the maximum final angle θ_{max} for a positron with final energy γ^{final} to be the angle between a circle and the channel boundary $y = \pm R$ illustrated in Figure 7.9. This circle is tangent to the central axis of the channel $y = 0$, and has radius $\gamma^{final} m_e c/e\langle B_z\rangle_{max}$. Figure 7.9 illustrates such definition of θ_{max} for the upper half of the system. The definition for the lower half is analogous.

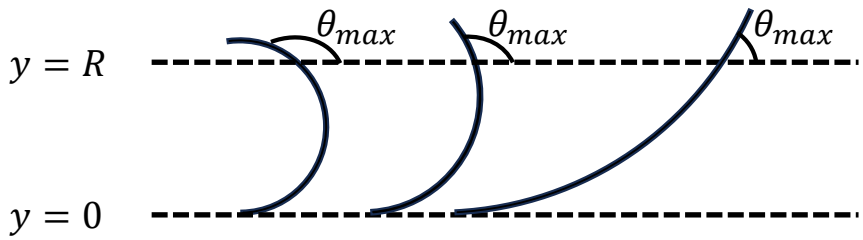

Figure 7.9. Illustration of the definition of θ_{max} for the upper half of the system. All arcs in the figure are part of circles tangent to the line $y = 0$ whose radii are $\gamma^{final} m_e c/e\langle B_z\rangle_{max}$.

Then, from pure geometric calculations, we obtain the following relation between θ_{max}

and γ^{final}:

$$\tan(\theta_{max}) = \sqrt{\frac{R}{\lambda}\cdot\frac{\gamma^{final}}{\langle\widetilde{B_z}\rangle_{max}}\cdot\frac{1}{2\pi} - (\frac{R}{\lambda})^2} \Big/ \left(\frac{R}{\lambda} - \frac{\gamma^{final}}{\langle\widetilde{B_z}\rangle_{max}}\cdot\frac{1}{2\pi}\right), \tag{7.21}$$

where $\langle\widetilde{B_z}\rangle_{max} = e\langle B_z\rangle_{max}/m_e c\omega$. Since we are estimating the upper bound for the angle, we use the value of $\langle\widetilde{B_z}\rangle_{max}$ in regions where laser pulse has past, so that we do not overestimate the deflection by $\langle\widetilde{B_z}\rangle_{max}$. Using $\langle\widetilde{B_z}\rangle_{max} = 20$ and $R = 6\lambda$, we obtain the two white dashed curves in Figure 7.5, which is in good agreement with the simulation result.

7.5 Backward acceleration of positrons in the single pulse setup

Besides the three spikes we see in the forward direction in Figure 7.5, we also observe there is a highlighted region in the backward direction of this figure in the regime $\varepsilon_{e^+} \lesssim 200$ MeV. These are the positrons who do not gain enough energy to leave the plasma channel, either by longitudinally overtaking the laser front or transversely leaving the channel, during their interaction with the laser fields. As a result, after the laser pulse has past, they are trapped inside the plasma channel by the azimuthal plasma magnetic fields $\langle B_Z\rangle$ who is illustrated in Figure 7.10(a). As the sign of the azimuthal magnetic fields flips between lower and upper half of the channel, these trapped positrons oscillate between lower and upper half of the channel, forming backward moving positron current. Figure 7.10 shows the trajectories of these backward moving positrons.

We can estimate the threshold energy above which positrons can no longer be trapped by equating the positron gyro radius to the channel radius R.

$$\frac{\gamma m_e c^2}{e\langle B_z\rangle} = R. \tag{7.22}$$

Here the magnitude of the azimuthal magnetic fields $\langle B_z\rangle$ is not a constant. We approximate its

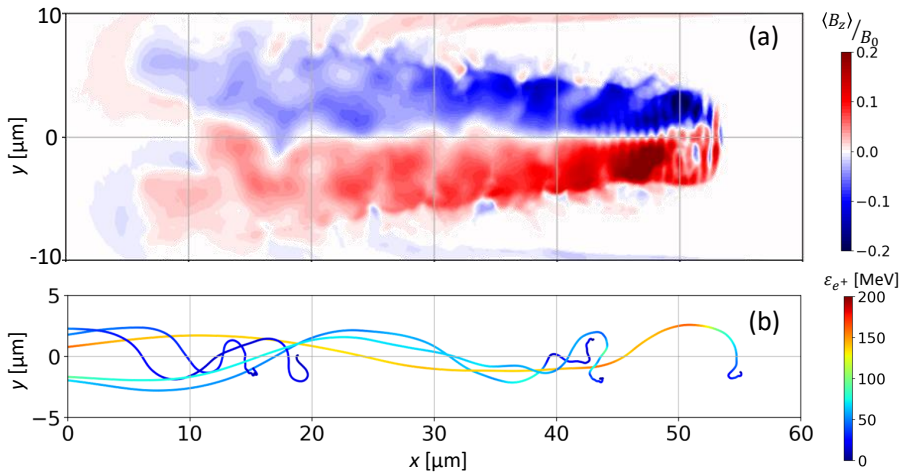

Figure 7.10. (a) Azimuthal plasma magnetic fields generated by laser driven electron current. $\langle B_Z \rangle$ is the z component of the magnetic fields averaged over 2 laser periods. B_0 is the peak laser magnetic fields in vacuum. (b) Trajectories of 5 randomly selected backward moving positrons in PIC simulation with color coding showing positron energy ε_{e^+}.

value such that $e\langle B_z \rangle / m_e c\omega \approx 12$. The approximated value set to be smaller than peak value of $\langle B_z \rangle$ from the simulation to account for the fact that $\langle B_z \rangle$ is weaker in the vicinity of the central axis of the channel. Assuming $R = 5\mu\text{m} = 6.25\lambda$, we thus get the threshold positron gamma factor γ_{th} being:

$$\gamma_{th} = 2\pi * \left(\frac{R}{\lambda}\right) * \frac{e\langle B_z \rangle}{m_e c\omega} \approx 500. \tag{7.23}$$

Comparing to Figure 7.5, our estimation for γ_{th} approximately agrees with the simulation result.

The importance of this backward moving positron population is that from our simulation, we typically observe that the majority of the produced linear BW positrons would end up backward-moving. The dominance of the backward-moving positrons is especially noticeable in the energy range in the order of $10^0 - 10^2$ MeV. Figure 7.11 shows the angular-energy distribution of backward and forward positrons within a cone of 10° around the central axis of the channel in 3D PIC simulations. Here we run a parameter scan on the laser focal spot (thus the peak intensity) and the target density shown in the figure. Parameters that are not listed in the figure are assumed

to be the same as those used in Chapter VI, Sec. 7.2, Sec. 7.3, and Sec. 7.4. From this figure, we see that the backward-moving population has the higher peak on the angle-energy distribution. Such dominance suggests that the backward-moving positrons may be less challenging to detect in experiments than other populations of positrons in the system.

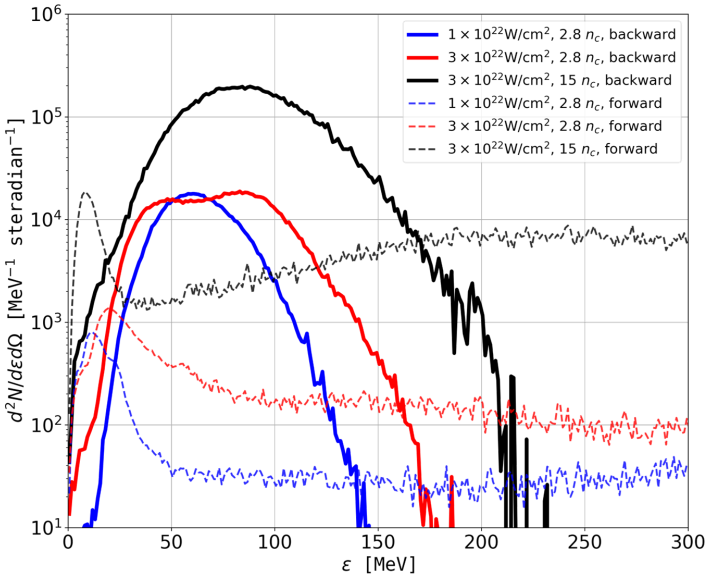

Figure 7.11. Angle-energy distribution $\partial^2 N/\partial\varepsilon_{e^+}\partial\Omega$ [MeV^{-1}steradian^{-1}] of linear BW positrons in 3D PIC simulations with different laser intensity and target density. Positrons are selected within cones of 10° opening angle around the central axis of the channel. Pulses with intensity $1 \times 10^2$2Wcm^{-2} are focused to a waist radius of 8μm, while pulses with intensity $3 \times 10^2$2Wcm^{-2} are focused to a waist radius of 4.6μm.

7.6 Direct laser acceleration of the linear BW positrons in dual pulse setup

In Chapter II, one of the surprising finding from our 2D simulations was that in the dual pulse setup, after the two pulses collide, the azithumal plasma magnetic fields would retain their polarity as the two remaining pulses propagating in the plasma channel. As a result, the polarity of the azimuthal magnetic fields with respect to each of the two pulses is reserved. We thus speculated that similar to the nonlinear BW positrons, the produced linear BW positrons

would also undergo direct laser acceleration by the remaining pulses while being confined by the azimuthal magnetic fields. This is confirmed by our PIC simulations using the same parameters as those used in Chapter II (with laser $a_0 = 190$). Figure 7.12 (a) shows trajectories of linear BW positrons who are accelerated by the remaining pulses to near GeV energies. The oscillatory feature of these trajectories clearly suggests these positrons were accelerated by the process of DLA. Figure 7.12 (b) shows the angle-energy spectrum of the linear BW positrons in the dual pulse system 104 fs after the laser collision. The two-lobe structure of Figure 7.12 (b) further confirms positrons are accelerated by the process of DLA in the system.

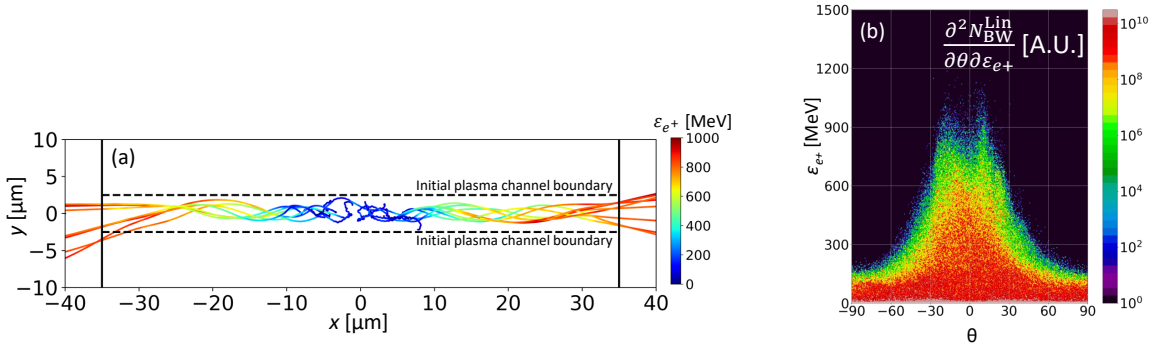

Figure 7.12. Direct laser acceleration of the linear BW positrons in the dual pulse setup in 2D PIC simulations. (a) Characteristic trajectories and energy gain of linear BW positrons accelerated by the remaining pulses. (b) Angle-energy spectrum $\partial^2 N_{BW}^{\mathrm{Lin}}/\partial\theta\partial\varepsilon_{e^+}$ [A. U.] of the linear BW positrons. Parameters for the simulation is the same as in Chapter II with $a_0 = 190$.

The retention of the azimuthal plasma magnetic fields after the laser collision in 3D PIC simulations is also confirmed. In these 3D simulations, parameters of the laser pulses are set to be the same with those of the High Power Laser System (HPLS) in ELI-NP [6], and a target similar to the one used in Chapter II is used. Details of the simualtions parameters are listed in Table. 7.1 in Appendix 7.10. Figure 7.13 shows the configuration of the plasma azimuthal magnetic fields before and after the collision of the two pulses. The most apparent feature is that the polarity of the azimuthal magnetic fields do flip after the collision of the two pulses. However, such flipping happens relatively slowly. At a fixed longitudinal position, the polarization of the azimuthal plasma magnetic fields flip after the passing of the laser pulses. Moreover, as shown

in Figure 7.13(b1), the flipping of the azimuthal magnetic fields starts from the outer ring of the channel, which leaves the polarity around the central axis of the channel where positron DLA takes place unchanged. Therefore, although the polarity of the azimuthal magnetic fields would eventually flip, produced positrons in the dual pulse setup can still be accelerated via the process of DLA. More quantitative results on such DLA of positrons in the dual pulse setup in 3D simulations are presented in Sec. 7.7.

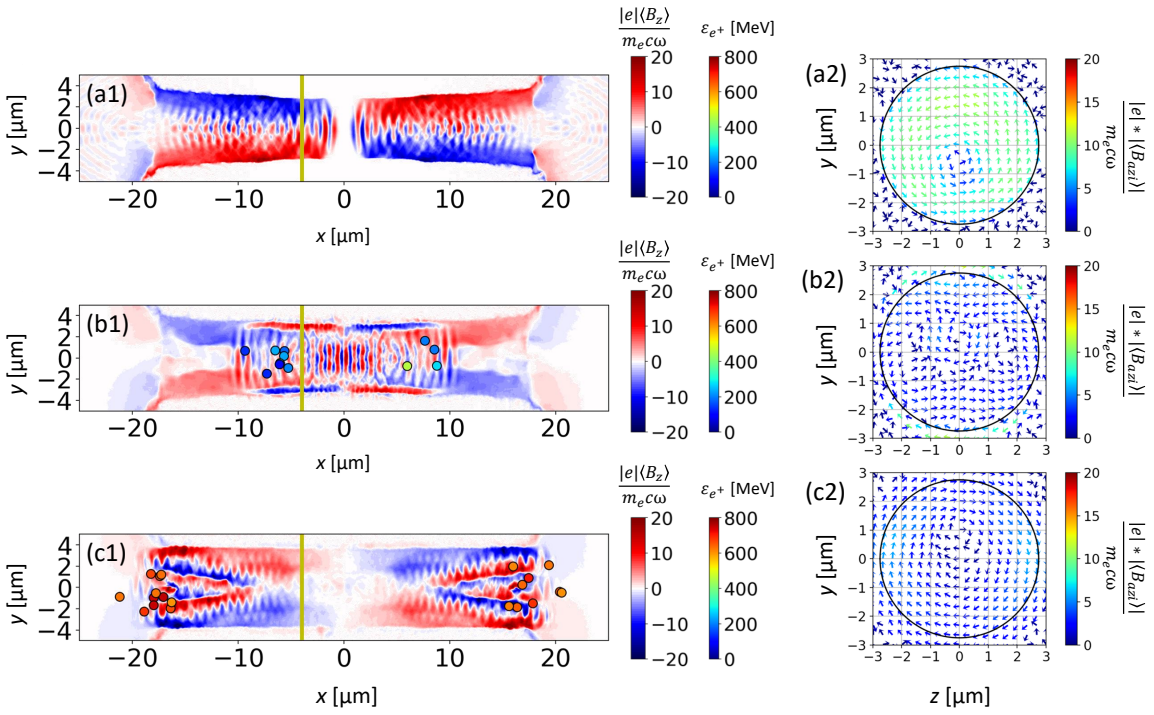

Figure 7.13. Configuration of the azimuthal plasma magnetic fields in 3D PIC simulations. (a1, b1, c1) Normalized $\langle B_z\rangle$ z at the $z=0$ plane. (a2, b2, c2) Direction and strength of $\langle B_{azi}\rangle$ at the plane $x=-4\mu$m (shown by the brown vertical line in (a1, b1, c1)). $\langle B_z\rangle$ z is the component of the magnetic fields averaged over 2 laser periods. $\langle B_{azi}\rangle$ is the azithumal component (in the $y-z$ plane) of the magnetic fields averaged over 2 laser periods. Snap shots are taken at the time of laser collision (a1, a2), 40 fs after laser collision (b1, b2), and 80 fs after laser collision (c1, c2).

Electrons in our system are accelerated by the pulses while confined by the azimuthal magnetic fields before the two pulses collide, whereas positrons in our system are accelerated by the remaining pulses while being confined by the same azimuthal magnetic fields. Although the equation of motion for the DLA of electrons and positrons are the same with fields being similar,

the uniqueness of positrons DLA is that positrons can easily possess initial conditions for DLA that are difficult to be achieved by electrons. It was suggested in previous studies [154, 155, 86] that the initial condition of the charged particle in DLA has a profound impact on the dynamics of the particle. For instance, it was shown that one of the integrals on motion which involves the particle momenta and background fields experienced by the particle could uniquely determine the energy gain of the particle by the process of DLA [86]. For electrons, they are initially approximately at rest with no background fields before the pulses arrive at the target. Although some of the electrons can be transversely injected into the pulses as suggested in [154, 155], the gamma factor associated to such injection is still relatively small. On the other hand, due to energy and momentum conservation during the pair creation processes, positrons are almost always produced with relativistic energies. Moreover, most of positrons in our system are produced at the same place and time of the overlapping of the two pulses, so the initial background fields experienced by the positrons are also expected to be very strong ($a_0 \gg 1$).

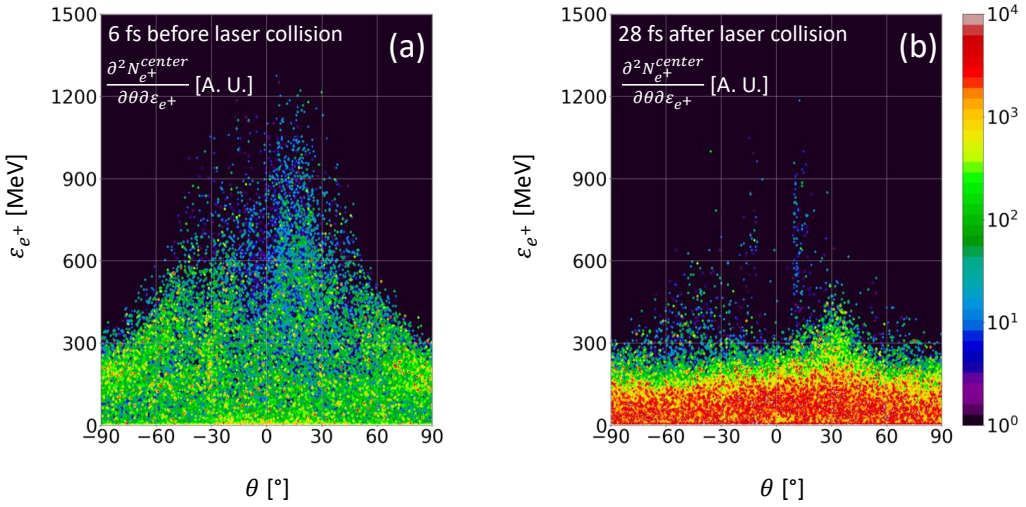

Figure 7.14. Angle-energy spectrum $\partial^2 N_{e^+}^{center}/\partial\theta\partial\varepsilon_{e^+}$ [A. U.] of the linear BW positrons inside the rectangular region defined by -10 μm $< x <$ 10μm and -5 μm $< x <$ 5μm before and after the laser collision. (a) 6 fs before laser collision. (b) 28 fs after laser collision.

In our system, such difference on the initial conditions of DLA is further enlarged by the acceleration of the positrons by the overlapping of the two pulses. Positrons started to be produced as soon as the two pulses collide, and they are continuously produced during the overlapping of the two pulses. Our simulation show that before the two pulses completely separate from each other, produced positrons are accelerated by the electromagnetic fields of the overlapping of the two pulses, forming an angularly uniform distribution of energetic positrons with energy up to a few hundreds of MeV. Figure 7.14(b) shows the angle-energy spectrum of the linear BW positrons inside the region where the two pulses collide shortly after the laser collision. From this figure we see the angularly isotropic energetic population of linear BW positrons. Figure 7.14(a) shows the same spectrum of linear BW positrons in the same region as in Figure 7.14(b) before the laser collision. Comparing the two panels of Figure 7.14, we conclude that the energetic positrons in Figure 7.14(b) are not from positrons accelerated in each of the two single pulse systems before the collision of the two pulses. We therefore confirm that energetic positrons Figure 7.14(b) are accelerated by the overlapping pulses. Such acceleration of the positrons creates initial conditions for the subsequent DLA process in a the regime of hundreds of MeV with arbitrary initial angle. These initial conditions are very challenging to be achieved by electrons in their DLA process under currently available technology. Whether the unique initial conditions for positron DLA in our system would lead to dramatic different particle dynamics is an interesting open question that is to be examined in the future.

7.7 Impact of the laser injection angle on the dual pulse setup

Most of the experimental facilities nowadays who can deliver ultra-intense laser pulses ($I \sim 10^{22}$ Wcm^{-2}, multi-PW, and $a_0 \sim 10^2$) would not allow shooting such pulses perpendicularly onto a solid surface. In this section, we benchmark our results in accordance with this experimental restriction by performing a parameter scan on the injection angle φ_{laser} of the

laser pulses with respect to the axis of the target channel in both 2D and 3D PIC simulations. Figure 7.15 shows the schematic setup of our simulations, where the angle φ_{laser} is on the polarization plane $(x-y)$ of each pulse. To be further consistent with experiments, we use laser parameters same with those of the High Power Laser System (HPLS) in ELI-NP [6]. Details of the laser and simulation parameters used in this section are listed in Table 7.2 and Table 7.3 in Appendix 7.10.

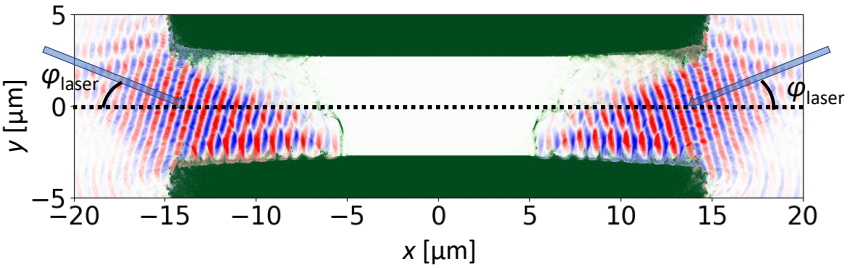

Figure 7.15. Schematic setup of the dual pulse system with laser injection angle φ_{laser}.

Figure 7.16(a) shows the pair yields by both linear and nonlinear Breit-Wheeler processes, as well as number of linear BW positrons being accelerated to above 500 MeV, in our simulations with different laser injection angle φ_{laser}. Our simulations show that as the pulses are obliquely injected into the target channel, the channel redirects their direction of propagation. The automatic redirection and alignment of the two pulses allow the system to resemble the system as if pulses were injected with no oblique angle. Therefore, the linear BW pair yields and the number of generated energetic linear BW positrons are robust to the oblique injection angle φ_{laser} of the pulses up to $\varphi_{\text{laser}} \lesssim 20°$, as shown in Figure 7.16(a). On the other hand, Figure 7.16(a) also shows the nonlinear BW pair yields are much more sensitive to φ_{laser}. This is because as a non-perturbative process, the nonlinear BW process is much more sensitive to the change on the laser amplitude and electron (thus photon) energy at the moment of the electron-laser collision in our system. The sensitivity of the nonlinear BW process to the injection angle φ_{laser} suggests that the oblique injection of laser pulses may be more than a experimental requirement. It could

potentially be utilized as a method of suppressing the nonlinear BW pair creation in our system without significantly affecting the linear BW pair yields.

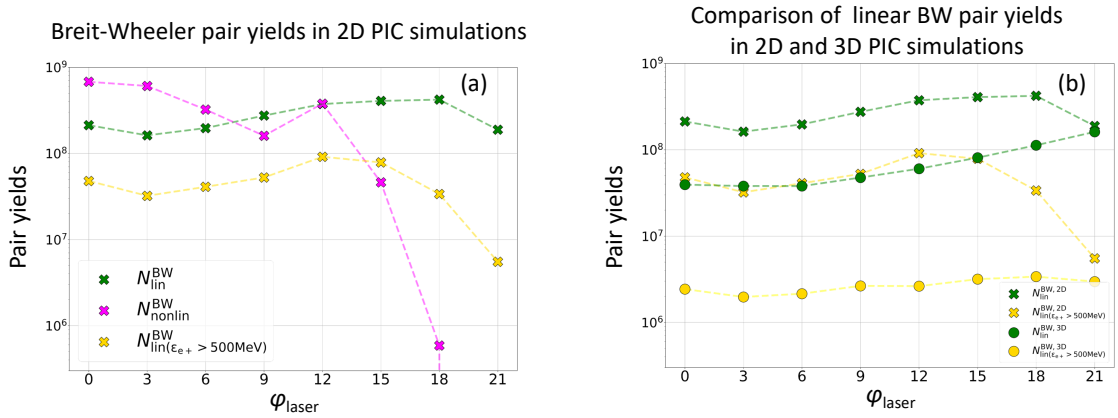

Figure 7.16. Breit-Wheeler pair yields with different laser injection angle φ_{laser}. (a) Pair yields by the linear BW (green markers) process, nonlinear BW (magenta markers) process, and the number of linear BW positrons accelerated to above 500 MeV (yellow markers). (b) Linear BW pair yields in 2D (green X markers) and 3D (green circular markers) PIC simulations. Number of linear BW positrons accelerated to above 500 MeV in 2D (yellow X markers) and 3D (yellow circular markers) simulations. Simulation parameters are listed in Table 7.2 and Table 7.3. The third dimension of 2D simulations are assumed to be 6 μm.

We also examined the impact of the oblique injection on the linear BW pair production and positron acceleration in 3D PIC simulations. Figure 7.16(b) shows the comparison on the linear BW pair yields and number of accelerated positrons between 2D and 3D simulation results. This Figure confirms that similar to 2D simulation results, both the pair yields and acceleration of positrons are robust to the injection angle φ_{laser} in 3D simulations up to $\varphi_{\text{laser}} \lesssim 20^{\circ}$. Moreover, as expected, the 3D pair yields are less than those of 2D. However, both the pair yields and the number of positrons accelerated to above 500 MeV are only about one orders of magnitude smaller than those in 2D simulations for the range of injection angle $\varphi_{\text{laser}} \lesssim 20^{\circ}$. This is because all of the key physical components (such as relativistic transparency, DLA of electron, generation of strong azimuthal magnetic fields) of our system, which are the building bricks for both the linear BW pair creation and positron acceleration, have been previously shown to exist also in 3D PIC simulations with some even in experiments [156, 157].

7.8 Summary of positron dynamics

In this section, we investigate the dynamics of linear BW positrons produced in the two setups we proposed in previous chapters.

We found that linear BW positrons in the single pulse setup can be classified into three groups: longitudinal positrons (Sec. 7.2), sideways positrons (Sec. 7.4), and backward positrons (Sec. 7.5). Longitudinal positrons are those who are accelerated by the co-propagating longitudinal electric field in the laser front. Sideways positrons are those who are accelerated by the laser fields and deflected transversely outward by the azimuthal magnetic fields. Finally, backward positrons are those who have not gained enough energy during their interaction with the laser pulse, and are thus trapped by the azimuthal magnetic fields forming backward moving positron current.

In the dual pulse setup, positrons are first heated by the fields of overlapping pulses, forming a angularly uniform population of positrons with energy up to a few hundred MeV. These positrons are then accelerated by the remaining pulses via the process of DLA after the two pulses separate, while confined by the azimuthal magnetic fields.

7.9 Acknowledgements

Chapter 7, in full, is currently being prepared for submission for publication of the material. The dissertation author was the primary investigator and author of this material.

7.10 Appendix

This appendix presents tables for the parameters of PIC simulations discussed in Sec. 7.6 and Sec. 7.7 of this chapter.

Table 7.1. Parameters of 3D PIC simulation discussed in Sec. 7.6.

Laser parameters	
Normalized field amplitude	$a_0 = 152$
Peak intensity range	$I_0 = 5 \times 10^{22}$ W/cm^2
Wavelength	$\lambda_0 = 0.8$ μm
Laser polarization	Linearly polarized in y
Focal plane of laser #1	$x = -20$
Focal plane of laser #2	$x = +20$
Laser profile (longitudinal and transverse)	Gaussian
Pulse duration (full width at half maximum for intensity)	23 fs
Focal spot size (full width at half maximum for intensity)	4.2 μm

Target parameters	
Cylindrical target diameter	11.5 μm
Target length (along x)	40 μm
Cylindrical Channel diameter	$d_{\mathrm{ch}} = 5.5$ μm
Composition	C^{+6}:$H^+ = 1:1$, and electrons
Channel density	$n_{\mathrm{e}} = 1.5 n_{\mathrm{c}}$
Bulk density	$n_{\mathrm{e}} = 30 n_{\mathrm{c}}$

Simulation parameters	
Simulation box	50 μm in x; 14 μm in y; 14 μm in z
Spatial resolution	30 cells per μm in x 30 cells per μm in y 30 cells per μm in z
Macro-particles per cell	2 for electrons 1 for carbon ions 1 for hydrogen ions

Table 7.2. Laser and target parameters for PIC simulations discussed in Sec. 7.7.

Laser parameters	
Normalized field amplitude	$a_0 = 152$
Peak intensity range	$I_0 = 5 \times 10^{22}$ W/cm^2
Wavelength	$\lambda_0 = 0.8$ μm
Laser polarization	Linearly polarized in y
Focal spot of laser #1	$x = -15$ μm; $y = z = 0$
Focal spot of laser #2	$x = +15$ μm; $y = z = 0$
Laser profile (longitudinal and transverse)	Gaussian
Pulse duration (full width at half maximum for intensity)	23 fs
Focal spot size (full width at half maximum for intensity)	4.2 μm
Plane of central axis of laser pulses	$(x-y)$ plane
Oblique angle of laser injection	$0-21$ degrees

Target parameters	
Cylindrical target diameter	11.5 μm
Target length (along x)	30 μm
Cylindrical Channel diameter	$d_{\rm ch} = 5.5$ μm
Composition	C^{+6}:$H^+ = 1:1$, and electrons
Channel density	$n_{\rm e} = 2n_{\rm c}$
Bulk density	$n_{\rm e} = 30n_{\rm c}$

Table 7.3. Parameters for the setup of simulations discussed in Sec. 7.7.

2D simulation parameters	
Simulation box	140 μm in x; 48 μm in y
Spatial resolution	40 cells per μm in x 40 cells per μm in y
Macro-particles per cell	40 for electrons 10 for carbon ions 10 for hydrogen ions

3D simulation parameters	
Simulation box	40 μm in x; 14 μm in y; 14 μm in z
Spatial resolution	30 cells per μm in x 30 cells per μm in y 30 cells per μm in z
Macro-particles per cell	2 for electrons 1 for carbon ions 1 for hydrogen ions

Summary

In this dissertation, we investigated the linear BW pair creation and dynamics of the produced positrons in ultra-intense laser-plasma interaction systems, enabled by numerical tools we developed.

We have proposed two experimental setups for the production of the linear BW pairs inside plasmas. In Chapter II, we propose the dual laser setup, and in Chapter III, we propose the single laser setup. Laser pulse(s) and targets used in both setups are currently experimentally available. The linear BW pair yields in our setups are approximately 2 to 3 orders magnitude higher than those reported in previously proposed setups. Besides proposing schemes for potentially the first experimental observation of the linear BW process using real photons, our results also suggest the non-negligibility and possible dominance (over the nonlinear BW and BH processes) of the linear BW process in ultra-intense laser-plasma systems.

In Chapter IV, we investigate the impact of the target parameters, namely target length and channel density, on the pair yields by the linear BW, nonlinear BW, and BH processes in the dual laser setup. We find that these two target parameters, which are controllable during manufacturing, can be used as control-knobs for the ratios among the three pair creation processes without changing the laser parameters.

In this dissertation, we present the three numerical tools for calculating and simulating the linear BW pair creation in the systems we studied. Chapter V presents the post-processing algorithm we developed for evaluating the linear BW yields presented in In Chapter II, Chapter III, and Chapter IV. By the time we developed this algorithm, it was the only numerical tool that was able to calculate the linear BW pair yields inside photon-emitting ultra-intense laser-plasma

interaction systems. Following the development of this algorithm and research presented in Chapter II, III, and IV, we then implemented the linear BW process into PIC codes PICLS and Epoch, in collaboration with Professor Sentoku's research group in Osaka University. These new implementations are able to simulate the produced positrons in the simulation, allowing us to investigate the dynamics of them after their creation in simulations.

We found, with the help of our newly implemented codes, that the produced positrons in the single laser setup can be divided into three major groups, and we investigated the dynamics of positrons in each of these three groups. The first group (Chapter VI and Section 7.2) includes positrons who are accelerated by the co-propagating longitudinal electric fields induced by charge separation in the laser front. These positrons form collimated positron beam in GeV energy level. The second group (Section 7.4) includes positrons transversely leaving the plasma channel due to the outward reflecting azimuthal magnetic fields. Finally, the third group (Section 7.5) includes positrons who do not gain enough energy to leave the plasma channel during their interaction with the laser fields. These positrons are then trapped inside the plasma channel by the azimuthal plasma magnetic fields, forming backward moving positron current. We found that this backward moving group has the highest positron density per unit energy per steradian among the three groups. Therefore, a potential experiment on the observation of the linear BW process in the future might consider aiming at detecting positrons that are backward-moving.

In the dual laser setup, before the collision of the two pulses, each of the two pulses resembles a system of the single laser setup until the two pulses collide which leads to much more pronounced events of the linear BW pair creation. In Section 7.6 and 7.7, we show that the produced positrons are first heated to up to a few hundred MeV by the two overlapping pulses, and then accelerated by one of the remaining pulses via DLA assisted by the confining azimuthal magnetic fields. The acceleration by the overlapping pulses enables initial conditions for the subsequent DLA process that are dramatically different from those that are typical for DLA of electrons, potentially influencing the dynamics of these positrons during DLA. Finally, results on the linear BW pair creation and positron acceleration in the dual laser setup are benchmarked

by 3D PIC simulations.

The formation of energetic positron beams in the systems we studied not only facilitates experimental detection of the produced linear BW positrons, it also shows that our setups could potentially serve as energetic positron sources in future experiments.

Appendix: review of basic physical concepts

9.1 Direct laser acceleration

The basic idea of DLA can be understood in the following simple toy model. Consider the equation of motion of an electron inside a plane wave:

$$\frac{d\vec{p}}{dt} = -|e|\vec{E} - \frac{|e|}{\gamma m_e c}\left[\vec{p}\times\vec{B}\right], \tag{9.1}$$

$$\frac{d\vec{r}}{dt} = \frac{c}{\gamma}\frac{\vec{p}}{m_e c}, \tag{9.2}$$

where $\vec{p}$ is the momentum of the electron, $\gamma = \sqrt{1+(p/m_e c)^2}$ is the Lorentz factor of the electron, m_e, e, and c are the electron mass, elementary charge, and vacuum speed of light. Here $\vec{E}$ and $\vec{B}$ are the electric and magnetic fields of the plane wave defined by:

$$\vec{E} = E_0 g(\xi)\exp\{i\xi\}\boldsymbol{e}_y, \tag{9.3}$$

$$\vec{B} = E_0 g(\xi)\exp\{i\xi\}\boldsymbol{e}_z, \tag{9.4}$$

where E_0 is the amplitude of the electric and magnetic fields, g is a function for the envelope, and $\xi = kx - \omega t$ is the phase for wavenumber k and frequency ω.

It's easy to see that this system has translational symmetry in z, so we will focus our

discussion on the $(x-y)$ plane. Defining dimensionless parameter

$$a = \frac{|e|E}{m_e c\omega} \tag{9.5}$$

being the normalized amplitude of the fields, one can check that the two integrals of motion are:

$$\frac{d}{dt}\left(\frac{p_y}{m_e c} - a\right) = 0, \tag{9.6}$$

$$\frac{d}{dt}\left(\gamma - \frac{p_x}{m_e c}\right) = 0. \tag{9.7}$$

For an electron initially at rest at $a = 0$, we have:

$$\sqrt{1+(\frac{p_x}{m_e c})^2 + a^2} - \frac{p_x}{m_e c} = 1. \tag{9.8}$$

Therefore:

$$\frac{p_x}{m_e c} = \frac{a^2}{2}, \tag{9.9}$$

$$\frac{p_y}{m_e c} = a. \tag{9.10}$$

For a wave with amplitude $a \gg 1$, we have $p_x \gg p_y$, and $\gamma \approx px/m_e c \gg 1$. Therefore, when such a wave propagates inside a plasma, it can drive a co-propagating ultra-relativistic electron beam. From here, we see in order to electron energy with $\gamma \gg 1$, a laser pulse with sufficiently high intensity ($a \gg 1$) is required.

In practice, as a laser pulse propagates inside a plasma and drives an electron current, the system is more complex than this simple model we discussed above. Multiple analytical and numerical studies have been done to investigate the impact of various factors on the electron dynamics in more realistic DLA systems. For example, factors that have significant influences on the electron dynamics include the radiation friction force on the electrons [158], the azimuthal

magnetic fields induced by the laser accelerated electrons [49], the detrimental role of the longitudinal component of the laser pulse due to its finite width, and the superluminosity [159] of the laser fields propagating inside the plasma.

9.2 Relativistic transparency

Recall the definition of critical density in the non-relativistic regime:

$$n_c = \frac{m_e \omega^2}{4\pi |e|^2}. \tag{9.11}$$

It is well known that an electromagnetic wave with frequency ω can propagate inside a plasma with density n_e only if $n_e < n_c$.

However, in the relativistic regime, due to the effective mass increase, the critical density increases by approximately a factor of γ. Therefore, the criterion for the wave to propagate inside a plasma becomes:

$$n_e \lesssim \gamma * n_c. \tag{9.12}$$

The phenomenon that an strong electromagnetic wave (such as an intense laser pulse) being able propagate inside a classically over-dense plasma is known as the relativistic transparency. In our research, this is the key to achieve high density of energetic electrons which results in high photon density for pronounced production of the linear BW pairs.

9.3 Radiation reaction

In our research, the mechanism for the emission of energetic photons for the linear BW pair production is the nonlinear inverse Compton scattering, also known as the radiation reaction or synchrotron emission.

In classical electrodynamics, according to Maxwell's equations, a moving electron will irradiate electromagnetic waves governed by the Lorentz–Abraham–Dirac equation. In the

quantum picture, this process is represented by the emission of photons by an electron as it interact with the strong background fields. The parameter characterizing this process is called the quantum nonlinearity parameter χ, defined as [95]

$$\chi = \frac{\left|F_{\mu\nu}p^{\nu}\right|}{E_s m_e c} = \frac{\gamma}{E_s} * \sqrt{[\vec{E} + \frac{1}{c}(\vec{v} \times \vec{B})]^2 - \frac{1}{c^2}(\vec{E} \cdot \vec{v})^2}, \tag{9.13}$$

where $F_{\mu\nu}$ and p^{ν} are the field tensor and four-momentum of the lepton respectively, $\vec{v}$ is the velocity vector, and $E_s = m^2c^3/e\hbar \approx 1.32 \times 10^{18}$ V/m is the Schwinger limit. For an electron moving in background electromagnetic fields, the probability P of emitting a photon over a unit amount of time approximately scales like $P \propto \chi$, and the characteristic energy ε_γ of this emitted photon approximately scales like $\varepsilon_\gamma \propto \chi$. For efficient generation of energetic photons, it is important to maximize χ of electrons.

Eq. (9.13) seems to suggest $\chi \approx \gamma|\vec{E}|/E_s$ for the fields of a laser pulse. However, for an electron being accelerated and co-propagating with a laser pulse, there is strong cancellation between the two terms $\vec{E}$ and $\vec{v}/c \times \vec{B}$ for the laser electric and magnetic fields, and $\vec{E} \cdot \vec{v}$ is also expected to be very small. In practice, as an intense laser pulse propagate inside a plasma, the primary contributor of χ of the accelerated energetic electrons are the azimuthal magnetic fields induced by the laser driven electron current. In this case, the value of χ can be estimated to be

$$\chi_{co} \approx B_{plasma} * \frac{\gamma}{E_s}, \tag{9.14}$$

where B_{plasma} is the azimuthal magnetic field generated by the laser accelerated electron beam. Typically, B_{plasma} is around 10% to 20% of the peak laser electric field E_{laser}. The emission of energetic photon beams by DLA electrons via the interaction with plasma azimuthal magnetic has been widely studied in the past decade [41].

The value of χ in Eq. (9.14) is below the order of $\gamma E_{laser}/E_s$ because of the cancellation between $\vec{E}$ and $\vec{v}/c \times \vec{B}$. for an electron who is, instead of co-propagating, counter-propagating

to the laser pulse, the flipping of the sign of $\vec{v}$ would result in the amplification of χ. In this case,

$$\chi_{counter} \approx 2E_{laser} * \frac{\gamma}{E_s}. \tag{9.15}$$

Comparing Eq. (9.15) to Eq.(9.14), we see that since $2E_{laser} \gg B_{plasma}$, we have $\chi_{counter} \gg \chi_{co}$. This means that compared to an electron co-propagating with a laser pulse, the value of χ can be greatly enhanced if the electron collides with a laser pulse. It also suggests that compared to co-propagating electrons, similar values of χ can be achieved by much less energetic electrons if these electrons were counter-propagating to a laser pulse.

Bibliography

[1] Breit G and Wheeler J A 1934 *Phys. Rev.* **46**(12) 1087–1091 URL https://link.aps.org/doi/10.1103/PhysRev.46.1087

[2] Gould R J and Schréder G 1966 *Phys. Rev. Lett.* **16**(6) 252–254 URL https://link.aps.org/doi/10.1103/PhysRevLett.16.252

[3] Burns M L and Harding A K 1984 *Astrophys. J.* **285** 747–757

[4] Zhang B and Qiao G J 1998 *Astron. Astrophys.* **338** 62–68 URL https://ui.adsabs.harvard.edu/abs/1998A&A...338...62Z

[5] Voisin G, Mottez F and Bonazzola S 2017 *Mon. Not. R. Astron. Soc.* **474** 1436–1452

[6] Lureau F, Matras G, Chalus O, Derycke C, Morbieu T, Radier C, Casagrande O, Laux S, Ricaud S, Rey G and et al 2020 *High Power Laser Science and Engineering* **8** e43

[7] Danson C N, Haefner C, Bromage J, Butcher T, Chanteloup J C F, Chowdhury E A, Galvanauskas A, Gizzi L A, Hein J, Hillier D I and et al 2019 *High Power Laser Science and Engineering* **7** e54

[8] Yoon, Kim Y G, Choi I W, Sung J H, Lee H W, Lee S K and Nam C H 2021 *Optica* **8** 630–635 URL http://www.osapublishing.org/optica/abstract.cfm?URI=optica-8-5-630

[9] Zhang P, Bulanov S S, Seipt D, Arefiev A V and Thomas A G R 2020 *Phys. Plasmas* **27** 050601

[10] Golub A, Villalba-Chávez S, Ruhl H and Müller C 2021 *Phys. Rev. D* **103**(1) 016009 URL https://link.aps.org/doi/10.1103/PhysRevD.103.016009

[11] Pike O, Mackenroth F, G H E and Rose S J 2014 *Nat. Photon.* **8** 434–436

[12] Ribeyre X, d'Humières E, Jansen O, Jequier S, Tikhonchuk V T and Lobet M 2016 *Phys. Rev. E* **93**(1) 013201 URL https://link.aps.org/doi/10.1103/PhysRevE.93.013201

[13] Wang T, Ribeyre X, Gong Z, Jansen O, d'Humières E, Stutman D, Toncian T and Arefiev A 2020 *Phys. Rev. Applied* **13**(5) 054024 URL https://link.aps.org/doi/10.1103/PhysRevApplied.13.054024

[14] Jansen O, Wang T, Stark D J, d'Humières E, Toncian T and Arefiev A V 2018 *Plasma Physics and Controlled Fusion* **60** 054006 URL https://doi.org/10.1088/1361-6587/aab222

[15] Chen H, Wilks S C, Bonlie J D, Liang E P, Myatt J, Price D F, Meyerhofer D D and Beiersdorfer P 2009 *Phys. Rev. Lett.* **102**(10) 105001 URL https://link.aps.org/doi/10.1103/PhysRevLett.102.105001

[16] Martinez B, Lobet M, Duclous R, d'Humières E and Gremillet L 2019 *Physics of Plasmas* **26** 103109 ISSN 1070-664X URL https://doi.org/10.1063/1.5118339

[17] Arber T D, Bennett K, Brady C S, Lawrence-Douglas A, Ramsay M G, Sircombe N J, Gillies P, Evans R G, Schmitz H, Bell A R and Ridgers C P 2015 *Plasma Phys. Control. Fusion* **57** 113001

[18] Erber T 1966 *Rev. Mod. Phys.* **38**(4) 626–659 URL https://link.aps.org/doi/10.1103/RevModPhys.38.626

[19] Di Piazza A, Müller C, Hatsagortsyan K Z and Keitel C H 2012 *Rev. Mod. Phys.* **84**(3) 1177–1228 URL https://link.aps.org/doi/10.1103/RevModPhys.84.1177

[20] Harding A K and Lai D 2006 *Rep. Prog. Phys.* **69** 2631–2708

[21] Ruffini R, Vereshchagin G and Xue S S 2010 *Phys. Rep.* **487** 1–40

[22] Burke D L, Field R C, Horton-Smith G, Spencer J E, Walz D, Berridge S C, Bugg W M, Shmakov K, Weidemann A W, Bula C, McDonald K T, Prebys E J, Bamber C, Boege S J, Koffas T, Kotseroglou T, Melissinos A C, Meyerhofer D D, Reis D A and Ragg W 1997 *Phys. Rev. Lett.* **79**(9) 1626–1629 URL https://link.aps.org/doi/10.1103/PhysRevLett.79.1626

[23] Reiss H R 1962 *J. Math. Phys.* **3** 59–67

[24] Ritus V I 1985 *J. Sov. Laser Res.* **6** 497–617 URL http://dx.doi.org/10.1007/BF01120220

[25] Bell A R and Kirk J G 2008 *Phys. Rev. Lett.* **101**(20) 200403 URL https://link.aps.org/doi/10.1103/PhysRevLett.101.200403

[26] Ridgers C P, Brady C S, Duclous R, Kirk J G, Bennett K, Arber T D, Robinson A P L and Bell A R 2012 *Phys. Rev. Lett.* **108**(16) 165006 URL https://link.aps.org/doi/10.1103/PhysRevLett.108.165006

[27] Timokhin A N and Harding A K 2019 *Astrophys. J.* **871** 12

[28] Kaw P and Dawson J 1970 *Phys. Fluids* **13** 472–481

[29] Palaniyappan S, Hegelich B M, Wu H C, Jung D, Gautier D C, Yin L, Albright B J, Johnson R P, Shimada T, Letzring S, Offermann D T, Ren J, Huang C, Hörlein R, Dromey B, Fernandez J C and Shah R C 2012 *Nat. Phys.* **8**(10) 763–769

[30] Zhu X L, Yu T P, Sheng Z M, Yin Y, Turcu I C E and Pukhov A 2016 *Nat. Commun.* **7** 13686

[31] Grismayer T, Vranic M, Martins J L, Fonseca R A and Silva L O 2017 *Phys. Rev. E* **95**(2) 023210 URL https://link.aps.org/doi/10.1103/PhysRevE.95.023210

[32] Gonoskov A, Bashinov A, Bastrakov S, Efimenko E, Ilderton A, Kim A, Marklund M, Meyerov I, Muraviev A and Sergeev A 2017 *Phys. Rev. X* **7**(4) 041003 URL https://link.aps.org/doi/10.1103/PhysRevX.7.041003

[33] Weber S, Bechet S, Borneis S, Brabec L, Bučka M, Chacon-Golcher E, Ciappina M, DeMarco M, Fajstavr A, Falk K, Garcia E R, Grosz J, Gu Y J, Hernandez J C, Holec M, Janečka P, Jantač M, Jirka M, Kadlecova H, Khikhlukha D, Klimo O, Korn G, Kramer D, Kumar D, Lastovička T, Lutoslawski P, Morejon L, Olšovcová V, Rajdl M, Renner O, Rus B, Singh S, Šmid M, Sokol M, Versaci R, Vrána R, Vranic M, Vyskočil J, Wolf A and Yu Q 2017 *Matter and Radiation at Extremes* **2** 149–176

[34] Gales S, Tanaka K A, Balabanski D L, Negoita F, Stutman D, Tesileanu O, Ur C A, Ursescu D, Andrei I, Ataman S, Cernaianu M O, D'Alessi L, Dancus I, Diaconescu B, Djourelov N, Filipescu D F, Ghenuche P, Ghita D G, Matei C, Seto K, Zeng M and Zamfir N V 2018 *Rep. Prog. Phys.* **81** 094301

[35] Papadopoulos D, Zou J, Le Blanc C, Chériaux G, Georges P, Druon F, Mennerat G, Ramirez P, Martin L, Fréneaux A, Beluze A, Lebas N, Monot P, Mathieu F and Audebert P 2016 *High Power Laser Science and Engineering* **4** e34

[36] Snyder J, Ji L L, George K M, Willis C, Cochran G E, Daskalova R L, Handler A, Rubin T, Poole P L, Nasir D, Zingale A, Chowdhury E, Shen B F and Schumacher D W 2019 *Phys. Plasmas* **26** 033110 URL https://doi.org/10.1063/1.5087409

[37] Bailly-Grandvaux M, Kawahito D, McGuffey C, Strehlow J, Edghill B, Wei M S, Alexander N, Haid A, Brabetz C, Bagnoud V, Hollinger R, Capeluto M G, Rocca J J and Beg F N 2020 *Phys. Rev. E* **102**(2) 021201 URL https://link.aps.org/doi/10.1103/PhysRevE.102.021201

[38] Bonometto S and Rees M J 1971 *Mon. Not. R. Astron. Soc.* **152** 21–35 ISSN 0035-8711

[39] Piran T 2005 *Rev. Mod. Phys.* **76**(4) 1143–1210 URL https://link.aps.org/doi/10.1103/RevModPhys.76.1143

[40] Chen A Y, Cruz F and Spitkovsky A 2020 *Astrophys. J.* **889** 69

[41] Stark D J, Toncian T and Arefiev A V 2016 *Phys. Rev. Lett.* **116**(18) 185003 URL https://link.aps.org/doi/10.1103/PhysRevLett.116.185003

[42] Williams J 2019 Private communications at General Atomics

[43] Ridgers C P, Kirk J G, Duclous R, Blackburn T G, Brady C S, Bennett K, Arber T D and Bell A R 2014 *J. Comp. Phys.* **260** 273–285 URL http://www.sciencedirect.com/science/article/pii/S0021999113008061

[44] Sauter F 1931 *Z. Phys.* **69** 742

[45] Heisenberg W and Euler H 1936 *Z. Phys.* **98** 714

[46] Schwinger J 1951 *Phys. Rev.* **82**(5) 664–679 URL http://link.aps.org/doi/10.1103/PhysRev.82.664

[47] Gonoskov A, Bastrakov S, Efimenko E, Ilderton A, Marklund M, Meyerov I, Muraviev A, Sergeev A, Surmin I and Wallin E 2015 *Phys. Rev. E* **92**(2) 023305 URL http://link.aps.org/doi/10.1103/PhysRevE.92.023305

[48] Sarri G, Schumaker W, Di Piazza A, Vargas M, Dromey B, Dieckmann M E, Chvykov V, Maksimchuk A, Yanovsky V, He Z H, Hou B X, Nees J A, Thomas A G R, Keitel C H, Zepf M and Krushelnick K 2013 *Phys. Rev. Lett.* **110**(25) 255002 URL http://link.aps.org/doi/10.1103/PhysRevLett.110.255002

[49] Gong Z, Mackenroth F, Wang T, Yan X Q, Toncian T and Arefiev A V 2020 *Phys. Rev. E* **102**(1) 013206 URL https://link.aps.org/doi/10.1103/PhysRevE.102.013206

[50] Neitz N and Di Piazza A 2013 *Phys. Rev. Lett.* **111**(5) 054802 URL http://link.aps.org/doi/10.1103/PhysRevLett.111.054802

[51] Blackburn T G, Ridgers C P, Kirk J G and Bell A R 2014 *Phys. Rev. Lett.* **112**(1) 015001 URL https://link.aps.org/doi/10.1103/PhysRevLett.112.015001

[52] Vranic M, Grismayer T, Fonseca R A and Silva L O 2016 *New J. Phys.* **18** 073035 URL http://stacks.iop.org/1367-2630/18/i=7/a=073035

[53] Cole J M, Behm K T, Gerstmayr E, Blackburn T G, Wood J C, Baird C D, Duff M J, Harvey C, Ilderton A, Joglekar A S, Krushelnick K, Kuschel S, Marklund M, McKenna P, Murphy C D, Poder K, Ridgers C P, Samarin G M, Sarri G, Symes D R, Thomas A G R, Warwick J, Zepf M, Najmudin Z and Mangles S P D 2018 *Phys. Rev. X* **8**(1) 011020 URL https://link.aps.org/doi/10.1103/PhysRevX.8.011020

[54] Poder K, Tamburini M, Sarri G, Di Piazza A, Kuschel S, Baird C D, Behm K, Bohlen S, Cole J M, Corvan D J, Duff M, Gerstmayr E, Keitel C H, Krushelnick K, Mangles S P D, McKenna P, Murphy C D, Najmudin Z, Ridgers C P, Samarin G M, Symes D R, Thomas A G R, Warwick J and Zepf M 2018 *Phys. Rev. X* **8**(3) 031004 URL https://link.aps.org/doi/10.1103/PhysRevX.8.031004

[55] Lobet M, Davoine X, d'Humières E and Gremillet L 2017 *Phys. Rev. Accel. Beams* **20**(4) 043401 URL https://link.aps.org/doi/10.1103/PhysRevAccelBeams.20.043401

[56] Ng Y J and Tsai W 1977 *Phys. Rev. D* **16**(2) 286–294 URL https://link.aps.org/doi/10.1103/PhysRevD.16.286

[57] Kozlenkov A A and Mitrofanov I G 1986 *Sov. Phys. JETP* **64**(6) 1173–1179 URL http://www.jetp.ac.ru/cgi-bin/e/index/e/64/6/p1173?a=list

[58] Hartin A 2018 *Int. J. Mod. Phys. A* **33** 1830011

[59] Hartin A 2006 *Second Order QED Processes in an Intense Electromagnetic Field* Ph.D. thesis University of London

[60] Baier V N, Katkov V M and Strakhovenko V M 1998 *Electromagnetic Processes at High Energies in Oriented Single Crystals* (Singapore: World Scientific)

[61] Jansen O, d'Humières E, Ribeyre X, Jequier S and Tikhonchuk V T 2018 *J. Comp. Phys.* **355** 582–596 ISSN 0021-9991 URL http://www.sciencedirect.com/science/article/pii/S0021999117308598

[62] Bragin S and Piazza A D 2020 Electron-positron annihilation into two photons in an intense plane-wave field (*Preprint* 2003.02231)

[63] Arefiev A V, Cochran G E, Schumacher D W, Robinson A P L and Chen G 2015 *Physics of Plasmas* **22** 013103 (*Preprint* https://doi.org/10.1063/1.4905523) URL https://doi.org/10.1063/1.4905523

[64] Gordon D and Hafizi B 2021 *Computer Physics Communications* **258** 107628 ISSN 0010-4655 URL https://www.sciencedirect.com/science/article/pii/S0010465520303015

[65] Tangtartharakul K, Chen G and Arefiev A 2021 *Journal of Computational Physics* **434** 110233 ISSN 0021-9991 URL https://www.sciencedirect.com/science/article/pii/S0021999121001285

[66] Bethe H and Heitler W 1934 *Proc. R. Soc. Lond. A* **146**(856) 83–112

[67] Motz J W, Olsen H A and Koch H W 1969 *Rev. Mod. Phys.* **41**(4) 581–639 URL https://link.aps.org/doi/10.1103/RevModPhys.41.581

[68] Denisenko O I 2008 *Laser Phys.* **18** 920–924

[69] Ilderton A, King B and MacLeod A J 2019 *Phys. Rev. D* **100**(7) 076002 URL https://link.aps.org/doi/10.1103/PhysRevD.100.076002

[70] Blackburn T G, MacLeod A J, Ilderton A, King B, Tang S and Marklund M 2021 *Physics of Plasmas* **28** 053103 (*Preprint* https://doi.org/10.1063/5.0044766) URL https://doi.org/10.1063/5.0044766

[71] Mourou G A, Tajima T and Bulanov S V 2006 *Rev. Mod. Phys.* **78**(2) 309–371 URL https://link.aps.org/doi/10.1103/RevModPhys.78.309

[72] Mourou G 2019 *Rev. Mod. Phys.* **91**(3) 030501 URL https://link.aps.org/doi/10.1103/RevModPhys.91.030501

[73] Ribeyre X, d'Humières E, Jansen O, Jequier S and Tikhonchuk V T 2016 *Plasma Physics and Controlled Fusion* **59** 014024 URL https://doi.org/10.1088/0741-3335/59/1/014024

[74] Ribeyre X, d'Humières E, Jequier S and Tikhonchuk V T 2018 *Plasma Physics and Controlled Fusion* **60** 104001 URL https://doi.org/10.1088/1361-6587/aad6da

[75] He Y, Blackburn T G, Toncian T and Arefiev A V 2021 *Communications Physics* **4** 139 URL https://doi.org/10.1038/s42005-021-00636-x

[76] Rinderknecht H G, Wang T, Garcia A L, Bruhaug G, Wei M S, Quevedo H J, Ditmire T, Williams J, Haid A, Doria D, Spohr K M, Toncian T and Arefiev A 2021 *New Journal of Physics* **23** 095009 URL https://doi.org/10.1088/1367-2630/ac22e7

[77] Arefiev A V, Breizman B N, Schollmeier M and Khudik V N 2012 *Phys. Rev. Lett.* **108**(14) 145004 URL https://link.aps.org/doi/10.1103/PhysRevLett.108.145004

[78] Robinson A P L, Arefiev A V and Neely D 2013 *Phys. Rev. Lett.* **111**(6) 065002 URL https://link.aps.org/doi/10.1103/PhysRevLett.111.065002

[79] Arefiev A V, Khudik V N and Schollmeier M 2014 *Physics of Plasmas* **21** 033104 URL https://doi.org/10.1063/1.4867491

[80] Nakamura T, Koga J K, Esirkepov T Z, Kando M, Korn G and Bulanov S V 2012 *Phys. Rev. Lett.* **108**(19) 195001 URL https://link.aps.org/doi/10.1103/PhysRevLett.108.195001

[81] Lezhnin K V, Sasorov P V, Korn G and Bulanov S V 2018 *Physics of Plasmas* **25** 123105 URL https://doi.org/10.1063/1.5062849

[82] Xue K, Dou Z K, Wan F, Yu T P, Wang W M, Ren J R, Zhao Q, Zhao Y T, Xu Z F and Li J X 2020 *Matter and Radiation at Extremes* **5** 054402 (*Preprint* https://doi.org/10.1063/5.0007734) URL https://doi.org/10.1063/5.0007734

[83] Stark D J, Bhattacharjee C, Arefiev A V, Toncian T, Hazeltine R D and Mahajan S M 2015 *Phys. Rev. Lett.* **115**(2) 025002 URL https://link.aps.org/doi/10.1103/PhysRevLett.115.025002

[84] Arefiev A, Stark D J, Toncian T and Murakami M 2020 *Physics of Plasmas* **27** 063106 URL https://doi.org/10.1063/5.0008018

[85] Huang T W, Zhou C T, Zhang H, Wu S Z, Qiao B, He X T and Ruan S C 2017 *Phys. Rev. E* **95**(4) 043207 URL https://link.aps.org/doi/10.1103/PhysRevE.95.043207

[86] Khudik V, Arefiev A, Zhang X and Shvets G 2016 *Physics of Plasmas* **23** 103108 URL https://doi.org/10.1063/1.4964901

[87] Zhang X, Khudik V N, Pukhov A and Shvets G 2016 *Plasma Physics and Controlled Fusion* **58** 034011 URL https://doi.org/10.1088/0741-3335/58/3/034011

[88] Jackson J D 1975 *Classical electrodynamics; 2nd ed.* (New York, NY: Wiley)

[89] Landau L D 2013 *The Classical Theory of Fields* vol 2 (Elsevier)

[90] Capdessus R, Gremillet L and McKenna P 2020 *New Journal of Physics* **22** 113003 URL https://doi.org/10.1088/1367-2630/abc1fa

[91] Gu Y J, Klimo O, Bulanov S V and Weber S 2018 *Commun. Phys.* **1** 93 URL https://doi.org/10.1038/s42005-018-0095-3

[92] Brady C S, Ridgers C P, Arber T D, Bell A R and Kirk J G 2012 *Phys. Rev. Lett.* **109**(24) 245006 URL https://link.aps.org/doi/10.1103/PhysRevLett.109.245006

[93] Gu Y J, Klimo O, Weber S and Korn G 2016 *New Journal of Physics* **18** 113023 URL https://doi.org/10.1088/1367-2630/18/11/113023

[94] Adam J, Adamczyk L, Adams J R, Adkins J K, Agakishiev G, Aggarwal M M, Ahammed Z, Alekseev I, Anderson D M, Aparin A, Aschenauer E C, Ashraf M U, Atetalla F G, Attri A, Averichev G S, Bairathi V, Barish K, Behera A, Bellwied R, Bhasin A, Bielcik J, Bielcikova J, Bland L C, Bordyuzhin I G, Brandenburg J D, Brandin A V, Butterworth J, Caines H, Calderón de la Barca Sánchez M, Cebra D, Chakaberia I, Chaloupka P, Chan B K, Chang F H, Chang Z, Chankova-Bunzarova N, Chatterjee A, Chen D, Chen J H, Chen X, Chen Z, Cheng J, Cherney M, Chevalier M, Choudhury S, Christie W, Crawford H J, Csanád M, Daugherity M, Dedovich T G, Deppner I M, Derevschikov A A, Didenko L, Dong X, Drachenberg J L, Dunlop J C, Edmonds T, Elsey N, Engelage J, Eppley G, Esha R, Esumi S, Evdokimov O, Ewigleben A, Eyser O, Fatemi R, Fazio S, Federic P, Fedorisin J, Feng C J, Feng Y, Filip P, Finch E, Fisyak Y, Francisco A, Fulek L, Gagliardi C A, Galatyuk T, Geurts F, Gibson A, Gopal K, Grosnick D, Hamad A I, Hamed A, Harris J W, He S, He W, He X, Heppelmann S, Heppelmann S, Herrmann N, Hoffman E, Holub L, Hong Y, Horvat S, Hu Y, Huang H Z, Huang S L, Huang T, Huang X, Humanic T J, Huo P, Igo G, Isenhower D, Jacobs W W, Jena C, Jentsch A, JI Y, Jia J, Jiang K, Jowzaee S, Ju X, Judd E G, Kabana S, Kabir M L, Kagamaster S, Kalinkin D, Kang K, Kapukchyan D, Kauder K, Ke H W, Keane D, Kechechyan A, Kelsey M, Khyzhniak Y V, Kikoła D P, Kim C, Kimelman B, Kincses D, Kinghorn T A, Kisel I, Kiselev A, Kisiel A, Klein S R, Kocan M, Kochenda L, Kosarzewski L K, Kramarik L, Kravtsov P, Krueger K, Kulathunga Mudiyanselage N, Kumar L, Kunnawalkam Elayavalli R, Kwasizur J H, Lacey R, Lan S, Landgraf J M, Lauret J, Lebedev A, Lednicky R, Lee J H, Leung Y H, Li C, Li W, Li W, Li X, Li Y, Liang Y, Licenik R, Lin T, Lin Y, Lisa M A, Liu F, Liu H, Liu P, Liu P, Liu T, Liu X, Liu Y, Liu Z, Ljubicic T, Llope W J, Longacre R S, Lukow N S, Luo S, Luo X, Ma G L, Ma L, Ma R, Ma Y G, Magdy N, Majka R, Mallick D, Margetis S, Markert C, Matis H S, Mazer J A, Minaev N G, Mioduszewski S, Mohanty B, Mooney I, Moravcova Z, Morozov D A, Nagy M, Nam J D, Nasim M, Nayak K, Neff D, Nelson J M, Nemes D B, Nie M, Nigmatkulov G, Niida T, Nogach L V, Nonaka T,

Odyniec G, Ogawa A, Oh S, Okorokov V A, Page B S, Pak R, Pandav A, Panebratsev Y, Pawlik B, Pawlowska D, Pei H, Perkins C, Pinsky L, Pintér R L, Pluta J, Porter J, Posik M, Pruthi N K, Przybycien M, Putschke J, Qiu H, Quintero A, Radhakrishnan S K, Ramachandran S, Ray R L, Reed R, Ritter H G, Roberts J B, Rogachevskiy O V, Romero J L, Ruan L, Rusnak J, Sahoo N R, Sako H, Salur S, Sandweiss J, Sato S, Schmidke W B, Schmitz N, Schweid B R, Seck F, Seger J, Sergeeva M, Seto R, Seyboth P, Shah N, Shahaliev E, Shanmuganathan P V, Shao M, Shen F, Shen W Q, Shi S S, Shou Q Y, Sichtermann E P, Sikora R, Simko M, Singh J, Singha S, Smirnov N, Solyst W, Sorensen P, Spinka H M, Srivastava B, Stanislaus T D S, Stefaniak M, Stewart D J, Strikhanov M, Stringfellow B, Suaide A A P, Sumbera M, Summa B, Sun X M, Sun Y, Sun Y, Surrow B, Svirida D N, Szymanski P, Tang A H, Tang Z, Taranenko A, Tarnowsky T, Thomas J H, Timmins A R, Tlusty D, Tokarev M, Tomkiel C A, Trentalange S, Tribble R E, Tribedy P, Tripathy S K, Tsai O D, Tu Z, Ullrich T, Underwood D G, Upsal I, Van Buren G, Vanek J, Vasiliev A N, Vassiliev I, Videbæk F, Vokal S, Voloshin S A, Wang F, Wang G, Wang J S, Wang P, Wang Y, Wang Y, Wang Z, Webb J C, Weidenkaff P C, Wen L, Westfall G D, Wieman H, Wissink S W, Witt R, Wu Y, Xiao Z G, Xie G, Xie W, Xu H, Xu N, Xu Q H, Xu Y F, Xu Y, Xu Z, Xu Z, Yang C, Yang Q, Yang S, Yang Y, Yang Z, Ye Z, Ye Z, Yi L, Yip K, Zbroszczyk H, Zha W, Zhang D, Zhang S, Zhang S, Zhang X P, Zhang Y, Zhang Y, Zhang Z J, Zhang Z, Zhao J, Zhong C, Zhou C, Zhu X, Zhu Z, Zurek M and Zyzak M (STAR Collaboration) 2021 *Phys. Rev. Lett.* **127**(5) 052302 URL https://link.aps.org/doi/10.1103/PhysRevLett.127.052302

[95] Berestetskii V B, Lifshitz E M and Pitaevskii L P 1982 *Quantum Electrodynamics* vol 4 (Elsevier)

[96] Blackburn T G, Ilderton A, Marklund M and Ridgers C P 2019 *New Journal of Physics* **21** 053040 URL https://doi.org/10.1088/1367-2630/ab1e0d

[97] Vranic M, Grismayer T, Meuren S, Fonseca R A and Silva L O 2019 *Physics of Plasmas* **26** 053103 (*Preprint* https://doi.org/10.1063/1.5090992) URL https://doi.org/10.1063/1.5090992

[98] Zhu X L, Yu T P, Chen M, Weng S M and Sheng Z M 2018 *New Journal of Physics* **20** 083013 URL https://doi.org/10.1088/1367-2630/aad71a

[99] Kettle B, Hollatz D, Gerstmayr E, Samarin G M, Alejo A, Astbury S, Baird C, Bohlen S, Campbell M, Colgan C, Dannheim D, Gregory C, Harsh H, Hatfield P, Hinojosa J, Katzir Y, Morton J, Murphy C D, Nurnberg A, Osterhoff J, Pérez-Callejo G, Põder K, Rajeev P P, Roedel C, Roeder F, Salgado F C, Sarri G, Seidel A, Spannagel S, Spindloe C, Steinke S, Streeter M J V, Thomas A G R, Underwood C, Watt R, Zepf M, Rose S J and Mangles S P D 2021 *New Journal of Physics* **23** 115006 URL https://doi.org/10.1088/1367-2630/ac3048

[100] Ji L L, Pukhov A, Nerush E N, Kostyukov I Y, Shen B F and Akli K U 2014 *Physics of Plasmas* **21** 023109 (*Preprint* https://doi.org/10.1063/1.4866014) URL https://doi.org/10.1063/1.4866014

[101] Zhang L q, Wu S d, Huang H r, Lan H y, Liu W y, Wu Y c, Yang Y, Zhao Z q, Zhu Z c and Luo W 2021 *Physics of Plasmas* **28** 023110 (*Preprint* https://doi.org/10.1063/5.0030909) URL https://doi.org/10.1063/5.0030909

[102] Zhang H, Zhao J, Hu Y, Li Q, Lu Y, Cao Y, Zou D, Sheng Z, Pegoraro F, McKenna P, Shao F and Yu T 2021 *High Power Laser Science and Engineering* **9** e43

[103] Wang X B, Hu G Y, Zhang Z M, Gu Y Q, Zhao B, Zuo Y and Zheng J 2020 *High Power Laser Science and Engineering* **8** e34

[104] He Y, Yeh I L, Blackburn T G and Arefiev A 2021 *New Journal of Physics* **23** 115005 URL https://doi.org/10.1088/1367-2630/ac3049

[105] Hund J F, Paguio R R, Frederick C A, Nikroo A and Thi M 2006 *Fusion Science and Technology* **49** 669–675 (*Preprint* https://doi.org/10.13182/FST06-A1184)

[106] Nagai K, Musgrave C S A and Nazarov W 2018 *Physics of Plasmas* **25** 030501 (*Preprint* https://doi.org/10.1063/1.5009689)

[107] Willingale L, Arefiev A V, Williams G J, Chen H, Dollar F, Hazi A U, Maksimchuk A, Manuel M J E, Marley E, Nazarov W, Zhao T Z and Zulick C 2018 *New Journal of Physics* **20** 093024 URL https://doi.org/10.1088/1367-2630/aae034

[108] Wang T, Gong Z and Arefiev A 2020 *Physics of Plasmas* **27** 053109 (*Preprint* https://doi.org/10.1063/5.0006295) URL https://doi.org/10.1063/5.0006295

[109] Esnault L, d'Humières E, Arefiev A and Ribeyre X 2021 *Plasma Physics and Controlled Fusion* **63** 125015 URL https://doi.org/10.1088/1361-6587/ac2e3e

[110] Blackburn T G, Ilderton A, Murphy C D and Marklund M 2017 *Phys. Rev. A* **96**(2) 022128 URL https://link.aps.org/doi/10.1103/PhysRevA.96.022128

[111] Wang T, Gong Z, Chin K and Arefiev A 2019 *Plasma Physics and Controlled Fusion* **61** 084004 URL https://doi.org/10.1088/1361-6587/ab2499

[112] Wang T and Arefiev A 2020 *Phys. Rev. Lett.* **125**(7) 079501 URL https://link.aps.org/doi/10.1103/PhysRevLett.125.079501

[113] Takizuka T and Abe H 1977 *Journal of Computational Physics* **25** 205–219 ISSN 0021-9991 URL https://www.sciencedirect.com/science/article/pii/0021999177900997

[114] Nanbu K 1997 *Phys. Rev. E* **55**(4) 4642–4652 URL https://link.aps.org/doi/10.1103/PhysRevE.55.4642

[115] Nanbu K 1997 *Phys. Rev. E* **56**(6) 7314–7314 URL https://link.aps.org/doi/10.1103/PhysRevE.56.7314

[116] Sentoku Y and Kemp A 2008 *Journal of Computational Physics* **227** 6846–6861 ISSN 0021-9991 URL https://www.sciencedirect.com/science/article/pii/S0021999108001988

[117] Higginson D P, Holod I and Link A 2020 *Journal of Computational Physics* **413** 109450 ISSN 0021-9991 URL https://www.sciencedirect.com/science/article/pii/S0021999120302242

[118] Arefiev A, Gong Z and Robinson A P L 2020 *Phys. Rev. E* **101**(4) 043201 URL https://link.aps.org/doi/10.1103/PhysRevE.101.043201

[119] He Y, Blackburn T G, Toncian T and Arefiev A 2022 *Physics of Plasmas* **29** 053105 URL https://doi.org/10.1063/5.0086577

[120] Medin Z and Lai D 2010 *Monthly Notices of the Royal Astronomical Society* **406** 1379–1404 ISSN 0035-8711 URL https://doi.org/10.1111/j.1365-2966.2010.16776.x

[121] Beloborodov A M 2008 *The Astrophysical Journal* **683** L41 URL https://dx.doi.org/10.1086/590079

[122] Philippov A A and Spitkovsky A 2018 *The Astrophysical Journal* **855** 94 URL https://dx.doi.org/10.3847/1538-4357/aaabbc

[123] Chen A Y, Uzdensky D and J D 2022 Synchrotron pair production equilibrium in relativistic magnetic reconnection (*Preprint* 2209.03249)

[124] Hakobyan H, Philippov A and Spitkovsky A 2023 *The Astrophysical Journal* **943** 105 URL https://dx.doi.org/10.3847/1538-4357/acab05

[125] Tanaka K A, Spohr K M, Balabanski D L, Balascuta S, Capponi L, Cernaianu M O, Cuciuc M, Cucoanes A, Dancus I, Dhal A, Diaconescu B, Doria D, Ghenuche P, Ghita D G, Kisyov S, Nastasa V, Ong J F, Rotaru F, Sangwan D, Söderström P A, Stutman D, Suliman G, Tesileanu O, Tudor L, Tsoneva N, Ur C A, Ursescu D and Zamfir N V 2020 *Matter and Radiation at Extremes* **5** 024402 ISSN 2468-2047 URL https://doi.org/10.1063/1.5093535

[126] Yoon J W, Jeon C, Shin J, Lee S K, Lee H W, Choi I W, Kim H T, Sung J H and Nam C H 2019 *Optics express* **27** 20412–20420

[127] Gonoskov A, Blackburn T G, Marklund M and Bulanov S S 2022 *Rev. Mod. Phys.* **94**(4) 045001 URL https://link.aps.org/doi/10.1103/RevModPhys.94.045001

[128] Di Piazza A, Willingale L and Zuegel J 2022 Multi-petawatt physics prioritization (mp3) workshop report (*Preprint* 2211.13187)

[129] Gessner S, Adli E, Allen J M, An W, Clarke C I, Clayton C E, Corde S, Delahaye J, Frederico J, Green S Z, Hast C, Hogan M J, Joshi C, Lindstrom C A, Lipkowitz N, Litos M, Lu W, Marsh K A, Mori W B, O'shea B, Vafaei-Najafabadi N, Walz D, Yakimenko V and Yocky G 2016 *Nature communications* **7** 1–6

[130] Zhou S, Hua J, An W, Mori W B, Joshi C, Gao J and Lu W 2021 *Physical Review Letters* **127** 174801

[131] Silva T, Amorim L, Downer M, Hogan M, Yakimenko V, Zgadzaj R and Vieira J 2021 *Physical review letters* **127** 104801

[132] Vieira J and Mendonça J 2014 *Physical Review Letters* **112** 215001

[133] Vranic M, Klimo O, Korn G and Weber S 2018 *Scientific reports* **8** 1–11

[134] Zhu X L, Chen M, Yu T P, Weng S M, He F and Sheng Z M 2019 *Matter and Radiation at Extremes* **4** 014401

[135] Liu J X, Yu T P, Cao L Q, Zhao Y, Zhang G B, Ma L, Qu S, Ma Y Y, Shao F Q and Zhao J 2019 *Plasma Physics and Controlled Fusion* **61** 065014

[136] Zhao J, Hu Y T, Lu Y, Zhang H, Hu L X, Zhu X L, Sheng Z M, Turcu I C E, Pukhov A, Shao F Q and Yu T P 2022 *Communications Physics* **5** 1–10

[137] Mercuri-Baron A, Grech M, Niel F, Grassi A, Lobet M, Piazza A D and Riconda C 2021 *New Journal of Physics* **23** 085006 URL https://dx.doi.org/10.1088/1367-2630/ac1975

[138] Martinez B, Barbosa B and Vranic M 2023 *Phys. Rev. Accel. Beams* **26**(1) 011301 URL https://link.aps.org/doi/10.1103/PhysRevAccelBeams.26.011301

[139] Ji L L, Pukhov A, Kostyukov I Y, Shen B F and Akli K 2014 *Phys. Rev. Lett.* **112**(14) 145003 URL https://link.aps.org/doi/10.1103/PhysRevLett.112.145003

[140] Audet T L, Alejo A, Calvin L, Cunningham M H, Frazer G R, Nersisyan G, Phipps M, Warwick J R, Sarri G, Hafz N A M, Kamperidis C, Li S and Papp D 2021 *Phys. Rev. Accel. Beams* **24**(7) 073402 URL https://link.aps.org/doi/10.1103/PhysRevAccelBeams.24.073402

[141] Krause-Rehberg R R 1999 *Positron annihilation in semiconductors: defect studies / R. Krause-Rehberg, H.S. Leipner.* Springer series in solid-state sciences, 127 (Berlin: Springer) ISBN 3540643710

[142] https://eli-laser.eu

[143] https://corels.ibs.re.kr/html/corels_en/

[144] Sentoku Y, Paraschiv I, Royle R, Mancini R and Johzaki T 2014 *Physical Review E* **90** 051102

[145] Pandit R R and Sentoku Y 2012 *Physics of Plasmas* **19** 073304

[146] Sentoku Y, Mima K, Taguchi T, Miyamoto S and Kishimoto Y 1998 *Physics of Plasmas* **5** 4366–4372

[147] Wilks S, Kruer W, Tabak M and Langdon A 1992 *Physical review letters* **69** 1383

[148] Koga J 2004 *Physical Review E* **70** 046502

[149] Sentoku Y, Kruer W, Matsuoka M and Pukhov A 2006 *Fusion Science and Technology* **49** 278–296

[150] Landau L D and Lifshitz E M 1978 *Quantum mechanics 3rd edition* (Pergamon,London)

[151] Royle R, Sentoku Y, Mancini R C, Paraschiv I and Johzaki T 2017 *Physical Review E* **95** 063203

[152] Lee C E 1962 *The discrete Sn approximation to transport theory* vol 2595 (Los Alamos Scientific Laboratory of the University of California)

[153] Hubbell J H, Gimm H A and O/verbo/ I 1980 *Journal of physical and chemical reference data* **9** 1023–1148

[154] Arefiev A V, Robinson A P L and Khudik V N 2015 *Journal of Plasma Physics* **81** 475810404

[155] Arefiev A V, Khudik V N, Robinson A P L, Shvets G, Willingale L and Schollmeier M 2016 *Physics of Plasmas* **23** 056704

[156] Wang T, Blackman D, Chin K and Arefiev A 2021 *Phys. Rev. E* **104**(4) 045206 URL https://link.aps.org/doi/10.1103/PhysRevE.104.045206

[157] Singh P K, Li Y F, Huang C K, Moreau A, Hollinger R, Junghans A, Favalli A, Calvi C, Wang S, Wang Y, Song H, Rocca J J, Reinovsky R E and Palaniyappan S 2022 *Nat. Commun.* **13**(54) URL https://doi.org/10.1038/s41467-021-27691-w

[158] Gong Z, Mackenroth F, Yan X Q and Arefiev A 2019 *Scientific reports* **9**

[159] Yeh I L, Tangtartharakul K, Rinderknecht H G, Willingale L and Arefiev A 2021 *New Journal of Physics* **23** 095010 URL https://dx.doi.org/10.1088/1367-2630/ac2394